



SMOS L2 OS Algorithm Theoretical Baseline
Document

Doc: SO-TN-ARG-GS-0007
Issue: 4 Rev: 1
Date: 12 February 2021
Page: i

Title: **SMOS L2 OS Algorithm Theoretical Baseline Document**

Doc code: **SO-TN-ARG-GS-0007**

Issue: **4**

Revision: **1**

Date: **12 February 2021**

	Name	Function	Company	Signature	Date
Prepared	N. Reul	Science Lead	IFREMER		12-02-2021
	J. Boutin	ESL	LOCEAN		12-02-2021
	JL. Vergely	ESL	ACRI-ST		12-02-2021
	A. Turiel	ESL	ICM-CSIC		12-02-2021
	J. Tenerelli	ESL	ODL		12-02-2021
Reviewed	M. Arias	Project Manager	ARGANS		12-02-2021
Released	R. Sabia	Technical Officer	ESA		

Proprietary/Copyright Information

This material contains proprietary and/or copyright information of ARGANS Ltd. (ARGANS) and may not be copied, used, or disclosed without permission of ARGANS.

© Copyright ARGANS Ltd. (2021)

COMMERCIAL IN CONFIDENCE



Change Record

Issue	Revision	Date	Description	Approval
Draft	1	14-06-2005	Initial version at Software Requirement Review	
Draft	2	17-06-2005	Minor updates before SRR	
Draft	3	24-06-2005	Updates before Preliminary Design Review	
Draft	4	7-11-2005	Major revision after Preliminary Design Review	
Draft	5	20-12-2005	Revision before Critical Design Review	
Draft	6	23-01-2006	Update after CDR	
Draft	6.4	3-04-2006	Update after Mid Term Review	

	Page #	Section #	Comments	Date
issue 1.0		1.2	Updated list of variables	30-06-2006
	38	3.5	Updated mathematical description of sunglint and bistatic scattering coefficients	
	121	4.14.2.3	Section on parameter update during iterative retrieval scheme.	
	145	5	Update of the secondary neural network retrieval algorithm	
	194	Annex	Updated table of TBD / TBC	

issue 1.0b	4	1.2	Changed sea state flags	21-07-2006
	6	1.2	Definition of Resolution confirmed	
	7	1.2	$\sigma_{Tb_model1, 2 \text{ and } 3}$	
	14	1.2	Added F_g and T_g for high TEC gradient	
	14	1.2	Changed names for variables τ_{GAS} $\tau_{GAS} \tau_{GAS} T_{bGAS} DT_{GAS}$	
	16	1.2	Changed numbers of referred AGDP tables (error coming from old version)	
	17, 18	1.2	Corrected name of variables $Dg_quality_SSSX$ (underscore missing)	
	17, 18	1.2	Corrected units in T_g and D_g for SSS	
	20	2.1.1	Two-scale is the default model	
	21	2.1.3	Corrected "decision tree" in figure	
	24	3.1	New flags for sea state development	

Proprietary/Copyright Information

This material contains proprietary and/or copyright information of ARGANS Ltd. (ARGANS) and may not be copied, used, or disclosed without permission of ARGANS.

© Copyright ARGANS Ltd. (2021)

COMMERCIAL IN CONFIDENCE



	39	4	Removed reference to non-standard document (its contents is in annex)	
	52	4.2.3	Removed reference to ECMWF current speed	
	88	4.8.2	Defined Fg and Tg for high TEC gradient	
	89-94	4.9	Major update of atmospheric section	
	117	4.14.2.2	Corrected name of variables Dg_quality_SSSX	
	118, 120	4.14.2.2	Added X to SSS variables names	
	122	4.15	Updated section on Tb42.5° computation	
	132	6	Updated description of Tb42.5° fields	
	133	6	Added Fg_quality_SSSX to UDP	
	134	6	Added Fg_TEC_gradient	
	136	6	ECMWF value and 999 for sigma in DAP when a parameter has not been retrieved	
	136	6	Added Tbgal, Tbatm and tau to DAP	
	several		Comments on text removed (except in AGDP) and transferred to Pending Actions list when necessary	

issue 1.1	v-vii	Table of contents	False titles purged throughout the document	15-09-2006
	10 18	1.2	Fg_outsideLUT_M1 added. Fg_quality_SSSX description updated. Tg_quality_SSSX removed.	
	52	4.2.1.2	Definition of Fg_outsideLUT_M1 added.	
	82	4.6.1	Sentence added to introduce the new sky glitter corrections annex	
	97	4.10	Introduced void section for numbering coherence	
	111-112	4.14.1.1	Definition of $\sigma_{Tb_model_1}$ added.	
	121	4.14.2.2	New definition of Fg_quality_SSSX.	
	133	6.1	units for SST set to °C instead of K	
	134	6.1	Fg_quality_SSSX description updated.	
	195-233	Annex	New annex on celestial sky glitter corrections	

Proprietary/Copyright Information

This material contains proprietary and/or copyright information of ARGANS Ltd. (ARGANS) and may not be copied, used, or disclosed without permission of ARGANS.

© Copyright ARGANS Ltd. (2021)

COMMERCIAL IN CONFIDENCE



issue 1.1b	1	1.1	New Reference and applicable documents section	14-12-2006
	3	1.2	Reference to SO-L2-SSS-ACR-013 for acronyms	
	3	1.2	New References list to Definitions section	
	19	1.3	Fm_RSC_FLAG removed from variables list	
	82	4.6.1	Sentence modified	
	87-124	4.7	Galactic noise 2 annex moved to new regular section	
	126	4.8	New Reference list to Faraday rotation section	
	135	4.10	New cardioid model section	
	144-145	4.13.1.1.1	Pseudo-Stokes instead of angle correction	
	149-152	4.14.1.1	Two cases considered in the iterative convergence approach (yes/no model error)	
	153	4.14.1.2	Text corrected accordingly	
	158	4.14.2	Introduced model uncertainty computation	
	166-169	4.17	New section on auxiliary data bias correction	
	179	6	Dg_QIX removed from UDP	
	182	6	Tbgal substituted by Tbgal_refl in DAP	
	183	6	Fm_RSC_FLAG removed from DAP	
	190	Annex 2	New Reference list to Annex 2	

issue 1.1c	13-14	1.3	Variables from 4.7 added to list	1-02-2007
	15	1.3	Variables from 4.10 added to list	
	52	4.2.1.2	Interpolation method updated for model 1 LUT, as well as out of LUT range flag	

issue 1.1d	many	several	All grid point flag names modified to include class (Fg_ctrl_..., Fg_sc_...)	1-6-2007
	5, 28, 30	1.3, 3.2, 3.3	L1c flags names modified	
	7	1.3	a_factor changed to nsig	
	8	1.3	Tm_angle_sun removed from variables list	

Proprietary/Copyright Information

This material contains proprietary and/or copyright information of ARGANS Ltd. (ARGANS) and may not be copied, used, or disclosed without permission of ARGANS.

© Copyright ARGANS Ltd. (2021)

COMMERCIAL IN CONFIDENCE



	8, 11, 13, 14	1.3	Out of LUT range flags in variables list	
	10	1.3	Thresholds for foam and roughness corrections added to variables list	
	11	1.3	Duplicated Tm_high_gal_noise removed	
	18	1.3	New cardioid variables	
	23	3	Explanation of code for flags classes	
	32	3.4	a_factor changed to nsig	
	40	3.5.4.3	Flags for out of Sunlint LUT range	
	55, 66, 73, 83, 84	4.2.2, 4.3.3, 4.4.3, 4.5.5	Switch for foam and roughness correction based on a threshold for wind speed value	
	55	4.2.1.2	Flags for out of Roughness 1 LUT range	
	66	4.3.2	Flags for out of Roughness 2 LUT range	
	83	4.5.4.3	Flags for out of Foam LUT range	
	90	4.6.2.3	New exception handling subsection	
	116	4.7.9.3	Exception handling for galactic noise 2	
	128	4.8.2	Corrected names for Fg and Tg_TEC_gradient	
	137-138	4.10	Modified cardioid model section	
	138	4.11	Comment on SBC implementation	
	148	4.13.1.2	Sentence modified	
	159, 161	4.14.1.2 , 4.14.2.2	New definition of Dg_chi2 and Dg_chi2_P	
	164	4.14.2.2	Dg_quality_SSSX definition updated with respect to Fg_sc_sea_state_X	
	181, 182, 184	6	Acard parameters in UDP	
	183, 184	6	Fg_sc_sea_state_X (1 to 6) in UDP instead of Fg_young_seas and Fg_old_seas	
	184	6	Fg_num_meas_low, min moved to confidence flags list	
	186	6	Acard parameters in DAP	
	186	6	Fm_L1c_sun included in DAP	
	187-188	6	Out of LUT range flags included in DAP	

Proprietary/Copyright Information

This material contains proprietary and/or copyright information of ARGANS Ltd. (ARGANS) and may not be copied, used, or disclosed without permission of ARGANS.

© Copyright ARGANS Ltd. (2021)

COMMERCIAL IN CONFIDENCE



	195	Annex	Added pending action on section 4.3 update Two actions removed	
--	-----	-------	---	--

issue 2.0	4, 26, 184	1.3, 3.1, 6	Fg_sc_in_clim_ice introduced	15-6-2007
	6, 28, 30	1.3, 3.2, 3.3	Tg_DT_ice changed to Tm_DT_ice	
	18, 138	1.3, 4.10	Thresholds for cardioid ice detection	
	20, 159	1.3, 4.14.1.2	Tg_lambda_diaMax introduced	
	20, 160, 183	1.3, 4.14.1.2, 6	Fg_ctrl_marq introduced	
	137, 190, 196, 197	4.10, Annexes	Numbered to Annex-1, 2 and 3	
	152	4.14.1.1	Added sentence on cardioid parameters to be retrieved	
	160-161	4.14.1.2	Further explanations on Dg_chi2_P_X	
	196	Annex-2	Slot to add Boutin et al. paper	
	197	Annex-3	New action on Out-of-LUT-range	

issue 2.0a	iv-v	Change log	Issues 2.0, 2.0a, 2.0b renumbered to 1.1c, 1.1d, 2.0 for coherence with delivery to ESA	19-07-2007
	18, 188	1.3, 6	T _{eff} corrected to T _{eff}	
	20-22	1.3	New cardioid variables and flags listed	
	27	3.1	If no ECMWF data, grid point not processed	
	162	4.14.2	The same iterative retrieval method used for SSS will be applied to cardioid model	
	182-183	6	Small typos corrected	
	183	6	All Fg_ctr from DAP moved to UDP	
	183	6	Process descriptor flags moved here	
	183	6	New Fg_ctr_no_aux_data	
	183	6	New flags for cardioid model	
	184	6	New quality descriptor for cardioid model	
	185	6	Process descriptors table removed	
	185	6	New Diff_TB_Acard[NM]	
	186-188	6	Placeholders for seven retrieved parameters for 3 roughness and cardioid models	

Proprietary/Copyright Information

This material contains proprietary and/or copyright information of ARGANS Ltd. (ARGANS) and may not be copied, used, or disclosed without permission of ARGANS.

© Copyright ARGANS Ltd. (2021)

COMMERCIAL IN CONFIDENCE



	188	6	T_eff and T_eff_sigma removed (included now in placeholders for cardioid model)	
	188-189	6	Grid point descriptors and Out-of-LUT-range flags moved to general DAP table	
	196	Annex 3	New action added to update section 4.14 for pseudo-dielectric constant inversion	

issue 2.0b	3-4	1.3	New specific ECMWF flags for missing data. General flag removed	8-10-2007
	21	1.3	Tx and Ty at 42.5° in variables list	
	22	1.3	New flags for out-of-range values in AGDP LUTs	
	28	3.1	Tg_num_meas_valid is used only for warning	
	28	3.1	Control on missing ECMWF data separated for the 4 retrievals	
	29	3.2	Measurements outside AF_FOV might not be used for retrieval	
	31-32	3.3	Modified measurement selection diagrams	
	169	4.15	Tb at 42.5° at antenna level will be computed. Explanation on surface Tb study modified	
	174	4.17	Introduced new OoR LUT AGDP flags	
	184	6	ECMWF flags for missing data in UDP	
	184	6	Tx and Ty at 42.5° in UDP	
	190	6	OoR LUT AGDP flags in DAP	
	198	Annex	New action added to establish a method for not using or weighting points in the EAF-FOV	
	198	Annex	New action on changing 5 thresholds names	
	198	Annex	New action on missing flags for Tb_42.5	
	198	Annex	Removed redundant action item on 4.17	

issue 2.1	198	Annex	New action to confirm use of Fg_OoR_LUTAGDPT_param	9-10-2007
-----------	-----	-------	--	-----------

Proprietary/Copyright Information

This material contains proprietary and/or copyright information of ARGANS Ltd. (ARGANS) and may not be copied, used, or disclosed without permission of ARGANS.

© Copyright ARGANS Ltd. (2021)

COMMERCIAL IN CONFIDENCE



issue 2.2	5, 30, 32, 191	1.3, 3.2, 6	Fm_sun_limit introduced	10-12-2007
	5, 28, 31, 184	1.3, 3.1, 3.3, 6	Fg_ctrl_valid introduced	31-1-2008
	5, 6, 7, 28, 30, 32, 186, 187, 192	1.3, 3.1, 3.2, 3.3, 6	Measurement discrimination due to polarised galactic noise	29-1-2008
	7, 30, 32	1.3, 3.2, 3.3	Updated measurement selection due to galactic noise error (wind speed dependent)	12-12-2007
	20, 185	1.3, 6	Fg_ctrl_marq repeated 4 times (4 retrievals)	12-12-2007
	21, 169, 185	1.3, 4.15, 6	Introduced Fg_ctrl_no_surface	10-12-2007
	22, 183	1.3, 6	Introduced 3rd coordinate of grid point	
	28	3.1	Dg_num_outliers shall be divided by Dg_num_meas_l1c to compare with Tg_num_outliers_max%	10-12-2007
	29	3.2	L1 RFI flag : « TBD by L1 » removed	24-1-2008
	30	3.2	Definition of Fm_valid referred to diagram in page 32	10-12-2007
	71	4.4.1.2	Fg_ctrl_foam_M3 removed from text as it is not used	10-12-2007
	169	4.15	Typo corrected	10-12-2007
	184	6	3 rd coordinate of grid point (altitude) in UDP	12-12-2007
	185	6	Fg_ctrl_no_aux_data removed (not used since issue 2.0b)	12-12-2007
	186	6	Excessive explanation removed from UDP	12-12-2007
	198	Annex	TBD/TBC column re-introduced in table	24-1-2008
	198	Annex	New action on generation of sky map	24-1-2008

	Page #	Section #	Comments	Date
issue 3.0	i, ii, all	cover, headings	Formatted to ARGANS version	9-6-2008
	vii	change log	Annotated missing change in issue 2.2	20-5-2008
	1	1	Change in annexes description	11-5-2008

Proprietary/Copyright Information

This material contains proprietary and/or copyright information of ARGANS Ltd. (ARGANS) and may not be copied, used, or disclosed without permission of ARGANS.

© Copyright ARGANS Ltd. (2021)

COMMERCIAL IN CONFIDENCE



	1	1.1	Updated applicable and reference documents	11-5-2008
	5, 6, 27, 28, 29	1.3	Several variables changed from percentage to fraction	7-5-2008
	8	1.3	New variables listed from 3.6 and 3.7	11-5-2008
	12, 69, 189	1.3, 4.3.2.3, 6	Fg_OoR_Rough2_dim5_Omega, not dim4	20-5-2008
	17, 19	1.3	Added missing units	11-5-2008
	17	1.3	Removed 4.11 variables from list	12-5-2008
	18	1.3	Introduced ECMWF codes in variables list	12, 22-5-2008
	19, 159, 184	1.3, 4.4.1.2, 6	Dg_num_iter is different for the 4 retrievals	20-5-2008
	20, 162	1.3, 4.14.2.2	Names for coefficients introduced in Tb sensitivity to SSS adjustment	7-2-2008
	several	1.3, 4.14, 4.17	AGDP renamed ECMWF Pre-Processing	7/12-5-2008
	21, 22	1.3	Completed variables list for 4.17 and 5	11-5-2008
	22, 182	1.3, 6	Grid point altitude removed from UDP	26-5-2008
	29	3.2	A switch to be implemented to optionally discard data outside the AF_FOV	14-5-2008
	43	3.6	Method to class sea state development	11-5-2008
	43, 44	3.7	Method to flag SST and SSS fronts	11-5-2008
	74	4.4.1.2	WC_U, WC_V changed to WSx, WSy	22-5-2008
	89	4.6	Galactic noise model 0 mentioned	8-2-2008
	142	4.11	Scene dependent bias section removed	12-5-2008
	154	4.14.1.1	Computation of theoretical uncertainties for retrieved parameters	12-5-2008
	155, 170	4.1.4.1.1.1, 4.17	Reference to SMOS ECMWF Pre-proc. doc.	11-5-2008
	156	4.14.1.2	Equation referred by number	12-5-2008
	173	4.17.3	New practical considerations section	12-5-2008
	184	6	Typos corrected in Dg_quality_SSSX	13-2-2008
	186	6	Lat, Long added to DAP	30-5-2008
	several	6	Merged cells in table (just aesthetics)	11-5-2008
	I, I-XVI, I	3 annexes	Pages renumbered to start at each annex	20-5-2008

Proprietary/Copyright Information

This material contains proprietary and/or copyright information of ARGANS Ltd. (ARGANS) and may not be copied, used, or disclosed without permission of ARGANS.

© Copyright ARGANS Ltd. (2021)

COMMERCIAL IN CONFIDENCE



	A1-I	Annex 1	Substituted by reference to Technical Note	20-5-2008
	A2-I - XVI	Annex 2	Added technical note on cardioid model	9/14-5-2008
	A3-I	Annex 3	New action to define Dg_quality_Acard	13-2-2008
	A3-I	Annex 3	Several pending actions closed	11/14-5-2008
	A3-I	Annex 3	New action on cross-checking ATBD-DPM variables names	18-5-2008
	9, 46	1.3, 4.1.1.1	Dielectric constant ϵ is expressed as $\epsilon' + j\epsilon''$	10-6-2008
	23	1.3	Dg_X_swath included in variables list	15-6-2008
	100, A3-I	4.7.2.2, A3	Removed TBD by N. Floury	1-7-2008
	173	4.17.3	New section on other auxiliary parameters bias removal (to match with TGRD)	1-7-2008
	A3-I	Annex 3	Removed action on checking SSA model	1-7-2008
	A3-I	Annex 3	New action on updating section 4.17	27-6-2008
	A3-I	Annex 3	Removed two completed actions and one comment	27-6/1-7-2008
	A1, A2, A3	Annex 1, 2 & 3	Added prefix to Annex page numbers	4-7-2008
	A3-I	Annex 3	Added new actions from AlgoVal#11	7-7-2008
	53, 99, A2-1	4.2, 4.6, Annex 2	Corrected missing references	8-7-2008
	1	1	Reference to annexes in introduction	30-9-2008
	145	4.13.1.1.1	Changes in text for coherence (word snapshot)	22-9-2008
	146	4.13.1.1.1	Strategy for Stokes 1 computation in full pol	19-9-2008
	155	4.14.1.1.1	Modified reference to ECMWF document	19-9-2008
	166	4.14.2.2	Dg_quality_Acard set to 0	19-9-2008
	166	4.14.3	Reference updated	22-9-2008
	A3-I - VII	Annex 3	New annex on Stokes 1 in full pol; previous Annex 3 becomes Annex 4	30-9-2008
	A4-I	Annex 4	Removed three pending actions	19-9-2008
	173	4.17.3	Added table of additional AGDP parameters	30-9-2008
	A4-I	Annex 4	Removed two pending actions	01-10-2008

Proprietary/Copyright Information

This material contains proprietary and/or copyright information of ARGANS Ltd. (ARGANS) and may not be copied, used, or disclosed without permission of ARGANS.

© Copyright ARGANS Ltd. (2021)

COMMERCIAL IN CONFIDENCE



	A4-I	Annex 4	Section 5: secondary Algorithm Description (neural network) moved to Annex 4; Annex 4 becomes Annex 5.	17-10-2008
	A5-I	Annex 5	Empty sections 4.7.9.2, 4.7.10 & four pending (obsolete) actions removed	17-10-2008
	175	5	SPH Quality Information Specification added	17-10-2008
	175	5	Edited SPH Quality Information Specification	27-10-2008

	Page #	Section #	Comments	Date
issue 3.1	147-150	4.13.1.1.2, 4.13.1	Corrections for galactic noise models behind a switch, updated dependencies table	21-01-2009

	Page #	Section #	Comments	Date
issue 3.2	22	1.3	Corrected Mean_Acq_Time definition & case: now called Mean_acq_time, as in IODD, code & product spec.	12-05-2009
issue 3.2	11, 67, 182	1.3, 4.3.3, 5	Corrected fg_oor_rough2_dim1..5 flags to match IODD LUT	22-05-2009
issue 3.2	4, 27, 31, 176	1.3, 3.1, 3.3, 5	Corrected meaning of fg_ctrl_ecmwf	27-05-2009

	Page #	Section #	Comments	Date
issue 3.3	18	1.3	Updated definitions of U* & WS	16-07-2009

	Page #	Section #	Comments	Date
issue 3.4	71-73	4.4.1	Roughness model 3 extended to cubic dependency on incidence angle	01-12-2009

	Page #	Section #	Comments	Date
issue 3.5		Annex 6	Added new Annex for OTTs	09-06-2010

	Page #	Section #	Comments	Date
issue 3.6		4.4	Complete rewrite of roughness model 3	07-12-2010
		4.3	Updated roughness model 2, especially 4.3.2	
		1.3	Renamed Fg_Oor_Roughx_xxx flags to Fg_Oor_Rough_dimx	

Proprietary/Copyright Information

This material contains proprietary and/or copyright information of ARGANS Ltd. (ARGANS) and may not be copied, used, or disclosed without permission of ARGANS.

© Copyright ARGANS Ltd. (2021)

COMMERCIAL IN CONFIDENCE



	Page #	Section #	Comments	Date
issue 3.7		3.4	Split into 3.4.1 (General approach for outlier detection) and 3.4.2 (RFI detection/mitigation)	27-04-2011
		3.1	Setting Fg_ctrl_suspect_RFI.true from Dg_RFI_L2	27-04-2011
		1.3	Added Tg_num_RFI_max, RFI_std RFI_nsig	27-04-2011
		3.3	Added Dg_RFI_L2, Fg_ctrl_suspect_RFI & Fm_L2_RFI; removed Dg_eaf_fov	27-04-2011
		3.3	Replaced Dg_L2_RFI by Dg_RFI_L2, JCD comment 9b(i)1 & 9d(i)	15-06-2011
	184	1.3, 3.2, table 1	Removed Dg_eaf_fov, JCD comment 9b(i)2	15-06-2011
		1.1	Changed test to “pertaining to this distribution”, JCD comment 9c(i)	15-06-2011
			See Appendix of FAT minutes for JCD comments referenced above.	22-06-2011
	29	3.2	Updated setting Fm_L1c_sun (DPM PRP_1_3-4)	22-06-2011
		Annex 5	Added pending actions from DPM Table 2	22-06-2011
	28	3.1	Clarified conditions setting Fg_ctrl_valid	12-09-2011
	52-61	4.2	Rewritten to take account of surface roughness model 1 revisions	12-09-2011
	34	3.4.2	Corrected default value for Tg_num_RFI_max	12-09-2011
	1	1	Added paragraph explaining salinity units	16-09-2011

	Page #	Section #	Comments	Date
issue 3.8	169-173	4.14.2.2, table 1	Added definitions of Fg_ctrl_poor_retrieval_X, Fg_ctrl_poor_geophysical_X, updated calculation of Dg_quality_SSSX	07-11-2011
	A6-1	Annex-6	Added note explaining use of different OTT for ascending and descending orbits	07-11-2011

Proprietary/Copyright Information

This material contains proprietary and/or copyright information of ARGANS Ltd. (ARGANS) and may not be copied, used, or disclosed without permission of ARGANS.

© Copyright ARGANS Ltd. (2021)

COMMERCIAL IN CONFIDENCE



	Cover		Date corrected	14-11-2011
		4.14.2.2 Table 1	Header repeated on each page, JCD comment 7di	14-11-2011
		1.3	Added Fg_ctrl_retriev_fail_X, Fg_ctrl_poor_retrieval_X & Fg_ctrl_poor_geophysical_X to list of variables table	14-11-2011

	Page #	Section #	Comments	Date
issue 3.9	42-44	3.5.2	Added sub-sections describing snapshot level RFI detection & use of AUX_DGGRFI	14-01-2013
		1.3, 3.1	Removed Fg_ctrl_gal_noise_pol, Fm_gal_noise_pol, Dg_galactic_noise_pol & associated thresholds, Tm_out_of_range; added Fm_L2_RFI_high_snapshot_std, Fm_L2_RFI_high_snapshot_std_stoke s3/4, Fg_ctrl_suspect_RFI, Fg_ctrl_RFI_prone_X/Y, Fg_ctrl_adjusted_ra, Tm_out_of_range_affov/eaffov, Tm_out_of_range_stokes3_affov/eaff ov, Tm_out_of_range_stokes4_affov/eaff ov, Ts_snapshot_out_of_range, Ts_meas_min, Ts_std, Ts_std_stokes3/4, Tg_current_RFI_max_X/Y, RFI_c1, RFI_c2	13-11-2012
	32	3.3	Added new section describing filters; subsequent sub-sections renumbered	13-11-2012
	177	4.14.1.2	Corrected definition of NFD (was NFD = number of measurements – number of parameters to be retrieved), now NFD = number of measurements. See ESL email JB 20/11/2012	21-11-2012
	119-128	4.7.5.3	Added new section describing the Semi-Empirical Geometrical Optics Scattering Model, including new equations 77-80.	29-11-2012
	137	4.7	Added references [26]-[38]	29-11-2012

Proprietary/Copyright Information

This material contains proprietary and/or copyright information of ARGANS Ltd. (ARGANS) and may not be copied, used, or disclosed without permission of ARGANS.

© Copyright ARGANS Ltd. (2021)

COMMERCIAL IN CONFIDENCE



		3	Adjusted section numbers 3.4 to 3.8	17-12-2012
		Annex 5	Removed Annex 5 (see FAT v600 minutes)	15-01-2013
		2.1.2 & Annex 4	Removed references to unimplemented neural network (see FAT v600 minutes); section 2.1.3 renumbered 2.1.2	15-01-2013
		Annex 6	Renumbered to Annex 4 after deletion of Annex 5 & 6	15-01-2013
		5	Removed redundant tables describing UDP/DAP (see FAT v600 minutes): reference to IODD added instead	15-01-2013
		4.14.2.2	Removed column "Rand/bias" from Table 1 (see FAT v600 minutes)	15-01-2013

	Page #	Section #	Comments	Date
issue 3.10		4.18	New section "TEC estimation from Stokes 3"	31-07-2013
		Annex D	Extended to include description of OTT post-processor algorithms (was Annex 5)	31-07-2013
		4.2.1.1.2, 4.4.1.3, 4.7.1, 4.7.9 Appendix B	Replaced "on the order" by "of the order"	11-10-2013
		Annex E	Removed reference to "SO-RP-ARG-GS-0070_L2OS-OTT_DPGS"	08-10-2013
		Annex D	Corrected deltaTB pseudo-code algorithm to show extraction of median deltaTBs in xi/eta cells (was mean)	08-10-2013

	Page #	Section #	Comments	Date
issue 3.11	182	4.14.1.2	Corrected definition of Chi2P (using gammp function, was incorrectly shown as gammq)	05/09/2014

Proprietary/Copyright Information

This material contains proprietary and/or copyright information of ARGANS Ltd. (ARGANS) and may not be copied, used, or disclosed without permission of ARGANS.

© Copyright ARGANS Ltd. (2021)

COMMERCIAL IN CONFIDENCE



	Page #	Section #	Comments	Date
issue 3.12		4.4.4	Added section describing latest AUX_RGHNS3 update; added new references	11/06/2015
		4.2.4	Added section describing latest AUX_RGHNS1 update	13/07/2015
		Annex 5	New section "Land (Mixed Scene) Contamination Correction (MSOTT)"	23/07/2015

	Page #	Section #	Comments	Date
issue 3.13	25	2	Added explanation that retrievals from roughness model 1 are in UDP, & all 3 models in DAP.	18/04/2016
	32	3.3	In list of filters, added Detect_RFI_outliers, Acard_measurement_decision_tree, Acard_grid_point_decision_tree, OTT_region_filter, OTT_snapshot_filter, OTT_stats_filter, Compute_angle_ignore_filter	18/04/2016
	209	5	Added description & figure showing nominal mapping of retrievals to UDP/DAP.	18/04/2016

	Page #	Section #	Comments	Date
issue 3.14		All document	Headers etc reformatted Equations typeset	
		4	Now MSOTT correction, all other sections moved down	28/02/18
		6	Information on OTT now added to main document	28/02/18
		ANNEX A	Surface roughness model 2 moved to annex	28/02/18
		ANNEX B	Surface roughness model 3 moved to annex	28/02/18
		ANNEX C	Foam contribution moved to annex	28/02/18
		1.2	Table of acronymns now in alphabetical order, added OTT, ADF, ISEA, MIRAS, RFI	27/02/18
		5.2	Surface roughness and foam 1 updated by LOCEAN	27/02/18

Proprietary/Copyright Information

This material contains proprietary and/or copyright information of ARGANS Ltd. (ARGANS) and may not be copied, used, or disclosed without permission of ARGANS.

© Copyright ARGANS Ltd. (2021)

COMMERCIAL IN CONFIDENCE



	Page #	Section #	Comments	Date
Issue 4.0	n/a	Whole document	Headers and footers reformatted. Removal of mention to the NN solution, never implemented nor under consideration. Completion of equation numbering in all sections.	09/10/2020
	1	Section 1	Update of introduction to contemplate current document structure.	09/10/2020
	32	Section 3.3	Alignment of ECMWF flags as per definition.	09/10/2020
	40	Section 3.6	Addition of Eq. numbering and format correction.	09/10/2020
	75	Section 4.4	Addition of missing equations. Reformatting for clarity.	09/10/2020
	40	Section 3.6	Sun glint has been removed from here and added to the retrieval section, under Section 4.5, after the other glints.	09/10/2020
	43	Section 4.1	Added new subsection 4.1.4 to describe the new (alternative) dielectric constant model	09/10/2020
	46	Section 4.1.2.1	Addition of the mixed scene correction as part of the systematic bias removal.	09/10/2020
	134	Section 4.5	Inserted here the sun glint contamination (old section 3.6), as corresponding.	09/10/2020
	183	Section 4.11	Insertion of a Post-processing section to host SSS anomaly computation and post-retrieval error adjustments.	09/10/2020
	311	Section 4.14	Not applicable. Transferred as Annex F.	09/10/2020
	n/a	Section 4.15	Addition of missing equations.	09/10/2020
	236	Section 5.5	Addition of mention to new additional OTT data filtering.	09/10/2020
	239	Section 5.8	Inclusion of new OTT data filtering for OTT computation.	09/10/2020

Proprietary/Copyright Information

This material contains proprietary and/or copyright information of ARGANS Ltd. (ARGANS) and may not be copied, used, or disclosed without permission of ARGANS.

© Copyright ARGANS Ltd. (2021)

COMMERCIAL IN CONFIDENCE

	SMOS L2 OS Algorithm Theoretical Baseline Document	Doc: SO-TN-ARG-GS-0007 Issue: 4 Rev: 1 Date: 12 February 2021 Page: xvii
---	---	---

	259	Section 6.4	New section created. Added explanation on how the LSC LUT is applied.	09/10/2020
	290	Annex C	Added missing constants definitions.	09/10/2020

In the current issue

Issue 4.1	Page #	Section #	Comments	Date
	43-52	Section 4.1	Minor corrections in the text. Addition of Boutin et al. 2020.	12/02/2021
		All document	Official release for L2OS v700.	12/02/2020

Proprietary/Copyright Information

This material contains proprietary and/or copyright information of ARGANS Ltd. (ARGANS) and may not be copied, used, or disclosed without permission of ARGANS.

© Copyright ARGANS Ltd. (2021)

COMMERCIAL IN CONFIDENCE



Table of contents

1	INTRODUCTION.....	1
1.1	REFERENCE AND APPLICABLE DOCUMENTS.....	2
1.2	DEFINITIONS, ACRONYMS, AND ABBREVIATIONS.....	2
1.3	LIST OF VARIABLES.....	4
2	ALGORITHM OVERVIEW	24
2.1	SEA SURFACE SALINITY RETRIEVAL SCHEME.....	24
2.1.1	<i>Iterative approach</i>	24
2.1.2	<i>General description</i>	25
3	MEASUREMENT DISCRIMINATION	26
3.1	APPLIED TO GRID POINTS.....	26
3.2	APPLIED TO EACH MEASUREMENT ON A GRID POINT.....	29
3.3	FILTERS.....	32
3.4	GENERAL DIAGRAM.....	33
3.5	OUTLIERS DETECTION	36
3.5.1	<i>General approach for outlier detection</i>	36
3.5.2	<i>RFI detection/mitigation</i>	36
3.5.2.1	Snapshot out-of-range (non-physical) tests on L1c measurements	36
3.5.2.2	Snapshot standard deviation tests	37
3.5.2.3	Outlier detection tests applied to each measurement.....	38
3.5.2.4	Combining RFI detection methods.....	39
3.5.2.5	Using AUX_DGGRFI.....	39
3.6	SEA STATE DEVELOPMENT.....	40
4	ALGORITHM DESCRIPTION.....	41
4.1	FLAT SEA.....	43
4.1.1	<i>Theoretical description</i>	43
4.1.1.1	Physics of the problem.....	43
4.1.1.2	Mathematical description of algorithm.....	44
4.1.1.3	Error budget estimates (sensitivity analysis)	45
4.1.2	<i>Practical considerations</i>	46
4.1.2.1	Calibration and validation.....	46
4.1.2.2	Exception handling	46
4.1.3	<i>Assumption and limitations</i>	46
4.1.4	<i>Alternative dielectric constant model</i>	46
4.2	SURFACE ROUGHNESS AND FOAM MODEL 1	54
4.2.1	<i>Theoretical description</i>	54
4.2.1.1	Physics of the problem.....	54
4.2.1.1.1	<i>Electromagnetic model</i>	55
4.2.1.1.2	<i>Sea surface roughness and foam models</i>	57
4.2.1.2	Mathematical description of algorithm.....	62
4.2.1.3	Error budget estimates (sensitivity analysis)	65
4.2.2	<i>Practical considerations</i>	65
4.2.2.1	Calibration and validation.....	65
4.2.2.2	Quality control and diagnostics	65
4.2.3	<i>Assumption and limitations</i>	65
4.3	GALACTIC NOISE CONTAMINATION 1.....	69
4.3.1	<i>Theoretical description</i>	69
4.3.1.1	Physics of the problem.....	69
4.3.2	<i>Mathematical description of algorithm</i>	69
4.3.2.1	Data conversion	69

Proprietary/Copyright Information

This material contains proprietary and/or copyright information of ARGANS Ltd. (ARGANS) and may not be copied, used, or disclosed without permission of ARGANS.

© Copyright ARGANS Ltd. (2021)

COMMERCIAL IN CONFIDENCE



4.3.2.2	Galactic noise reflected towards the radiometer.....	71
4.3.2.3	Integration over the antenna beam.....	73
4.3.2.4	Error budget estimates (sensitivity analysis).....	73
4.3.3	<i>Practical considerations</i>	74
4.3.3.1	Calibration and validation.....	74
4.3.3.2	Quality control and diagnostics.....	74
4.3.3.3	Exception handling.....	74
4.3.4	<i>Assumption and limitations</i>	74
4.4	GALACTIC NOISE CONTAMINATION 2.....	75
4.4.1	<i>Overview of the Problem</i>	75
4.4.2	<i>Generation of an L-band Sky map to be used for SMOS data processing</i>	77
4.4.2.1	Overview.....	77
4.4.2.2	Main sources of data.....	79
4.4.2.2.1	<i>Continuum</i>	79
4.4.2.3	Hydrogen line.....	79
4.4.2.3.1	<i>Integration of HI into the continuum map</i>	79
4.4.3	<i>Formulation of the Sky glitter contribution at surface level</i>	82
4.4.4	<i>Transport to antenna level and Integration over the Antenna Pattern</i>	85
4.4.4.1	Tracing the galactic noise from surface to antenna level.....	85
4.4.4.2	Integration over the Antenna Pattern.....	87
4.4.5	<i>Modelling the Scattering Cross Sections</i>	91
4.4.5.1	Modelling the Rough Surface.....	91
4.4.5.2	The Asymptotic Electro magnetic Scattering Models.....	92
4.4.5.3	The Semi-Empirical Geometrical Optics Scattering Model.....	94
4.4.6	<i>Representation of the Scattered Galactic Noise Signal</i>	104
4.4.7	<i>Fast Implementation Method for Calculating Scattered Signal</i>	108
4.4.8	<i>Error budget estimates</i>	115
4.4.9	<i>Practical consideration</i>	116
4.4.9.1	Calibration and validation.....	116
4.4.9.2	Exception handling.....	117
	APPENDIX A Auxiliary datasets used in the generation of the sky map.....	121
	APPENDIX B Reference frames and transformation matrices.....	122
	APPENDIX C Properties of the Angle Φ_{si}	128
	APPENDIX D Multi-dimensional Hermite Interpolation.....	131
4.5	SUN GLINT CONTAMINATION.....	134
4.5.1	<i>Theoretical description</i>	134
4.5.1.1	Physics of the problem.....	134
4.5.2	<i>Mathematical description</i>	137
4.5.2.1	Simplified scattered solar radiation contributions.....	137
4.5.2.2	Efficient Implementation of Bistatic scattering coefficients at L-band.....	138
4.5.3	<i>Error budget estimates</i>	140
4.5.4	<i>Practical considerations</i>	141
4.5.4.1	Calibration and validation.....	141
4.5.4.2	Quality control and diagnostics.....	141
4.5.4.3	Exception handling.....	142
4.5.5	<i>Assumption and limitations</i>	142
4.6	FARADAY ROTATION COMPUTATION FROM GEOMAGNETIC FIELD.....	144
4.6.1	<i>Theoretical description</i>	144
4.6.1.1	Physics of the problem.....	144
4.6.2	<i>Mathematical description of algorithm</i>	144
4.6.3	<i>Assumptions and limitations</i>	145
4.7	ATMOSPHERIC EFFECTS.....	147
4.7.1	<i>Theoretical description</i>	147
4.7.1.1	Physics of the problem:.....	147
4.7.1.1.1	<i>The radiative transfer equation</i>	147
4.7.1.1.2	<i>Dry atmosphere</i>	148
4.7.1.1.3	<i>Water vapour</i>	149

Proprietary/Copyright Information

This material contains proprietary and/or copyright information of ARGANS Ltd. (ARGANS) and may not be copied, used, or disclosed without permission of ARGANS.

© Copyright ARGANS Ltd. (2021)

COMMERCIAL IN CONFIDENCE



4.7.1.1.4	Clouds.....	149
4.7.1.1.5	Rain	150
4.7.2	Mathematical description of algorithm.....	151
4.7.2.1	Radiative transfer for gaseous components	151
4.7.2.2	Monolayer model.....	151
4.7.2.3	Error budget estimates (sensitivity analysis)	153
4.7.3	Practical considerations.....	153
4.7.3.1	Calibration and validation	153
4.7.4	Assumption and limitations.....	153
4.8	TRANSPORT GROUND LEVEL TB TO ANTENNA LEVEL.....	155
4.8.1	Theoretical description.....	155
4.8.1.1	Physics of the problem.....	155
4.8.2	Mathematical description of the algorithm.....	155
4.9	SUM OF CONTRIBUTIONS.....	158
4.9.1	Theoretical description.....	158
4.9.1.1	Physics of the problem.....	158
4.9.1.1.1	Note on first Stokes parameter computation	158
4.9.1.1.2	Sum of modules.....	159
4.9.2	Mathematical description of algorithm.....	160
4.9.3	Error budget estimates (sensitivity analysis).....	162
4.9.4	Practical considerations.....	162
4.9.4.1	Calibration and validation	162
4.9.4.2	Quality control and diagnostics	162
4.9.5	Assumption and limitations.....	162
4.10	ITERATIVE SCHEME	164
4.10.1	Theoretical description.....	164
4.10.1.1	Physics of the problem.....	164
4.10.1.1.1	Case 1 – Model error neglected	164
4.10.1.1.2	Case 2 Model error taken into account.....	165
4.10.1.1.3	Parameters to be retrieved:.....	169
4.10.1.2	Mathematical description of algorithm.....	169
4.10.1.3	Error budget estimates (sensitivity analysis)	175
4.10.2	Practical considerations.....	175
4.10.2.1	Quality control and diagnostics	176
4.10.3	Assumption and limitations.....	181
4.11	POST-PROCESSING.....	183
4.11.1	SSS Anomaly computation.....	183
4.11.1.1	Introduction	183
4.11.1.2	Classical definition of SSS anomaly	184
4.11.1.3	The special Case of SMOS SSS data.....	184
4.11.1.4	SMOS-based climatology production.....	186
4.11.1.5	Parametric dependencies of the reference SMOS fields.....	191
4.11.1.6	Review of SSS Data Filtering criteria to build up the SMOS climatology	191
4.11.1.7	SMOS period of reference for SSS anomaly computation	193
4.11.1.8	SSS Anomaly final adjustment	194
4.11.1.9	SSS anomaly computation at L2 OS	194
4.11.2	Post-retrieval theoretical error adjustment	196
4.11.2.1	Introduction	196
4.11.2.2	Input LIC TB uncertainty characterization	197
4.11.2.3	Implementation in the algorithm	210
4.12	CARDIOID MODEL	211
4.13	BRIGHTNESS TEMPERATURE AT SURFACE LEVEL	213
4.14	MEASUREMENTS SELECTION (POLARISATION).....	214
4.15	AUXILIARY GEOPHYSICAL PARAMETERS BIAS CORRECTION	216
4.16	TEC ESTIMATION FROM STOKES 3 (A3TEC)	217
4.16.1	Introduction.....	217
4.16.2	Algorithm.....	217
4.16.2.1	Assumptions about TEC	217

Proprietary/Copyright Information

This material contains proprietary and/or copyright information of ARGANS Ltd. (ARGANS) and may not be copied, used, or disclosed without permission of ARGANS.

© Copyright ARGANS Ltd. (2021)

COMMERCIAL IN CONFIDENCE



4.16.2.2	Global processing	217
4.16.2.3	Latitude position (step 3)	218
4.16.2.4	TEC from Stokes 3 (step 4 and step 5)	220
4.16.2.5	Quality of the TEC estimation (step 6)	227
4.16.2.6	Estimation of TEC for each SMOS measurement (step 7)	228
4.16.2.7	Link with the OTT computation	228
5	OCEAN TARGET TRANSFORMATION (OTT).....	229
5.1	INTRODUCTION.....	229
5.2	OTT REGION.....	230
5.3	OTT PROCESS.....	231
5.4	DATA SELECTION AND OTT COMPUTATION	232
5.5	OTT CALCULATION	235
5.6	APPLYING THE OTT CORRECTION.....	236
5.7	VALIDITY PERIOD OF THE OTT	239
5.8	ADDITIONAL CONSIDERATIONS.....	239
5.8.1	<i>OTT and A3TEC</i>	239
5.8.2	<i>OTT model-related flaws</i>	240
5.8.3	<i>Additional steps for the OTT generation scheme</i>	242
5.8.4	<i>Assessment of new OTT</i>	243
5.8.4.1	Descending orbits	244
5.8.4.2	Ascending orbits	246
5.8.5	<i>Conclusions and recommendations</i>	249
6	LAND (MIXED SCENE) CONTAMINATION CORRECTION (MSOTT).....	250
6.1	INTRODUCTION.....	250
6.2	DEVELOPMENT OF THE METHOD.....	254
6.3	TEMPORAL STABILITY OF THE CORRECTION.....	258
6.4	APPLICATION.....	259
7	OUTPUT PRODUCTS	261
ANNEX A	Surface roughness 2: Empirically modified SSA/SPM.....	263
ANNEX B	Surface roughness 3: empirical	281
ANNEX C	Foam Contribution.....	289
ANNEX D	Technical note on geometry conventions for SMOS	303
ANNEX E	Technical note on the calculation of Stokes 1 parameter in full polarisation	304
ANNEX F	Auxiliary geophysical parameters bias correction	311

Proprietary/Copyright Information

This material contains proprietary and/or copyright information of ARGANS Ltd. (ARGANS) and may not be copied, used, or disclosed without permission of ARGANS.

© Copyright ARGANS Ltd. (2021)

COMMERCIAL IN CONFIDENCE



1 Introduction

The purpose of this Algorithm Theoretical Baseline Document (ATBD) is to establish the procedure that will be used in the SMOS mission to generate the Sea Surface Salinity data from brightness temperatures (T_b) recorded by the MIRAS radiometer. The output product (SMOS SSS Level 2 product) will consist of files containing half-orbit data (from pole to pole) on the ISEA grid defined at Level 1.

As it is not possible to transform the T_b into SSS through a univocal mathematical expression. L-band emission of the sea surface is computed using a series of mathematical models that have as independent variables the different geophysical parameters (including SSS) that determine this emission. These parameters are obtained from sources external to SMOS, and for SSS a guessed value is considered. The computed T_b, for all angular configurations that correspond to the specific satellite passage, are compared to the measured ones, and then the independent variables are modified in an iterative process until reaching the maximum similarity between both T_b values. The SSS that corresponds to this situation is the value retrieved from SMOS.

In Section 2 an overview of the algorithm is presented, with a scheme of its application in the case of iterative retrieval. Section 3 describes the tests that must be performed every time that the SSS retrieval is attempted, to select the measurements that are suitable to be used and flag any special conditions that may occur. Section 4 is a detailed description of all the parts of the algorithm, the different modules or sub-models that are used to compute the different contributions to sea surface T_b as well as the procedures to compare it with the measured T_b and the iterative convergence method. Section 5 describes the process to generate the Ocean Target Transform required in the retrieval. Section 6 describes the method to determine the land-sea contamination correction. Section 7 presents the contents and structure of the output information after SSS retrieval. Six annexes provide additional information, including the description of alternative roughness models developed by IFREMER (Annex A) and BEC (Annex B), foam contribution to roughness (Annex C), as the geometry convention to relate Earth and satellite reference frames (Annex D), the possible strategies to compute the first Stokes parameter in full polarisation mode (Annex E), and the proposal of debiasing of auxiliary geophysical parameters (Annex F).

The Intergovernmental Oceanographic Commission adopted the new International Thermodynamic Equation of Seawater - 2010 that describes salinity through the Absolute Salinity definition in g/kg instead of Practical Salinity (PS Scale - 78) to take into account the spatial variability of seawater composition and to use IS units. However, measuring systems, both in situ and remotely sensed, will continue being based on conductivity, so all instruments and data bases will deliver practical salinity as before. For historical reasons, all the SMOS data processing algorithms presented here use practical salinity regardless of labels in different modules (no units/psu/pss/pss-78). SMOS is a data provider and users may apply

ARGANS Ltd.



the new TEOS-2010 formulae to convert conductivity-based practical salinity to the more correct Absolute Salinity values when appropriate.

1.1 Reference and applicable documents

See the Software Release Document SO-RN-ARG-GS-0019 pertaining to this distribution.

1.2 Definitions, acronyms, and abbreviations

Table 1: Definitions and Acronyms

ADF	Auxiliary Data File.
DGG	Discrete Global Grid, the ensemble of Grid Points on Earth Surface. Position of Grid Points are computed using hexagonal ISEA function with aperture 4 and resolution 9 (ISEA4H9).
Dwell line	Ensemble of Measurements at the same Grid Point available in SMOS L1c product.
First guesses	Initial values of the geophysical parameters to be retrieved that are introduced in the first step of the minimisation process, and that will be successively modified during the iterations until achieving a retrieved value
Footprint	3db contour of WEF once WEF has been projected on Earth surface. Footprint is centred on a Grid Point and defined by major and minor axes of an ellipse. Axes lengths are provided by SMOS L1c product.
Grid Point	Point on Earth surface where Measurements are available in SMOS L1c product.
ISEA	Icosahedral Snyder Equal Area grid, the gridding system used to describe Grid Point positions on the Earth.
Measurement	Brightness temperature measured in one MIRAS polarisation mode, along with relevant information (radiometric noise, observation conditions, contributions as computed by the model, flags, polarisation direction). A measurement is associated with one Grid point, one Snapshot, one WEF and one Footprint
MIRAS	Microwave Imaging Radiometer with Aperture Synthesis, the single payload aboard SMOS.
MIRAS operating mode	MIRAS has two operating modes: <ul style="list-style-type: none">▪ Dual polarization mode: measurement sequence is - HH – VV – HH – VV – HH – VV – ...

ARGANS Ltd.

Commercial in Confidence



	<ul style="list-style-type: none"> ▪ Full polarization mode: Measurement cycle is - HH – HV – VV – VH – HH – HV – VV – VH – HH - ... (see SO-TN-DME-L1PP-0024)
MIRAS Polarization mode	<p>MIRAS measures brightness temperatures in four polarization modes:</p> <ul style="list-style-type: none"> ▪ HH along polarization direction H. ▪ VV along polarization direction V. ▪ HV: one arm set to H; the two others set to V. ▪ VH: one arm set to V; the two others set to H. <p>HV and VH mode produce complex brightness temperatures that are complex conjugates. In L1C product, both HV and VH modes feed the HV brightness temperature data field with real and imaginary parts (see SO-TN-DME-L1PP-0024 and SO-IS-DME-L1PP-0002).</p>
Modified Stokes vector	Full polarimetric set of temperatures proportional to modified Stokes parameters as defined by Ulaby, p. 1086
OTT	Ocean Target Transformation - empirical characterization of the systematic instrumental error
Prior values	Values of the geophysical parameters, obtained from external sources, that are introduced, with their uncertainties, in the cost function, as reference information of the variability range during the iterative retrieval
Polarization direction	Axes of the polarization frames: H and V for the MIRAS antenna polarization frame (H is along SX axis, V is along SY axis of the figure in section 4.12), E_H and E_V for the target polarization frame at surface.
Retrieval Polarization mode	<p>Three retrieval modes are possible:</p> <ul style="list-style-type: none"> ▪ Stokes 1 retrieval mode uses the Stokes 1 parameter, i.e. the sum of brightness temperatures in H and V polarization directions. ▪ Dual Pol retrieval mode uses brightness temperatures in H and V polarization directions.



	<ul style="list-style-type: none">▪ Full Pol retrieval mode uses brightness temperatures in H and V directions and real and imaginary part in HV.
RFI	Radio Frequency Interference, for SMOS this is L-band emission in the protected frequencies, from sources such as military bases or telecommunications.
Snapshot	Ensemble of measurements acquired at the same time. Distinction of snapshots per polarization is done.
SSS	Sea Surface Salinity. Salinity of the uppermost fraction of the ocean that contributes to L-band emission (approx. 1 cm)
SSS spatial resolution (or equivalent footprint diameter)	Diameter D of the equivalent circle, centred on a Grid Point , where SSS is retrieved. The area of the equivalent circle is equal to the mean area of the footprint ellipses of the Dwell line Measurements deemed valid for SSS retrieval $D = \sqrt{\text{mean}(\text{axis1} * \text{axis2})}$
SST	Sea Surface Temperature. When measured by SMOS it is the temperature of the upper fraction of the ocean that contributes to L-band emission (approx. 1 cm)
WEF	2D weighting function derived from synthetic antenna gain of MIRAS interferometer, apodization function used at reconstruction and fringe wash factor. Also termed synthetic antenna pattern or equivalent array factor. The two dimensions are differential cosines in the antenna reference frame.

1.3 List of variables

The modified Stokes vector in the antenna reference frame is [A1, A2, A3, A4] instead of [T_{xx}, T_{yy}, T_{xy}] in Level 1, with:

$$A1 = T_{xx}$$

$$A2 = T_{yy}$$

$$A3 = 2 \text{Re}(T_{xy})$$

$$A4 = 2 \text{Im}(T_{xy})$$



Variable name	Descriptive Name	Units	ATBD reference	Comments
General				
SSS	Sea surface salinity	psu		
SST	Sea surface temperature	K		
TEC	Total electron content	Tecu = 10^{16} m^{-2}		
Tb_p	Brightness temperature at p polarization (H,V)	K		
$[Tb_{hh}, Tb_{hv}, Tb_{vh}, Tb_{vv}]$	Brightness temperature polarisations in earth reference frame			
$[Tb_{xx}, Tb_{xy}, Tb_{yx}, Tb_{yy}]$	Brightness temperature polarisations in antenna reference frame			
$[I, Q, U, V]$	Stokes vector			
$[Tb_1, Tb_2, Tb_3, Tb_4]$	Modified Stokes vector			
$[A1, A2, A3, A4]$	Modified stokes vector rotated to antenna $[Tb_{xx}, Tb_{yy}, U_{Antenna}, V_{Antenna}]$			
3. Measurement discrimination				
Fg_sc_land_sea_coast1	land/sea	Y/N		
Fg_sc_land_sea_coast2	coast/no coast	Y/N		
Fg_sc_ice	Presence of sea ice in grid point	Y/N		ECMWF
Fg_sc_suspect_ice	Grid point suspect of ice contamin.	Y/N		ECMWF
Fg_sc_in_clim_ice	Gridpoint with maximum extend of sea ice accordy to monthly climatology	Y/N		ECMWF
Fg_sc_rain	Heavy rain point	Y/N		ECMWF
Fg_sc_low_SST	Low SST	Y/N		ECMWF
Fg_sc_high_SST	High SST	Y/N		ECMWF
Fg_sc_low_SSS	Low SSS	Y/N		
Fg_sc_high_SSS	High SSS	Y/N		
Fg_sc_low_wind	Low wind speed	Y/N		ECMWF
Fg_sc_high_wind	High wind speed	Y/N		ECMWF
Fg_sc_sea_state_1	Sea state development class 1	Y/N		
Fg_sc_sea_state_2	Sea state development class 2	Y/N		

ARGANS Ltd.

Commercial in Confidence

Page 5

Use, duplication, or disclosure of this document or any information contained herein is subject to the restriction on the title page of this document.



Variable name	Descriptive Name	Units	ATBD reference	Comments
Fg_sc_sea_state_3	Sea state development class 3	Y/N		
Fg_sc_sea_state_4	Sea state development class 4	Y/N		
Fg_sc_sea_state_5	Sea state development class 5	Y/N		
Fg_sc_sea_state_6	Sea state development class 6	Y/N		
Fg_sc_SST_front	Presence of a temperature front	Y/N		
Fg_sc_SSS_front	Presence of a salinity front	Y/N		
Fg_ctrl_ECMWF_1	No missing ECMWF data for SS1 retrieval	Y/N		roughness models
Fg_ctrl_ECMWF_2	No missing ECMWF data for SS2 retrieval	Y/N		ditto
Fg_ctrl_ECMWF_3	No missing ECMWF data for SS3 retrieval	Y/N		ditto
Fg_ctrl_ECMWF_4	No missing ECMWF data for Acard retrieval	Y/N		ditto
Fg_ctrl_num_meas_low	Grid point with number of valid measurements below threshold	Y/N		measurement discrimination
Fg_ctrl_num_meas_min	Grid point discarded due to very few measurements	Y/N		measurement discrimination
Fg_ctrl_many_outliers	Grid point with number of outlier measurements above threshold	Y/N		measurement discrimination
Fg_ctrl_sunlint	Grid point with number of measurements flagged for sunlint above threshold	Y/N		
Fg_ctrl_moonglint	Grid point with number of measurements flagged for moonglint above threshold	Y/N		
Fg_ctrl_gal_noise	Grid point with number of measurements flagged for galactic noise above threshold	Y/N		
Fg_ctrl_valid	Grid point used in the retrieval	Y/N		measurement discrimination

ARGANS Ltd.

Commercial in Confidence

Page 6

Use, duplication, or disclosure of this document or any information contained herein is subject to the restriction on the title page of this document.



Variable name	Descriptive Name	Units	ATBD reference	Comments
Fg_ctrl_suspect_RFI	Grid point with number of measurements flagged for RFI above threshold	Y/N		
Fg_ctrl_RFI_prone_X	Grid point likely to be contaminated by RFI in X pol as indicated by AUX_DGGRFI	Y/N		
Fg_ctrl_RFI_prone_Y	Grid point likely to be contaminated by RFI in Y pol as indicated by AUX_DGGRFI	Y/N		
Fg_ctrl_adjusted_ra	Grid point with radiometric accuracy adjusted due to RFI flagging in AUX_DGGRFI	Y/N		
Fm_out_of_range	Tb out of range	Y/N		
Fm_resol	Measurement with spatial resolution (i.e. major axis length) above threshold	Y/N		
FmL1c_af_fov	Measurement inside AF_FOV	Y/N		L1c
FmL1c_border_fov	Border measurements	Y/N		L1c
FmL1c_RFI	Marked RFI by L1	Y/N		L1c
Fm_suspect_ice	Measurement above threshold in test for possible ice detection	Y/N		
Fm_outlier	Outliers measurements	Y/N		
Fm_L1c_sun	L1C information on sun contaminated measurements	Y/N		
Fm_low_sun_glint	After Sun glint IFREMER model	Y/N		
Fm_high_sun_glint	After Sun glint IFREMER model	Y/N		
Fm_sun_limit	Sun contamination above threshold	Y/N		
Fm_moon_specdir	Moon glint	Y/N		
Fm_gal_noise_error	Error in galactic map above threshold	Y/N		
Fm_high_gal_noise	Measurements with specular direction toward a strong galactic source	Y/N		
Fm_valid	Measurement is valid	Y/N		
FmL1c_sun_tails	Flag comming from L1	Y/N		From L1
FmL1c_sun_glint_area	Flag comming from L1	Y/N		From L1
FmL1c_sun_glint_fov	Flag comming from L1	Y/N		From L1
Fm_L2_RFI_high_snapsh ot_std	Snapshot RFI contaminated due to high std/ra in XX/YY	Y/N		

ARGANS Ltd.

Commercial in Confidence

Page 7

Use, duplication, or disclosure of this document or any information contained herein is subject to the restriction on the title page of this document.



Variable name	Descriptive Name	Units	ATBD reference	Comments
Fm_L2_RFI_high_snapshot_std_stokes3	Snapshot RFI contaminated due to high std/ra in Stokes 3	Y/N		
Fm_L2_RFI_high_snapshot_std_stokes4	Snapshot RFI contaminated due to high std/ra in Stokes 4	Y/N		
Tg_dland1	Distance 1 (short) to land	Km		
Tg_dland2	Distance 2 (long) to land	Km		
Tg_ice_concentration	Threshold (fraction) in ECMWF ice concentration	dl		
Tg_low_SST_ice	Value of SST under which to perform ice test	K		
Tg_suspect_ice	Minimum fraction of measurements where ice test is positive to flag point	dl		
Tg_max_rainfall	threshold of maximum rain accepted	mm/h		
Tg_low_SST	Upper limit for very low SST	K		
Tg_medium_SST	Boundary between 'low SST' and 'medium SST'	K		
Tg_high_SST	Boundary between 'medium SST' and 'high SST'	K		
Tg_low_SSS	Upper limit for very low SSS	psu		
Tg_medium_SSS	Boundary between 'low SSS' and 'medium SSS'	psu		
Tg_high_SSS	Boundary between 'medium SSS' and 'high SSS'	psu		
Tg_low_wind	Upper limit for very low wind speed	m/s		
Tg_medium_wind	Boundary between 'low wind' and 'medium wind'	m/s		
Tg_high_wind	Boundary between 'medium wind' and 'high wind'	m/s		
Dg_num_meas_l1c	Number of measurement available in L1C product	dl		L1c
Dg_num_meas_valid	Number of valid measurements	dl		measurement discrimination
Tg_num_meas_valid	Threshold of number of valid measurements to flag	dl		
Tg_num_meas_min	Minimum number of valid measurements to perform retrieval	dl		

ARGANS Ltd.

Commercial in Confidence

Page 8

Use, duplication, or disclosure of this document or any information contained herein is subject to the restriction on the title page of this document.



Variable name	Descriptive Name	Units	ATBD reference	Comments
Dg_num_outliers	number of outlier measurements	dl		measurement discrimination
Tg_num_meas_outliers_min	minimum number of measurements per polarisation to apply outlier detection	dl		
Tg_num_meas_RFI_outliers_min	minimum number of measurements per polarisation to apply RFI outlier detection	dl		
Tg_num_outliers_max	minimum fraction of outlier measurements to flag a grid point	dl		
Tg_num_RFI_max	minimum fraction of RFI measurements to flag a grid point	dl		
Tg_num_RFI_outlier_max	minimum fraction of RFI outlier measurements to flag a grid point	dl		
Tg_sunglint_max	minimum fraction of measurements flagged for sunglint to flag a grid point	dl		
Tg_moonglint_max	minimum fraction of measurements flagged for moonglint to flag a grid point	dl		
Tg_gal_noise_max	min. fraction of measurements flagged for galactic noise to flag a grid point	dl		
Tg_current_RFI_max_X	Minimum % to flag a grid point as likely to be contaminated by X pol RFI as indicated by AUX_DGGRFI	dl, %		
Tg_current_RFI_max_Y	Minimum % to flag a grid point as likely to be contaminated by Y pol RFI as indicated by AUX_DGGRFI	dl, %		
Tm_out_of_range_affov	threshold for Tb out of range in AFFOV, XX/YY pol measurements	K		
Tm_out_of_range_eaffov	threshold for Tb out of range in EAFFOV, XX/YY pol measurements	K		
Tm_out_of_range_stokes3_affov	threshold for Tb out of range in AFFOV, Stokes 3 measurements	K		
Tm_out_of_range_stokes3_eaffov	threshold for Tb out of range in EAFFOV, Stokes 3 measurements	K		

ARGANS Ltd.

Commercial in Confidence



Variable name	Descriptive Name	Units	ATBD reference	Comments
Tm_out_of_range_stokes4_affov	threshold for Tb out of range in AFFOV, Stokes 4 measurements	K		
Tm_out_of_range_stokes4_eaffov	threshold for Tb out of range in EAFFOV, Stokes 4 measurements	K		
Ts_snapshot_out_of_range	Maximum proportion of land/ice within snapshot, below which all measurements are discarded (fm_l2_snapshot_out_of_range set) if any have fm_out_of_range set	dl, %		
Ts_meas_min	Minimum proportion of measurements for computing snapshot standard deviation	dl, %		
Ts_std	Threshold for snapshot XX/YY standard deviation, above which all measurements in a snapshot are discarded	K		
Ts_std_stokes3	Threshold for snapshot Stokes 3 standard deviation, above which all measurements in a snapshot are discarded	K		
Ts_std_stokes4	Threshold for snapshot Stokes 4 standard deviation, above which all measurements in a snapshot are discarded	K		
RFI_c1, RFI_c2	Coefficients used to adjust measurement radiometric accuracy from the current RFI LUT AXU_DGGRFI	dl		
Resolution	length of major axis of the measurement footprint	Km		
Dg_num_high_resol	number of measurements exceeding maximum allowed resolution	dl		
Tg_resol_max_ocean	maximum footprint resolution (i.e. major axis length) to be accepted for measurements in ocean points	Km		
Dg_af_fov	counter on number of measurements in alias free FOV	dl		L1c
Dg_border_fov	counter on number of measurements on the border of FOV.	dl		L1c

ARGANS Ltd.

Commercial in Confidence

Page 10

Use, duplication, or disclosure of this document or any information contained herein is subject to the restriction on the title page of this document.



Variable name	Descriptive Name	Units	ATBD reference	Comments
Dg_RFI_L1	number of measurements discarded due to being flagged RFI at L1	dl		L1c
Tm_DT_ice	threshold for test on possible presence of ice	K		
Dg_suspect_ice	number of measurements suspect of being contaminated by ice	dl		measurement discrimination
Dg_sunglint_L1	number of meas. with L1 sunglint flag	dl		L1c
Dg_sunglint_L2	number of meas. with L2 sunglint flag	dl		sunglint module
Tm_high_sun_glint	upper limit for very low sun_glint	K		
Tm_medium_sun_glint	boundary between 'low sun glint' and 'medium sun glint'	K		
Tm_low_sun_glint	boundary between 'medium sun glint' and 'high sun glint'	K		
Tm_sun_limit	limit of sun glint, between to process or not	K		
Dg_sun_fov	number of measurements affected by L1C flag SUN_FOV	dl		L1c
Dg_sun_tails	number of measurements with SUN_TAILS flag raised	dl		L1c
Dg_sun_glint_area	number of measurements with SUN_GLINT_AREA flag raised	dl		L1c
Dg_sun_glint_fov	number of measurements with SUN_GLINT_FOV flag raised	dl		L1c
Dg_moonglint	N. of meas. with L2 moonglint raised	dl		moonglint module
Tm_angle_moon	angle between Target to Moon direction and specular direction	deg		
Tm_max_gal_noise_error	Threshold of the galactic noise error	K		
Tm_high_gal_noise	Definition of strong galactic source	K		
Q_CSWeF	Second Stokes parameter map weighted by a centrosymmetric WeF	K		
U_CSWeF	Third Stokes parameter map weighted by a centrosymmetric WeF	K		



Variable name	Descriptive Name	Units	ATBD reference	Comments
Tg_WS_gal	Minimum WS to discard measurements contaminated by erroneous galactic noise	m/s		
Dg_gal_noise_error	Number of measurements with galactic noise error flag raised	dl		measurement discrimination
Dg_sky	Number of measurements with specular direction toward a strong galactic source	dl		
nsig	Factor to multiply σT_b in outliers detection	dl		
RFI_std	Factor to multiply std_theory in RFI detection	dl		
RFI_nsig	Factor to multiply radiometric_noise in RFI detection	dl		
σT_b _radiometric_noise	Radiometric noise of a single meas.	K		
σT_b _model1	Model error estimate in outliers detection	K		roughness 1
σT_b _model2	Model error estimate in outliers detection	K		roughness 2
σT_b _model3	Model error estimate in outliers detection	K		roughness 3
3.5 Outliers Detection				
$T_{b_{L1c}}$	Measured T_b			
$T_{b_{model}}$	Modelled T_b			
σT_b	Error estimate on T_b			
n	Constant			
t	time			
<u>Erreur ! Source du r envoi introuvable.</u> <u>Erreur ! Source du r envoi introuvable.</u>				
$\overline{n_i}$	Direction of incoming radiation			
$\overline{n_s}$	Scattered radiation			
$\beta_{Sun}/2$	The angular radius of the sun as viewed from earth	deg		

ARGANS Ltd.

Commercial in Confidence

Page 12

Use, duplication, or disclosure of this document or any information contained herein is subject to the restriction on the title page of this document.



Variable name	Descriptive Name	Units	ATBD reference	Comments
σ_p^0	Bistatic scattering coeffs of the sea surface at 1.4 GHz for polarisations p = HH, HV, VV, VH			
Ω_{Sun}	Solid angle intercepting the sun as seen from the earth	Sr		
$T_{Sun}(\bar{n}_i, t)$	The brightness temp of the sun at 1.4 GHz in direction n and time t.	K		
T	Position on earth' surface.	(degN, degE, t)		
ϕ, ψ	Lat and Long			
t	Time			
θ_i	Incidence angle	deg		
$\sigma_{\alpha\alpha_0}$	Dimensionless scattering cross section			
α, α_0	Polarisations			
(q_k, q_i)	Vertical projections of wave vectors	Radm ⁻¹		
$B_{\alpha\alpha_0}(\bar{n}_s, \bar{n}_i)$	Kernel Functions			
$\rho(\bar{r})$	The correlation function of roughness.			
$h(\bar{r}_x)$,	Surface elevation signal for x 1,2	m		
Q	$= q_k + q_i$	Radm ⁻¹		
$W(\bar{k})$	the directional wavenumber spectrum of the rough sea surface at surface wavenumber vector \bar{k} .			
u_{10}	10 m wind speed	m s ⁻¹		
ϕ_w	Wind direction	deg		
Φ_{si}	the angle of the difference between the scattered and incident wavevectors	deg		
μ	Used in the interpolation, $\frac{x-x_k}{x_{k+1}-x_k}$			
a_x	Functions of μ in the interpolation. X = 0..3			
w	Weight functiins			
y_j	Values from the LUT			



Variable name	Descriptive Name	Units	ATBD reference	Comments
3.6 Sea state development				
Hsw	Significant wave height of wind waves	m		
Tg_swell	Threshold for classification of sea state between swell or not swell dominated	dl		
Tg_old_sea	Upper limit of inverse wave age for old seas	dl		
Tg_young_sea	Lower limit of inverse wave age for young seas	dl		
4.1 Flat sea				
$Tb_{Flat,p}$	Brightness temperature in H and V pol due to a flat sea; p is polarization	K		
$Tb_{Rough,p}$	Brightness temperature due to the roughness of the sea surface.			
θ	Incidence angle	deg		
\overline{P}_{Rough}	Vector of parameters that describes the roughness of the sea			
E	Emissivity of the sea	dl		
$\Gamma_{h,v}$	Reflection coefficient in h / v polarization	dl		
$R_{h,v}$	Flat sea reflection coefficient in h / v polarization	dl		
ϵ	Complex dielectric constant	dl		
ϵ'	real part of dielectric constant	dl		
ϵ''	imaginary part of dielectric constant	dl		
ϵ_{∞}	Electrical permittivity at very high frequencies	dl		
ϵ_s	Static dielectric constant	dl		
τ	Relaxation time	s		
σ	Ionic conductivity	Siemens		
ϵ_0	Permittivity of the free space	Farads/m		
m	Coefficients vector for ϵ_s	dl		
t	Coefficients vector for τ	dl		
s	Coefficients vector for σ	dl		

ARGANS Ltd.

Commercial in Confidence

Page 14

Use, duplication, or disclosure of this document or any information contained herein is subject to the restriction on the title page of this document.



Variable name	Descriptive Name	Units	ATBD reference	Comments
4.2 Surface roughness and foam model 1				
θ	Incidence Angle	deg		
ϕ	Azimuth angle	deg		
E	Sea surface emissivity			
SST	Sea Surface Temp	K		
a	Sea surface Absorpivity			
Γ	Sea surface reflectivity			
λ_0	Radiometer wavelength	?		
WS	Wind speed	ms^{-1}		
λ_c	Cutoff wavelength			
(S_x, S_y)	Dimensions of the slopes domain			
(S'_x, S'_y)	Surface slopes along and across the radiometer azimuth directions respectively			
P	A probability density function			
Tb_l	Local brightness temp	K		
Tb_{Sea}	Brightness temp of the sea	K		
Tb_{Flat}	Brightness temperature of the flat sea	K		
θ_l, ϕ_l	Local incidence and azimuth angles	deg		
R_{ss}	Reflectivity of a small-scale roughness covered surface			
R_c, R_i	Coherent and incoherent part of R_{ss}			
R_{hh}, R_{vv}	Reflectivity in h and v pol			
g_p	Functions?			
k_c	Cutoff wavenumber			
k	Wavenumber			
$C(k, \phi)$	2D surface curvature spectrum			
$\xi, g'_{p,n}$	Scattering weighting functions			
Tb_{Rough}	Roughness contribution to brightness temp			
Tb_{Foam}	Foam contribution to brightness temp			
$W(k'_\rho, \phi')$	2D surface power spectrum			
g	Acceleration due to gravity	$9.81 ms^{-1}$		

ARGANS Ltd.

Commercial in Confidence

Page 15

Use, duplication, or disclosure of this document or any information contained herein is subject to the restriction on the title page of this document.



Variable name	Descriptive Name	Units	ATBD reference	Comments
a_0	Constant, wave spectrum			
b, c	Parameters of the foam coverage model			
$v_{a,f}$	Void fraction at the air sea interface			
z	Altitude			
U^*	Friction Velocity			
u_c	Surface velocity (surface current)	ms^{-1}		
κ	Von Karman's constant = 0.4			
z_0	Roughness length	m		
Ψ	Function of the stability parameter			
L	Monim-Obhukov length scale			
C_D	Drag coefficient			
WS_n	10 m neutral wind speed.	ms^{-1}		
Tb_{tot}	The Tb from flat sea, rough sea and foam contributions			
Tb_{Wind}	Brightness temperature induced by wind			
ϕ_w	Wind direction	deg		
ϕ_r	Radiometer look direction	deg		
ϕ_a	Azimuthal angle between ϕ_w and ϕ_r	deg		
T_{Air}, T_{Sea}	Air temperature and Sea Temperature	K		
4.3.3 Galactic noise contamination 1				
P	Power	W		
P_{int}	Integrated power			
k	Boltzmann constant	J K^{-1}		
B	Bandwidth of receiver	Hz		
v, v_0	Frequency and centre frequency	Hz		
v	Velocity	m s^{-1}		
c	Light speed	m s^{-1}		
Tb_{SMOS}	Brightness temp as measured by SMOS	K		
Tb_{Gal}	Brightness temperature of galactic radiation	K		
θ_i, ϕ_i	Incidence and azimuth angles	deg		

ARGANS Ltd.

Commercial in Confidence

Page 16

Use, duplication, or disclosure of this document or any information contained herein is subject to the restriction on the title page of this document.



Variable name	Descriptive Name	Units	ATBD reference	Comments
θ_{iGal}	Incidence angle of galactic ray	deg		
R_E	Radius of the earth	km		
h_{rad}	Altitude of radiometer	km		
el	Elevation angle	deg		
δ, α	Declination and right ascension, the celestial coordinate system			
φ, ψ	Lat and long			
Γ	Reflectance coefficient			
R_{Rough}	Contribution of roughness to reflectance coefficient			
σ_0	Galactic noise over whole sky			
$Tb_{Gal_{refllobe}}$	The reflected galactic noise measured by antenna	K		
P_{lobe}	The normalised power pattern of antenna			
	<u>Erreur ! Source du r</u> <u>envoi introuvable.</u> <u>Erreur ! Source du r</u> <u>envoi introuvable.</u>			
T_{sky}	Sky temperature	K		
ψ_{uh}	Orientation angle	deg		
T_{CMB}	Equivalent brightness temperature at L band from the cosmic microwave background	K		
T_{HI}	Brightness temperature from the hydrogen line	K		
T_{cont}	Brightness temperature from the continuum background	K		
B_{SMOS}	SMOS bandwidth	Hz		
B_{HI}	Bandwidth of HI line	Hz		
	Frequency of the HI line	Hz		
f	frequency	Hz		
v	velocity	$m s^{-1}$		
	Beam width of antenna			
	Boresight observation angle	deg		
	Azimuthal angle	deg		
	An incremental sea surface area	m		

ARGANS Ltd.

Commercial in Confidence

Page 17

Use, duplication, or disclosure of this document or any information contained herein is subject to the restriction on the title page of this document.



Variable name	Descriptive Name	Units	ATBD reference	Comments
\vec{n}_0	Directions of illumination	deg		
\vec{n}_s	Directions of scattering	deg		
	Solid angle	deg		
	Surface sky glitter brightness temperature in the direction \vec{n}_s , at polarisation p	K		
(,)	Surface windspeed vector			
	Bistatic scattering coefficients of the sea surface at scattered direction \vec{n}_s where q is the polarisation of the incident wave.			
p, q	polarisations			
T_s	Sea surface temperature	K		
A_u	The upward path attenuation matrix			
ω	Faraday rotation matrix			
M_l	MIRAS antenna polarisation matrix			
M_{fu}	Faraday rotation matrix			
M_α	Combined rotation matrix			
G	Antenna Gain			
Γ_p	Total reflectivity at polarisation p			
R_{hh}, R_{vv}	Reflectivity in hh and vv polarisation.			
$\varepsilon(S, T)$	Dielectric constant at salinity S and temperature T			
TEC	Total electron count	TECu		
Ω_p	Vector antenna pattern solid angle			
W	Apodisation function			
\tilde{r}	Fringe washing factor			
(u, v)	Baseline coordinates in the frequency domain			
d	Antenna element spacing			
f_0	Central frequency			
(ξ, η)	Central director cosine coordinates			
(ξ', η')	Running director cosine coordinates			
ρ	Surface correlation function			
$W(\xi_x, \xi_y)$	Directional wavenumber spectrum of the rough sea surface			
Ω	Inverse wave age			
u_{10}	10 m neutral windspeed			

ARGANS Ltd.

Commercial in Confidence

Page 18

Use, duplication, or disclosure of this document or any information contained herein is subject to the restriction on the title page of this document.



Variable name	Descriptive Name	Units	ATBD reference	Comments
φ_w	Wind direction (towards which the wind is blowing)			
\vec{k}_0, \vec{k}_s	Incident and scattered wave vectors			
I_K	Kirchoff integral			
$P\left(-\frac{q_x}{q_z}, -\frac{q_y}{q_z}\right)$	Surface slope probability density function			
<u>4.6 Faraday rotation computation from geomagnetic field</u>				
ω	Faraday rotation			
TEC	Total electron count			
\mathbf{B}	Magnetic field vector			
\mathbf{U}_{LS}	Unitary vector			
O_{xyz}	Local geographic reference frame (O_x towards East, O_y toward North, O_z upwards)			
(θ_g, φ_n)	Polar geographical coordinates			
<u>4.7 Atmospheric effects</u>				
Tb_m	Measured brightness temperature by satellite	K		
Tb_s	Surface brightness temperature	K		
SST	Sea Surface Temperature	K		
ϵ	Sea surface emissivity			
Γ	Surface reflection coefficient			
Tb_{up}	brightness temperature self-emitted by the atmosphere upwards	K		
Tb_{down}	brightness temperature self-emitted by the atmosphere downwards	K		
τ_{atm}	Equivalent optical thickness of the atmosphere			
k_{O_2}	Linear absorption of Oxygen			
k_{H_2O}	Linear absorption of water vapour			
ρ_v	Water vapour density	g/kg		
γ_1	Line width parameter			
k_r	Residual term			



Variable name	Descriptive Name	Units	ATBD reference	Comments
4.8 Transport ground level Tb to antenna level				
θ_g, ϕ_g	Angles from nadir	deg		
θ, ϕ, ψ	Angles	deg		
ω	Faraday rotation angle	deg		
a	Rotation angle	deg		
$MR2, MR4$	Rotation matrix for dual pol or full pol measurements			
4.9 Sum of contributions				
θ_{mean}	Mean incidence angle	deg		
θ_x, θ_y	Components of incidence angle			
Tb_{sea}	Brightness temperature contribution from sea	K		
Tb_{flat}, Tb_{rough}	Brightness temperature contributions from flat and rough sea	K		
Tb_{BOA}	Brightness temperature at bottom of atmosphere	K		
$Tb_{reflected}$	radiometric temperature from the sky and atmosphere scattered by the surface	K		
Tb_{DN}	Downward emitted atmospheric radiation	K		
Tb_{UP}	Upwards emitted atmospheric radiation	K		
$Tb_{gal_{refl}}$	Radiation emitted by the galaxy, reflected in the sea surface	K		
$e^{\tau_{atm}}$	Attenuation of the radiation by the atmosphere	K		
Γ	Reflection coefficient			
Tb_{TOA}^{EARTH}	Brightness temperature in the earth reference frame at top of atmosphere	K		
$Tb^{ANTENNA}$	Brightness temperature in the antenna reference frame	K		

ARGANS Ltd.

Commercial in Confidence

Page 20

Use, duplication, or disclosure of this document or any information contained herein is subject to the restriction on the title page of this document.



Variable name	Descriptive Name	Units	ATBD reference	Comments
4.10 Iterative Scheme				
σ	Theoretical error/uncertainty			
P_{rough}	Vector including the parameters used in the forward model to describe sea roughness			
H_s	Significant wave height	m		
ϕ	Wind direction			
Ω	Inverse wave age			
TEC	Total electron count			
θ	Incidence angle of measurements from nadir	deg		
C_{Earth}^{mod}	Variance-covariance matrix for modelled brightness temperature in the earth reference frame			
C_{Ant}^{mod}	Variance-covariance matrix for modelled brightness temperature in the antenna reference frame			
M	The pseudo hessian			
C_0	The covariance matrix			
F	The Jacobian			
P_j, P_j^{prior}	Parameters to be retrieved, and their prior values			
C_{P_j}	Variance/covariance matrix of P_j			
N_p	Number of parameters			
a	The vector of N_p parameters to be retrieved			
d, D	Gradient and Hessian of the cost function			
4.12 Cardioid model				
ϵ', ϵ''	The real and imaginary part of the dielectric constant			
$A_{card}, B_{card}, m_{card}$	Components of the cardioid model.			
χ^2	The cost function			
4.13 Brightness temperature at surface level				

ARGANS Ltd.

Commercial in Confidence



Variable name	Descriptive Name	Units	ATBD reference	Comments
Tb_{BOA}	Brightness temperature at bottom of atmosphere	K		
Tb_{flat}	Brightness temperature contribution of a flat sea	K		
Tb_{rough}	Brightness temperature contribution of rough sea	K		
Tb_{DN}	Downwards emitted radiation from atmosphere	K		
Γ	Reflection coefficient			
$Tb_{gal_{refl}}$	Radiation emitted by the galaxy reflected by the sea surface	K		
$e^{\tau_{atm}}$	Attenuation of the radiation by the atmosphere			
4.15 Auxiliary geophysical parameters bias correction				
W_t	True wind speed	$m s^{-1}$		
φ	Wind direction	deg		
α_i	Wind speed gain			
β_i	Wind speed bias	$m s^{-1}$		
n_{xi}, n_{yi}	Normally distributed noise with zero mean and unit amplitude			
δ_i	Amplitude of the normally distributed random noise	$m s^{-1}$		
A	Scale parameter			
C	Shape parameter			
4.16 TEC estimation from Stokes 3 (A3TEC)				
$(latSat, lonSat)$	Subsatellite point position			
$(latGP, lonQP)$	Grid point position			
(xGP, yGP, zGP)	Coordinates of the gridpoint			
$(xSat, ySat, zSat)$	Coordinates of the satellite			
$Rearth$	Earth Radius	km		
$Hsat$	Altitude of the satellite	km		
$Htec$	TEC altitude			
ω_F	Faraday rotation			

ARGANS Ltd.

Commercial in Confidence

Page 22

Use, duplication, or disclosure of this document or any information contained herein is subject to the restriction on the title page of this document.



Variable name	Descriptive Name	Units	ATBD reference	Comments
5 Ocean Target Transformation (OTT)				
Tb	Brightness Temperature	K		
Tb_{L1c}	Measured Tb	K		
Tb_{model}	Modelled Tb	K		
ΔTb	Difference between Tb_{L1c} and Tb_{model}	K		
(ξ, η)	The director cosine coordinates (antenna coordinate system)			
(x, y)				
OTT	Ocean target transformation	K		
$\Delta Tb_{merged,XX}$	The merged long and short XX pol ΔTb	K		
$\Delta Tb_{long,XX}, \Delta Tb_{short,XX}$	The long and short ΔTb values for XX pol.	K		
$n_{long,XX}, n_{short,XX}$	Number of long and short measurements in XX pol			
$w_{long,XX}, w_{short,XX}$	Merge weights for long and short XX pol ΔTb			



2 Algorithm overview

In the considered algorithm approach (iterative retrieval) a series of physical models (separate modules 4.1 to 4.10 in this ATBD) are applied to auxiliary data (SST, wind speed, etc.) and a first guess SSS, to compute the brightness temperature that should be measured at a specific polarization and geometric configuration. These values are transported to SMOS antenna level (module 4.12) and then compared to measured T_b . An iterative process (considering all measurements/views of a single grid point obtained in consecutive snapshots, module 4.14) allows minimization of the difference between modelled and measured values, until identifying a retrieved SSS for this grid point, altogether with retrieved SST and wind speed values. Three different models are proposed for the effect of ocean surface roughness in L-band emissivity (modules 4.2 to 4.4); several retrieval processes will be run in parallel and retrieved SSS values provided in the L2 Output Product. In the current version of the operational L2 processor the User Data Product (UDP) contains salinity retrieved using the two-scale salinity model (model 1, see section Surface roughness and foam model 1) with & without land-sea (mixed-scene) correction; outputs from all 3 models are available in the Data Analysis Product (DAP). For details of the UDP/DAP nominal retrieval configuration, see section Output Products.

The SSS retrieval algorithms described in this ATBD will be applied to all ISEA grid points included in a SMOS L1c product (half-orbit swath).

2.1 Sea Surface Salinity retrieval scheme

2.1.1 Iterative approach

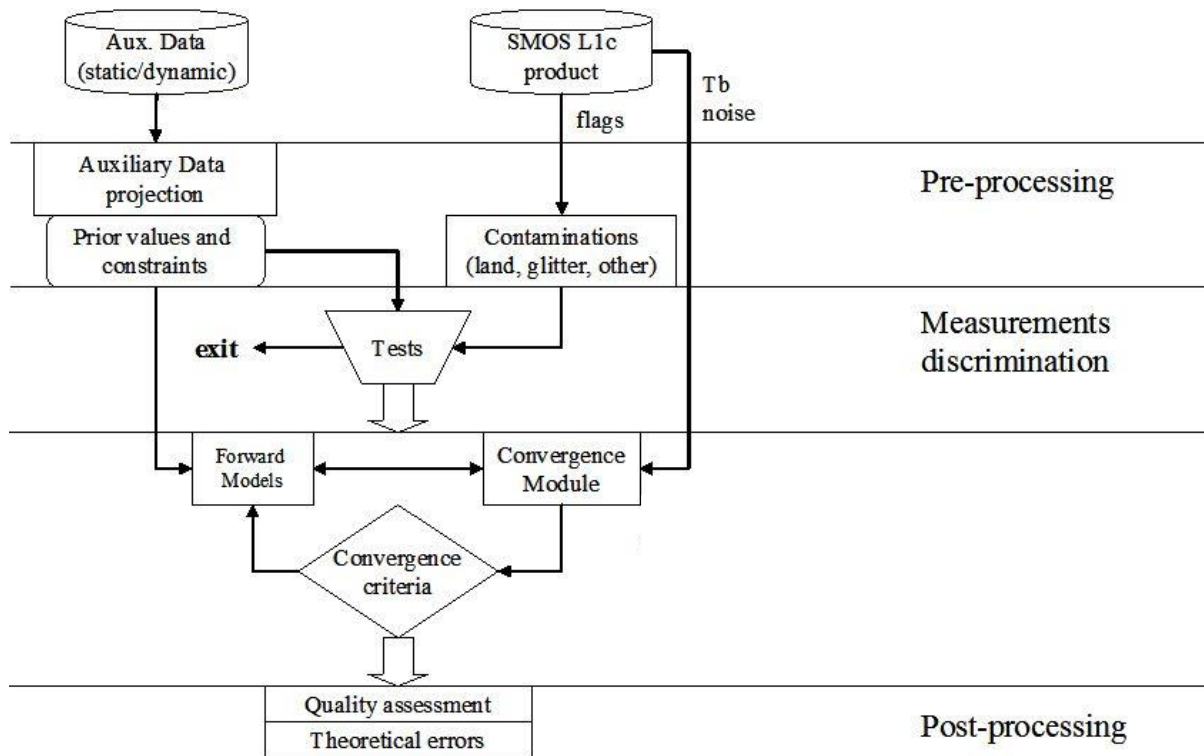
Per each ISEA grid point (once selected as coast/ocean or ocean) on each SMOS half-orbit the following actions are executed:

- Get pre-processed auxiliary data (SST, wind etc)
- For all L1c T_b measurements available
 - Perform a decision on processing/flagging according to several tests
 - Compute forward model for T_b at each angular measurement θ :
 - Emissivity of flat sea at θ with auxiliary SST and guessed SSS
 - Add roughness effects (3 model options + foam)
 - Add external noise (reflected signals: atmosphere, galactic, sun effects)
 - Add atmospheric attenuation and emission to antenna
 - Transport modelled T_b from TOA to antenna level
- Compare modelled with measured T_b
- Perform an iterative convergence to retrieve SSS and adjust other parameters
- Output values: SSS , SST , roughness descriptors, TEC (depending on model options) corresponding to this specific grid point

As three different options are being studied to describe the effect of surface roughness on Tb, three SSS values will be retrieved at the end of the process. In some sub models, reference values for Tb are needed to compute flags. In this case one of the three roughness models will be used as default for the computation. At Qualification Review 1 (19 July 2006) it was decided that Two-scale will be the default model. In 2016 the so-called Model 1 was selected as the most adequate to describe the sea surface roughness contribution to Tb.

2.1.2 General description

The chart below describes schematically the various modules of the salinity retrieval inversion scheme.



3 Measurement discrimination

The purpose of the measurement discrimination is to check the conditions of all the grid points and measurements coming from L1c to decide whether they are processed or not to retrieve salinity and to provide the user with information about the measurements, grid points and snapshots. Additional information is provided in the Output Product in terms of flags to describe some conditions that can raise warnings for some L3 applications or indicate that future specific reprocessing could be implemented.

A simple convention is used for naming flags:

Fx_class_name_of_flag

- F: the variable is a flag.
- x = **s/m/g/f**: Flag applies to **snapshot**, **measurement**, **grid point**, **full half orbit**.
- Class = ctrl for control flag, sc for science flag
- name_of_flag.

A flag is a boolean (true/false). Numbers are descriptors (computed by the processor), named Dx_name_of_descriptor or thresholds (available in auxiliary/configuration files), named Tx_name_of_threshold.

A series of tests, with defined threshold values, have to be run consecutively before applying the SSS retrieval algorithm to it. Only Grid Points with Fg_ctrl_valid set to true and measurements with Fm_valid are processed to retrieve SSS.

3.1 Applied to grid points

The **Fg_ctrl_valid** is used to flag grid points according to some of the tests below, and is nominally set false (ie invalid) if Fg_ctrl_num_meas_min is true, Fg_sc_land_sea_coast1 is false (ie land or too near to coast), Fg_sc_ice is true, or Fg_ctrl_ecmwf is true (as specified in the "Grid_point_decision_tree" filter).

<i>Subject</i>	<i>Test</i>	<i>Threshold</i>	<i>Decision</i>
Classification of grid points with respect to distance to land (4 categories)	Applying land mask based on distance of grid point to land.	1) Land: grid point inside land (coastline) 2) Coast/Land: grid point between coast and Tg_dland1 3) Coast/Ocean: grid point between Tg_dland1 and Tg_dland2 4) Ocean: grid point outside Tg_dland2	1) Land point. SSS retrieval is not performed 2) SSS retrieval is not performed and grid point is flagged as land contaminated 3) SSS retrieval performed, grid point flagged as Coast/ Ocean 4) SSS retrieval performed This classification will be implemented using two booleans for four states: (Fg_sc_land_sea_coast1; Fg_sc_land_sea_coast2)

ARGANS Ltd.

Commercial in Confidence

Page 26

Use, duplication, or disclosure of this document or any information contained herein is subject to the restriction on the title page of this document.



			<p>with (false;false)=Land (false>true)=Water, with distance to coast <= Tg_dland1 (true>true)=Water, with distance to coast <= Tg_dland2 and >Tg_dland1 (true>false)=Water, with distance to coast >Tg_dland2>Tg_dland1. Fg_sc_land_sea_coast1 defines the land contamination of the grid point and Fg_sc_land_sea_coast2 coastal grid points</p> <p>Note: both flags are computed offline and stored in an auxiliary file. If Tgdland1 and Tg_dland2 are modified too often, they will become processor configuration parameters and the processor will set both flags on the fly.</p>
Presence of ice	Applying sea ice mask (evolving info.: ECMWF sea ice concentration + fixed info.: monthly extent climatology)	<p>1) Grid point with ice concentration > Tg_ice_concentration 2) Grid point with ice concentration below threshold but within monthly climatological maximum extent of sea ice (Fg_sc_in_clim_ice) and (in case SSTprior < Tg_low_SST_ice) positive test for possible ice in at least Tg_suspect_ice of measures 3) Other grid points</p>	<p>1) Ice present. SSS retrieval is not performed (Fg_sc_ice.true) 2) Potentially sea ice contaminated. SSS retrieval is performed but point flagged (Fg_sc_suspect_ice.true) 3) No ice. SSS retrieval is performed</p>
Heavy rain	Intense rainfall is reported in at least one of 4 ECMWF cells around the grid point	Rainfall above threshold Tg_max_rainfall	Process and flag as point affected by heavy rain (Fg_sc_rain.true)

ARGANS Ltd.

Commercial in Confidence

Page 27

Use, duplication, or disclosure of this document or any information contained herein is subject to the restriction on the title page of this document.

Sea surface types	Build a descriptor (or several flags) to indicate different ocean surface conditions	<p>1) SST. Four ranges of SST (very low, low, medium, high) can be defined using Tg_low_SST, Tg_medium_SST and Tg_high_SST</p> <p>2) SSS. Four ranges of SSS using Tg_low_SSS, Tg_medium_SSS and Tg_high_SSS</p> <p>3) Wind speed. Flag according to WS below/above neutral wind Tg_low_wind, Tg_medium_wind or Tg_high_wind</p> <p>4) Sea state development. To distinguish between 6 different classes according to altimetry and ECMWF WAM model (see SMOS ECMWF PreProcessor)</p> <p>5) Presence of SSS and/or SST fronts in (or around) the grid point</p>	<p>1) Two booleans for SST range (Fg_sc_low_SST and Fg_sc_high_SST) (false:false) SST <= Tg_low_SST (true:false) Tg_low_SST < SST <= Tg_medium_SST (true:true) Tg_medium_SST < ST <= Tg_high_SST (false:true) SST > Tg_high_SST</p> <p>2) Same for SSS range using (Fg_sc_low_SSS and Fg_sc_high_SSS)</p> <p>3) Same for wind speed classification using (Fg_sc_low_wind and Fg_sc_high_wind)</p> <p>4) Sea state development described (see section 3.6) by Fg_sc_sea_state_X.true (X 1 to 6)</p> <p>5) Two flags (see section 3.7) Fg_sc_SST_front and Fg_sc_SSS_front</p>
Number of valid measurements	Use the counter of measurements accepted for SSS retrieval in this grid point	If number of measurements used Dg_num_meas_valid < threshold Tg_num_meas_valid flag grid point If < Tg_num_meas_min do not perform retrieval	Flag grid point with Fg_ctrl_num_meas_low.true if below Tg_num_meas_valid (just for warning) and Fg_ctrl_num_meas_min.true if retrieval not performed
Number of outlier measurements	Use the counter of measurements flagged as outliers in this grid point	If number of outliers Dg_num_outliers / Dg_num_meas_l1c > Tg_num_outliers_max	Flag grid point (Fg_ctrl_many_outliers.true)
Number of RFI outlier measurements	Use the counter of measurements flagged as RFI	If number of RFI outliers	Flag grid point (Fg_ctrl_suspect_RFI.true)



	outliers in this grid point	$(Dg_RFI_L2_X + Dg_RFI_L2_Y) / Dg_num_meas_l1c > Tg_num_RFI_max$	
Number of measur. flagged for sunglint	Use the counter of measurements flagged for sunglint in this grid point	If $Dg_sunglint_2 / Dg_num_meas_l1c > Tg_sunglint_max$	Flag grid point (Fg_ctrl_sunglint.true)
Number of measur. flagged for moonlint	Use the counter of measurements flagged for moonlint in this grid point	If $Dg_moonglint / Dg_num_meas_l1c > Tg_moonglint_max$	Flag grid point (Fg_ctrl_moonglint.true)
Number of measur. flagged for galactic noise	Use the counter of measurements flagged for galactic noise in this grid point	If $(Dg_gal_noise_error + Dg_sky) / Dg_num_meas_l1c > Tg_gal_noise_max$	Flag grid point (Fg_ctrl_gal_noise.true)
Missing ECMWF data	Check that all the ECMWF data necessary for the four retrievals are made available to the OS processor	<ol style="list-style-type: none"> 1) Some parameter needed for SSS1 retrieval is missing in the grid point 2) Some parameter needed for SSS2 is missing 3) Some parameter needed for SSS3 is missing 4) Some parameter needed for Acard is missing 	<ol style="list-style-type: none"> 1) SSS1 retrieval not performed (Fg_ctrl_ECMWF_1.false) 2) SSS2 retrieval not performed (Fg_ctrl_ECMWF_2.false) 3) SSS3 retrieval not performed (Fg_ctrl_ECMWF_3.false) 4) Acard retrieval not performed (Fg_ctrl_ECMWF_4.false)

3.2 Applied to each measurement on a grid point

All measurements that have successfully passed the tests described below are flagged with **Fm_valid** (see diagram in page 34 and “Measurement_decision_tree” in section 3.3 below) and used for the SSS retrieval in the concerned grid point. When the Measurement discrimination concludes that in a grid point no retrieval is performed, the corresponding fields in the Output Product will be set to default (clearly differentiated) values.

Subject	Test	Threshold	Decision
Tb out of range	Based on first comparison default model vs. measure	$Abs(Tb\ measure - Tb\ model) (h\ or\ v) > threshold$	Discard measurements flagged (Fm_out_of_range.true)

ARGANS Ltd.

Commercial in Confidence



		(Tm_out_of_range), then flag <i>See note 1</i>	
Footprint size	Check resolution (i.e. major axis length) of footprint	Only measurements with Resolution < Tg_resol_max_ocean is used in the retrieval. Flag others	SSS retrieval is performed with selected measurements (Fm_resol.false) Set counters for the measurements not used due to this excess of resolution Dg_num_high_resol
L1 flags: Grid points position within Field of View	Grid points are classified by L1 as belonging to Alias Free FOV, Extended AF FOV and (being inside) near the border of it. The definition of border will be configurable. First approach considers 30 km	Counters will allow knowing how many measurements of each type have been recorded for a grid point Dg_af_fov Dg_border_fov	1) Grid points outside EAF_FOV will not be processed (if any) (FmL1c_af_fov.true) 2) Measurements outside AF_FOV may not be used (FmL1c_af_fov.false). A switch is to be implemented for activation in case these measurements appear to be of too poor quality 3) Border measurements are rejected (FmL1c_border_fov.true)
L1 flag: RFI	L1 will not apply an RFI static mask (difficult due to being angle dependent) but build a table that will be further filled	Affected measurements will be flagged and a counter for the grid point incremented Dg_RFI_L1	Measurements will be marked with L1_RFI flag (Fm_L1c_RFI.true) but this will not be considered to discard data (done through outliers' detection)
Possible presence of ice	Test applied to measures on grid points within monthly climatological maximum extent of sea ice and SSTprior < Tg_Low_SST_ice	If Tb > Tbflat + Tm_DT_ice then the measure is considered as possibly contaminated by ice	The measurement is flagged (Fm_suspect_ice) and a counter for the grid point is incremented (Dg_suspect_ice) to be used later in the percentage comparison to the threshold Tg_suspect_ice



Outliers	See description of test in section 3.4	For each outlier measurement a counter is incremented for the grid point (Dg_num_outliers)	Outliers are flagged and not processed (Fm_outlier.true)
Sun contamination	L1C will provide information on sun contaminated measurements through the Fm_sun_fov and Fm_sun_point flags. This is summarized in a unique Fm_L1c_sun.true and counters set for the point Dg_sun_tails , Dg_sun_glint_area , Dg_sun_glint_fov	At L2 Sun glint IFREMER model will be applied and measurements will be classified as no glint, low glint, medium glint, high glint using two booleans Fm_low_sun_glint Fm_high_sun_glint and three thresholds (Tm_high_sun_glint , Tm_low_sun_glint , Tm_medium_sun_glint)	Measurements flagged with Fm_L1c_sun.true will not be processed Measurements classified at L2 as sun glint contaminated with intensity above Tm_sun_limit (that can coincide with the low, medium, or high thresholds) will be flagged (Fm_sun_limit.true) and not processed Counters for discarded measurements as flagged in L1c and L2 Dg_sunglint_L1 , Dg_sunglint_L2
Moon glint	Check angle between Target to Moon direction & specular direction	Flag if angle less than Tm_angle_moon and increment a counter Dg_moonglint	Not process flagged measurements (Fm_moon_specdir.true)
Galactic noise	Check galactic background error maps (potential error due to strong sources and error due to the centrosymmetrical WEF assumption)	1) If quadratic sum of all errors greater than Tm_max_gal_noise_error 2) If galactic noise greater than Tm_high_gal_noise	1) If wind speed is below Tg_WS_gal , flag and do not use measurement in the retrieval (Fm_gal_noise_error.true) and increment a counter Dg_gal_noise_error 2) Flag (Fm_high_gal_noise.true), and count (Dg_sky) measurements with specular direction toward a strong galactic source

Note 1: In the three cases (Tb out of range, possible presence of ice, outliers detection) where measured Tb has to be compared with modelled values under the same configuration (viewing geometry, sea surface conditions) we have to deal with values at antenna level (measured) and values at surface (modelled). To simplify the tests we can just perform the

ARGANS Ltd.



tests with Th+Tv (first Stokes parameter) and using the default roughness model plus simplified corrections (atmospheric, galactic) that will allow a clear identification of measurements to be discarded, although not providing high quality modelled Th and Tv for SSS retrieval

3.3 Filters

To make filtering criteria explicit, allow changes to criteria without recompilation, and to decouple code deliveries with decisions about which flags (especially L1c flags, which may change independently of L2OS deliveries) to test at each measurement discrimination (and other decision) steps, configurable filters are provided in AUX_CNFOSE/D. Each filter consists of a combination of tests on measurement flags (L1c or L2); and on grid point control, science, and out-of-range flags. Flag names are also defined in the configuration files. The following filters are supported:

Filter name	Description	ATBD section
Detect_snapshot_out_of_range	Filter applied to grid point and measurements before performing snapshot level out-of-range tests	3.5.2
Detect_snapshot_outliers	Filter applied grid point and measurements before performing snapshot level outlier tests based on std/ra	3.5.2.2
Detect_outliers	Filter applied to grid points before performing measurement level outlier tests	3.5.2.3
Detect_RFI_outliers	Filter applied to grid points before performing measurement level RFI outlier tests	3.5.2.4
Detect_measurement_outliers	Filter applied to measurements before performing measurement level outlier tests	3.5.2.3
Set_RFI_flag_from_outlier_tests	Set Fm_L2_RFI from RFI outlier tests	3.5.2.4
Set_RFI_flag_from_snapshot_tests	Set Fm_L2_RFI from RFI snapshot tests	3.5.2.4
Set_sun_flag_from_L1c	Set Fm_L1c_sun measurement flag from L1c flag(s)	
Set_RFI_flag_from_L1c	Set Fm_L1c_RFI measurement flag from L1c flag(s)	
Measurement_decision_tree	Clear Fm_valid for suspicious measurements	

ARGANS Ltd.

Commercial in Confidence

Page 32

Use, duplication, or disclosure of this document or any information contained herein is subject to the restriction on the title page of this document.



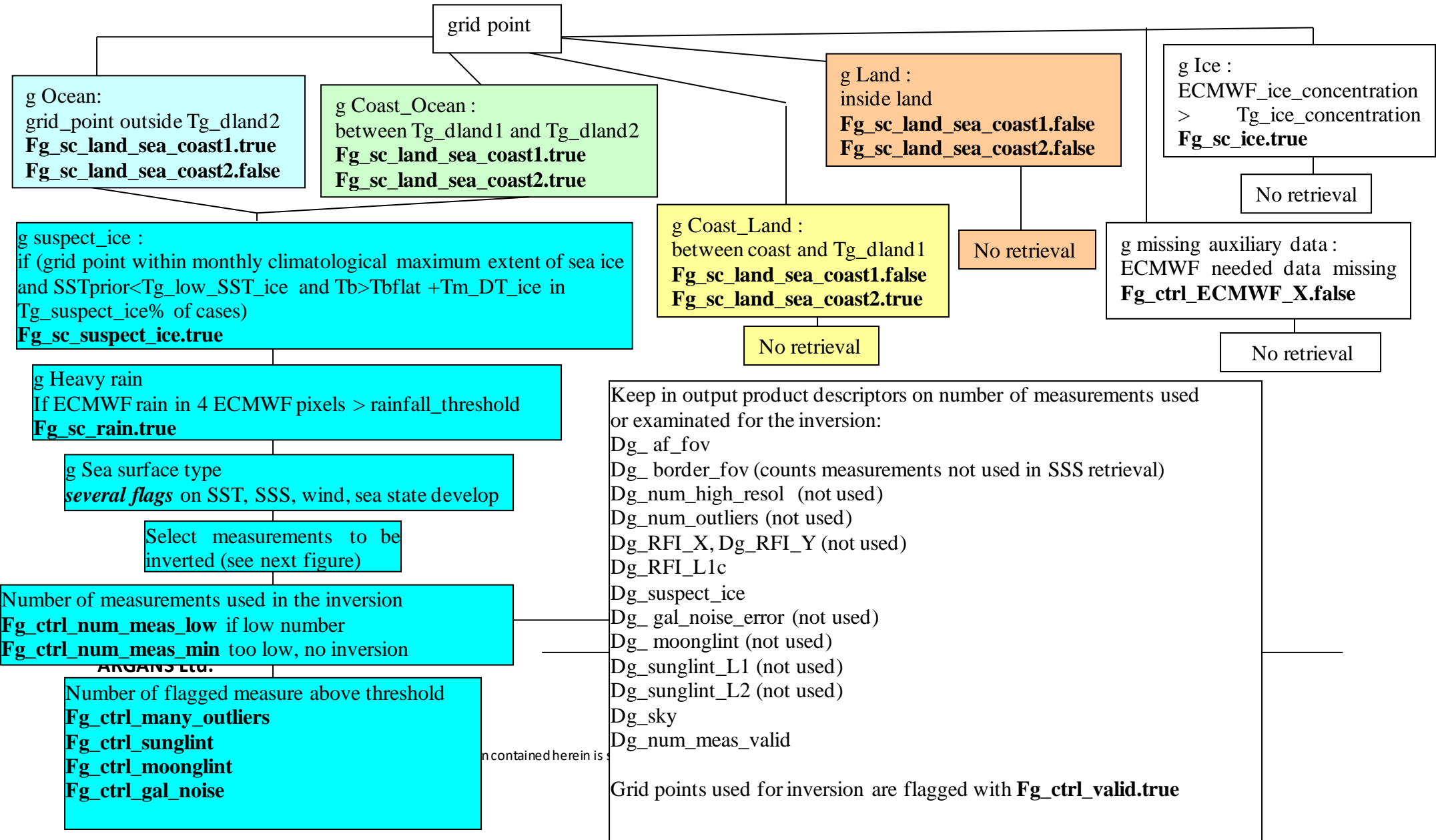
Grid_point_decision_tree	Clear Fg_ctrl_valid for ignored grid points	
Poor_quality	Set Fg_ctrl_poor_retrieval if retrieval results flagged as suspicious	3.3
Poor_quality_Acard	Set Fg_ctrl_poor_retrieval for Acard if retrieval results flagged as suspicious	
Poor_geophysical	Set Fg_ctrl_poor_geophysical if geophysical conditions may have contaminated retrievals	
Poor_geophysical_Acard	Set Fg_ctrl_poor_geophysical for Acard if geophysical conditions may have contaminated retrievals	
Dg_user	Criteria for Dg_user DAP counter defined in AUX_CNFOSE/D	
Acard_measurement_decision_tree	Clear Fm_valid for suspicious measurements	
Acard_grid_point_decision_tree	Clear Fg_ctrl_valid for ignored grid points	
OTT_region_filter	Select grid points & measurements for OTT computation	
OTT_snapshot_filter	Select snapshots for OTT computation	
OTT_stats_filter	Select measurements for computing filtered statistics	
Compute_angle_ignore_filter	Set Fg_ctrl_ignore to skip grid points when computing angles	

3.4 General diagram

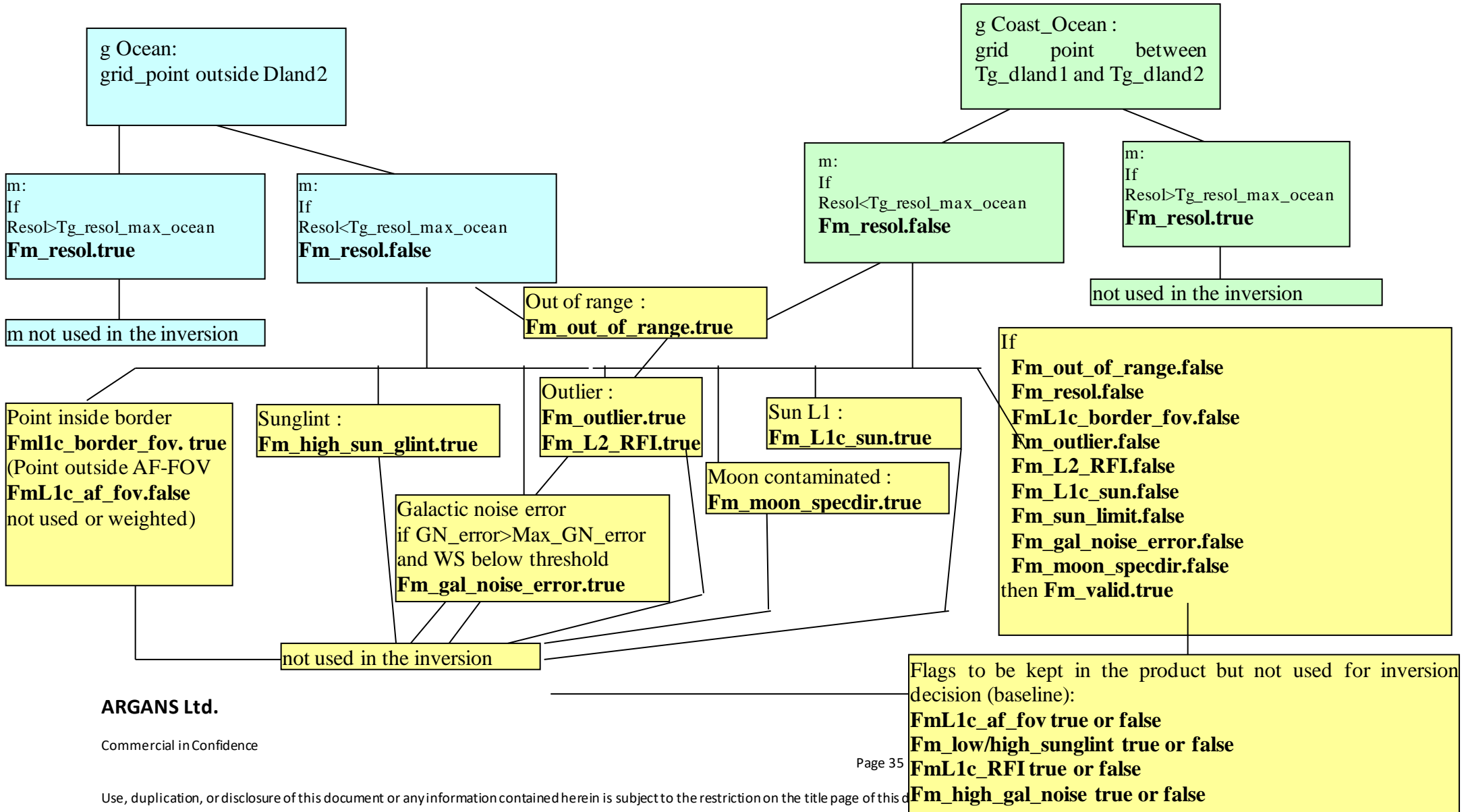
In the following diagram the conceptual application of the nominal measurement discrimination is schematised.



Classification of grid point:



contained herein is



ARGANS Ltd.

Commercial in Confidence

Use, duplication, or disclosure of this document or any information contained herein is subject to the restriction on the title page of this document.

Flags to be kept in the product but not used for inversion decision (baseline):
FmL1c_af_fov true or false
Fm_low/high_sunlint true or false
FmL1c_RFI true or false
Fm_high_gal_noise true or false

3.5 Outliers detection

3.5.1 General approach for outlier detection

Outlier detection is the process of finding measurements of Tb which are out of range and therefore erroneous, in a grid point.

To accomplish this the measurements are tested and rejected if,

$$|Tb_{L1c} - Tb_{model} - \text{median}(Tb_{L1c} - Tb_{model})| > n\sigma Tb \quad 3.5.1$$

Where the median is computed using all Tb measured at same polarisation in the grid point and n typically equal to 5 (may be adjusted). The error estimate σTb is given by

$$\sigma Tb = \sqrt{[\sigma Tb_{radiometric\ noise}^2 + \sigma Tb_{model}^2]} \quad 3.5.2$$

where σTb_{model} is an estimate of the error on the model.

This method has several advantages, firstly the median is a robust estimator even with small number of measurements, the mean biases (model or instrument biases) are removed and it takes into account corrections for atmosphere, galactic noise, incidence angle variations and others.

This test is not performed on a polarisation dwell line if the number of measurements is less than a threshold ($Tg_num_meas_outliers_min$, nominally 16 measurements).

In the L2OS processor the **OTT** is applied and then snapshot **RFI** is detected, before detecting measurement outliers and outlier RFI. The OTT is then un-applied.

3.5.2 RFI detection/mitigation

RFI over ocean areas (emissions from Island military bases such as Ascension Island, long range contamination from land-based sources, etc) can have considerable impact on Tb values. Detection of RFI in the L2OS processor is performed at snapshot level, and then per measurement. Snapshot level RFI detection is performed before outlier RFI detection and measurement discrimination.

3.5.2.1 Snapshot out-of-range (non-physical) tests on L1c measurements

Measurements rejected by the "Detect_snapshot_out_of_range" filter (nominally not near to land, ice, with sun point or border flags set) are not used in snapshot out-of-range tests. Snapshot level discrimination cannot be performed near to land or ice because high land/ice



Tb values within a snapshot will falsely be flagged as RFI. The difference between L1c Tb and forward model Tb are tested against thresholds as follows,

$$|Tb_{L1c} - Tb_{modelled}| > \text{threshold} \quad 3.5.3$$

If (3.5.3) is true, the measurement and the snapshot are flagged with `Fm_out_of_range` and `Fs_out_of_range` respectively.

Nominal thresholds are 50K in AFFOV, 100K in EAFFOV. Thresholds are one of:

`Tm_out_of_range_affov`, `Tm_out_of_range_eaffov`

`Tm_out_of_range_stokes3_affov`, `Tm_out_of_range_stokes3_eaffov`

`Tm_out_of_range_stokes4_affov`, `Tm_out_of_range_stokes4_eaffov`

For all snapshots with `Fs_out_of_range` set, the number of measurements in the snapshot near to land or ice is counted; if few measurements are near land or ice (nominally < 20%, `Ts_snapshot_out_of_range`), then all measurements in the snapshot are discarded by setting `Fm_L2_RFI_snapshot_out_of_range` for all snapshot measurements.

3.5.2.2 Snapshot standard deviation tests

Measurements rejected by the “Detect_snapshot_outliers” filter (nominally `Fm_out_of_range`, not near to land, ice, in EAFFOV, with sun point or border flags set) are not used in snapshot standard deviation tests. To help avoid false detection of land/sea transitions as RFI, snapshots that are only partially complete (`Ts_meas_min`, nominally < 35%) are also ignored.

The standard deviation is calculated,

$$\sigma \left(\frac{Tb_{L1c} - TB_{modelled}}{RadiometricAccuracy} \right) \quad 3.5.4$$

For XX & YY snapshots if (3.5.4) is greater than the threshold `Ts_std` defined in the `AUX_CNFOSF` configuration file, then the snapshot is flagged with `fs_high_std` and all the measurements in the snapshot are flagged with `fm_l2_rfi_high_snapshot_std`.

For cross-pol snapshots, (3.5.4) is tested against the thresholds `Ts_std_stokes3` or `Ts_std_stokes4` depending on the snapshot polarisation. The adjacent (previous) snapshot with the same polarisation will have `fs_high_std_stokes3` or `fs_high_std_stokes4` set, and all measurements in this and the adjacent (previous) snapshot with the same polarisation have `fm_l2_rfi_high_snapshot_std_stokes3` or `fm_l2_rfi_high_snapshot_std` set.

3.5.2.3 Outlier detection tests applied to each measurement

Detection of RFI outliers in the L2OS processor is performed by a two-step algorithm which first identifies grid points at risk of RFI contamination, and then applies a reduced outlier threshold to all measurements on these grid points. This algorithm is known to be sensitive to other sources of contamination (e.g. land and ice) and is therefore applied only in ocean areas far from land (>200 km). The RFI detection algorithm is applied independently for each measurement polarisation.

Measurements rejected by the “Detect_outliers” (nominally not near to land, ice) and Detect_measurement_outliers” filters (nominally Fm_L2_RFI_snapshot_out_of_range, Fm_L2_RFI_high_snapshot_std, Fm_L2_RFI_high_snapshot_std_Stokes3, Fm_L2_RFI_high_snapshot_std_Stokes4) are not used in outlier detection tests.

The standard deviation is computed over the whole dwell line and compared to 1.2 times of the theoretical standard deviation (i.e. the sum, over all measurements included in the dwell line, of the radiometric noise and the modelled error). The factor 1.2 corresponds to the 99% confidence interval. In case there is a risk of outlier, if the difference between the measured TB and the modelled TB are higher than 3 time of the radiometric noise, this measurement is discarded from the retrieval.

This test is not performed on a polarisation dwell line if the number of measurements is less than a threshold (Tg_num_meas_RFI_outliers_min, nominally 16 measurements).

Firstly, identify for each grid point whether there is a risk of RFI outliers,

$$\sigma_{theory} = \sqrt{\frac{(\Sigma (radiometricNoise^2 + error(Tb_{model})))}{n}} \quad 3.5.5$$

$$riskRFI = \sigma(Tb_{model} - Tb_{L1c}) > \sigma_{RFI} \sigma_{theory} \quad 3.5.6$$

Where n is the number of measurements and $\sigma_{RFI} = 1.2$

If $riskRFI$ then for each measurement flag as fm_l2_rfi_outlier if for a certain polarisation,

$$|Tb_{model} - Tb_{L1c}| > RFI_n * radiometricNoise \quad 3.5.7$$

is true, where $RFI_n = 3$.



False positives are then removed, a false positive is a measurement where less than Tg_num_RFI_outlier_max measurements are flagged with fm_l2_rfi_outlier.

3.5.2.4 Combining RFI detection methods

Fm_L2_RFI is set for all measurements returned by the “Set_RFI_flag_from_outlier_tests” (nominally Fm_L2_RFI_outlier) or “Set_RFI_flag_from_snapshot_tests” (nominally Fm_L2_RFI_snapshot_out_of_range, Fm_L2_RFI_high_snapshot_std, Fm_L2_RFI_high_snapshot_std_Stokes3, or Fm_L2_RFI_high_snapshot_std_Stokes4) filters. The number of RFI contaminated measurements is counted,

Dgg_RFI_X = count(Fm_L2_rfi) for XX & XXY measurements

Dgg_RFI_Y = count(Fm_L2_rfi) for YY & YYX measurements

If mean Dgg_RFI_X/Y is above a threshold (Tg_num_RFI_max, nominal 33%), flag the grid point (set Fg_ctrl_suspect_rfi):

3.5.2.5 Using AUX_DGGRFI

The optional **ADF** AUX_DGGRFI is used to flag grid points if they are known to be prone to RFI,

if dggRFI_X / dggRFI_snapshots > Tg_current_RFI_max_X then
set Fg_ctrl_RFI_prone_X

if dggRFI_Y / dggRFI_snapshots > Tg_current_RFI_max_Y then
set Fg_ctrl_RFI_prone_Y

where

Tg_current_RFI is nominally 1%.

Once L2OS has completed all RFI detection tests, if a grid point is considered free from RFI (Fg_ctrl_suspect_rfi = 0), but has a non-zero RFI probability in one or both polarisations as indicated by AUX_DGGRFI, then weight the radiometric accuracy before retrieval and set Fg_ctrl_adjusted_ra:

$cRFI = 1 + (RFI_{c1} * t) / (1 + t)$
Pixel_RadiometricAccuracy *= cRFI

if cRFI > 1.0 then set Fg_ctrl_adjusted_ra

where

ARGANS Ltd.

Commercial in Confidence

Page 39

Use, duplication, or disclosure of this document or any information contained herein is subject to the restriction on the title page of this document.

$$rRFI = (dggRFI_X + dggRFI_Y) / dggRFI_snapshots$$

$$t = rRFI^{RFI_c2}$$

nominal values for RFI_c1 = 6.0, RFI_c2 = 1.0

3.6 Sea state development

The classification of sea state development at each grid point in 6 classes (Fg_sc_sea_state_X, X = 1 to 6) is done using ECMWF wave model data. At present there is no established or tested methodology to derive this information and will be investigated in the framework of SMOS reprocessing.

As first approach the SMOS SSS L2 processor will implement a flag computation derived only from ECMWF data, using three of the auxiliary variables: significant wave height (Hs), significant wave height of wind waves (Hsw), and inverse wave age (Ω).

For each grid point the fraction of swell will be computed as (Hs-Hsw)/Hs. The highest value (1) would mean that there are no wind waves, then all the waves are due to presence of swell. The lowest value (0) corresponds to significant wave height only due to wind waves, then no presence of swell. Establishing a threshold value **Tg_swell**, for example equal to 0.5, allows classifying all grid points as swell dominated (fraction above threshold) or wind waves dominated (below threshold).

For the inverse wave age two thresholds (**Tg_old_sea** and **Tg_young_sea**) will allow classifying the wave age in three ranges: old, medium and young according to the parameter Ω being lower than Tg_old_sea, between Tg_old_sea and Tg_young_sea, or above Tg_young_sea.

Finally, the combination of the two criteria allows the definition of the six classes of sea state development. The corresponding flags are set to true according to the table:

Flag set to true	Fraction of swell	Inverse wave age
Fg_sc_sea_state_1	below Tg_swell	below Tg_old_sea
Fg_sc_sea_state_2	above Tg_swell	below Tg_old_sea
Fg_sc_sea_state_3	below Tg_swell	between Tg_old_sea and Tg_young_sea
Fg_sc_sea_state_4	above Tg_swell	between Tg_old_sea and Tg_young_sea
Fg_sc_sea_state_5	below Tg_swell	above Tg_young_sea
Fg_sc_sea_state_6	above Tg_swell	above Tg_young_sea

4 Algorithm description

In the following sections it is necessary to consider that polarised brightness temperature (of a plane wave measured by a radiometer) can be described through the polarisation vector,

$$\overline{Tb} = [Tb_{hh}, Tb_{hv}, Tb_{vh}, Tb_{vv}]$$

in the Earth reference frame and

$$\overline{Tb} = [Tb_{xx}, Tb_{xy}, Tb_{yx}, Tb_{yy}]$$

in the antenna reference.

Otherwise, through the Stokes vector $[I, Q, U, V]$, where,

$$\begin{aligned} I &= Tb_{hh} + Tb_{vv} \text{ or } Tb_{xx} + Tb_{yy} \\ Q &= Tb_{hh} - Tb_{vv} \text{ or } Tb_{yy} - Tb_{xx} \\ U &= Tb_{hv} + Tb_{vh} \text{ or } Tb_{xy} + Tb_{yx} \\ V &= 0 \end{aligned}$$

I represents the total power transported by the wave; Q , the second Stokes parameter, represents the linear polarisation oriented in the reference direction.

U , the third Stokes parameter, is the difference between linear polarisation components oriented in $+45^\circ$ and -45° , and V , the fourth Stokes parameter, is interpreted as the difference between left-hand and right-hand circularly polarised brightness temperature; all measurements indicate that it is negligible at L-band, so for most applications V is assumed to be 0.

Most of times, instead of the Stokes vector, the modified Stokes vector $[T1, T2, T3, T4]$ ($[Tb_{hh}, Tb_{vv}, U_{Earth}, V_{Earth}]$ or $[Tb_{xx}, Tb_{yy}, U_{Antenna}, V_{Antenna}]$ depending on reference frame) is used, as it is composed by the quantities actually measured by a fully polarised radiometer:

$$\text{Modified stokes vector} = \frac{\lambda^2}{kB\eta} [\langle |E_H|^2 \rangle, \langle |E_V|^2 \rangle, 2\text{Re}\langle E_V E_H^* \rangle, 2\text{Im}\langle E_V E_H^* \rangle]$$

where λ is the radiometer's wavelength, k the Boltzmann constant, B the bandwidth, and η the medium impedance (air). E_H and E_V are the two orthogonal components of the plane wave.



To avoid any misunderstanding with other parameters used throughout this document we will designate the modified Stokes vector by $[A_1, A_2, A_3, A_4]$ in the antenna reference (instead of Level 1 output $[Tb_{xx}, Tb_{yy}, Tb_{xy}]$, with

$$\begin{aligned}A_1 &= Tb_{xx} \\A_2 &= Tb_{yy} \\A_3 &= 2\text{Re}(Tb_{xy}) \\A_4 &= 2\text{Im}(Tb_{xy})\end{aligned}$$

and $[Tb_h, Tb_v, Tb_3, Tb_4]$ in the Earth reference (instead of $[Tb_{hh}, Tb_{yy}, U_{Earth}, V_{Earth}]$). This convention was adopted as part of the harmonisation activities in L2 processor development.

4.1 Flat sea

4.1.1 Theoretical description

4.1.1.1 Physics of the problem

The brightness temperature can be expressed as the sum of two terms; the brightness temperature in the case of a completely flat sea and the additional brightness temperature (T_b) due to the surface roughness, as follows:

$$T_{b,p}(\theta, SST, SSS, P_{rough}) = T_{b_{Flat,p}}(\theta, SST, SSS) + T_{b_{Rough,p}}(\theta, SST, SSS, \overline{P_{Rough}}) \quad 4.1.1$$

The first term is $T_{b_{Flat,p}}$ due to the emission of a flat sea surface, which is well described by the Fresnel equations and is polarization dependent (p). The second term is the increment of brightness temperature due to sea roughness, which can be described through several parameters ($\overline{P_{Rough}}$) related to processes that modify this roughness. θ is the angle under which T_b is measured, and SST is the sea surface temperature and SSS the sea surface salinity.

The brightness temperature is defined as,

$$T_b(\theta) = E(\theta)SST \quad 4.1.2$$

where $E(\theta)$ is the surface emissivity at L-Band which carries the major information regarding SSS . Assuming thermodynamic equilibrium, the Kirchhoff laws applies, and emissivity is considered equal to absorption, and equal to $(1 - \text{reflectivity})$.

It can be written, as follows,

$$E(\theta, \phi) = 1 - \Gamma(\theta, \varepsilon, \phi, roughness) \quad 4.1.3$$

where Γ is the reflectivity, which is dependent on the incident radiation nadir angle θ , on the complex dielectric constant of sea water $\varepsilon (\varepsilon' + i\varepsilon'')$, the azimuth angle ϕ , the roughness and the polarisation.

In the case of a smooth surface sea, the reflectivity can be calculated straightforwardly using the Fresnel reflection laws and providing an accurate dielectric constant model.

The Fresnel reflection coefficients R , for each polarisation, are defined as function of the sea water dielectric constant and the incidence angle, as follows:

$$Rh = \left| \frac{\cos \theta - \sqrt{\varepsilon - \sin^2 \theta}}{\cos \theta + \sqrt{\varepsilon - \sin^2 \theta}} \right|^2 \quad 4.1.4$$

$$Rv = \left| \frac{\varepsilon \cos \theta - \sqrt{\varepsilon - \sin^2 \theta}}{\varepsilon \cos^2 \theta + \sqrt{\varepsilon - \sin^2 \theta}} \right|^2$$

Therefore Tb_h and Tb_v for a flat surface are computed as:

$$\begin{aligned} T_{h_{flat}}(\theta, SST, SSS) &= (1 - Rh(\theta, \varepsilon)) \cdot SST \\ T_{v_{flat}}(\theta, SST, SSS) &= (1 - Rv(\theta, \varepsilon)) \cdot SST \end{aligned} \quad 4.1.5$$

The complex dielectric constant of the sea water is dependent on temperature and on the concentration of salt. It can be calculated at any frequency, within the microwave band, from the Debye (1929) expression:

$$\varepsilon = \varepsilon_{\infty} + \frac{(\varepsilon_s - \varepsilon_{\infty})}{1 + i \omega \tau} - i \frac{\sigma}{\omega \varepsilon_0} \quad 4.1.6$$

in which i is the imaginary number, ε_{∞} is the electrical permittivity at very high frequencies, ε_s is the static dielectric constant, τ is the relaxation time, σ is the ionic conductivity, and ε_0 is the permittivity of free space. ε_s , τ and σ are functions of the temperature and salinity of sea-water, and have been evaluated by, among others, Klein and Swift (1977), Ellison et al. (1998) and Blanch and Aguiasca (2004).

After some comparisons and analysis (Camps et al., 2004; Wilson et al., 2004) when the mission was launched, the Klein and Swift dielectric constant model was agreed to be the model that better expresses this parameter. However, the dielectric constant model has been revised based on the pseudo-dielectric constant retrieved from SMOS measurements (Boutin et al, 2020).

The term $Tb_{Rough,p}$ is described by 3 different models in section 4.2 for nominal roughness contribution estimation, and 7ANNEX A and 7ANNEX B for alternative models (not distributed to users currently).

4.1.1.2 Mathematical description of algorithm

Some of the parameters in equations 4.1.1 - 4.1.6 can be expressed through polynomial functions of salinity (SSS in the case of SMOS) in psu (practical salinity units, UNESCO, 1978) and water temperature, T in °C

$$\varepsilon_s = (m(0) + m(1)T + m(2)T^2 + m(3)T^3)(m(4) + m(5)T \cdot SSS + m(6)SSS^2 + m(8)SSS^3) \quad 4.1.7$$

$$\tau = (t(0) + t(1)T + t(2)T^2 + t(3)T^3)(t(4) + t(5)T \cdot SSS + m(6)SSS + m(7)SSS^2 + m(8)SSS^3) \quad 4.1.8$$

$$\sigma = SSS(s(0) + s(1)SSS + s(2)SSS^2 + s(3)SSS^3) \exp((T - 25)(s(4) + s(5)(25 - T) + s(6)(25 - T)^2 - SSS(s(7) + s(8)(25 - T) + s(9)(25 - T)^2))) \quad 4.1.9$$

The values of these parameters are provided in SMOS TGRD document. The present version considers the model provided by Klein and Swift (1977), but this will be modified if a more accurate model is available.

The dielectric constant ε is computed following equation (4.1.6) and a complex value result.

4.1.1.3 Error budget estimates (sensitivity analysis)

The error of ε_∞ is 20% but this is negligible at L-band.

Cox quotes that the ionic conductivity of the sea water, σ , has an error of $\pm 0.03\%$ for salinities between 30 and 40 psu, which is also negligible.

The static permittivity, ε_s , has a maximum per cent error of 0.49 with respect the measurements, and an average per cent error of 0.11.

The relaxation time, τ , has been derived from measurement with an accuracy of 2.12×10^{-13} and this is the assumed error for that parameter.

Ho's estimated error for ε' is 0.2%.

Taking $\varepsilon = 75 + i42$, which is the approximate value of the dielectric constant of the sea water at 1.43 GHz when $SSS = 20 \text{ psu}$ and $T = 20^\circ\text{C}$, it then follows that the error associated with this particular choice is,

$$\delta\varepsilon \cong 1.15(\delta\varepsilon' + \delta\varepsilon'')10^{-3}$$

Using the above-mentioned values, $\delta\varepsilon' \approx 0.15$ and $\delta\varepsilon'' \approx 0.13$. Hence, the error in the brightness temperature with $T = 293\text{K}$ is

$$\delta T_b = \delta E T \cong 0.09 \text{ K}$$



4.1.2 Practical considerations

4.1.2.1 Calibration and validation

Any global bias occurring in the direct model will be corrected by the **OTT** calibration as described in section 5.

In addition, the systematic land/sea contaminating appearing in the L1c TBs used by the L2 OS algorithm are corrected by applying the mixed scene contamination described in section 6.

4.1.2.2 Exception handling

There is no particular exception handling in the mathematical algorithm except if the following auxiliary data are not provided by the processor or exceed the ranges: *SST*, *SSS*, incidence angles at SMOS pixel. In that case the computation can not be done.

4.1.3 Assumption and limitations

The measurements, on which the Klein & Swift model has been based, were obtained from NaCl solutions and some from real sea water samples. Few measurements were done on the salinity range from 30-40 psu, which are the most common values in the world's ocean. However, the authors confirm that the model should be valid for sea waters that have a salinity range between 3 and 35 psu. Recent measurements from the University of Washington (Lang et al. 2016) suggest that Klein and Swift model could be improved especially at low SST. The relevance of changing from Klein and Swift model to another parametrization is under study via comparisons with SMOS measurements.

4.1.4 Alternative dielectric constant model

Along the investigations done over existing SMOS SSS biases and limitations, it has been identified that there are some limitations on the Klein&Swift dielectric constant model related to low temperatures. These limitations introduce some non-geophysical patterns at higher latitudes requiring correction.

Based on the information that SMOS Acard has, as a proxy of dielectric constant parameters (see section 4.12 for further details in Acard), the ESL team has introduced a new dielectric constant model as alternative to the one from Klein&Swift. This model is now in the L2 OS retrieval algorithm and may be activated by means of a switch in the configuration control.

The new dielectric constant model is written following a single Debye relaxation law, derived according to the model of Somaraju and Trumpf (2006). After neglecting the second relaxation frequency that is negligible at L-band, and keeping the formalism of Somaraju and Trumpf (2006), the dielectric constant is written as:

$$\varepsilon = \varepsilon_1 + \frac{\varepsilon_s - \varepsilon_1}{1 + j\gamma/\gamma_1} - \frac{j\sigma}{\gamma (2\pi\varepsilon_0)} \quad 4.1.10$$

ε_1 is the intermediate frequency dielectric constant (that could also be noted ε_∞ by analogy with classical notations employed in Debye relaxation model; as underlined by Ellison et al., it is in reality a ‘fudge factor’ determined so that the model fits as best as possible a Debye function); ε_s is the static (zero frequency) relative permittivity, γ_1 is the relaxation frequency (in gigahertz), γ is the electromagnetic frequency of the radiometer (in gigahertz), σ is the conductivity of sea water (in siemens per meter), ε_0 is the vacuum electric permittivity

$$\left(\frac{1}{2\pi\varepsilon_0}\right) = 17.975 \times 10 \text{ GHz m/S).} \quad 4.1.11$$

The model of Somaraju and Trumpf (2006) is considerably simpler than the models of Klein and Swift (1977) and Meissner and Wentz (2004, 2012); in particular ε_1 and γ_1 are the ones of fresh water while KS and MW2012 added a S dependency, and it involves much simpler dependency of ε_s with salinity. It uses the same freshwater parameters and σ as MW 2004 and MW2012, and α was fitted on previous dielectric constant models.

$$\varepsilon(T, S) = \varepsilon_1(T, S = 0) + \frac{\varepsilon_s(T, S = 0) \times (1 - \alpha S) - \varepsilon_1(T, S = 0)}{1 + j\gamma/\gamma_1(T, S = 0)} - \frac{j\sigma(T, S)}{\omega_0 \varepsilon_0} \quad 4.1.12$$

Using the α parameter proposed by Somaraju and Trumpf (2006) ($\alpha = 0.00314$) gives a dielectric constant very close to the one of Meissner and Wentz (2012):

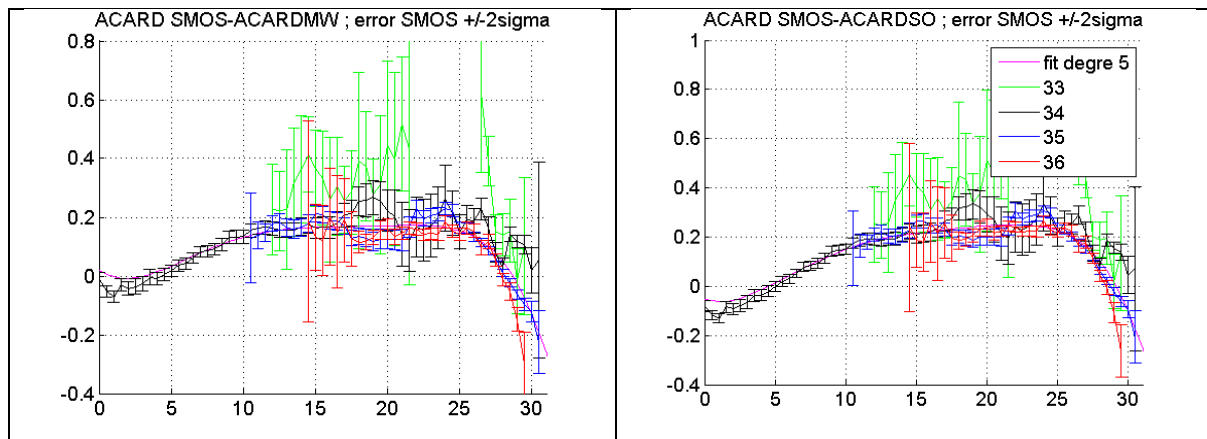


Figure 1: left) ACARD (pseudo-dielectricconstant) retrieved from SMOS Tbs minus ACARD computed from MW 2012, right) ACARD from SMOS minus ACARD computed with SO 2006.

To reduce the difference between SMOS derived ACARD and modelled ACARD, we revise α and make it dependent on T.

$$\alpha(T) = PP(1)*T^3 + PP(2)*T^2 + PP(3)*T + PP(4)$$

4.1.13

with

$$PP = [0.000000001749069, 0.000001088535951, -0.000038972693320, 0.003228077425434]$$

With these new parametrizations, the SST dependency of SMOS ACARD becomes very close to the one of modelled ACARD. The SSS dependency remains slightly different which could be due to uncertainty in the SSS used to compute modelled ACARD in case of fresh water:

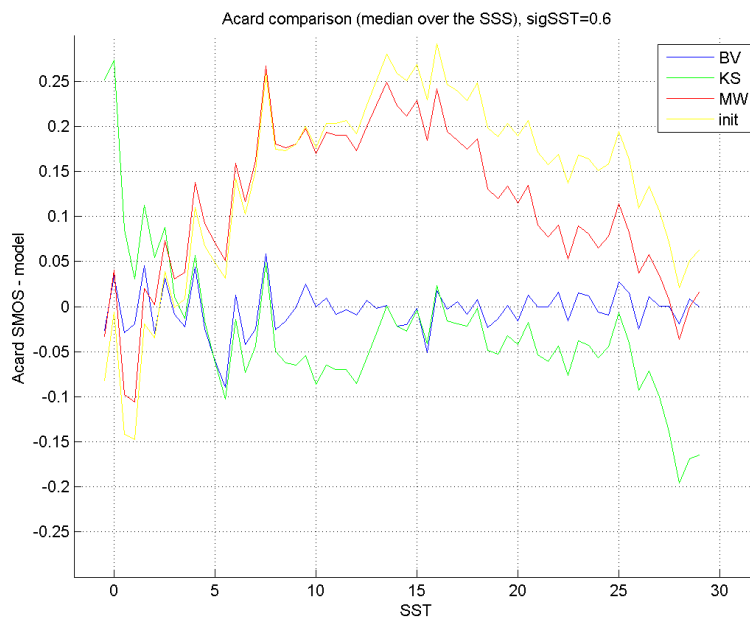


Figure 2: ACARD from SMOS minus ACARD computed with various dielectric constant model. (new model is in blue)

In our model derived from Somaraju's formulation, the computation of the dielectric constant is as follows:

$$\varepsilon = \varepsilon_1 + \frac{\varepsilon_s - \varepsilon_1}{1 + j\gamma/\gamma_1} - \frac{j\sigma}{\gamma(2\pi\varepsilon_0)}$$

4.1.14

where all the coefficients are derived from auxiliary data.

$$\gamma = freq_smos$$

γ is given in GHz

ARGANS Ltd.

Commercial in Confidence

$$\frac{1}{(2\pi\epsilon_0)} = 17.975 \times 10 \text{ GHz m/S} \quad 4.1.15$$

We consider the conductivity from Stogryn (1995), derived as follows:

$$\text{sig35} = s(1) + s(2) \times T + s(3) \times T^2 + s(4) \times T^3 + s(5) \times T^4 \quad 4.1.16$$

$$r15 = \text{SSS} \times (s(6) + s(7) \times \text{SSS} + s(8) \times \text{SSS}^2) / (s(9) + s(10) \times \text{SSS} + \text{SSS}^2) \quad 4.1.17$$

$$\text{alpha0} = (s(11) + s(12) \times \text{SSS} + s(13) \times \text{SSS}^2) / (s(14) + s(15) \times \text{SSS} + \text{SSS}^2) \quad 4.1.18$$

$$\text{alpha1} = s(16) + s(17) \times \text{SSS} + s(18) \times \text{SSS}^2; \quad 4.1.19$$

$$\text{rtr15} = 1.0 + (T - 15.0) \cdot \text{alpha0} / (\text{alpha1} + T); \quad 4.1.20$$

$$\sigma = \text{sig35} \cdot r15 \cdot \text{rtr15}; \quad 4.1.21$$

The various coefficients required are seen below.

s(1)	2.903602
s(2)	8.60700e-2
s(3)	4.738817e-4
s(4)	- 2.9910e-6
s(5)	4.3047e-9
s(6)	37.5109
s(7)	5.45216
s(8)	1.4409e-2
s(9)	1004.75
s(10)	182.283
s(11)	6.9431
s(12)	3.2841
s(13)	-9.9486e-2
s(14)	84.850
s(15)	69.024
s(16)	49.843
s(17)	- 0.2276
s(18)	0.198e-2

$$\epsilon_s = \frac{ms(1) + ms(2) \times T}{ms(3) + T} (1 - \text{alpha} \times \text{SSS}) \quad 4.1.22$$



With

$$\alpha = ms(4) * T^3 + ms(5) * T^2 + ms(6) * T + ms(7) \quad 4.1.23$$

and its associated coefficients, below.

Ms(1)	3.70886e4
Ms(2)	- 8.2168e1
Ms(3)	4.21854e2
Ms(4)	0.000000001749069
Ms(5)	0.000001088535951
Ms(6)	-0.000038972693320
Ms(7)	0.003228077425434

Compute first Debye relaxation frequency (in GHz):

$$\gamma_1 = (f(1) + T)/(f(2) + f(3)*T + f(4).*T^2) \quad 4.1.24$$

with the coefficients below.

f(1)	45.00
f(2)	5.0478e+00
f(3)	-7.0315e-02
f(4)	6.0059e-04

Add the definition of the intermediate frequency dielectric constant

$$\gamma_1 = x(1) + x(2) * T + x(3) * T^2 \quad 4.1.25$$

and the coefficients below.

x(1)	5.7230e+00
x(2)	2.2379e-02
x(3)	-7.1237e-04

Remarks :

$\epsilon = \epsilon_1 + \frac{\epsilon_s - \epsilon_1}{1 + j\gamma/\gamma_1} - \frac{j\sigma}{\omega_0 \epsilon_0}$ is equivalent to $\epsilon = \epsilon_1 + \frac{\epsilon_s - \epsilon_1}{1 - j\gamma/\gamma_1} + \frac{j\sigma}{\omega_0 \epsilon_0}$ (which is the equation for Somaraju relationship), (it depends on the sign adopted for imaginary part, in fine it is the module which matters for computing Acard and R.

ARGANS Ltd.



Some examples of impact:

With Klein and Swift

SSS = 33
SST = 0 15 30
epsr = 76.6880 -45.9168i 73.9412 -58.1977i 69.7717 -74.4763i

SSS = 35
SST = 0 15 30
epsr = 76.1953 -47.7527i 73.5036 -60.9531i 69.3977 -78.2257i

SSS=38
SST = 0 15 30
epsr= 75.4400 -50.4924i 72.8316 -65.0568i 68.8220 -83.8030i

With new parametrisation :

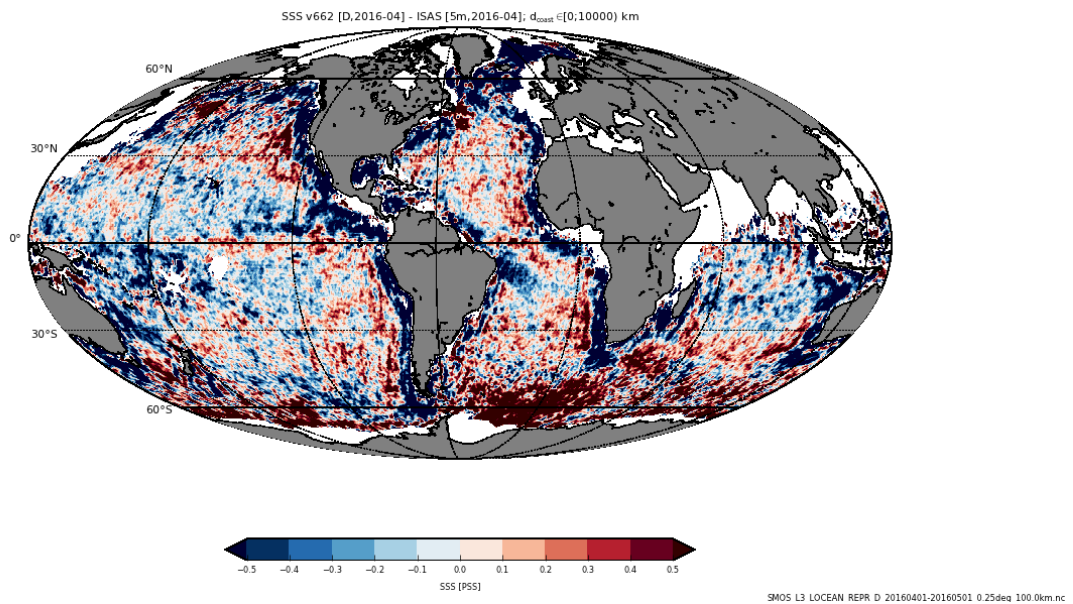
SSS = 33
SST = 0 15 30
epsr=76.7664 -46.2706i 73.5982 -58.3569i 68.5527 -74.5406i

SSS = 35
SST = 0 15 30
epsr = 76.2127 -48.1005i 73.1275 -61.1103i 68.0818 -78.2870i

SSS=38
SST = 0 15 30
epsr= 75.3822 -50.8181i 72.4215 -65.1952i 67.3755 -83.8418i

Period of test

April 2016 (anomaly in Southern Atlantic) :



Implementation was tested starting with a test over 1 day (15 April 2016) in descending orbit, then 1 month in descending orbit because descending orbits are less affected by ice edge.

References

- Blanch, S. and Aguiasca, A. (2004). Seawater dielectric permittivity model from measurements at I-band. Proceedings of IGARSS 2004, Alaska.
- Boutin, J., Vergely, J. L., Dinnat, E. P., Waldteufel, P., d'Amico, F., Reul, N., ... & Thouvenin-Masson, C. (2020). Correcting sea surface temperature spurious effects in salinity retrieved from spaceborne L-band Radiometer measurements. IEEE Transactions on Geoscience and Remote Sensing.
- Camps, A., Font, J., Gabarró, C., Miranda, J., Obligis, E., Labroue, S., Boone, C., Sabia, R., Vall-llosera, M., Reul, N., June 2004. WP1100, ESTEC ITT 1-4505/03/NL/Cb
- Debye, P. (1929). Polar Molecules. New York: Reinhold.
- Ellison, W., Balana, A., Delbos, G., Lamkaouchi, K., Eymard, L., Guillou, C., and Prigent, C. (1998). New Permittivity Measurements of Sea Water. Radio Science, 33(3):639–648.
- Klein, L. and Swift, C. (1977). An Improved Model for the Dielectric Constant of Sea Water at Microwave Frequencies. IEEE Transactions on Antennas and



Propagation, AP-25(1):104–111.

Lang, R., Y. Zhou, C. Utku, and D. Le Vine (2016), Accurate measurements of the dielectric constant of seawater at L band, *Radio Sci.*, 51, 2–24, doi:10.1002/2015RS005776.

Swift, C. (1980). Passive Microwave Remote Sensing. *Boundary-layer Meteorology*, 18:25–54.

UNESCO (1981) The Practical Salinity Scale 1978 and the International Equation of State of Seawater 1980. 10th report of the Joint Panel on Oceanographic Tables and Standards. UNESCO Technical Papers in Marine Science, 36

Wilson, W., Yueh, S., Dinardo, S., and Li, F. (2004). High stability I-band radiometer measurements of saltwater. *IEEE Transactions on Geoscience and Remote Sensing*, 42(9):1829–1835.

4.2 Surface roughness and foam model 1

4.2.1 Theoretical description

For a complete description of the sea surface roughness model, the reader should refer to (Yueh, 1997).

4.2.1.1 Physics of the problem

Sea surface brightness temperature, Tb , in the direction defined by the incidence angle θ and the azimuth angle ϕ is,

$$Tb(\theta, \phi) = SST \cdot E(\theta, \phi) \quad 4.2.1$$

where E is sea surface emissivity and SST are sea surface temperature. Assuming thermodynamic equilibrium, the Kirchhoff law applies and $E = a = 1 - \Gamma$, where a and Γ are sea surface absorptivity and reflectivity, respectively. The modified Stokes vector is written as

$$Tb = \begin{bmatrix} Th \\ Tv \\ T3 \\ T4 \end{bmatrix} = SST \left(\begin{bmatrix} 1 \\ 1 \\ 0 \\ 0 \end{bmatrix} - \Gamma \right) \quad 4.2.2$$

where Tv and Th are Tb in vertical and horizontal polarisations (hereafter V- and H-pol) respectively, related to first and second Stokes parameters by $I = Tb_v + Tb_h$ and $Q = Tb_v - Tb_h$ respectively, and T_3 and T_4 are the third (U) and fourth (V) Stokes parameters respectively.

Due to the sea surface not being flat, scattering induced by sea waves slightly modifies the reflectivity from Fresnel's equations. Consequently, Γ depends not only on incidence angle θ and sea water dielectric constant (and in turn on SST and SSS) but also on ϕ and shape of the surface, i.e. the roughness.

The sea surface is never flat, with roughness at very different scales being created by both local and instantaneous wind and distant wind (inducing swell), as well as by wave interactions. Roughness of the sea surface scatters impinging electromagnetic waves and consequently modifies reflection from Fresnel's equation. Numerical rigorous solution of Maxwell's equations is not considered as they cannot be resolved explicitly. There are two widely used approximated models, the two scales model and the so-called one-scale small slopes approximation. A simpler approach based on geometric optics (GO) (Stogryn (1967), Prigent and Abba (1990)) is discarded for use at low frequency. Indeed, whereas at high frequencies (i.e. in the millimetre domain) waves smaller than λ_0 (the radiometer

wavelength) have a negligible contribution and all ocean waves can be considered as large-scale, simulations at 21 cm showed that a significant signal is induced by small scales and that a large part of roughness-induced signal is not predicted by GO (*Dinnat et al, 2002b*). Noticeably, GO predicts very small roughness effect on Tb at nadir and moderate incidence angles, in contradiction with observations from *Hollinger (1971)*, *Swift (1974)*, *Webster and Wilheit (1976)*, *Camps et al. (2004a)* and *Etcheto et al. (2004)*, as well as those from *Blume et al. (1977)* at 2.65 GHz. Note that it is very unlikely that the observed Tb variations correlated with wind speed variations are due to foam only, because they were observed also at small wind speed WS and the trend was close to linear in WS (in the limit of measurements precision).

4.2.1.1.1 Electromagnetic model

In the two-scale model, the surface is modelled as the superimposition of small waves upon large waves, roughness scales being parted into small and large scales by a cut-off wavelength λ_c . Small scales are sea waves whose height is small compared to λ_0 and large scales are waves whose curvature radius is large compared to λ_0 . Below we summarize main elements of the two-scale model of *Yueh (1997)*. The reader should refer to the original paper for a complete description.

To derive Tb , one combines both large and small scales by integrating contributions of all large waves over the slopes domain (S_x, S_y) and weighting contributions by the slopes probability density function (PDF) of the large waves $(P(S_x, S_y))$. It follows that

$$Tb_{Sea}(\theta, \phi) = \iint Tb_l(\theta, \phi) P(S_x, S_y) (1 - S'_x \tan \theta) dS_x dS_y$$

where P is assumed to be Gaussian, and its width depends on the mean square slope (MSS) of the large-scale waves, S'_x and S'_y are the surface slopes along and across the radiometer azimuth observation direction, respectively. Local brightness temperature for a large wave (Tb_l) differs from Tb_{Flat} because firstly, incidence and azimuth angles are modified because of the large wave's tilting, resulting in local incidence and azimuth angles (θ_l, ϕ_l) and secondly diffracting small-scale roughness is present on the large wave. Hence, Tb is expressed as

$$Tb_l(\theta_l, \phi_l) = SST (1 - R_{ss}(\theta_l, \phi_l)) \quad 4.2.3$$

Where $R_{ss} = R_c + R_i$ is the reflectivity of a small-scale roughness covered surface, separated into a coherent (R_c) and an incoherent (R_i) component. The incoherent term accounts for waves impinging from non-specular direction and scattered toward the radiometer, according to first order small-perturbation method (SPM1, *Rice (1951)*). The incoherent term is written as,

$$R_i(\theta_l, \phi_l) = \int_0^{\frac{\pi}{2}} \sin\theta_\alpha d\theta_\alpha \int_0^{2\pi} \frac{\cos\theta_\alpha}{4\pi\cos\theta_l} \begin{bmatrix} \gamma_{hhhh} + \gamma_{hv hv} \\ \gamma_{vvvv} + \gamma_{vhvh} \\ 2 \operatorname{Re}(\gamma_{vhhhh} + \gamma_{vvhv}) \\ 2 \operatorname{Im}(\gamma_{vhhh} + \gamma_{vvhv}) \end{bmatrix} d\phi_\alpha \quad 4.2.4$$

where γ functions are the bistatic scattering coefficients, dependent on sea surface power spectrum of small-scale roughness (W_{SS}).

The coherent term R_c , that expresses reflection and scattering of the power impinging from specular direction, is modeled using a second order small perturbation method (SPM2, Yueh *et al.* (1988)). Coefficients derived from SPM2 are (Yueh, 1997),

$$R_c(\theta, \phi) = \begin{bmatrix} |R_{hh}^{(0)}|^2 \\ |R_{vv}^{(0)}|^2 \\ 0 \\ 0 \end{bmatrix} + \int_0^{2\pi} d\phi_\alpha \int_0^\infty k_0^2 k_{\rho\alpha} W_{SS}(\bar{k}_c) \begin{bmatrix} 2 \operatorname{Re}(R_{hh}^{(0)*} g_{hh}^{(2)}) \\ 2 \operatorname{Re}(R_{vv}^{(0)*} g_{vv}^{(2)}) \\ 2 \operatorname{Re}((R_{hh}^{(0)*} - R_{vv}^{(0)*}) g_{vh}^2) \\ 2 \operatorname{Im}((R_{hh}^{(0)*} + R_{vv}^{(0)*}) g_{vh}^2) \end{bmatrix} dk_{\rho\alpha} \quad 4.2.5$$

Johnson and Zhang (1999) introduce the unified equation that unifies R_i and R_c ,

$$R_{SS} = \begin{bmatrix} |R_{hh}^{(0)}|^2 \\ |R_{vv}^{(0)}|^2 \\ 0 \\ 0 \end{bmatrix} + \underbrace{\int_0^\infty k_0^2 k'_\rho dk'_\rho \int_0^{2\pi} W(k'_\rho, \phi') \begin{bmatrix} g_h \\ g_v \\ g_3 \\ g_4 \end{bmatrix} d\phi'}_{\delta R_{SS}} = \begin{bmatrix} R_h(\theta_i, \phi_i) \\ R_v(\theta_i, \phi_i) \\ 0 \\ 0 \end{bmatrix} + \delta R_{SS} \quad 4.2.6$$

where the first term is the reflectivity of a flat sea, W is the surface power spectrum, $k_c = \frac{2\pi}{\lambda_c}$ is the cutoff wavenumber and g_{pp} functions ($p = v, h, 3$ or 4) that account for both coherent and incoherent contributions to δR_{SS} , the correction to flat sea reflectivity induced by small-scale waves. Expanding physical quantities in a Fourier series with respect to azimuth direction, and under the assumption of even symmetry for surface roughness, one has:

$$\delta R_{SS} = \delta R_{SS,0} + \delta R_{SS,2} f(2\phi_0) \quad 4.2.7$$

$$C(k, \phi) = C_0(k) + C_2(k) \cos(2\phi_0) \quad 4.2.8$$

$$g_p = g_{p,0} + g_{p,2} f(2\phi_0) \quad 4.2.9$$

where f is the cosine for T_v and T_h and sine for T_3 and T_4 , $C(k, \phi) = k^4 W(k, \phi)$ is the 2D surface curvature spectrum. Therefore, the omnidirectional component ($\delta R_{SS}, 0$) and

ARGANS Ltd.

Commercial in Confidence

Page 56

Use, duplication, or disclosure of this document or any information contained herein is subject to the restriction on the title page of this document.

second harmonic amplitude ($\delta R_{ss,2}$) result from weighted integrals of the respective harmonics of the curvature spectrum:

$$\delta R_{ss,0} = \int_{\frac{k_c}{k_0}}^{\infty} C_0(k'_\rho) \begin{bmatrix} g'_{h,0} \\ g'_{v,0} \\ g'_{3,0} \\ g'_{4,0} \end{bmatrix} d\xi \quad 4.2.10$$

and

$$\delta R_{ss,2} = \int_{\frac{k_c}{k_0}}^{\infty} C_2(k'_\rho) \begin{bmatrix} g'_{h,2} \\ g'_{v,2} \\ g'_{3,2} \\ g'_{4,2} \end{bmatrix} d\xi \quad 4.2.11$$

Where $\xi = k/k_0$ and $g'_{p,n} = g_{p,n}/\xi$ scattering weighting functions given by *Johnson and Zhang (1999)*.

Dinnat and Drinkwater (2004) assessed the relative influence of the various scales on Tb from above weighting functions. Similarly, to the radar case, there is a specific range of wavelengths (i.e. typically around λ_0) that contributes most to Tb , particularly when θ is small. However, significant additional contributions arise also from various scales especially at large θ . **Therefore, good knowledge of roughness is required over a wide range of scales (typically from 1 m to 2 cm).**

4.2.1.1.2 Sea surface roughness and foam models

In addition to the roughness effect, in case the ocean is partly covered by foam, Tb can be separated in two components: one related to the emissivity of a rough sea, and one to the emissivity of foam, Tb_{foam} , according to the percentage of the ocean surface covered by foam (the foam fraction, Fr):

$$Tb_{tot} = (1 - Fr)(Tb_{Flat} + TB_{Rough}) + Fr Tb_{Foam} \quad 4.2.12$$

where Tb_{Flat} is Tb modelled for a flat sea, Tb_{Rough} is the signal induced by the roughened sea, Tb_{Foam} is modelled for an ocean surface entirely covered of foam. We describe below the method used to derive each of these components.

Sea surface roughness is described using a 2D surface power spectrum $W(k'_\rho, \phi')$ i.e. a Fourier transform of the autocorrelation function of sea surface height, that appears in R_c and R_{ss} equations and implicitly in R_i , or using 2D curvature spectrum $C(k, \phi)$ that appears in $\delta R_{ss,0}$ and $\delta R_{ss,2}$ equations. ψ is also used in the composite model to compute large-scale

MSS that defines the slopes probability density function (PDF) of the large waves (P) used in T_b equation. There exists in literature many very different wave spectrum models (e.g. *Durden and Vesecky* (1985), *Donelan and Pierson* (1987), *Apel* (1994), *Yueh* (1997), *Elfouhaily et al.* (1997), *Lemaire* (1998), *Kudryavtsev et al.* (1999) and others). In the following we focus on *Durden and Vesecky* (1985) (hereafter DV) model as it has been widely used to simulate $T_{b_{Rough}}$ at L-band. The DV model is a semi-analytic spectrum, that relies on work by *Pierson and Moskowitz* (1964) for gravity waves ranges, on *Phillips* (1977) for general form in equilibrium range, and that is fitted to HH-pol radar data at 13.9 GHz in order to account for deviation from the Phillips spectrum. The model is tuned to agree with *Cox and Munk* (1954) (hereafter CM) measured MSS. *Yueh* (1997) proposes to multiply the DV model by a factor 2 (hereafter DV2) to account for possible underestimation of MSS measured by *Cox and Munk* (1954), as suggested by *Donelan and Pierson* (1987) and *Apel* (1994), and to better fit data at 19.65 and 37 GHz. It should be noted however that, if needed, the multiplying factor is quite uncertain, and $T_{b_{Rough}}$ is directly proportional to this factor.

In L2OS processor versions before 3.17, the DV model was multiplied by a factor 2 and the foam effect was neglected as it was found that in that case simulated L-band T_b were in relative good agreement with airborne campaign measurements. However, SMOS data evidence that wind induced emissivity is nonlinear with respect to wind speed. A reasonable fit to SMOS data is obtained when introducing a foam coverage parametrization in model 1 and reducing the multiplicative factor in front of DV spectrum.

The omnidirectional part of the DV sea surface wave spectrum has the following form

$$S(k) = a_0 k^{-3} \left(\frac{1.25 k u_*^2}{g_*} \right)^{0.225 \log_{10}(k/2)} \quad 4.2.13$$

where $g_* = g + 7.25 \times 10^{-5} k^2$, $g = 9.81 \text{ ms}^{-2}$, k is wave number and $a_0 = 0.004$. Lately, Yin et al (2012,2016) found that the best fit to SMOS data is obtained for $a_0 = 0.005$.

The foam coverage of has the following form

$$F = b U_{10}^c \quad 4.2.14$$

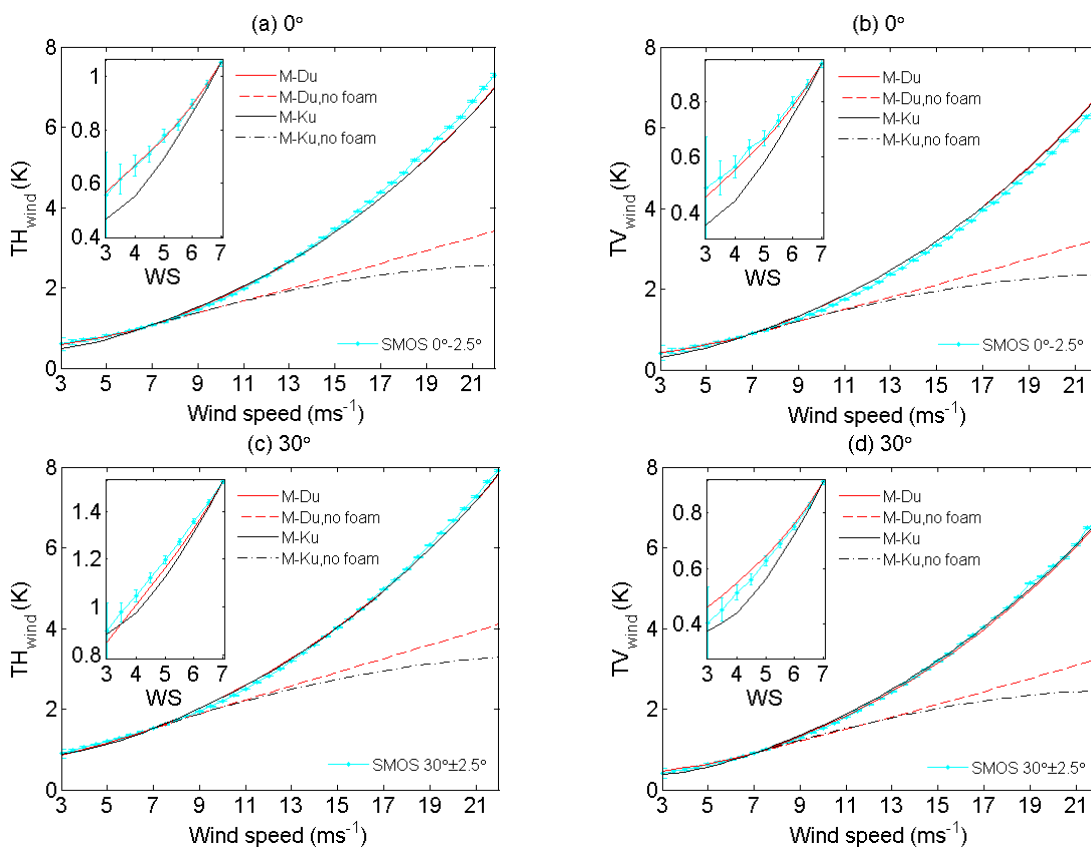
Where U_{10} is the 10-m wind speed. Parameters of the roughness/foam model have been adjusted using the same methodology as in Yin et al. (2016), using 10 months of SMOS L1c data v6 (August to November 2010 and 2012 in the eastern Pacific region). The emissivity model for foam is derived with an incoherent model approach [Anguelova and Gaiser, 2013; Ulaby and Long, 2014]. The values for the void fraction at the air-sea interface, $v_{a,f}$, and effective thickness, $h_{f,e}$, have been fitted with SMOS data. The b and c parameters of the

foam coverage model (see 7ANNEX C) have been fitted with SMOS data, as well as the multiplicative factor in front of the Durden and Vesecki (1985) wave spectrum (a_0). Fitted parameters are indicated in **Table 2**:

Table 2: New parameters of the Durden-Vesecky (1985) spectrum and the macroscopic characteristics, as defined in Yin et al., 2016.. Since a_1 is always 0 it is not listed here.

Main Characteristics of fits	a_0	v_{af}	h_{fe}	b	c
Durden-Vesecky spectrum and wind induced components collocated with ECMWF WS (e_{wE})	0.005	0.97	1.85	1.12e-6	3.15

Comparison between this model and SMOS wind-induced Tb averaged per wind speed bins shows a large improvement at high wind speed, with respect to Yin et al., 2012 which uses a foam model, implemented in previous L2OS v5 is shown in Figure 1.



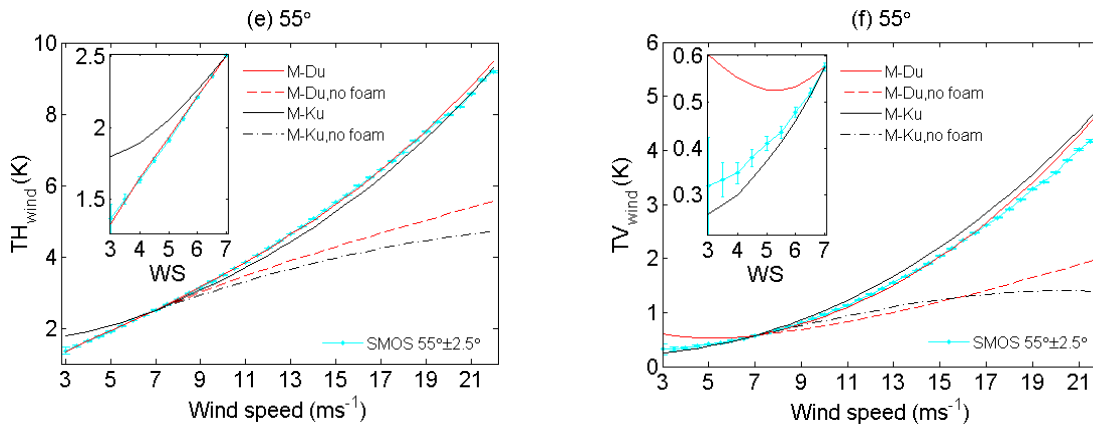


Figure 1: Tb_w at 20°C for 0° , 30° and 55° incidence angles (from up to down) in H polarization (left column) and in V polarization (right column). SMOS Tb_w collocated with ECMWF WS are shown by cyan star-curves with error bars. Tb_w simulated with the Durden-Vesecky model and the Kudryavtsev spectrum model without foam are shown by red dashed and black dashed curves, respectively. Tb_w simulated with the Durden-Vesecky spectrum and the Kudryavtsev spectrum including foam using the M-Du-E (the one used in the L2OS v6 processor) and the M-Ku-E parameterization are shown by red and black curves, respectively. All curves are arbitrarily shifted to the SMOS data at 7 ms^{-1} .

Upwind/downwind Tb asymmetry is uncertain at L-band: using the empirical model for roughness asymmetry developed by Yueh (1997) from high frequency radiometric data, it is estimated to be up to $\pm 0.2\text{ K}$ (with $a_0 = 0.005$) at $\theta = 60^\circ$ and $WS = 8\text{ ms}^{-1}$, and very small at moderate incidence angles. Upwind/crosswind asymmetry is very dependent on the spectrum model. Elfouhaily et al. (1998) model predicts asymmetry 3 times larger than DV2 model (and hence 6 times larger than DV), but still at most $\pm 0.3\text{ K}$ for $WS = 10\text{ ms}^{-1}$.

Sensitivity to roughness and model uncertainty studies are reported in Dinnat et al. (2003a).

In this model, influence of roughness on Tb depends slightly on SST and SSS . Using a constant SST over the global ocean for estimating roughness effect would induce an error on retrieved SSS of the order of 0.5 psu between regions having SST differing by 30°C (the SSS effect is less important as a variation of 7 psu on SSS leads to a less than 0.1 psu error on retrieved SSS) (note that in reality, roughness and SST may be correlated especially close to fronts). **Therefore, Tb_{Rough} dependence on SST should not be neglected in case of SSS retrieval in the context of largely variable SST , as for example for global ocean measurements where there is a risk to introduce regional biases.**

Over most of the incidence angles measured by SMOS, the major contributors to Tb rough are the small scales.

In the studies mentioned above, these small scales have been parametrized using WS assuming a neutral atmosphere (no air-sea temperature difference), i.e. a unique relationship between the friction velocity, U^* , and WS . However, this is usually not the case in the real

world and atmospheric instability may create variations of the order of 5-10% on U^* . Wind speed, WS , at an altitude z , and U^* are classically related using the Monin-Obukhov equation:

$$WS(z) - u_c = \frac{U^*}{\kappa} \left[\ln \left(\frac{z}{z_0} \right) + \Psi \right] \quad 4.2.15$$

where u_c is the surface velocity (i.e. the surface current), κ is von Karman's constant (normally assigned to a value of 0.4), z_0 is the roughness length (often parametrized as a function of U^* and possibly dependent on wave age, in meters), and Ψ is a function of the stability parameter z/L where L is the Monin Obukhov length that classically depends on temperature difference between air and sea, on SST and on relative humidity, or using a drag coefficient,

$$\frac{U^{*2}}{WS(10m)^2} = C_D \quad 4.2.16$$

that depends on the above-mentioned parameters.

In Dinnat's model, when looking at Tb_{Rough} as a function of WS or as a function of U^* for variations of C_D of 5 to 12%, we observe that Tb_{Rough} better correlates to U^* than with WS ; on Figure 17 Tb_{Rough} through simulations (using DV2 wave spectrum) are presented for a 50° incidence angle (for which we expect the largest influence of both WS and U^* because of the competitive effect of small and large scales (Fig.16)): nevertheless the correlation with U^* is still much better than with WS and the scatter induced by the varying C_D is always less than 0.1 K for a given U^* (which is not true for a given WS).

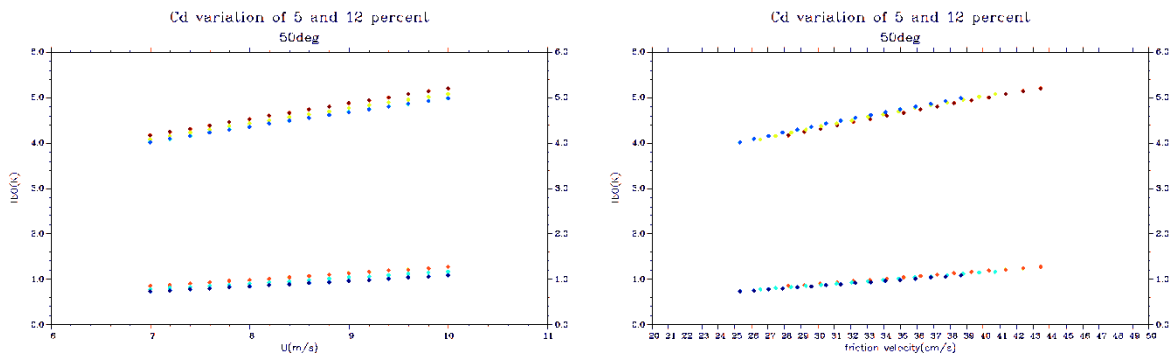


Figure 2 : Tb_{Rough0} (omnidirectional) at 50° incidence angle in Vpol (bottom points) and Hpol(top points) as a function of wind speed (left) and as a function of U^* (right) simulated for neutral conditions (blue points) and for C_D varying by 5% (yellow and light blue) and by 12% (red and brown)

Therefore, instead of parametrizing Tb_{Rough} variations as a function of WS only, we propose to relate them to U^* , and to introduce the neutral equivalent wind speed parameter that is the parameter usually retrieved from scatterometer measurements.

Since a scatterometer is primarily sensitive to U^* , a neutral equivalent wind speed, WS_n , has been introduced in the scatterometer community (Liu and Tang 1996) that represents the wind speed that would be measured at 10m height if the atmosphere were neutral and if the surface speed was zero,

$$WS_n = \frac{U^*}{\kappa} \left[\ln \left(\frac{10}{Z_0} \right) \right] \quad 4.2.17$$

Given air-sea temperature differences and relative humidity observed over various regions of the open ocean, systematic differences of 0.5 to 1m/s over some particular regions may occur between WS and WS_n (Liu and Tang 1996) (e.g. in the equatorial Pacific).

4.2.1.2 Mathematical description of algorithm

Equation 5.2.12 can be written as,

$$Tb_{tot} = Tb_{Flat} + (1 - Fr)Tb_{Rough} - Fr Tb_{Flat} + Fr Tb_{Foam}$$

The brightness temperature induced by the wind can be defined as,

$$Tb_{Wind} = (1 - Fr)Tb_{Rough} - Fr Tb_{Flat} + Fr Tb_{Foam}$$

Tb_{Rough} is decomposed as the sum of an omnidirectional signal plus first and second harmonics:

$$Tb_{Rough} = \begin{bmatrix} Tb_{n_0} + Tb_{n_1} \cos(\phi_a) + Tb_{n_2} \cos(2\phi_a) \\ Tb_{v_1} + Tb_{v_2} \cos(\phi_a) + Tb_{v_3} \cos(2\phi_a) \\ U_1 \sin(\phi_a) + U_2 \sin(2\phi_a) \\ V_1 \sin(\phi_a) + V_2 \sin(2\phi_a) \end{bmatrix}$$

where ϕ_a is the azimuth angle between wind direction (ϕ_w) and the azimuthal observation angle of radiometer look direction (ϕ_r) such that $\phi_a = \phi_w - \phi_r$ with all these angles counted counter clockwise, with origin on x axis (mathematical convention).

Thus, we can write

$$Tb_{Wind} = Tb_0 + Fr Tb_{Foam} + Tb_1 \cos(\phi_a) + Tb_2 \cos(2\phi_a) \quad 4.2.18$$

and define

$$Tb_{w0} = Tb_0 + FrTb_{Foam}, \quad 4.2.19$$

which considers both the contributions of the constant term of the roughness expression and the brightness temperature induced by the foam.

Considering all four polarisations, Tb_{Wind} looks like,

$$Tb_{Wind} = \begin{bmatrix} Tb_{h_{w0}} + Tb_{h_1} \cos(\phi_a) + Tb_{h_2} \cos(2\phi_a) \\ Tb_{v_{w1}} + Tb_{v_1} \cos(\phi_a) + Tb_{v_2} \cos(2\phi_a) \\ U_1 \sin(\phi_a) + U_2 \sin(2\phi_a) \\ V_1 \sin(\phi_a) + V_2 \sin(2\phi_a) \end{bmatrix} \quad 4.2.20$$

Since the model computation is very intensive, tabulations of

$Tb_{h_{w0}}, Tb_{h_1}, Tb_{h_2}, Tb_{v_{w0}}, Tb_{v_1}, Tb_{v_2}, U_1, U_2, V_1,$ and V_2

are provided as functions of, incidence angle, SSS, SST and 10 m neutral wind speed WS_n . The tabulation for SSS is provided between 30 and 39 psu, for SST between 0 and 30°C, for WS_n between 2 and 30 ms^{-1} and incidence angles between 0 and 68°. When $WS_n = 0, Tb_{Wind}$ are set to 0. For the interpolation of the table, a switch allows the user to choose between a linear interpolation (following the method described in TGRD) and a Hermite interpolation. The Hermite interpolation results in a continuous theoretical error on SSS but is computationally heavy. The linear interpolation is faster, but it results in a discontinuity of the theoretical error on SSS , linked to the non-linearity of the model for wind speeds of $7ms^{-1}$.

If one of the prior values of the retrieved geophysical parameters is out of the LUT range, or if any retrieved geophysical parameters goes out of LUT range during the retrieval, different flags

Fg_OoR_Rough_dim1
Fg_OoR_Rough_dim2
Fg_OoR_Rough_dim3
Fg_OoR_Rough_dim4

are raised. No extrapolation is done, and the boundary value is taken.

Tb_{Wind} is shown in Figure 3,

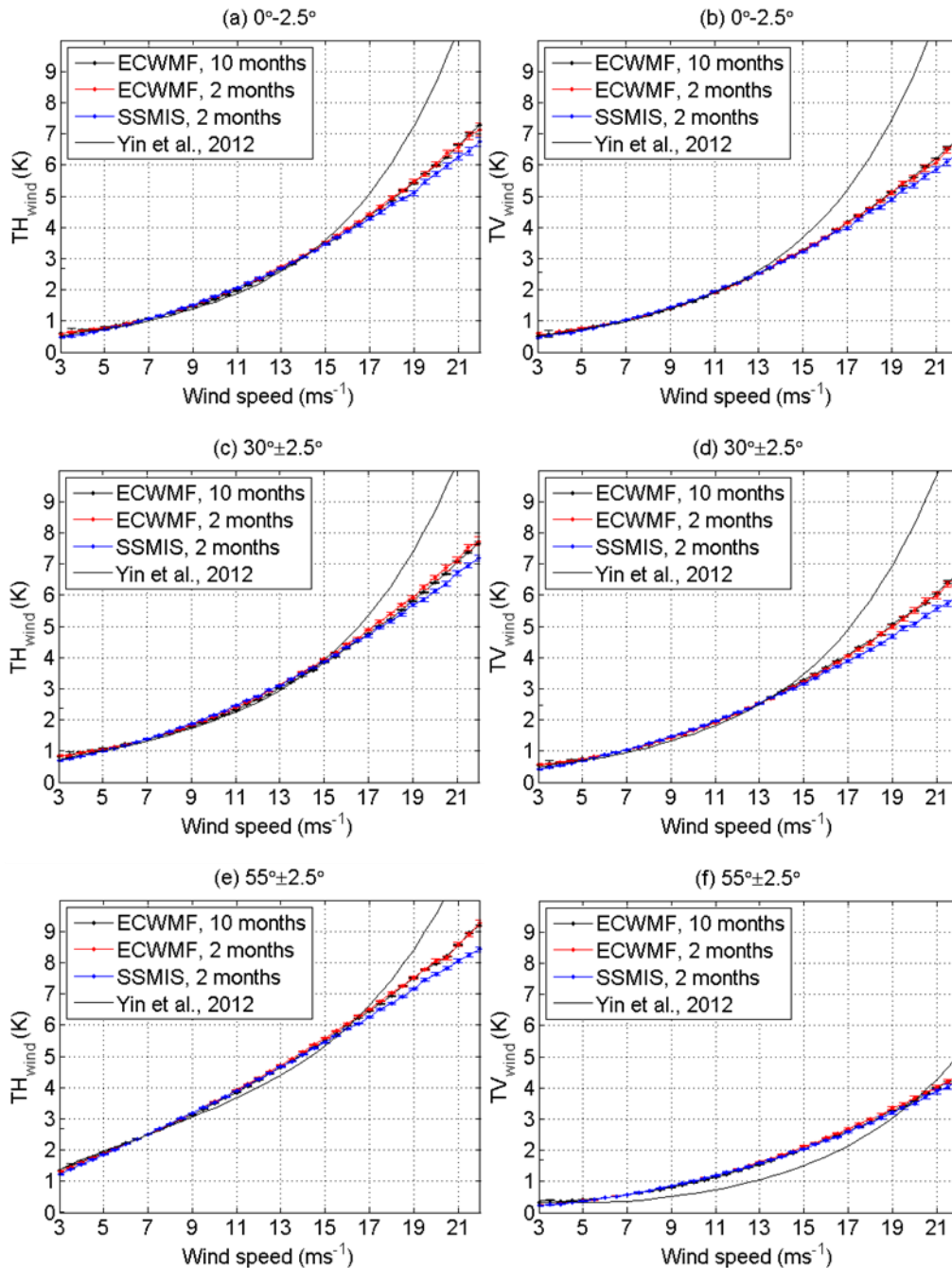


Figure 3: T_{b_wind} SMOS (in colours) at 20°C as a function of the various wind speeds and for different incidence angles and polarisations; Yin et al. (2012) model is superimposed as a black line.

We will assume that T_{b_Rough} can be entirely described using WS_n in future versions, depending on the accuracy of ECMWF WS , possibility of deducing a reliable U^* from ECMWF



WS and $T_{Air} - T_{Sea}$ and the sensitivity of Tb_{Rough} to WS/U^* we could add a dependency on WS .

4.2.1.3 Error budget estimates (sensitivity analysis)

The advantage of retrieving WS_n is that it is comparable to scatterometer derived wind speed.

4.2.2 Practical considerations

4.2.2.1 Calibration and validation

The algorithm described above was derived from L1c v6.20 data and the new LUT has been implemented since L2OS v6.62.

4.2.2.2 Quality control and diagnostics

Values outside the min/max ranges given in the Tb_{wind} tabulations should be deduced from a linear extrapolation of the two edge values of the tabulations (since most of the dependencies are close to linear), except for low wind speed where Tb_{Rough} at WS between 0 and 2ms^{-1} should be deduced from a linear interpolation between 0 and Tb_{Rough} (2ms^{-1}). By default, the roughness correction is always applied (`Fg_ctrl_roughness_M1, true`). There is also the possibility (controlled by a switch based on a minimum wind speed `Tg_WS_roughness_M1`) that no roughness correction is applied in these low wind cases (due to lack of confidence in the model), and in such case a flag will be raised (`Fg_ctrl_roughness_M1, false`)

We included the foam modelling in the roughness model 1 LUT (i.e. Tb_{wind} model 1) because it was easier to handle it. Hence it is not relevant to use simultaneously to model 1 the foam model implemented in L2OS (a flag is raised (`Fg_ctrl_foam_M1, false`) because the foam model is not explicitly used).

4.2.3 Assumption and limitations

In the present approach, surface speed (u_c) is neglected while studies like [Kelly *et al.*, 2001] evidence that current speed has an impact on scatterometer measurements in case of strong currents gradients (equatorial Pacific); this issue will be studied in the future, including the best source for this auxiliary information.

Roughness is not necessarily related to local and instant wind only, and wind effects also imply its duration and action distance, as well as the presence of swell. These effects are not included in the present model but may be included in U^* computation.

Additional phenomena are likely to cause noticeable modification of Tb . The first one is foam, that appears above a threshold wind speed, and whose permittivity largely differs from the

ARGANS Ltd.

one of sea water. During experimental campaigns it is very difficult to separate roughness and foam effect so that it is possible that the factor of 2 applied to DV spectrum is slightly overestimated but it was not possible using WISE and Eurostarrs data to demonstrate that dependence of Tb with respect to WS was non linear, implying that foam effect was weak. The second one, still to be investigated for L-band radiometry, is the presence of surface slicks of natural or non-natural origin. Slicks are known to damp roughness at specific scales, and their permittivity different from that of sea water might change Tb .

References

- Blume, H.-J. C., A.W. Love, M. J. V. Melle, and W.W. Ho, Radiometric observations of sea temperature at 2.65 GHz over Chesapeake Bay, *IEEE Transactions on Antennas and Propagation*, AP-25, 121–128, 1977.
- Boutin, J., E. Obligis, and E. Dinnat, WP1120, Influence of Surface Roughness on Tb Simulated in L-Band by Yueh-LODYC Emissivity Model and by UCL Model - Analyse of the Differences, in *Scientific requirements and impact of space observation of ocean salinity for modeling and climate studies: final report*, NERSC technical report n_214 under contract n_14273/00/NL/DC European Space Agency, 2002.
- Boutin, J., P. Waldteufel, N. Martin, G. Caudal, and E. Dinnat, Salinity Retrieved from SMOS Measurements over Global Ocean: Imprecisions Due to Surface Roughness and Temperature Uncertainties, *Journal of Atmospheric and Oceanic Technology*, 21, 1432–1447, 2004.
- Camps, A., et al., L-band sea surface emissivity: Preliminary results of the WISE-2000 campaign and its application to salinity retrieval in the SMOS mission, *Radio Science*, 38, 2003.
- Camps, A., et al., The WISE 2000 and 2001 field experiments in support of the SMOS mission: sea surface L-band brightness temperature observations and their application to sea surface salinity retrieval, *IEEE Transactions on Geoscience and Remote Sensing*, 42, 804–823, 2004a.
- Cox, C., and W. Munk, Measurement of the roughness of the sea surface from photographs of the sun's glitter, *Journal of the Optical Society of America*, 44, 838–850, 1954.
- Dinnat, E., J. Etcheto, J. Boutin, G. Caudal, A. Weill, A. Camps, J. Miller, and S. Contardo, Sea state influence on L-band emissivity in various fetch conditions, in *Geoscience and Remote Sensing Symposium, 2002. IGARSS '02. 2002 IEEE International*, vol. 6, pp. 3632–3634, 2002a, tY - CONF.
- Dinnat, E. P., De la détermination de la salinité de surface des océans à partir de mesures radiométriques hyperfréquence en bande L, Ph.D. thesis, Université Pierre et Marie Curie, Paris, France, 2003.
- Dinnat, E. P., and M. Drinkwater, Optimizing the Active/Passive Synergy in the Frame of Sea Surface Salinity Retrieval from Microwave Measurements at L-Band, in *Proceedings MicroRad'04*, Rome, Italy, 2004.



- Dinnat, E. P., J. Boutin, G. Caudal, J. Etcheto, and P. Waldteufel, Influence of sea surface emissivity model parameters at L-band for the estimation of salinity, *International Journal of Remote Sensing*, 23, 5117–5122, 2002b.
- Dinnat, E. P., J. Boutin, G. Caudal, and J. Etcheto, Issues concerning the sea emissivity modeling at L-band for retrieving surface salinity, *Radio Science*, 38, 25–1–25–11, 2003a.
- Dinnat, E. P., J. Boutin, G. Caudal, J. Etcheto, and S. Contardo, On the use of EuroSTARRS and WISE data for validating L-band emissivity models, in *First Results Workshop, EuroSTARRS/WISE/LOSACCampaigns, ESA SP-525*, pp. 117–124, ESTEC/European Space Agency, 2003b.
- Donelan, M. A., and W. J. Pierson, Jr., Radar scattering and equilibrium ranges in wind-generated waves with applications to scatterometry, *Journal of Geophysical Research*, 92, 4971–5029, 1987.
- Donelan, M. A., F. W. Dobson, S. D. Smith, and R. J. Anderson, On the dependence of sea surface roughness on wave development, *Journal of Physical Oceanography*, 23, 2143–2149, 1993.
- Durden, S. L., and J. F. Vesecky, A physical radar cross-section model for a wind-driven sea with swell, *IEEE Journal of Oceanic Engineering*, OE-10, 445–451, 1985.
- Etcheto, J., E. Dinnat, J. Boutin, A. Camps, J. Miller, S. Contardo, J. Wesson, J. Font, and D. Long, Wind Speed Effect on L-Band Brightness Temperature Inferred from EuroSTARRS and WISE 2001 Field Experiments, *IEEE Transactions on Geoscience and Remote Sensing*, 42, 2206–2213, 2004.
- Etcheto, J., E. Dinnat, J. Boutin, A. Camps, J. Miller, S. Contardo, J. Wesson, J. Font, and D. Long, Wind speed effect on L-band brightness temperature inferred from EuroSTARRS and WISE 2001 field experiments, *IEEE Transactions on Geoscience and Remote Sensing*, 42, 2206–2214, 2004.
- Hollinger, J. P., Passive microwave measurements of sea surface roughness, *IEEE Transactions on Geoscience Electronics*, GE-9, 165–169, 1971.
- Kelly, K.A., S. Dickinson, M.J. McPhaden, and G.C. Johnson, Ocean currents evident in satellite wind data, *Geophysical Research Letters*, 28, 2469–2472, 2001.
- Liu, W.T., and W. Tang, *Equivalent neutral wind*, 8 pp. JPL/NASA Publ. 96-17, 1 Aug. 1996.
- Prigent, C., and P. Abba, Sea surface equivalent brightness temperature at millimeter wavelengths, *Annales Geophysicae*, 8, 627–634, 1990.
- Monahan E. and I. O'Muircheartaigh, "Whitecaps and the passive remote sensing of the ocean surface," *Int. J. Remote Sensing*, vol. 7, no. 5, pp. 627–642, 1986.
- Rice, S. O., Reflection of Electromagnetic Waves from Slightly Rough Surfaces, *Communications on Pure and Applied Mathematics*, 4, 351–378, 1951.
- Sasaki, Y., I. Asanuma, K. Muneyama, G. Naito, and T. Suzuki, The dependence of sea-surface microwave emission on wind speed, frequency, incidence angle and polarization over the frequency range 1 to 40 GHz, *IEEE Transactions on Geoscience and Remote Sensing*, GE-25, 138–146, 1987.



- Stogryn, A., The apparent temperature of the sea at microwave frequencies, *IEEE Transactions on Antennas and Propagation*, 77, 1658–1666, 1967.
- Stogryn A., “The emissivity of sea foam at microwave frequencies,” *J. Geophys. Res.*, vol. 77, no. 9, pp. 1658-1666, 1972
- Swift, C. T., Microwave radiometer measurements of the Cape Cod Canal, *Radio Science*, 9, 641–653, 1974.
- Webster, W. J., Jr., and T. T. Wilheit, Spectral characteristics of the microwave emission from a winddriven foam-covered sea, *Journal of Geophysical Research*, 81, 3095–3099, 1976.
- Weill, A., T. Besnard, S. Contardo, J. Etcheto, and J. Boutin, WISE results from whitecapping and stereophotogrammetry: a tentative of superposition of topography and foam surface to retrieve active and fossil foam, in *First Results Workshop, EuroSTARRS/WISE/LOSAC Campaigns, ESA SP-525*, pp.89–94, ESTEC/European Space Agency, 2003.
- Yin, X., J. Boutin, N. Martin, and P. Spurgeon, Optimization of L-band sea surface emissivity models deduced from SMOS data, submitted to *IEEE Transactions on Geoscience and Remote Sensing*, 2011.
- Yueh, H. A., R. T. Shin, and J. A. Kong, Scattering of electromagnetic waves from a periodic surface with random roughness, *Journal of Applied Physics*, 64, 1657–1670, 1988.
- Yueh, S. H., Modeling of wind direction signals in polarimetric sea surface brightness temperatures, *IEEE Transactions on Geoscience and Remote Sensing*, 35, 1400–1418, 1997.
- Yueh, S. H., Estimates of Faraday rotation with passive microwave polarimetry for microwave sensing of Earth surfaces, *IEEE Transactions on Geoscience and Remote Sensing*, 38, 2434–2438, 2000.
- Yueh, S. H., R. West, W. J. Wilson, F. K. Li, E. G. Njoku, and Y. Rahmat-Samii, Error sources and feasibility for microwave remote sensing of ocean surface salinity, *IEEE Transactions on Geoscience and Remote Sensing*, 39, 1049–1060, 2001.



4.3 Galactic noise contamination 1

4.3.1 Theoretical description

This section has been written with the help of [*LeVine and Abraham, 2004*] and [*Delahaye et al., 2002*] papers.

A new approach (Galactic noise 2) to the celestial sky glitter was proposed in September 2006 and included as section 4.4, being currently the one used. The simplistic case of a constant galactic noise of 3.7 K (Galactic noise 0) is also used in a minimalist model.

4.3.1.1 Physics of the problem

At L-band, radiation from celestial sources is strong and spatially variable; they have been reviewed by *Delahaye et al. (2002)*, *Le Vine and Abraham (2004)*, and associated corrections needed to interpret L-band radiometric measurements have been thoroughly described by *Le Vine and Abraham (2004)*. Radiation originates from three types of sources. The hydrogen line emission corresponds to a hyperfine atomic transition in neutral hydrogen: the radiation is maximum around the plane of the galaxy, most of the time less than 2 K. The cosmic background is a remnant signal of the origin of the universe and is almost constant in space and time (2.7 K). In addition to the almost constant cosmic background, a very variable (in space) continuum radiation (up to more than 10 K) is due to emissions from discrete radiosources.

As in the case of atmospheric emission, the cosmic background adds a contribution to the radiometric temperature that depends on the incidence angle linked to the reflection of the signal on the sea surface.

The two other types of sources add a signal that varies according to the incidence and azimuth angle of the measurement.

4.3.2 Mathematical description of algorithm

4.3.2.1 Data conversion

The common practice in passive microwave remote sensing of the earth is to consider equivalent brightness temperatures. Thence, for the purpose of L-band radiometry, it is common to present data from radio astronomy surveys in the form of equivalent black-body temperatures, i.e., as if they were from an equivalent thermal source with total power:

$$P = kTb\Delta B$$

4.3.1

where k is the Boltzmann constant and ΔB is the bandwidth of the receiver used for the survey, or as a total power integrated over a frequency range as in the case of the hydrogen line emission.

a) Hydrogen Line emission:

The line emission has a relatively narrow spectrum. For hydrogen at rest, it occurs at a frequency associated with the hyperfine transition at 21.106 cm. However, the line is shifted by the motion of the hydrogen relative to the observer (Doppler shift) and spread by thermal energy of the gas (collisions and vibrations). Nevertheless the spectrum is relatively narrow: Leiden/Dwingeloo survey (Hartmann and Burton 1997) in the Northern hemisphere and IAR survey in the southern hemisphere (Arnal, Bajaja et al. 2000) cover the velocity range from -450 to +400km/s which corresponds to a frequency range of 4.025MHz (see below) about the centre frequency of 1.42GHz of hydrogen at rest. The integrated power reported in radio astronomy survey, P , is given in Kelvin kilometres per second ($K \text{ kms}^{-1}$). In order to convert it to a brightness temperature that will be recorded by a radiometer having a bandwidth ΔB , it is necessary to convert it in Kelvin-MHz using the line emission bandwidth and then to calibrate it with respect to the radiometer bandwidth.

Given the standard form for Doppler shift,

$$v = v_0(1 - v/c) \quad 4.3.2$$

with v_0 the center frequency (1.42GHz), v the frequency associated with the velocity v and c the light speed, a velocity range from -450 to +400kms⁻¹ corresponds to a frequency bandwidth of 4.025MHz.

Thence the integrated power reported in radio astronomy survey corresponding to a velocity range of 850kms⁻¹, P_{int} , can be converted in Kelvin-MHz using:

$$P_{int}(\text{K MHz}) = P_{int}(\text{K kms}^{-1}) \cdot 4.735 \times 10^{-3} \quad 4.3.3$$

Since the SMOS radiometer bandwidth, Tb_{SMOS} in MHz, is well above 4MHz, this value can be converted to get an equivalent Tb for SMOS, as follows:

$$Tb = \frac{P_{int}(\text{K MHz})}{\Delta B_{SMOS}} = P_{int}(\text{K kms}^{-1}) \cdot 4.735 \times \frac{10^{-3}}{\Delta B_{SMOS}} \quad 4.3.4$$

b) Continuum radiation and cosmic background

These radiations are usually given in terms of effective brightness temperature, T_b , i.e. they include the correction for the bandwidth of the survey (e.g. Reich and Reich maps). Thence, as these radiations are supposed to be homogeneous over the frequency range of SMOS bandwidth, there is no need to correct T_b deduced from radio astronomy surveys.

4.3.2.2 Galactic noise reflected towards the radiometer

In the following we will call the effective brightness temperature of the galactic radiation, $T_{b_{Gal}}$, as the sum of the hydrogen emission line plus the continuum radiation plus the cosmic background.

First it is necessary to determine the location in the celestial sky from which incident radiation will be reflected from one point in the field of view into the antenna. Given θ_i and ϕ_i respectively the incidence and the azimuth (0 towards the north; positive westward) angles of one radiometer measurement at this point, the incident galactic ray that will be specularly reflected towards the radiometer comes from an incidence angle, θ_{iGal} :

$$\theta_{iGal} = \sin^{-1} \left(\frac{R_E + h_{rad}}{R_E} \sin \theta_i \right) \quad 4.3.5$$

where R_E is the earth radius and h_{rad} is the altitude of the radiometer.

The elevation angle (in degrees; 0 towards the horizon and positive above the horizon) is defined as:

$$el = 90 - \theta_{iGal} \quad 4.3.6$$

Usually celestial maps are given in celestial coordinates system (declination, δ , and right ascension, α). It is therefore necessary to derive δ and α from the latitude, φ , longitude, ψ , sidereal time, T , θ_i and ϕ_i . This can be done by solving the following implicit equations:

$$\tan(\phi) = \frac{-\sin(H)}{\tan(\delta) \cos(\varphi) - \cos(H) \sin(\varphi)} \quad 4.3.7$$

$$\sin(el) = \sin(\varphi) \sin(\delta) + \cos(\varphi) \cos(H) \quad 4.3.8$$

where H is the sidereal angle (see for instance Appendix C of *Le Vine and Abraham (2004)*) defined as:

$$H = T - \psi - \alpha$$

In the following we consider two cases:

- a) a simple case assuming a rough sea and a homogeneous sky
- b) a more complicated case where we consider the sea surface roughness and the sky inhomogeneity.

In the following we will distinguish two polarizations for Tb_{Gal} . At present, existing galactic maps do not distinguish between V and H pol but there is suspicion about a possible polarization dependency.

- a) Assuming a homogeneous sky:

In that case the contribution of roughness to the reflectance coefficient Γ , R_{rough} computed for estimating Tb_{Rough} , can be used:

$$\begin{aligned}
 Tb_{Gal_{refl}}(\varphi, \psi, T, \theta_i, \phi_i, p) \\
 = Tb_{Gal}(\delta, \alpha, p) \cdot (R(\theta_{iGal}, SSS, SST, p) \\
 + R_{Rough}(\theta_{iGal}, SSS, SST, p))
 \end{aligned}
 \tag{4.3.9}$$

where $R_{Rough} = -\frac{Tb_{Rough}}{SST}$ ($R_{Rough} < 0$)

If the sky were homogeneous, it is expected that the introduction of the roughness would have a small effect in most cases: for instance, for a 10ms^{-1} wind speed, (the reflection coefficient is modified by about 2.5% (at nadir)) and a galactic noise of 5K, neglecting the roughness effect would introduce an error of less than 0.08K.

- b) Assuming an inhomogeneous sky:

Introducing bistatic reflection coefficients that can be extracted from 2-scale or from SSA models, σ_0 in theory the galactic noise over the whole sky should be convoluted with these scattering coefficients. However, since they are expected to decrease rapidly outside of the specular reflection, the integration could be done over an interval $\pm d\theta_{iGal}$ which value will be specified in the TGRD.

$$\begin{aligned}
 Tb_{Gal_{refl}}(\varphi, \psi, T, \theta_i, \phi_i, v) \\
 = \frac{1}{4\pi \cos \theta_i} \int_0^{2\pi \theta_{iGal} + \delta \theta_i} \int_{\theta_{iGal}} (\sigma_{vv}^0(\theta_s, \phi_s, \theta_i, \phi_i) Tb_{Gal}(\theta_s, \phi_s, v) \\
 + \sigma_{vh}^0(\theta_s, \phi_s, \theta_i, \phi_i) Tb_{Gal}(\theta_s, \phi_s, h)) \sin \theta_s d\theta_s d\phi_s
 \end{aligned}
 \tag{4.3.10}$$

$$\begin{aligned}
 T b_{Gal_{refl}}(\varphi, \psi, T, \theta_i, \phi_i, h) \\
 = \frac{1}{4\pi \cos \theta_i} \int_0^{2\pi} \int_{\theta_{iGal}}^{\theta_{iGal} + \delta \theta_i} \left(\sigma_{hh}^0(\theta_s, \phi_s, \theta_i, \phi_i) T b_{Gal}(\theta_s, \phi_s, h) \right. \\
 \left. + \sigma_{hv}^0(\theta_s, \phi_s, \theta_i, \phi_i) T b_{Gal}(\theta_s, \phi_s, h) \right) \sin \theta_s d\theta_s d\phi_s
 \end{aligned}$$

Both cases a) and b) should be kept. A switch will allow to select the desired case.

4.3.2.3 Integration over the antenna beam

In addition it is necessary to integrate the reflected brightness temperature over the antenna pattern to obtain, $T b_{Gal_{refl_{lobe}}}$ which is the quantity measured by the radiometer,

$$T b_{Gal_{refl_{lobe}}}(\theta_i, \phi_i) = \int_0^{2\pi} d\phi_i \int_{\theta_i - \frac{\pi}{2}}^{\theta_i + \frac{\pi}{2}} d\theta_i' \int T b_{Gal_{refl}}(\theta_i) P_{lobe}(\theta_i' - \theta_i, \phi_i) \quad 4.3.11$$

where P_{lobe} is the normalized power pattern of the antenna. In case P_{lobe} is an axially symmetric pattern, according to *Le Vine and Abraham (2004)* it is possible to make the integration on δ and α and thence to precalculate galactic maps integrated over the antenna pattern before computing the reflection over the sea surface. Since the SMOS lobe varies across the FOV and is not symmetric, it will be necessary to test if such an approximation is acceptable.

4.3.2.4 Error budget estimates (sensitivity analysis)

The main uncertainty is expected to come from inaccuracies of the galactic noise maps. (Reich and Reich 1986) estimate the accuracy on their maps (due to the calibration of the instrument) of 0.5K. From SRS study, a constant bias of 0.5K on galactic noise map will induce a mean bias on retrieved SSS of 1psu.

In addition to a constant bias, uncertainties are likely to appear on these maps close to the equatorial galactic plane. Comparisons between the maps derived from the Stockert survey, commonly called the Reich and Reich map, and the ones deduced from the Effelsberg survey are in progress to better apprehend the error on these maps. Both maps include the continuum radiation and the cosmic background; Stockert survey was performed with a 34mn angular resolution instrument while Effelsberg used a 9mn angular resolution instrument. Stockert map for the northern hemisphere and Effelsberg maps are available on the <http://www.mpifr-bonn.mpg.de/survey.html> site; the Stockert map for southern hemisphere was provided by ESA. Stockert maps are global but region around Cassiopeia is excluded (no



data) and strong sources are suspected to be underestimated; Effelsberg survey is concentrated close to the equatorial plane (Cygnus excluded).

4.3.3 Practical considerations

4.3.3.1 Calibration and validation

As suggested before, it may be necessary to introduce a calibration factor proportional to Tb_{Gal} during the Cal/Val phase to correct for calibration and saturation problems of the existing surveys.

4.3.3.2 Quality control and diagnostics

Looking towards North (azimuth=0) with an incidence angle equal to the elevation of the observer, one looks towards the celestial North pole which location is invariant.

4.3.3.3 Exception handling

If a parameter goes out of LUT range during the retrieval, a flag (Fg_OoR_dim1_gam1_dec, Fg_OoR_gam1_ra) is raised. No extrapolation is done, and the boundary value is taken.

4.3.4 Assumption and limitations

Depending on the reliability we can put on galactic noise maps, it could be necessary to discard some SMOS Tb affected by radiation coming from the galactic plane if it is demonstrated that this radiation is very badly known. Tests are in progress to estimate the impact of radiation errors in the galactic plane (as estimated from the difference between Effelsberg and Stockert surveys) on the retrieved SSS. Measurements affected by errors in the determination of the galactic noise will be flagged by Fm_gal_noise_error (if the error is above Tm_max_gal_noise_error). For further analysis, if necessary, measurements with high galactic noise (above Tm_high_gal_noise) will be flagged with Fm_high_gal_noise.

References

Arnal, E.M., E. Bajaja, J.J. Lararte, R. Morras, and W.J.L. Poppel, A high sensitivity HI survey of the sky at $\delta \leq -25^\circ$, *Astron. Astrophys. Suppl. Series*, 142, 35-40, 2000.

Delahaye, J.Y., P. Golé, and P. Waldteufel, Calibration error of L-band sky-looking ground-based radiometers, *RadioSci.*, 37, 10.1029/2001RS002490, 2002.

Hartmann, D., and W.B. Burton, *Atlas of galactic neutral hydrogen*, 235 pp., Cambridge university press, New York, 1997.

LeVine, D.M., and S. Abraham, Galactic noise and passive microwave remote sensing from space at L-Band, *IEEE Transactions on Geoscience and Remote Sensing*, 42, 119-129, 2004.

Reich, P., and W. Reich, A radio continuum survey of the northern sky at 1420 MHz, *Astron. Astrophys. Suppl. Ser.*, 63, 205-292, 1986.



4.4 Galactic noise contamination 2

4.4.1 Overview of the Problem

Estimation of the down-welling celestial sky radiation at L-band that is scattered by the sea surface and sensed by earth viewing radiometers, hereafter referred to as the *sky glitter* phenomenon, is of particular concern for the remote sensing of sea surface salinity (*SSS*) [1], [2], [3]. At L-band, celestial sky radiation originates from the uniform Cosmic Microwave Background (about 2.7 K), hereafter denoted *CMB*, the line emission from hydrogen and a continuum background [3], [4]. Sea surface scattered sky radiation might hamper accurate *SSS* retrievals from space borne measurements of up welling sea surface brightness temperatures at L-band mainly because of three factors:

First, the expected dynamical range of sea surface brightness temperature (T_b) change at L-band due to *SSS* variation is relatively small, being in average smaller than about 4 K for open ocean conditions.

The T_b sensitivity to salinity indeed ranges from about 0.2 K to 0.8 K per psu in that microwave band [2] (depending on ocean surface temperature, considered incidence angle and polarization), and the open ocean salinities are generally in the range between 32 and 37 psu.

Second, although the sky glitter contribution to the effective brightness temperature measured by an L-band radiometer antenna depends on the sources intensity, the surface conditions, the observation geometry and the antenna characteristics (e.g., beam width, gain pattern), it can be of the same order or even greater than the surface salinity impact. For instance, it was found by [3] that the total effective background radiation (sum of line emission, continuum and *CMB* weighted by the antenna gain pattern) at the locus of the reflected rays on the sky, assuming a surface reflectivity of 1 and for a sun-synchronous orbiting antenna with a beam width of the order of 10° , an orbit inclination of 95° and a 6 A.M./6 P.M. equatorial crossing time, changes from a little less than 4 K to more than 9 K. The potential changes within that range are functions of the orientation of the sensor, the spacecraft location along the orbit and the time of year. Accounting for the fact that the actual ocean surface reflectivity may range from about 30% to 80 % at 1.4 GHz (depending on the sea surface physical state, the polarization and bistatic configuration considered), celestial sky glitter contribution is expected to vary between about 1 to more than 7 K, which is very significant with respect to the surface salinity signature.

Third, the line emission from hydrogen and the continuum background exhibit sources that are spatially varying, being strongest in the direction of the plane of the galaxy and at several localized strong spots (Cassiopeia A, Cygnus A etc). Given the relative motion between the sun-synchronous satellite's orbit, the earth and the celestial sky during a year, sky glitter contamination is expected to be geographically and seasonally variable. Correction strategies for this contamination are therefore needed to be able to retrieve unbiased large scale

ARGANS Ltd.



seasonal and geographical features of the global SSS field using the iterative optimization method.

For the SMOS mission, the multi-directional character of the surface brightness temperature sensing and the large spatial extent of the swath reinforce the need to make accurate corrections for this contribution in the salinity data processing. Ideally, to reach 0.1 psu accuracy on the Level 2 retrieved salinity, the sky glitter contribution would need to be estimated with an uncertainty better than about 0.05 K. However, this represents a drastic constraint about the respective accuracy of either SMOS radiometric measurements or the available sky brightness temperature maps. Rough sea surface-microwave interaction models at L-band is another important source of uncertainty in evaluating such contribution. Nevertheless, a physically based forward model is required to anticipate all major expected dependencies of the sky glitter contamination and *in fine* minimize potential biases in the SSS retrieval.

To correct for reflected sky noise in radiometric data acquired during scientific campaigns performed in the frame of the SMOS and Aquarius/SAC-D mission preparation, the perfectly smooth ocean surface assumption has been extensively used by authors ([11]-[14]). Same assumption was used in [2], [3] and [15] to provide preliminary estimate of the expected sky radiation contamination for the Aquarius/SAC-D and SMOS missions, respectively. In such approach, the locii on the celestial sphere of the specular rays with respect to the radiometer observation direction within the antenna pattern are first determined. The high-resolution T_{sky} map is then weighted by the considered sensor antenna gain pattern, multiplied by the flat sea surface reflectivity computed from the observed Earth target salinity and surface temperature, polarization and incidence angle and finally integrated over the antenna pattern.

Over a flat sea surface, the L-band reflectivity varies from about 50% to 80% for incidence angles below 60°. Combining available radiometric data collected at L-band in that incidence angle range over water surfaces [12]-[14] (see figures in the ATBD section describing the SSA/SPM roughness correction), the absolute surface emissivity (and therefore reflectivity) sensitivity to wind speed is never observed to exceed about 2×10^{-3} /m/s at L-band. This translates, for a 10 m/s increase in wind speed, into a reflectivity decrease by less than 2% compared to perfectly flat sea surface. Therefore, if the sky sources were assumed spatially uniform, sea surface roughness impact on the reflected sky contamination would be relatively small. However, sky radiation are not spatially uniform and as observed during the airborne LOSAC campaign [11], optimal correction of the radiometric data involved removing reflected galactic noise with an effective reflection coefficient varying between 0.6 and 0.9 times Fresnel coefficients for wind speeds from 20 to 0 ms^{-1} , respectively. This effect, which might correspond to up to a 40% decrease in reflected signal intensity compared to a flat sea, is mostly a consequence of the angular spreading and associated attenuation of directional

ARGANS Ltd.

Commercial in Confidence

Page 76

Use, duplication, or disclosure of this document or any information contained herein is subject to the restriction on the title page of this document.

reflectivity in presence of roughness. Accounting for the roughness impact on the estimated reflected sky contamination is therefore an important issue for SSS remote sensing. In the following, we describe an efficient method for operational implementation of a correction taking into account the rough sea surface scattering impact.

We first recall the generation of the L-band Sky map to be used for SMOS data processing. This is basically a reproduction of the note by N. Floury.

In order to place the scattering calculations in context, and to reveal any assumptions made in the development, in a second section, we first trace the path of the galactic radiation from the source through the atmosphere to the scattering surface, and then back up to the radiometer. We summarize all the transformations required to calculate the expected impact at the radiometer in terms of the incoming signal for the specific case of assumed unpolarised sky map. We then discuss integration of the signal over the antenna gain pattern. As part of this discussion, we review formulations of the sky glitter contribution for SMOS at antenna level assuming the surface is either rough or flat, since a specific transport processing is required for each case.

Next, we detail the rough surface and electromagnetic scattering models we employ in the calculations and review the geometry involved in the calculation. This is a key aspect of the development of the proposed efficient method for operational implementation of the correction.

The representation of the scattered signal, given the geometry of the problem is further described. In this context, we introduce a parametrization in terms of an orientation angle, ψ_{uh} , which, roughly speaking, is the orientation of the scattering upper hemisphere in the celestial frame. With this new variable, we detail a fast method of calculating the surface scattered signal in terms of zeroth and second harmonics of the wind direction given as input to the processor in precomputed Look up Tables. As demonstrated, due to the spatially nonhomogeneous sky, the latter wind direction harmonics can indeed have significant impact on the azimuthal behaviour of the overall L1C signal. We present an overview of the structure of the lookup tables to be used for the processing. The generation method for the LUTs is described in detail in the associated TGRD document.

4.4.2 Generation of an L-band Sky map to be used for SMOS data processing

4.4.2.1 Overview

In [3], a method was presented to produce assumed unpolarised map of the equivalent brightness temperature of radiation at L-band from the CMB (hereafter denoted T_{CMB}), from the Hydrogen line (T_{HI}), and from the continuum background (T_{cont}), based on recent radio astronomy surveys ([5]-[10]).



In the following, we denote T_{sky} the sum of the three contributions. Such a map for T_{sky} includes T_{HI} and T_{cont} contributions with sufficient spatial resolution ($0.25^\circ \times 0.25^\circ$) and radiometric accuracy to be relevant for remote sensing applications. Note that authors of the continuum radio astronomy surveys used in [3] mentioned that some strong sources were not included in their continuum map. This is for example the case of Cassiopeia A which peculiarities (high power flux) made it impossible to be measured accurately through the standard procedure. Nevertheless, it was shown in [4] that to first order, the model given in [3], is consistent with measurements made with several modern remote sensing instruments directly pointing towards the sky, although the data suggest a slight polarization signature. The agreement is particularly good (RMS differences of 0.05-0.10 K) if small changes in the level (bias) of the radiometer measurements are permitted. Without such adjustments, agreement is obtained to within 0.5 K even in the worst case.

In the general context of the SMOS data processing, a sky brightness temperature map at L-band was generated using an approach like [3]. Missing data (e.g. Cassiopeia A area) and other strong sources into the Reich and Reich continuum map might however induce underestimation of the reflected sky noise corrections, particularly over calm sea surfaces. To alleviate this problem and flag associated potential errors in the estimation of the sky noise contribution, an additional error map using higher resolution surveys identifying celestial sphere position and values of sources, which intensity are under evaluated in the sky map, is generated. The complete sky map and associated error field generated to flag missing strong sources is described in the following.

Three components are required to build a map of the sky emission at L-band [3]:

- The hydrogen HI line: this strong emitting line is centred at 1420.4058 MHz (\pm additional Doppler). It is usually rejected by a band-stop filter in surveys of the continuum,
- The continuum at ~ 1.4 GHz includes a variety of emission mechanisms (other lines than HI, synchrotron, free-free, thermal, blended emission of discrete radio sources ...), and,
- The Cosmic Microwave Background (quasi constant value of 2.725 K)

The equatorial system of coordinates (right ascension, declination) is used here to define the domain covered by existing surveys. The reference system used here is B1950.

4.4.2.2 Main sources of data

To provide a coverage of the whole sky, the datasets must combine observations from both the North and the South hemispheres. It is assumed that experts took care of all the issues related to this combination (cross calibration, overlap, angular resolution, etc.)

4.4.2.2.1 Continuum

The dataset identified here is a combination of the North Sky survey made with the Stockert radio telescope ([5]-[7]) and the South Sky survey made with the radio telescope of the Instituto Argentino de Radioastronomia [9]. When the bandwidth of the receiver was overlapping the HI emission, a stop-band filter centred over the HI line and 2MHz wide was applied to the measurement to reject it. Data are sampled with a $0.25^\circ \times 0.25^\circ$ resolution in declination \times right ascension (equatorial coordinates, B1950 system). The sensitivity (defined as $3 \times$ rms brightness temperature noise) of the merged dataset is 0.05K. In the following, this dataset will be referred as the Reich and Testori map.

It is assumed that the "continuum" signal is broadband and does not vary in this region of the spectrum. Thus, one can combine surveys made at slightly different centre frequencies and with slightly different bandwidths. The "continuum" dataset includes the 2.725K cosmic background.

4.4.2.3 Hydrogen line

The Leiden-Argentina-Bonn (LAB) dataset was used here [21]. The LAB survey contains the final data release of observations of 21-cm emission from Galactic neutral hydrogen over the entire sky, merging the Leiden/Dwingeloo Survey ([10]) of the sky north of -30° with the Instituto Argentino de Radioastronomia Survey ([8]) of the sky south of -25° . The velocity spans a range between -450 km/s and +400 km/s, with a resolution of 1.3km/s. The rms brightness temperature noise of the merged dataset is 0.07-0.09K (for each 1.3 kms^{-1} layer). Data are sampled with a $0.5^\circ \times 0.5^\circ$ resolution in latitude \times longitude (galactic coordinates). This dataset will be referred in the following as the HI map.

4.4.2.3.1 Integration of HI into the continuum map

SMOS measures a bandwidth B_{SMOS} of 19MHz that includes the HI line (1420.4058 MHz) so that the latter has to be integrated into the continuum map in the context of SMOS data processing. The continuum signal is broadband, with almost constant brightness levels, hereafter denoted T_{cont} , over SMOS bandwidth. It is understood that the data in (Reich & Testori) includes T_{cont} as well as the 2.725K cosmic background T_{CMB} , while HI data ([21]) does not include T_{CMB} .

To derive HI-line contribution over SMOS bandwidth from HI line velocity range data, we used a Doppler relation between velocity range and frequency shift. The HI line frequency is f_o

=1420.4058 MHz. The relation between frequency f and velocity v is given by the Doppler shift

$$f = f_0 \left(\frac{c}{c + v} \right) \quad 4.4.1$$

with c the speed of light and v the speed of the source relative to the observer (positive away from observer). The stopband filter applied to the Reich & Reich measurements is centred on f_0 and is $B_{HI} = 2\text{MHz}$ wide. This corresponds to a velocity range of $[-211.2 \text{ km s}^{-1}, +211.4 \text{ km s}^{-1}]$. Over this bandwidth, the contribution of HI signal is:

$$T_{HI}^{2\text{MHz}} = \frac{1}{(211.4 + 211.2)} \int_{-211.2 \text{ km s}^{-1}}^{211.4 \text{ km s}^{-1}} T_{HI}(v) dv \quad 4.4.2$$

Finally, the resulting sky noise to be considered in SMOS measurement is

$$T_{sky} = T_{CMB} + T_{cont} + T_{HI}^{2\text{MHz}} \frac{B_{HI}}{B_{SMOS}}. \quad 4.4.3$$

Gaps in the continuum survey: use of alternative surveys and source catalogues for missing data integration

Some areas of the Reich and Testori continuum survey are void of data; this is for example the case of Cassiopeia A which peculiarities (high power flux) made it impossible to be measured accurately through the standard procedure. Similarly, it may be that some strong punctual sources are not properly considered in the continuum survey. Higher resolution surveys are available that can alleviate this problem by providing auxiliary 1.4GHz flux measurements for these problematic areas. These datasets usually come in two forms:

- Higher resolution local sky maps, where for a given area of the sky a radio flux is associated to each [right ascension, declination] cell. This enables to assess the slow variations of the background flux when it results from the combination of minor sources that cannot be individually identified. Once rescaled and converted to the proper geometry, these datasets can be used to patch the continuum map where data is missing.
- Source catalogues that identify strong sources with small angular extensions and provide their total flux. These datasets can be useful to identify strong sources in otherwise quiet areas of the sky. Unfortunately, these high-resolution surveys have

still not been compiled into a global map of the radio sources of the sky. Several databases have thus been used here, with the related issues in terms of format / coordinate system / projection / units (main beam or full beam) and homogeneity of the available data. For example, the density of measurements available for the northern sky is larger than for the southern sky. See Appendix A for a discussion on the data from auxiliary surveys / catalogues used to generate the sky map.

- 1) *Cassiopeia A area*: In Reich and Testori map, the area around Cassiopeia has been left blank. There are two problems linked with this area:
 - This remnant of a recent supernova presents a large angular extension, with a complex structure of its flux component,
 - The measured flux varies in time Effelsberg survey [23], [24] was used here to give an idea of the spatial structure of the radio flux, but the complexity of this area and its temporal variations makes it unsuitable to accurate corrections without spending more effort on the analysis of the properties of this area (data are available on the temporal variation of the emission but are not considered in this algorithm).

Consequently, the Reich & Testori map is complemented by the Effelsberg survey of the Cassiopeia area, rescaled (to the T_b for a 35 arcmin beam as in the Reich & Testori survey) and resampled (to the 0.25° -pixel size). Moreover, an error T_b fields for the sky map was generated in which the Cassiopeia area is set to the rescaled and resampled value to flag the issue.

- 2) *Other strong sources*: One objective here is to check whether strong sources are properly considered in the Reich and Testori mapping. The authors mentioned that some strong sources (Orion A, Cygnus A, Taurus A ...) were not included in the continuum map. In addition, it could be that measurement limitations or processing issues would reduce the intensity of some strong radio sources in the map. To check that the input of strong sources is well quantified, a map of strong sources is generated from L-band source catalogues [25], [26] and the corresponding brightness temperatures that would be collected by the Stockert/IAR radiotelescopes (35 arcmin beamwidth) is computed. These sources were extracted from the NVSS (North) and from the Parkes (South) catalogues. Here, individual sources stronger than 0.3 Jy are selected (such a flux would contribute to around 0.015K error in the Reich and Reich map). It is anyway expected that sources of this strength or fainter are considered in the continuum measurement. The resulting brightness temperatures were compared to the combination of the Reich and Testori and HI map. Most sources exhibit a T_b that is equal or smaller to the one of the continuums (as the sources are embedded into a strong emission area which is preponderant in the relatively large beam of the telescope). However, some strong sources (Cassiopeia A) can be identified. It is difficult to do a sensible modification of the Reich and Reich map as because of the large beam width - the angular area around the sources should also be corrected.

Hence, the values of Reich and Testori are left untouched in the final map for the sake of consistency. Most differences in flux are quite small and are expected to be smoothed out when SMOS beam is applied. The strongest discrepancies (several 100s of K) occur for Cygnus A and the area of Cassiopeia A. In the sky data generated for SMOS, the sky map itself is not corrected, but the value of the source (in K) is reported in the error field of the corresponding pixel, where a Stockert/Testori beam was approximately applied (resolution 35 arcmin, sampling 0.25°). Hot celestial sources can radiate downwards radiation with effective brightness temperature up to about 400 K at L-band.

Some approximations had to be used at that stage to simplify the implementation. Note also, that as in [3], the sky map generated for SMOS and used here for the present version of the algorithm assumed unpolarised radiation.

4.4.3 Formulation of the Sky glitter contribution at surface level

Figure 4 depicts a radiometer antenna of circular beam width β_a , viewing the surface at a boresight observation angle θ_r , and azimuthal angle Φ_r . An incremental sea surface area dA located within the field of view, is illuminated by the sky along all directions $\vec{n}_o = (\theta_o, \Phi_o)$ within the solid angle Ω_s subtended by the upper hemisphere seen from dA (in Figure 4, only one particular sky illumination direction is plotted for illustration). Part of the intercepted energy is then scattered in the direction $\vec{n}_s = (\theta_s, \Phi_s)$, i.e., toward the radiometer antenna. The sky energy scattered by dA in the direction \vec{n}_s is represented by the radiometric temperature $T_p^s(\vec{n}_s)$. The **unpolarised** sky brightness temperature incident in the direction \vec{n}_o is the sky brightness temperature $T_{sky}(\vec{n}_o)$, and is further attenuated along its downward path across the atmosphere. Assuming that the rough sea surface can be described by the surface wind speed vector alone, namely (u_{10}, ϕ_w) , the surface *sky glitter brightness temperature* in the direction \vec{n}_s and at polarization p , $T_p^s(\vec{n}_s)$, can be related to $T_{sky}(\vec{n}_o)$ by the following integral equation:

$$T_p^s(\theta_s, \phi_s, u_{10}, \phi_w) = \frac{1}{4\pi \cos \theta_s} \int_0^{\pi/2} \int_0^{2\pi} [\sigma_{pp}(\theta_o, \phi_o, \theta_s, \phi_s) + \sigma_{pq}(\theta_o, \phi_o, \theta_s, \phi_s)] T_{sky}(\theta_o, \phi_o) e^{-\tau \sec \theta_o} \sin \theta_o d\phi_o d\theta_o, \quad 4.4.4$$

where $\sigma_{pq}^o(\vec{n}_s, \vec{n}_o)$ are the bistatic scattering coefficients of the sea surface at scattered direction \vec{n}_s and incident direction \vec{n}_o . The notation is such that the first subscript p refers to

where $T_p^s(\vec{n}_s)$ is now the Stokes vector, M_s is the so-called Mueller scattering matrix for unpolarised incoming signals, in which all components but the upper left 2x2 matrix of entries is zero, so that we have

$$M_s = \begin{pmatrix} \sigma_{hh}(\theta_o, \phi_o, \theta_s, \phi_s) & \sigma_{hv}(\theta_o, \phi_o, \theta_s, \phi_s) & 0 & 0 \\ \sigma_{vh}(\theta_o, \phi_o, \theta_s, \phi_s) & \sigma_{vv}(\theta_o, \phi_o, \theta_s, \phi_s) & 0 & 0 \\ 0 & 0 & 0 & 0 \\ 0 & 0 & 0 & 0 \end{pmatrix}. \quad 4.4.6$$

and where A_d is a downward path atmospheric attenuation matrix given by

$$A_d = \begin{pmatrix} a_d^2 & 0 & 0 & 0 \\ 0 & a_d^2 & 0 & 0 \\ 0 & 0 & a_d^2 & 0 \\ 0 & 0 & 0 & a_d^2 \end{pmatrix}, \quad 4.4.7$$

with $a_d^2 = e^{-\tau \sec \theta_o}$. Therefore, in our formulation of the sky glitter problem, only the first and second Stokes parameter in $T_p^s(\vec{n}_s)$ are non-zero.

For later reference, it is also useful to define the total reflectivity polarisation p by

$$\Gamma_p = \frac{1}{4\pi \cos \theta_s} \int_0^{\pi/2} \int_0^{2\pi} [\sigma_{pp}(\theta_o, \phi_o) + \sigma_{pq}(\theta_o, \phi_o)] \sin \theta_o d\phi_o d\theta_o. \quad 4.4.8$$

For a perfectly flat sea surface, this expression reduces to

$$|R_{hh}^{(0)}(S, T_s, \theta_s)|^2 = \left| \frac{\cos \theta_s - \sqrt{\varepsilon(S, T_s) - \sin^2 \theta_s}}{\cos \theta_s + \sqrt{\varepsilon(S, T_s) - \sin^2 \theta_s}} \right|^2$$

$$|R_{vv}^{(0)}(S, T_s, \theta_s)|^2 = \left| \frac{\varepsilon(S, T_s) \cos \theta_s - \sqrt{\varepsilon(S, T_s) - \sin^2 \theta_s}}{\varepsilon(S, T_s) \cos \theta_s + \sqrt{\varepsilon(S, T_s) - \sin^2 \theta_s}} \right|^2 \quad 4.4.9$$

where $\varepsilon(S, T_s)$ is the dielectric constant for seawater given by the Klein and Swift model. S is the salinity and T_s is the sea surface temperature. Note there is no cross-pol reflectivity in the flat-surface case, and the reflected signal is

$$T_p^f(\theta_s) = \int_0^{\pi/2} \int_0^{2\pi} |R_{pp}^{(0)}(S, T_s, \theta_s)|^2 \delta(\theta_s - \theta_o, \phi_s - \phi_o + \pi) T_{sky}(\theta_o, \phi_o) e^{-\tau \sec \theta_o} \sin \theta_o d\phi_o d\theta_o \quad \mathbf{4.4.10}$$

which simplifies to

$$T_p^f(\theta_s) = |R_{pp}^{(0)}(S, T_s, \theta_s)|^2 T_{sky}(\theta_s, \phi_s - \pi) e^{-\tau \sec \theta_s} \quad \mathbf{4.4.11}$$

For typical ocean values of SST (0-38°C) and SSS (20-40 psu), the sensitivity to SSS of the flat sea surface reflectivity at L-band vary from about $0.5 \times 10^{-3} \text{psu}^{-1}$ to $3.5 \times 10^{-3} \text{psu}^{-1}$ and its sensitivity to SST vary from about 0.2×10^{-3} per °C to 2×10^{-3} per °C, considering both linear polarizations and all incidence angles between 0 and 60°. Despite some previously listed very localized bright spots (Cassiopeia A, Orion A, Cygnus A, Taurus A, ...) for which the down welling signal can reach up to about 400 K, the sky brightness temperature at L-band vary in general from 2.75 K to around 10 K. Assuming a 10 K bright source, the sensitivity of the specularly reflected celestial brightness temperature signals to SSS and SST might reach around 0.03Kpsu^{-1} and $0.02 \text{K per } ^\circ\text{C}$. These values are representative of an average worst case scenario since the surface reflectivity drops significantly in presence of roughness. To make possible the operational implementation of the sky glitter calculation, we nevertheless make the assumption that the sky glitter results at nonzero wind speed weakly depends on these two surface parameters. We therefore selected ocean average values of $T_s = 15^\circ\text{C}$ and $S = 35 \text{ psu}$. For the flat sea surface cases, we however account for expected variations in these parameters.

4.4.4 Transport to antenna level and Integration over the Antenna Pattern

Although the focus of that part of the ATBD is on representing the sky scattered signal at surface level, we also discuss here issues related to the transport from the ground to the antenna and to the integration over the antenna pattern, as different processing are required whether the surface is rough or flat.

4.4.4.1 Tracing the galactic noise from surface to antenna level

Having derived the scattered signal at the surface, we then must apply attenuation on the upward path to the radiometer. We obtain

$$\begin{pmatrix} Tb_1^{s'} \\ Tb_2^{s'} \\ Tb_3^{s'} \\ Tb_4^{s'} \end{pmatrix} = \begin{pmatrix} a_u^2 & 0 & 0 & 0 \\ 0 & a_u^2 & 0 & 0 \\ 0 & 0 & a_u^2 & 0 \\ 0 & 0 & 0 & a_u^2 \end{pmatrix} \begin{pmatrix} Tb_1^s \\ Tb_2^s \\ Tb_3^s \\ Tb_4^s \end{pmatrix} = A_u \begin{pmatrix} Tb_1^s \\ Tb_2^s \\ Tb_3^s \\ Tb_4^s \end{pmatrix} \quad 4.4.12$$

where A_u is the upward path atmospheric attenuation matrix with $a_u^2 = \exp(-\tau \sec \theta_s)$. The upward signals are then subject to a Faraday rotation counter clockwise by angle ω_{fu} , across the ionosphere,

$$\begin{pmatrix} Tb_1^{s''} \\ Tb_2^{s''} \\ Tb_3^{s''} \\ Tb_4^{s''} \end{pmatrix} = \begin{pmatrix} \cos^2 \omega_{fu} & \sin^2 \omega_{fu} & -\cos \omega_{fu} \sin \omega_{fu} & 0 \\ \sin^2 \omega_{fu} & \cos^2 \omega_{fu} & \cos \omega_{fu} \sin \omega_{fu} & 0 \\ \sin(2\omega_{fu}) & -\sin(2\omega_{fu}) & \cos(2\omega_{fu}) & 0 \\ 0 & 0 & 0 & 1 \end{pmatrix} \begin{pmatrix} Tb_1^{s'} \\ Tb_2^{s'} \\ Tb_3^{s'} \\ Tb_4^{s'} \end{pmatrix} \quad 4.4.13$$

$$= M_{fu} \begin{pmatrix} Tb_1^{s'} \\ Tb_2^{s'} \\ Tb_3^{s'} \\ Tb_4^{s'} \end{pmatrix}$$

and then rotation into the Ludwig-3 basis to correctly project the polarization basis onto the MIRAS antenna polarization basis vector,

$$\begin{pmatrix} Tb_1^{s'''} \\ Tb_2^{s'''} \\ Tb_3^{s'''} \\ Tb_4^{s'''} \end{pmatrix} = \begin{pmatrix} \cos^2 \Psi_l & \sin^2 \Psi_l & -\cos \Psi_l \sin \Psi_l & 0 \\ \sin^2 \Psi_l & \cos^2 \Psi_l & \cos \Psi_l \sin \Psi_l & 0 \\ \sin(2\Psi_l) & -\sin(2\Psi_l) & \cos(2\Psi_l) & 0 \\ 0 & 0 & 0 & 1 \end{pmatrix} \begin{pmatrix} Tb_1^{s''} \\ Tb_2^{s''} \\ Tb_3^{s''} \\ Tb_4^{s''} \end{pmatrix} \quad 4.4.14$$

$$= M_l \begin{pmatrix} Tb_1^{s''} \\ Tb_2^{s''} \\ Tb_3^{s''} \\ Tb_4^{s''} \end{pmatrix}$$

Letting $T_p^a = (Tb_{1_e}''''s, Tb_{2_e}''''s, Tb_{3_e}''''s, Tb_{4_e}''''s)$ be the upward sky glitter brightness temperature Stokes vector at the antenna level, and combining all of the transformations from source to radiometer, we have for an unpolarised sky

$$T_p^a = M_l M_{fu} A_u \int_{\Omega_s} (M_s A_d) T_{sky} d\Omega \quad 4.4.15$$

It is usual to combine $M_l M_{fu}$ into one rotation matrix, M_α , so we have

$$T_p^a = M_\alpha A_u \int_{\Omega_s} (M_s A_d) T_{sky} d\Omega \quad 4.4.16$$

The Faraday rotation angle is a function of the total electron content (TEC) as well as the Earth's magnetic field, so that $M_\alpha = M_\alpha(\theta_s, \phi_s, TEC)$, but we will use the notation $M_\alpha(\theta_s, \phi_s)$ for simplicity.

4.4.4.2 Integration over the Antenna Pattern

To recapitulate the above results, accounting for the rough surface, the total upward scattered power normal to a unit area dA of sea surface impinging the antenna in the direction (θ_s, ϕ_s) after all transformations of the radiation from the source to the antenna, is as a function of angle (θ_a, ϕ_a) in the antenna spherical coordinate system,

$$T_p^a(\theta_a, \phi_a) = (M_\alpha A_u) T_p^s = \frac{1}{4\pi \cos \theta_s} (M_\alpha A_u) \int_{\Omega_s} (M_s A_d) T_{sky} d\Omega_s, \quad 4.4.17$$

where T_{sky} is the unpolarised sky brightness temperature given in the celestial frame. But this is the flux in some direction. To obtain the total power at a classical radiometer antenna, we must integrate this over all incident directions within the antenna pattern and weight the impinging signals by the antenna gain G , so that the total antenna temperature vector is

$$\bar{T}_p^a = \frac{1}{\Omega_p} \int_{\Omega_a} G(\Omega_a) T_p^a(\Omega_a) d\Omega_a = \int_{\Omega_a} G(\Omega_a) (M_\alpha A_u) T_p^s d\Omega_a \quad 4.4.18$$

where Ω_p is the vector antenna pattern solid angle, which simply normalizes the gain pattern weighting function G :

$$\Omega_p = \int_{\Omega_a} G d\Omega_a. \quad 4.4.19$$

In the SMOS case, the antenna temperature is still given by an equation of the form (15), however, owing to the interferometric processing, the retrieved brightness temperature in direction (θ_a, ϕ_a) corresponds to an integral over a synthetic gain pattern centred at that direction.

Switching to director cosine coordinates, with

$$\begin{aligned}\xi &= \sin \theta_a \cos \phi_a \\ \eta &= \sin \theta_a \sin \phi_a\end{aligned}\quad 4.4.20$$

and with

$$d\Omega = \sin \theta_b d\theta d\phi = \frac{d\xi d\eta}{\cos \theta_b} = \frac{d\xi d\eta}{\sqrt{1-\xi^2-\eta^2}}. \quad 4.4.21$$

the synthetic antenna pattern, or Equivalent Array Factor (EAF), is

$$AF_{eq}(\xi, \xi', \eta, \eta') = \frac{\sqrt{3}}{2} d^2 \sum_m \sum_n W(u_{mn}, v_{mn}) \tilde{r} \left(-\frac{u_{mn} \cdot \xi + v_{mn} \cdot \eta}{f_o} \right) e^{j2\pi(u_{mn} \cdot (\xi - \xi') + v_{mn} \cdot (\eta - \eta'))} \quad 4.4.22$$

where

- W is the apodisation function
- \tilde{r} is the fringe-washing factor (FWF) which accounts for the spatial decorrelation between antennas.
- u, v are the baseline coordinates in the frequency domain
- d is the antenna element spacing (= 0.875)
- f_o is the central frequency (1413 MHz)
- ξ, η are the central director cosines (DC) coordinates; ξ', η' are running DC coordinates.

Defining $D = \{\xi', \eta': \xi'^2 + \eta'^2 < 1\}$ as the domain of integration, the rigorous expression for the polarized sky-glitter temperature contribution at antenna level expressed in the director cosines (DC) coordinates is given by

$$\bar{T}_p^a(\xi, \eta) = \iint_D \frac{AF_{eq}(\xi, \xi', \eta, \eta')}{\sqrt{1-(\xi'-\xi)^2-(\eta'-\eta)^2}} (M_\alpha(\xi', \eta') A_u(\xi', \eta')) T_p^s(\xi', \eta') d\xi' d\eta' \quad 4.4.23$$

The variations in atmospheric attenuation and geometrical rotation are sufficiently small within the narrow (2-3°) synthetic beam that these factors can be approximated by their values at the central director cosines (DC) coordinates (ξ, η) , so that we have

$$\bar{T}_p^a(\xi, \eta) \approx (M_\alpha(\xi, \eta) A_u(\xi, \eta)) \iint_D \frac{AF_{eq}(\xi, \xi', \eta, \eta')}{\sqrt{1 - (\xi' - \xi)^2 - (\eta' - \eta)^2}} T_p^s(\xi', \eta') d\xi' d\eta' \quad 4.4.24$$

As demonstrated in IFREMER technical note, in presence of roughness, it turns out that the impact of the narrow synthetic antenna pattern is negligible assuming homogeneous roughness within the pixel. This is mainly due to the much larger angular spreading of the contributing part of the scattering coefficients compared to the narrow synthetic beam, which induces making the scattered signal within the beam uniform. Therefore, in the present algorithm, we neglect the array factor impact for rough sea surface conditions so that finally, the polarized sky-glitter temperature contribution at antenna level for rough sea conditions reads:

$$\bar{T}_p^a(\xi, \eta) \approx (M_\alpha(\xi, \eta) A_u(\xi, \eta)) T_p^s(\xi, \eta) \quad 4.4.25$$

where T_p^s is given in equation (4.4.4).

However, as revealed in [15], in the case of a perfectly flat sea surface, i.e., wind speed equal zero ms^{-1} , the *EAF* factor impact is no more negligible considering a 0.25° resolution sky map.

T_p^s is indeed replaced by $T_p^f(\theta_s)$, and the integral becomes,

$$\bar{T}_p^{fa}(\xi, \eta) \approx (M_\alpha(\xi, \eta) A_u(\xi, \eta)) \iint_D \frac{AF_{eq}(\xi, \xi', \eta, \eta')}{\sqrt{1 - (\xi' - \xi)^2 - (\eta' - \eta)^2}} T_p^f(\xi', \eta') d\xi' d\eta'. \quad 4.4.26$$

But

$$T_p^f = |R_{pp}^{(0)}(S, T_s, \theta_s)|^2 T_{sky}(\theta_s, \phi_s - \pi) \quad 4.4.27$$

and so

$$\bar{T}_p^{fa}(\xi, \eta) \approx (M_\alpha(\xi, \eta) A_u(\xi, \eta)) \iint_D \frac{AF_{eq}(\xi, \xi', \eta, \eta')}{\sqrt{1 - (\xi' - \xi)^2 - (\eta' - \eta)^2}} |R_{pp}^{(0)}(S, T_s, \theta_s(\xi', \eta'))|^2 T_{sky}(\xi', \eta') d\xi' d\eta' \quad 4.4.28$$

It turns out that the Fresnel power reflection coefficients, like the atmospheric attenuation and geometrical rotation effects can be assumed to vary weakly over the significant portion of the synthetic beam, so that

$$\left| R_{pp}^0(S, T_s, \theta_s(\xi', \eta')) \right|^2 \approx \left| R_{pp}^0(S, T_s, \theta_s(\xi, \eta)) \right|^2 \quad 4.4.29$$

and

$$\bar{T}_p^{fa}(\xi, \eta) \approx (M_a(\xi, \eta) A(\xi, \eta)) R_{pp}^{(0)}(S, T_s, \theta(\xi, \eta))^2 \times \iint_D \frac{AF_{eq}(\xi, \xi', \eta, \eta')}{\sqrt{1 - (\xi - \xi')^2 - (\eta - \eta')^2}} T_{sky}(\xi, \eta') d\xi' d\eta' \quad 4.4.30$$

As derived in (4.4.18), further simplification can be made by noting that the Array Factor is a rather narrow, centre-symmetric function, independent of the location of the viewing point in the field of view, time independent 2-D pattern. The following analytical approximation has been tuned to the EAF with no FWF effect:

$$AF_{eq}(\xi, \xi', \eta, \eta') \cdot \approx F_{cs}(\rho(\xi, \xi', \eta, \eta')) = \max \left\{ 0, \left[\frac{\sin k_f \cdot \rho}{k_f \cdot \rho} \right]^{k_k} \cdot \frac{1}{1 + k_g \cdot \rho^{k_h}} \right\} \quad 4.4.31$$

where $\rho = \sqrt{(\xi' - \xi)^2 + (\eta' - \eta)^2}$ is the distance in director cosine coordinates, $k_f = 73.30$, $k_g = 524.5$, $k_h = 2.1030$ and $k_k = 1.4936$. Thus, switching to polar coordinates, we have

$$\bar{T}_p^{fa}(\xi, \eta) \approx (M_a(\xi, \eta) A(\xi, \eta)) R_{pp}^{(0)}(S, T_s, \theta(\xi, \eta))^2 \iint_{D_\rho} \frac{F_{cs}(\rho)}{\sqrt{1 - \rho^2}} T_{sky}(\xi, \eta, \rho, \phi) d\phi d\rho \quad 4.4.32$$

where $D_\rho = \{\rho, \phi : (\xi'(\rho, \phi))^2 + \eta'(\rho, \phi)^2 < 1\}$ is the polar coordinated domain corresponding to D .

Equations (4.4.25) and (4.4.32) are the two quantities that have to be calculated by the processor to be used as final correction to the modelled Tb at antenna level. Equation (4.4.32) shall be used in the rough sea surface cases, while Equation (4.4.31) shall be used in the purely flat sea surface cases.

In the flat sea surface case, we see that the sky map weighted by the centre-symmetric WEF, used in (4.4.32), namely, \bar{T}_{sky} , can be precomputed using:

$$\bar{T}_{sky} = \iint_{D_\rho} \frac{F_{cs}(\rho)}{\sqrt{1 - \rho^2}} T_{sky}(\rho, \phi) d\phi d\rho \quad 4.4.33$$

4.4.5 Modelling the Scattering Cross Sections

A key sub-model in the sky glitter evaluation in presence of roughness is the model for bistatic scattering coefficients of the rough sea surface at L-band. As anticipated, the intensity and spread of the sky glitter contamination will depend not only on the measurement geometry but also on the sea surface roughness conditions. Knowing that SMOS multi-angular capabilities range from 0° to about 60°, we seek to model scattering of radiation at directions varying almost from specular to grazing directions.

As mentioned, to compute the scattered signal at the Earth's surface, we need to obtain expressions for the scattering cross sections $\sigma_{pq}(\theta_o, \phi_o, \theta_s, \phi_s)$ in terms of known quantities. Clearly, these cross sections will depend on characteristics of the incident radiation and of the rough surface. In this section we briefly review the rough surface and electromagnetic models used in the algorithm.

4.4.5.1 Modelling the Rough Surface

To employ the electromagnetic scattering models, we need a model for the rough surface itself, in order to compute the correlation functions required for the scattering models. The choice for the sea surface spectrum model used in the calculation of the sky glitter is certainly an important issue. The surface correlation function $\rho(\vec{x})$ is defined by

$$\rho(x, y) = \int_{-\infty}^{\infty} \int_{-\infty}^{\infty} W(\xi_x, \xi_y) e^{i\vec{\xi} \cdot \vec{x}} d\xi_x d\xi_y, \quad 4.4.34$$

where $W(\xi_x, \xi_y)$ is the directional wavenumber spectrum of the rough sea surface as a function of surface wavenumber vector in Cartesian number wavespace $\vec{\xi} = (\xi_x, \xi_y)$. The sea surface elevation function is assumed here to be a Gaussian random process and ρ is obtained from the inverse Fourier transform of the sea surface spectrum as computed using the models of Kudryavtsev al. [1999]. This wave model produces spectra that depend primarily on the 10 m wind speed u_{10} and inverse wave age Ω , so that

$$W = W(\xi_x, \xi_y; u_{10}, \Omega). \quad 4.4.35$$

In the present algorithm, we only consider wind speed dependence, assuming the wind sea is fully developed ($\Omega=0.81$) and we therefore refer to the spectrum using the notation $W(\xi_x, \xi_y)$ and we refer to the corresponding correlation function by $\rho(x, y)$. Also, since the directional wavenumber spectrum exhibits simpler structure in polar coordinates than in cartesian coordinates, and since the electromagnetic scattering problem is naturally expressed in spherical coordinates, it is expedient to introduce polar coordinates for both physical space and surface wavenumber space.

In cylindrical coordinates, the correlation function is decomposed into a zeroth and second harmonic:

$$\rho(r, \Phi) = \rho_0(r) - \rho_2(r) \cos 2(\Phi - \varphi_w), \quad 4.4.36$$

where φ_w is the wind direction (towards which the wind is blowing), and where the isotropic part is given by $\rho_0(r)$ and the anisotropic azimuthal wavenumber 2 part is given by $\rho_2(r)$. These harmonics are used directly in the electromagnetic scattering model to compute harmonics of the scattering cross sections.

4.4.5.2 The Asymptotic Electromagnetic Scattering Models

Having introduced the generic approach for representing the rough surface, we now introduce the electromagnetic scattering models, the Kirchhoff (KA) model and the lowest-order model (SSA-1) based on the Small Slope Approximation theory. The validity of KA approach is restricted to surfaces with large curvatures and to large Rayleigh parameters. The SSA has been proposed by Voronovich as an alternative to efficiently bridge Small Perturbation Model (SPM) and KA models. SSA strictly meets SPM as the roughness goes to zero. Analytical expressions are in principle available for the SSA at all orders in slope. In practice, however, only the first two orders are tractable. The first order SSA (SSA-1) implies the same single integral as in KA to determine a particular Fourier coefficient of the surface elevation coherence structure function with a different geometrical factor. The second order approximation (SSA-2), however, is a double oscillating integral, that is found very difficult to compute accurately, especially in the dielectric case where convergence problems and computational time demands become prohibitive. For the present algorithm, we thus consider first-order SSA (SSA-1) and the Kirchhoff approaches. These two approaches can be considered to provide the asymptotic limits within a consistent framework of scattering slope expansions. Importantly, these two approaches lack directly considering the surface geometrical properties to predict the level of polarization. With the proposed models, this polarization level is independent of roughness states. SSA-1 is expected to exaggerate the polarization effects while KA will minimize them. Note as well, that at order 1, SSA-1 meets SPM only at order 1 while KA converge asymptotically up to second order in SPM. At the specular direction, which is the dominant contributor, both models give however the same asymptotic solution.

To facilitate discussion we introduce a local Cartesian coordinate system $(\hat{x}, \hat{y}, \hat{z})$ with basis vector \hat{x} pointing eastward, basis vector \hat{y} pointing northward, and basis vector \hat{z} pointing upwards normal to the horizontal surface. For convenience of notation, we use incident and scattered wavevectors interchangeably with directions:

$$\begin{aligned}(\theta_0, \phi_0) &\rightarrow \vec{k}_0 \\(\theta_s, \phi_s) &\rightarrow \vec{k}_s\end{aligned}\tag{4.4.37}$$

Application of either SSA-1 or the Kirchhoff approximation for scattering from the slightly rough ocean surface yields the following expression for a dimensionless bistatic scattering cross section $\sigma_{\alpha\alpha_o}^O$ for scattering of the incoming wave of polarization α_o into the outgoing wave of polarisation α :

$$\sigma_{\alpha\alpha_o}(\vec{k}_s, \vec{k}_o) = \frac{1}{\pi} \left| \frac{2q_s q_o T_{\alpha\alpha_o}(\vec{k}_s, \vec{k}_o)}{q_s + q_o} \right|^2 e^{-(q_s + q_o)^2 \rho(0)} \cdot I_K\tag{4.4.38}$$

where $T_{\alpha\alpha_o}(\vec{k}_s, \vec{k}_o)$ is a polarization-dependent kernel that is different for SSA-1 and the Kirchhoff models. I_K is often referred to as the Kirchhoff Integral and is given in Cartesian coordinates by

$$I_K = \int_{-\infty}^{\infty} \int_{-\infty}^{\infty} \left\{ e^{[(q_s + q_o)^2 \rho(\vec{x})]} - 1 \right\} e^{-i(\vec{k}_s - \vec{k}_o) \cdot \vec{x}} dx dy,\tag{4.4.39}$$

where we use the notation \vec{x} to denote the horizontal displacement vector and the integral is evaluated over all possible displacements in the horizontal plane. In Eqs. (4.4.38) and (4.4.39), $(q_s, q_o) = (\hat{z} \cdot \vec{k}_s, -\hat{z} \cdot \vec{k}_o)$ represents the vertical projection of the wavevectors. As the kernel T depends on the dielectric properties of the scattering surface, we use the Klein and Swift's model to estimate the dielectric constant of sea water at L-band at SSS=35 psu and SST=15°C.

Using the harmonic decomposition of the correlation function as derived from the surface models, we can decompose the Kirchhoff integral into harmonics as well, so that in cylindrical coordinates we obtain

$$I_K = 2\pi \int_0^{\infty} \left[J_0(q_H r)(r) + I_0(a) J_0(b) e^{q_z^2 \rho_0(r)} \right] r dr + \sum_{m=1}^{\infty} I_K^m \cos 2m(\Phi_{si} - \varphi_w),\tag{4.4.40}$$

where Φ_{si} is the angle of the difference between the scattered and incident wavevectors, and can be written as:

$$\Phi_{si}(\theta_o, \phi_o, \phi_s, \theta_s) = \tan^{-1} \left(\frac{q_{Hy}}{q_{Hx}} \right) = \tan^{-1} \left(\frac{\sin \theta_s \sin \phi_s + \sin \theta_o \sin \phi_o}{\sin \theta_s \cos \phi_s + \sin \theta_o \cos \phi_o} \right).\tag{4.4.41}$$

and where, for m from 1 to ∞ ,

ARGANS Ltd.

$$I_K^m = 4\pi \int_0^\infty I_m(a) J_{2m}(b) e^{q_z^2 \rho_0(r)} r dr, \quad 4.4.42$$

is the coefficient of harmonic $2m$ in a cosine series decomposition of the Kirchhoff Integral.

If we further let

$$I_K^0 = 2\pi \int_0^\infty \left[J_0(q_H r)(r) + I_0(a) J_0(b) e^{q_z^2 \rho_0(r)} \right] r dr \quad 4.4.43$$

then we see that

$$I_K = I_K(\Phi_{si} - \varphi_w) = \sum_{m=0}^{\infty} I_K^m \cos 2m(\Phi_{si} - \varphi_w). \quad 4.4.44$$

In the above, $a(r) = q_z^2 \rho_2(r)$ and $b(r) = q_H r$. J_m is the Bessel function of the first kind and order m , and I_m denotes the modified Bessel function of the first kind and order m . We can incorporate the polarization-dependent coefficients multiplying the Kirchhoff Integral into the sum over the Kirchhoff Integral harmonics to obtain

$$\sigma_{\alpha\alpha_o}(\vec{k}_s, \vec{k}_o, u_{10}, \varphi_w) = \sum_{m=0}^{\infty} \sigma_{\alpha\alpha_o}^{2m}(\vec{k}_s, \vec{k}_o) \cos 2m(\Phi_{si} - \varphi_w), \quad 4.4.45$$

where we have explicitly included the dependence of the final scattering coefficients on the wind speed u_{10} and wind direction φ_w (towards which the wind is blowing), and where

$$\sigma_{\alpha\alpha_o}^{2m}(\vec{k}_s, \vec{k}_o) = \frac{1}{\pi} \left| \frac{2q_s q_o T_{\alpha\alpha_o}(\vec{k}_s, \vec{k}_o)}{q_s + q_o} \right|^2 e^{-(q_s + q_o)z} \rho(0) \cdot I_K^m \quad 4.4.46$$

Note that the scattering coefficient harmonics are independent of wind direction. Moreover, these harmonics only depend on the incoming and scattered radiation incidence angles, the wind speed, and difference between the incoming and scattered radiation azimuth angles. Thus, switching from vector notation to angles, we can write the scattering coefficients as

$$\sigma_{\alpha\alpha_o}(\theta_o, \phi_o, \theta_s, \phi_s, u_{10}, \varphi_w) = \sum_{m=0}^{\infty} \sigma_{\alpha\alpha_o}^{2m}(\theta_o, \phi_s - \phi_o, \theta_s, u_{10}) \cos 2m(\Phi_{si} - \varphi_w), \quad 4.4.47$$

4.4.5.3 The Semi-Empirical Geometrical Optics Scattering Model

While the models discussed in the preceding section are attractive because of their applicability to a large range of scattering geometries and ocean surface roughness

ARGANS Ltd.

conditions, they are difficult to empirically correct if their predictions are not accurate. Indeed, we have found that the predictions obtained from both the Kirchhoff and SSA-1 models do not agree well with the scattered celestial sky brightness inferred from the data, especially near the galactic plane where the sky brightness is strongest and also strongly varying as a function of position in the celestial sky. In order to improve the predictions, we have adopted a geometrical optics model, which is more amenable to empirical adjustment than the Kirchhoff and SSA-1 models.

Owing its analytical simplicity and flexibility, scattering models based upon the geometrical optics approximation became widely used in the 1960s, there is a large body of literature on the subject (see [26-32,35,36,38] and references therein), with applications ranging from the interpretation of radar backscatter from the lunar surface to interpretation of microwave emission and scattering from the rough ocean surface.

Taking the high-frequency limit of the Kirchhoff expression (4.4.42) for the scattering cross sections, as is done in [28], we obtain the general form of the geometrical optics approximation for the bistatic scattering cross sections,

$$\sigma_{\alpha\alpha_o}(\vec{k}_s, \vec{k}_o) = \frac{4\pi}{(q_s + q_o)^2} \left| \frac{2q_s q_o}{q_s + q_o} T_{\alpha\alpha_o}(\vec{k}_s, \vec{k}_o) \right|^2 P(-q_x / q_z, -q_y / q_z) \quad 4.4.48$$

In this equation (q_x, q_y, q_z) are the three components of the difference between the scattered and incident wave vectors, and the function $P\left(-\frac{q_x}{q_z}, -\frac{q_y}{q_z}\right)$, which is not yet specified, is the surface slope probability density function. For a given scattering geometry (incidence and azimuth angles) this function is evaluated at the specular surface slope whose orthogonal components are given by the ratios $\left(-\frac{q_x}{q_z}, -\frac{q_y}{q_z}\right)$. The kernel function is taken to be that for the Kirchhoff approximation and is based on the tangent plane approximation for the surface fields.

It remains to specify the slope probability density function, and for this we assume, as is frequently done, that the slope distribution is Gaussian. Begin by defining a Cartesian coordinate system with the x-axis directed downwind and the y-axis directed crosswind, and define the upwind and crosswind surface slopes, respectively, as

$$S_u = \frac{q_x}{q_z} \quad 4.4.49$$

$$S_c = -\frac{q_y}{q_z} \quad 4.4.50$$

Assuming that the slope variance is isotropic and equal to σ^2 in both the upwind and crosswind directions, with the total slope variance equal to the Gaussian slope then the PDF takes the form

$$P\left(-\frac{q_x}{q_z}, -\frac{q_y}{q_z}\right) = P(S_u, S_c) = \frac{1}{2\pi\sigma^2} \exp\left\{-\frac{S_u^2 + S_c^2}{2\sigma^2}\right\} \quad 4.4.51$$

With this formulation the (isotropic) slope variance is the only free parameter, and if this electromagnetic model accurately describes the underlying physics of the scattering process, this parameter would be a function only of the surface roughness. However, as this model is the high frequency limit of a model which is itself an approximate solution to the problem, we suppose that the slope variance is 'effective' and depends upon the scattering geometry and electromagnetic frequency. Indeed, it is common practice in the literature to introduce frequency dependence into the slope variance when this type of model is used for scattering and emission calculations at microwave frequencies [32, 35, 36]. Only recently the potential for incidence angle dependence has been clearly elucidated [37].

To find the slope variance as a function of incidence angle and wind speed, reconstructed brightness temperatures are obtained for the open-ocean portion of all (good) ascending and descending passes from June 2010 through June 2012. We exclude data before June 2010 owing to the large and rapidly varying biases in that period. Using the model for the scene brightness over the ocean all contributions to the total brightness incident at the instrument except for celestial sky radiation are removed, leaving only the contribution from the celestial sky. The resulting contributions are binned by specular location in the celestial sky, wind speed and incidence angle and then averaged over the entire period. In performing this average two key bias corrections are applied.

First, at each grid point withing the AF-FoV a 10-day (Gaussian weighted) running average difference between the complete forward model and the reconstructed brightness temperatures is obtained. To minimize the impact of celestial sky brightness on this bias, the averaging only involves descending passes from January through June and ascending passes from July through December. Second, to reduce the impact of orbital drift in the FoV-averaged bias, the FoV-averaged difference between the model and the data is removed for each collection of snapshots that produce a complete Stokes vector. This approach retains the spatial variability associated with the sharp peak in brightness around the galactic plane while removing the orbital drift that appears to be associated with the drift in the calibrated NIR antenna temperatures, for which a robust solution at Level 1 does not yet exist.

Examples of the resulting bias corrected celestial sky brightness temperature maps derived from the measurements, in terms of the first Stokes parameter divided by two, are shown for ascending (left) and descending (right) passes in Figure 5. In this example, only data for which

the incidence angle lies between 35° and 45° and for which the ECMWF 10-m wind speed lies at or below 3 m/s are considered in the average. Thus, these maps represent the scattered celestial sky brightness (in terms of the first Stokes parameter) for very low wind speeds, and likely include some data for which the surface specularly reflects the brightness.

For declinations between about -15° and $+15^\circ$ both pass directions yield solutions, but the solutions are noticeably different, with the descending pass brightness being about 1 kelvin higher than that for the descending passes, despite the fact that we have removed the impact of any orbital drift in the NIR antenna temperatures.

At first glance this result may seem surprising and that, for a given specular point and roughness conditions, the scattered celestial sky brightness should be independent of pass direction. But this is, in fact, not the case. Indeed, for any given specular point near the galactic plane (where the celestial sky brightness is strongest), the distribution of the brightness in the upper hemisphere is different for ascending and descending passes, so that if the scattering cross sections are not symmetric about the specular direction, the total scattered brightness will also be different for the two pass directions.

All model solutions we have examined, including those from the Kirchhoff and SSA-1 asymptotic models, exhibit differences in the order of up to half a kelvin in $(T_x+T_y)/2$ between ascending and descending passes. However, the descending-ascending differences predicted by the models do not correspond well to those found in the data, with the data suggesting much larger differences (up to about one kelvin in $(T_x+T_y)/2$) near the galactic plane. It is speculated that this deficiency of the models is related to errors in the directional distribution of the scattering cross sections, especially those associated with scattering outside the incidence plane. This is just a hypothesis, however, and this problem requires further work.

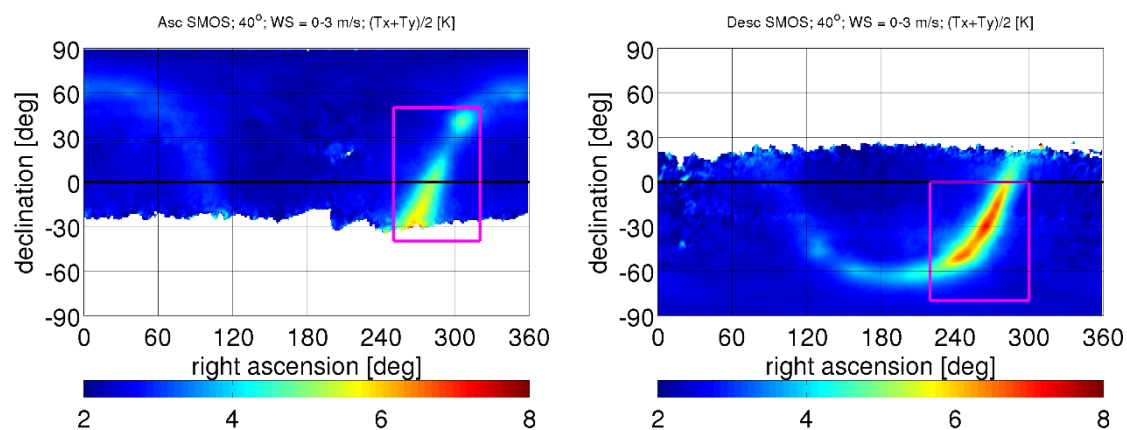


Figure 5 : First Stokes parameter divided by two of the scattered celestial sky radiation as inferred from the MIRAS reconstructed brightness temperatures for ECMWF wind speeds below 3 m/s and for incidence angles ranging from 35° to 45° . Average is over the open ocean portion of all passes from June 2010 through June 2012.

Left: Ascending passes; Right: Descending passes. Brightness temperatures are expressed in kelvin. Magenta boxes show the domains over which the geometrical optics model is fit to the data.

At present, we adopt a pragmatic solution to this problem by fitting the geometrical optics model to descending and ascending passes separately. As a first step, the geometrical optics model is evaluated at a fixed set of slope variances that have been determined to span the range of sky brightness diffusion observed in the data. The fits are then computed by finding the slope variance that minimizes the absolute difference in the first Stokes parameter between the geometrical optics model and the data within each incidence angle and wind speed bin over the portions of the celestial sky shown by magenta rectangles in Fig. 20. Note that because sky coverage for the two pass directions is different, the domain over which the cost function is evaluated differs for the two cases.

The resulting fits are shown in Figure 6 for ascending (left) and descending (right) passes. Also shown is the slope variance derived by extrapolating the formula presented in [35] to 1.4135 GHz (brown) and the slope variance presented in [36] that was derived to match the rough surface emission inferred from brightness temperature measurements made from the Argus Island tower by Hollinger [38]. Note that the slope variance of [36] is about 1/3 that derived by Cox and Munk [34] from optical measurements over a clean ocean surface (i.e. with no oil slick which would reduce the roughness). The green curves show the slope variance derived by Cox and Munk for a surface with an oil slick.

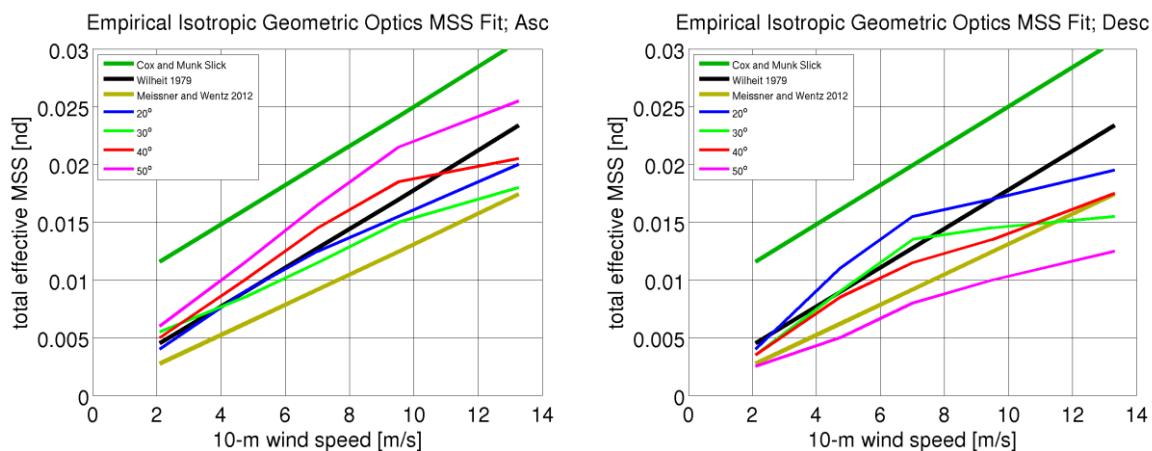


Figure 6: Total (assumed isotropic) mean square slope (or equivalently the total slope variance σ^2) derived by fitting a geometrical optics model to the SMOS ascending (left) and descending (right) passes over the brightest portion of the galactic plane. The best fit slope variances are functions of both ECMWF wind speed and incidence angle. In each plot the brown curve shows the total MSS obtained by extrapolating the fit presented in [35] to 1.4135 GHz while the black curve shows the fit presented in [36], which was used to interpret L-band radiometer measurements made by Hollinger at the Argus Island tower [38].

All slope variances derived from the data lie below Cox and Munk slick result, and the fits based upon ascending passes bracket the fits from [35] and [36]. The ascending pass fit at 20°

and 40° incidence angles are close to the fit from [36], but the fit is lower at 30° and consistently higher at 50°.

In the incidence angle range 45°-55° the slope variances derived from descending passes are about half those derived from ascending passes, while for the range 15°-25° descending pass variances are larger than those for ascending passes at moderate wind speed, while at high and low wind speeds the variances are similar for ascending and descending passes. Overall, the discrepancy in slope variances is largest at the highest incidence angles and highest wind speeds. The dependence of the descending-ascending discrepancy upon both wind speed and incidence angle is not inconsistent with the hypothesis, presented above, that differences in the scattered sky brightness between the two pass directions may be related to errors in the directional distribution of the scattering cross sections.

An example of the impact of the new geometrical optics models upon the bias of the first Stokes parameter (divided by two) in the celestial sky is shown in Figure 7. This example shows biases for descending passes and for incidence angles between 35° and 45°, and for the wind speeds between 3 and 6 m/s. The results show the average difference between the predictions and the data for the original Kirchhoff model evaluated at 3 m/s (left), the ascending pass geometrical optics model (middle) and descending pass model (right). Biases are most evident for the Kirchhoff and ascending pass GO models around the galactic plane, where these two models underpredict the scattered radiation very near the plane and overpredict the radiation far away from the plane. Although the descending pass GO model also exhibits biases, they are generally smaller in magnitude than for the other models.

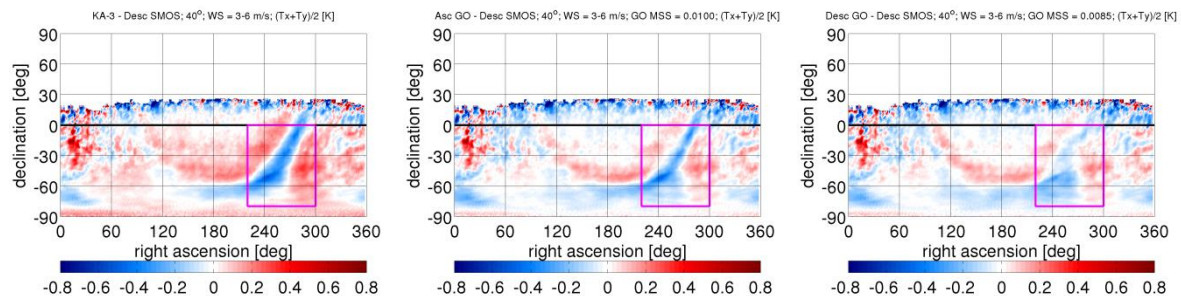


Figure 7: Bias between three model solutions and the scattered celestial sky brightness inferred from the data. Differences are in terms of the first Stokes parameter divided by two. The comparison incorporates open-ocean portions of all (good) descending passes from June 2010 through June 2012. Only data and solutions for which the incidence angle lies between 35° and 45° and for which the ECMWF 10-m wind speed lies between 3 and 6 m/s are included in the averaging. Left: Kirchhoff-based model evaluated at a fixed wind speed of 3 m/s; Middle: Empirical geometrical optics model fit to ascending pass data; Right: Empirical geometrical optics model fit to descending pass data. In the Kirchhoff-based model (left panel) the correlation function required to evaluate the Kirchhoff integral is obtained from the Kudryavtsev wave spectrum evaluated at a wind speed of 3 m/s. Magenta boxes show the domains over which the descending pass geometrical optics model is fit to the data.

One of the key improvements obtained with the new geometrical optics models is the re-introduction of wind speed dependence in the scattered brightness. The pre-launch Kirchhoff



model did provide solutions that depend upon wind speed, but the solutions tend to over-diffuse the radiation resulting in underpredictions near the galactic plane and overpredictions further away. The initial fix, introduced for the first reprocessing of ESA, was to use the least rough Kirchhoff solution, corresponding to a 3 m/s wind speed (denoted hereafter the KA-3 model). Although this solution better matches the data for moderate wind speeds in ascending passes, it tends to underpredict the brightness near the galactic plane in descending passes and in ascending passes at wind speeds below 7 m/s. An example of this is illustrated in Figure 8 which presents, along a line through the galactic plane at a declination of -10° , the various model solutions and the data for both light (left panels) and moderate (right panels) wind speeds in the incidence angle range 45° - 55° . The comparison is made in terms of $(T_x+T_y)/2$. For the ascending passes at light to moderate wind speeds (upper left) the KA-3 prediction is very close to the data and to the ascending pass GO model, while the descending pass model overpredicts $(T_x+T_y)/2$ by nearly one kelvin along the galactic plane. At slightly higher wind speeds of 6-8 m/s the KA-3 overpredicts the brightness along the galactic plane owing to its lack of wind speed dependence, while the ascending pass GO model continues to match the data well.

Although the ascending pass GO model apparently matches the data well in ascending passes, it generally underpredicts the scattered radiation in the descending passes in both wind speed ranges, as shown in the bottom panels in Figure 8. By contrast, the descending pass GO solutions are much closer to the data within about 5° on either side of the galactic plane. Both the GO models exhibit the proper dependence upon wind speed, with the predicted brightness decreasing with increasing wind speed along the galactic plane.

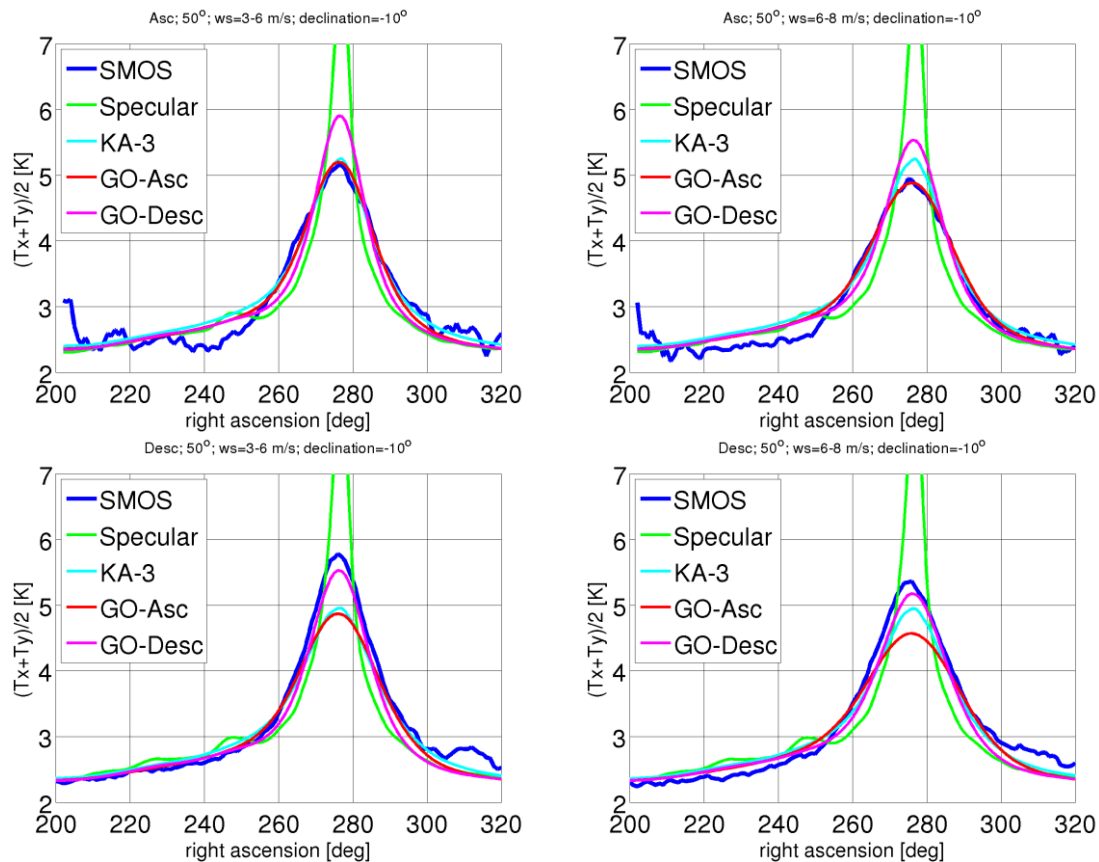


Figure 8 Cross sections through the celestial sky at a declination of -10° . Curves, which are plotted as a function of right ascension, show the first Stokes parameter divided by two for incidence angles ranging from 45° to 55° as derived from the MIRAS brightness temperatures (blue) and the following models: specular reflection weighted by the synthetic beam (green), the Kirchhoff model with the Kudryavtsev wave spectrum evaluated at 3 m/s (cyan), and the geometrical optics models based on ascending passes (red) and the descending passes (blue). The top row shows solutions for ascending passes and for wind speeds from 0-3 m/s (left) and 6-8 m/s (right). The bottom row panels are identical to those in the top row except that they are based upon descending passes. Data include all (good) half-orbits from June 2010 through June 2012.

Differences between the models are also evident in individual swaths of dwell line averaged retrieved salinity bias. Fig. 24 shows maps of retrieved salinity for all descending passes in the Pacific Ocean from 7 through the 9 October 2012. For this time of year, the impact of scattered galactic radiation is strong and maximum to the right of the ground track in the alias-free field of view. The salinity has been retrieved using the nearly linear dependence of the first Stokes parameter of specular emission to salinity. The specular emission is computed by subtracting from the brightness temperatures all contributions to the brightness except specular emission, including that from scattered celestial sky radiation. For this example, salinity is retrieved using the two Kirchhoff models (variable and 3 m/s wind speed) and the two GO models. The bias varies significantly over the domain; however the effectiveness of the galactic model can be visually assessed by the extent to which the along-track trough of negative salinity bias is reduced in magnitude. As may be anticipated, the trough is least

apparent for the descending GO model (lower right) and most apparent for the variable wind Kirchhoff model (upper left). Also, both the KA-3 (upper right) and ascending GO (lower left) models are associated with noticeable salinity troughs, which is not surprising considering the results presented in the previous figure.

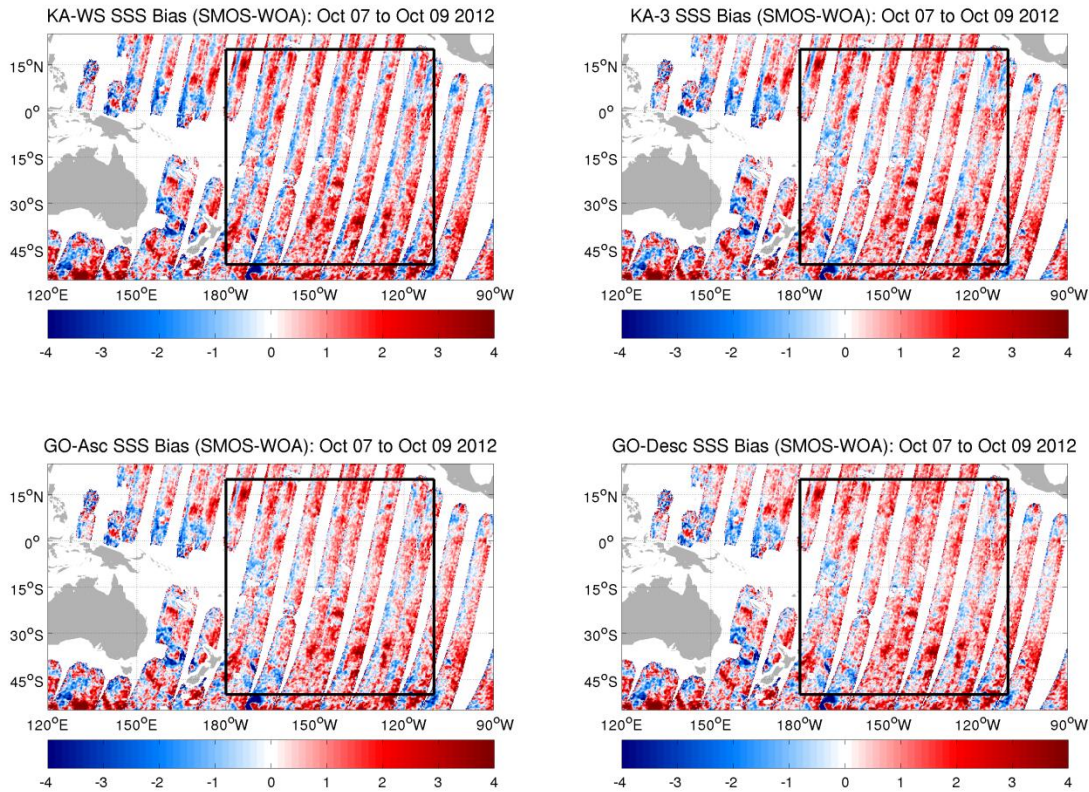


Figure 9 Alias-free dwell-line averaged retrieved salinity bias for three days of descending Pacific passes from 7-9 October 2012 obtained using four scattering models. Upper left: the original Kirchhoff-based model evaluated at the ECMWF 10-m wind speed; Upper right: Kirchhoff-based model evaluated at a fixed wind speed of 3 m/s; Lower left: the empirical geometrical optics model fit to ascending pass data; Lower right: the empirical geometrical optics model fit to descending pass data. In the Kirchhoff-based models the correlation function required to evaluate the Kirchhoff integral is obtained from the Kudryavtsev wave spectrum. The black boxes show the domain in which the bias statistics are computed.

Although the impact of the galactic model deficiencies can often be seen in the form of along-track troughs or ridges in retrieved salinity bias in September and October descending passes, it is useful to have a more objective and comprehensive measure of the effectiveness/weaknesses of the models. Since the impact of the models tends to be strongest near the galactic plane where galactic radiation is strongest, one possible approach involves sorting the salinity biases for individual earth dwell-lines by the level of the predicted dwell-line averaged scattered galactic radiation itself and then examining the variation of bias with respect to the level of the scattered radiation. In this method it is important to perform the sorting on individual swaths rather than on multi-day average maps since any averaging

may mask the along-track bias associated with the galactic radiation. Deficiencies in the galactic scattering model near the galactic plane should appear as variations of the bias as a function of the scattered radiation itself.

To this end, the daily retrieved salinity biases at all surface grid points over the region outlined by the black boxes in Figure 9 are collected and binned by both wind speed and the dwell-line averaged first Stokes parameter of scattered sky radiation (as computed using the descending pass GO model). The salinity biases are obtained using only ascending pass OTTs to avoid the possibility that the OTT itself may correct for deficiencies in the scattering models. Figure 10 shows the resulting salinity biases for September-October descending passes from 2010 through 2012 as a function of scattered celestial sky brightness. Each panel corresponds to a different wind speed range: very low (left), low (middle), and moderate (right) ECMWF 10-m wind speeds. In each panel biases are shown for four models: specular reflection, Kirchhoff at 3 m/s, and the two GO models. For the lowest scattered sky brightness there is bias that is independent of wind speed and galactic model. This bias does not represent a problem with the galactic models; instead, it is related to the fact that we have used OTTs based upon ascending passes only and so any orbital drift will appear as a salinity bias in the statistics. The most important indicator of the effectiveness of any galactic model in these plots is the variation of the bias with the strength of the galactic brightness. Ideally, the bias should not vary with the level of the scattered radiation. Based upon this criterion the descending pass model performs better than all other scattering models in all wind speed ranges shown. However, for very low wind speeds of 0-3 m/s the specular reflection model seems to perform better up to around the 5 K level. Indeed, examination of individual swaths does show that for very low ECMWF wind speeds, below about 2-3 m/s, the specular model is often required to adequately remove the low salinity bias in the vicinity of the galactic plane. However, this is not always true, and more work is required to improve and refine the solution strategy at very low wind speeds.

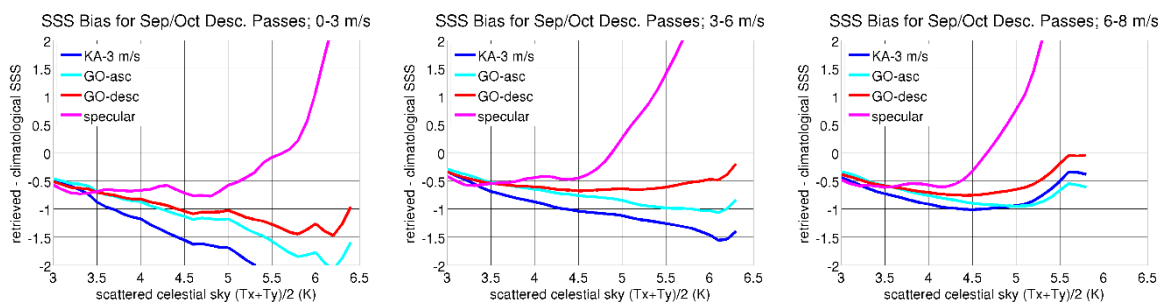


Figure 10 Retrieved salinity bias as a function of scattered celestial sky brightness for all September and October descending passes for 2010 through 2012. Biases are evaluated for each pass individually and only inside the black boxes shown in the previous figure. The sky brightness according to which the data are binned is computed using the descending pass geometrical optics model). Left: 0-3 m/s; Middle: 3-6 m/s; Right: 6-8 m/s. Wind speed obtained from ECMWF operational forecasting system.

Another aspect that requires more work is the modelling of the scattering at high incidence angle at any wind speed. Figure 11 shows the difference between the descending pass GO model predictions and the data for wind speed ranges of 3-6 m/s (left) and 6-8 m/s (right) and for incidence angles between 45° and 55°. Although the prediction is not bad along the galactic plane, on either side the model underpredicts $(T_x+T_y)/2$ of the scattered radiation by up to one kelvin. Although this error is much smaller than that associated with the other models, it is still significant for ocean salinity retrieval. Moreover, no choice of slope variance has been found that removes the error both along the galactic plane and on either side, so that there is no simple modification of existing models that can correct this problem. One possible approach that requires further research involves adopting a different form for the slope probability distribution in the geometrical optics model. Such an approach has proven useful in studies of near-nadir backscatter and may provide the flexibility required to better match the data.

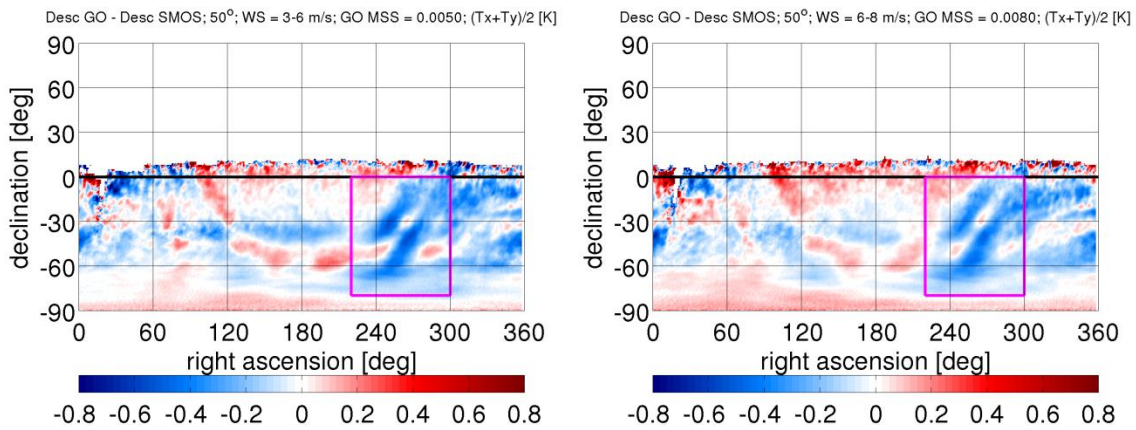


Figure 11 Bias between the descending pass geometrical optics fit and the scattered celestial sky brightness inferred from the data. Differences are in terms of the first Stokes parameter divided by two. Data are based upon the open-ocean portions of all descending passes from June 2010 through June 2012. Only data and solutions for which the incidence angle lies between 45° and 55° are included in the averaging. Left: ECMWF wind speeds between 3 and 6 m/s; Right: ECMWF 10 m wind speed between 6 and 8 m/s.

4.4.6 Representation of the Scattered Galactic Noise Signal

As mentioned before, to obtain the total sky scattered signal in a given direction toward the radiometer defined by (θ_s, ϕ_s) , we must integrate the brightness temperature contributions from waves incident at the target from all directions over the upper hemisphere, so that at polarization p , the total scattered signal is

$$T_p^s(\theta_s, \phi_s, u_{10}, \varphi_w) = \frac{1}{4\pi \cos \theta_s} \int_{\Omega_s} [\sigma_{pp} + \sigma_{pq}] T_{sky}(\Omega_s) d\Omega_s \quad 4.4.52$$

where Ω_s refers to angular position in the upper hemisphere.

Now, since the noise distribution over the upper hemisphere is a function of target position on Earth and time, the rough surface scattered galactic signal at polarization p , T_p^s , is a function of latitude ϑ_g , longitude φ_g , and time t as well as scattering incidence and azimuth angles, wind speed and wind direction, so that in general we have

$$T_p^s = T_p^s(\vartheta_g, \varphi_g, t, \theta_s, \phi_s, u_{10}, \varphi_w). \quad 4.4.53$$

The portion of the sky covered by the upper hemisphere is only a function of target latitude, longitude, and time. Moreover, changing the time or the target longitude only alters the right ascension of every point in the upper hemisphere by some constant independent of position in the upper hemisphere.

The upper hemisphere pole corresponds to the unit normal to the Earth surface at the target latitude and longitude. Denoting the right ascension and declination of the projection of this point in the celestial frame by (α_n, δ_n) , we can remove the explicit dependence on time in (4.4.53) by introducing (α_n, δ_n) as independent variables and expressing the scattered galactic noise as $\bar{T}_p^s(\alpha_n, \delta_n, \theta_s, \phi_s, u_{10}, \varphi_w)$.

However, this parametrization is not optimal for representing the functional dependence of the scattered signal, since we know that the dominant source of scattered signal is associated with noise in the specular direction. Therefore, we seek to represent the scattered signal in terms of the location in the sky of the specular direction, which we denote $(\alpha_{spec}, \delta_{spec})$. In order to represent the scattering solution in terms of these variables, we must find a mapping between $(\alpha_{spec}, \delta_{spec})$ and (α_n, δ_n) . This mapping will necessarily involve θ_s and ϕ_s , so that we can write the mapping function as

$$T : (\alpha_n, \delta_n, \theta_s, \phi_s) \rightarrow (\alpha_{spec}, \delta_{spec}, \theta_{spec}, \psi^{uh}), \quad 4.4.54$$

where θ_{spec} is the incidence angle of the specular direction in the upper hemisphere altitude-azimuth frame, and where we have introduced the angle ψ^{uh} , which represents the orientation of the upper hemisphere at the specular point $(\alpha_{spec}, \delta_{spec})$. The mapping operator T can be seen to be that function which rotates the unit normal vector in the upper hemisphere frame into the unit vector in the specular direction.

ψ^{uh} must be defined so as to allow construction of an inverse mapping operator T^{-1} that maps a specular direction $(\alpha_{spec}, \delta_{spec})$ uniquely into an upper hemisphere unit normal (α_n, δ_n) . To facilitate a definition of ψ^{uh} , we first establish alt-azimuth coordinate systems and associated basis vectors in both the upper hemisphere and celestial frames along the line of

ARGANS Ltd.

sight in the specular direction. Detailed definitions of reference frames and associated transformation used in the derivation of Ψ^{uh} are given in Appendix B. This transformation can be performed with the use of CFI. The basis vectors are analogous to horizontal and vertical polarization basis vectors used to describe electromagnetic plane waves. In the upper hemisphere frame, which is the topocentric frame whose origin is the surface target, also called the earth alt-azimuth frame, we define the 'horizontal' basis vector $\hat{h}^u = \hat{n}^u \times \hat{r} / \|\hat{n}^u \times \hat{r}\|$, where \hat{n}^u is the unit normal to the surface at the target and \hat{r} is directed outward towards the specular direction from the target. Next, we define a 'vertical' basis vector by $\hat{v}^u = \hat{h}^u \times \hat{r} / \|\hat{h}^u \times \hat{r}\|$.

If we let ϕ_{spec} and θ_{spec} be the specular azimuth and altitude, respectively, of \hat{r} in the upper hemisphere frame, then we have

$$\begin{aligned}\hat{h}^u &= -\sin \phi_{spec} \hat{x}^u + \cos \phi_{spec} \hat{y}^u, \\ \hat{v}^u &= -\cos \phi_{spec} \sin \theta_{spec} \hat{x}^u - \sin \phi_{spec} \sin \theta_{spec} \hat{y}^u + \sin \theta_{spec} \hat{z}^u,\end{aligned}\tag{4.4.55}$$

where \hat{x}^u , \hat{y}^u , and \hat{z}^u are basis vectors for the topocentric Earth frame that determines the upper hemisphere. Analogous basis vectors can be defined in the celestial frame as

$$\begin{aligned}\hat{h}^c &= -\sin \alpha_{spec} \hat{x}^c + \cos \alpha_{spec} \hat{y}^c, \\ \hat{v}^c &= -\cos \alpha_{spec} \sin \delta_{spec} \hat{x}^c - \sin \alpha_{spec} \sin \delta_{spec} \hat{y}^c + \sin \delta_{spec} \hat{z}^c,\end{aligned}\tag{4.4.56}$$

where α_{spec} and δ_{spec} are the specular right ascension and declination, respectively, of \hat{r} in the celestial frame.

If we denote the components of a vector normal to the line-of-sight in the upper hemisphere alt-azimuth (\hat{h}_u, \hat{v}_u) frame by (V^{hu}, V^{vu}) , then its components in the celestial (\hat{h}_c, \hat{v}_c) frame, denoted by (V^{hc}, V^{vc}) , are

$$\begin{pmatrix} V^{hc} \\ V^{vc} \end{pmatrix} = \begin{pmatrix} \hat{h}^c \cdot \hat{h}^u & \hat{h}^c \cdot \hat{v}^u \\ \hat{v}^c \cdot \hat{h}^u & \hat{v}^c \cdot \hat{v}^u \end{pmatrix} \begin{pmatrix} V^{hu} \\ V^{vu} \end{pmatrix}\tag{4.4.57}$$

It turns out that the preceding matrix is just a rotation matrix, so we can write this transformation as

$$\begin{pmatrix} V^{hc} \\ V^{vc} \end{pmatrix} = \begin{pmatrix} \cos \Psi_{uh} & -\sin \Psi_{uh} \\ \sin \Psi_{uh} & \cos \Psi_{uh} \end{pmatrix} \begin{pmatrix} V^{hu} \\ V^{vu} \end{pmatrix} \quad 4.4.58$$

where Ψ_{uh} is the angle one must rotate a vector defined in the upper hemisphere alt-azimuth frame counter clockwise about the line-of-sight in the specular direction to obtain the vector components in the celestial sphere alt-azimuth frame. Equivalently, it is the angle one must rotate the alt-azimuth basis vectors at earth target clockwise to obtain the basis vectors for the celestial alt-azimuth frame. This angle is analogous to the Claassen angle in radiometry, and, referring to the previous equation, we see that an explicit expression for it is

$$\Psi_{uh} = \tan^{-1} \left(-\frac{\hat{h}^c \cdot \tilde{v}^u}{\hat{h}^c \cdot \tilde{h}^u} \right) \quad 4.4.59$$

where \tilde{h}^u and \tilde{v}^u are basis vectors for the upper hemisphere frame transformed into the celestial frame by applying the transformation matrix T_{ac} defined in Appendix D:

$$\begin{aligned} \tilde{h}^u &= T_{ac} \hat{h}^u, \\ \tilde{v}^u &= T_{ac} \hat{v}^u, \end{aligned} \quad 4.4.60$$

For convenience we repeat here the definition of T_{ac} , the transformation from alt-azimuth frame on earth, with origin at geodetic latitude \mathcal{G}_g and geodetic longitude φ_g , to the Celestial frame at time t :

$$T_{ac}(\mathcal{G}_g, \varphi_g, t) = T_{ec}(H)T_{ae}(\mathcal{G}_g, \varphi_g), \quad 4.4.61$$

where T_{ec} and T_{ae} are transformations from the Earth fixed frame to the Celestial frame and from the alt-azimuth frame to the Earth fixed frame, respectively. Both transformations are also completely defined in Appendix B. H is the Earth rotation angle, which in turns is the sum of G , the Greenwich sidereal angle and a nutation angle μ . As shown in Appendix D, these transformations can be easily evaluated using Earth Observation CFI library.

Given the specular location in the celestial sphere, $(\alpha_{spec}, \delta_{spec})$, and given the incidence angle in the specular direction θ_{spec} at the earth target in the upper hemisphere along with the orientation angle ψ_{uh} , rotating a vector from the specular direction by θ_{spec} in the direction ψ_{uh} brings it into the direction normal to the target, for which the position in the celestial spherical coordinate system is (α_n, δ_n) . Once this normal is computed, the latitude and longitude of the target is easily derived using the time t , and from this location together with the specular location in the sky given by $(\alpha_{spec}, \delta_{spec})$, the specular azimuth ϕ_{spec} can be computed. Therefore, at some specific acquisition time t , the inverse mapping operator T^{-1} maps a specular direction $(\alpha_{spec}, \delta_{spec})$ uniquely into an upper hemisphere unit normal (α_n, δ_n) and the complete representation of the scattering geometry is uniquely determined by the following set of variables

$$\{\alpha_{spec}, \delta_{spec}, \theta_{spec}, \psi_{uh}\} \quad 4.4.62$$

where we have omitted the geophysical variables u_{10} and φ_w that obviously enter into the full scattering problem. A useful representation of the functional form of the scattered signal in some scattering direction (θ_s, ϕ_s) is then

$$T_p^s \rightarrow T_p^s(\alpha_{spec}, \delta_{spec}, \theta_{spec}, \psi_{uh}, u_{10}, \varphi_w). \quad 4.4.63$$

4.4.7 Fast Implementation Method for Calculating Scattered Signal

Neglecting surface salinity and temperature dependencies in the rough sea surface reflectivity, we have seen that we can uniquely represent the scattered noise as a function of six variables:

$$T_p^s \rightarrow T_p^s(\alpha_{spec}, \delta_{spec}, \theta_{spec}, \psi_{uh}, u_{10}, \varphi_w). \quad 4.4.64$$

The total scattered signal, can, in turn, be represented as an integral over the upper hemisphere of the incoming noise,

$$T_p^s(\theta_s, \phi_s, u_{10}, \varphi_w, \vartheta_g, \varphi_g, t) = \frac{1}{4\pi \cos \theta_s} \int_0^{\pi/2} \int_0^{2\pi} [\sigma_{pp}(\theta_o, \phi_o, \theta_s, \phi_s) + \sigma_{pq}(\theta_o, \phi_o, \theta_s, \phi_s)] T_{sky}(\theta_o, \phi_o) e^{-\tau \sec \theta_o} \sin \theta_o d\phi_o d\theta_o, \quad 4.4.65$$

where the portion of incoming sky is determined uniquely by the set $\{\alpha_{spec}, \delta_{spec}, \theta_{spec}, \psi_{uh}\}$.

To allow efficient implementation of the above equation, it is further assumed here that the atmospheric attenuation of celestial radiation during the downward path toward the surface is uniform within the upper hemisphere and set equal to its value at the specular direction, so that the term $\exp(-\tau \sec \theta_o)$ can be pulled out of the integral using:

$$T_p^s(\theta_s, \phi_s, u_{10}, \varphi_w) \approx \frac{e^{-\tau \sec \theta_s}}{4\pi \cos \theta_s} \int_0^{\pi/2} \int_0^{2\pi} [\sigma_{pp}(\theta_o, \phi_o, \theta_s, \phi_s) + \sigma_{pq}(\theta_o, \phi_o, \theta_s, \phi_s)] T_{sky}(\theta_o, \phi_o) \sin \theta_o d\phi_o d\theta_o, \quad 4.4.66$$

Now, we recall that the bistatic scattering cross sections have the form

$$\sigma_{\alpha\alpha_o}(\theta_o, \phi_o, \theta_s, \phi_s, u_{10}, \varphi_w) = \sum_{m=0}^5 \sigma_{\alpha\alpha_o}^{2m}(\theta_o, \phi_s - \phi_o, \theta_s, u_{10}) \cos 2m(\Phi_{si} - \varphi_w). \quad 4.4.67$$

where the variables have the standard meanings and the angle Φ_{si} is the angle of the difference between the scattered and incident wavevectors, defined in (4.4.42). As amplitudes for bistatic scattering cross sections harmonics greater than two have magnitudes at least about a factor of ten lower than the second harmonic, hereafter we only consider the zeroth and second harmonics. Retaining only the zeroth and second harmonics, and using the trigonometric identity $\cos(a+b) = \cos a \cos b - \sin a \sin b$ to factor out the wind direction φ_w from the above expression, we obtain :

$$\begin{aligned} \sigma_{\alpha\alpha_o}(\theta_o, \phi_o, \phi_s, \theta_s, u_{10}, \varphi_w) &= \sigma_{\alpha\alpha_o}^0(\theta_o, \phi_s - \phi_o, \theta_s, u_{10}) \\ &+ \left[\sigma_{\alpha\alpha_o}^2(\theta_o, \phi_s - \phi_o, \theta_s, u_{10}) \cos(2\Phi_{si}) \right] \cos(2\varphi_w) \\ &+ \left[\sigma_{\alpha\alpha_o}^2(\theta_o, \phi_s - \phi_o, \theta_s, u_{10}) \sin(2\Phi_{si}) \right] \sin(2\varphi_w). \end{aligned} \quad 4.4.68$$

As demonstrated in Appendix C, a useful property of the angle Φ_{si} is:

$$\Phi_{si}(\theta_o, \phi_o, \phi_s, \theta_s) = \Phi_{si}(\theta_o, \phi_o - \phi_s, 0^\circ, \theta_s) + \phi_s = \Phi_{si}^0(\theta_o, \phi_o - \phi_s, \theta_s) + \phi_s. \quad 4.4.69$$

since

$$\Phi_{si} - \varphi_w = \Phi_{si} - \phi_s - (\varphi_w - \phi_s), \quad 4.4.70$$

and with $\Phi_{si} - \phi_s = \Phi_{si}^0$, we have

$$\Phi_{si} - \varphi_w = \Phi_{si}^0 - (\varphi_w - \phi_s) = \Phi_{si}^0 - \varphi_w^r \quad 4.4.71$$

where φ_w^r is the now the wind direction (towards which the wind is blowing) relative to the radiometer azimuth. Using this result, we can redevelop the scattering coefficients in terms of Φ_{si}^0 and $\varphi_w^r = \varphi_w - \phi_s$, so that the modified scattering cross sections become

$$\begin{aligned} \sigma_{\alpha\alpha_o}(\theta_o, \phi_o, \phi_s, \theta_s, u_{10}, \varphi_w) &= \sigma_{\alpha\alpha_o}^0(\theta_o, \phi_s - \phi_o, \theta_s, u_{10}) \\ &+ \left[\sigma_{\alpha\alpha_o}^2(\theta_o, \phi_s - \phi_o, \theta_s, u_{10}) \cos(2\Phi_{si}^0) \right] \cos(2\varphi_w^r) \\ &+ \left[\sigma_{\alpha\alpha_o}^2(\theta_o, \phi_s - \phi_o, \theta_s, u_{10}) \sin(2\Phi_{si}^0) \right] \sin(2\varphi_w^r). \end{aligned} \quad 4.4.72$$

For convenience, we now let

$$\begin{aligned} a_{\alpha\alpha_o}^{(0)}(\theta_o, \phi_s - \phi_o, \theta_s, u_{10}) &= \sigma_{\alpha\alpha_o}^0(\theta_o, \phi_s - \phi_o, \theta_s, u_{10}), \\ a_{\alpha\alpha_o}^{(2)}(\theta_o, \phi_s, \phi_o, \theta_s, u_{10}) &= \sigma_{\alpha\alpha_o}^2(\theta_o, \phi_s - \phi_o, \theta_s, u_{10}) \cos(2\Phi_{si}^0), \\ b_{\alpha\alpha_o}^{(2)}(\theta_o, \phi_s, \phi_o, \theta_s, u_{10}) &= \sigma_{\alpha\alpha_o}^2(\theta_o, \phi_s - \phi_o, \theta_s, u_{10}) \sin(2\Phi_{si}^0) \end{aligned} \quad 4.4.73$$

By introducing Φ_{si}^0 and the wind direction relative to the radiometer azimuth φ_w^r , we have shifted all of the dependence on absolute radiometer azimuth and wind direction into the $\cos(2\Phi_{si}^0)$ and $\sin(2\Phi_{si}^0)$ factors, and that the coefficients of these factors, $a^{(2)}$ and $b^{(2)}$, only depend on the relative azimuth $\phi_s - \phi_o$.

The total scattering coefficients can now be written as

$$\sigma_{\alpha\alpha_o}(\theta_o, \phi_o, \phi_s, \theta_s, u_{10}, \varphi_w) = a_{\alpha\alpha_o}^{(0)} + a_{\alpha\alpha_o}^{(2)} \cos(2\varphi_w^r) + b_{\alpha\alpha_o}^{(2)} \sin(2\varphi_w^r). \quad 4.4.74$$

Since we will be concerned with the polarized scattering of unpolarised incident radiation, we define the combined scattering cross section coefficients (including co-pol and cross-pol terms):

$$\begin{aligned}
 a_p^{(0)}(\theta_o, \phi_s - \phi_o, \theta_s, u_{10}) &= a_{pp}^{(0)}(\theta_o, \phi_s - \phi_o, \theta_s, u_{10}) + a_{pq}^{(0)}(\theta_o, \phi_s - \phi_o, \theta_s, u_{10}), \\
 a_p^{(2)}(\theta_o, \phi_s, \phi_o, \theta_s, u_{10}) &= a_{pp}^{(2)}(\theta_o, \phi_s, \phi_o, \theta_s, u_{10}) + a_{pq}^{(2)}(\theta_o, \phi_s, \phi_o, \theta_s, u_{10}), \\
 b_p^{(2)}(\theta_o, \phi_s, \phi_o, \theta_s, u_{10}) &= b_{pp}^{(2)}(\theta_o, \phi_s, \phi_o, \theta_s, u_{10}) + b_{pq}^{(2)}(\theta_o, \phi_s, \phi_o, \theta_s, u_{10}),
 \end{aligned} \tag{4.4.75}$$

and the combined scattering cross section as

$$\begin{aligned}
 \sigma_p(\theta_o, \phi_o, \phi_s, \theta_s, u_{10}, \varphi_w) &= \sigma_p^0(\theta_o, \phi_s - \phi_o, \theta_s, u_{10}) \\
 &+ \left[\sigma_p^2(\theta_o, \phi_s - \phi_o, \theta_s, u_{10}) \cos(2\Phi_{si}^0) \right] \cos(2\varphi_w^r) \\
 &+ \left[\sigma_p^2(\theta_o, \phi_s - \phi_o, \theta_s, u_{10}) \sin(2\Phi_{si}^0) \right] \sin(2\varphi_w^r).
 \end{aligned} \tag{4.4.76}$$

Now when we consider calculating the total scattered signal in the direction (θ_s, ϕ_s) , we must integrate the product of these scattering cross sections with the incident power (assumed here to be unpolarised with brightness temperature T_{sky}) over the entire upper hemisphere, so that at polarization p the scattered signal is

$$T_p^s(\mathcal{G}_g, \varphi_g, t, \theta_s, \phi_s, u_{10}, \varphi_w) = \frac{\exp(-\tau \sec \theta_s)}{4\pi \cos \theta_s} \int_{\Omega_s} T_{sky}(\Omega_s) \sigma_p d\Omega_s \tag{4.4.77}$$

where Ω_s refers to solid angle in the upper hemisphere. This can be written more explicitly as

$$T_p^s(\mathcal{G}_g, \varphi_g, t, \theta_s, \phi_s, u_{10}, \varphi_w) = \frac{\exp(-\tau \sec \theta_s)}{4\pi \cos \theta_s} \int_0^{\pi/2} \int_0^{2\pi} P(\theta_o, \phi_o, \mathcal{G}_g, \varphi_g, \theta_s, \phi_s, u_{10}, \varphi_w, t) \sin \theta_o d\phi_o d\theta_o. \tag{4.4.78}$$

where

$$P(\theta_o, \phi_o, \mathcal{G}_g, \varphi_g, \theta_s, \phi_s, u_{10}, \varphi_w, t) = T_{sky}(\theta_o, \phi_o, \mathcal{G}_g, \varphi_g, t) \sigma_p(\theta_o, \phi_o, \theta_s, \phi_s, u_{10}, \varphi_w), \tag{4.4.79}$$

and where the dependence of the incoming noise upon latitude \mathcal{G}_g and longitude φ_g of the target and time t is shown explicitly. Also,

$$\sigma_p(\theta_o, \phi_o, \phi_s, \theta_s, u_{10}, \varphi_w) = a_p^{(0)} + a_p^{(2)} \cos(2\varphi_w^r) + b_p^{(2)} \sin(2\varphi_w^r). \tag{4.4.80}$$

Since the dependence of the scattering cross sections on φ_w occurs alone as multiplicative harmonic factors, this dependence can be factored out of all integrals, so that we can write the total scattered signal at polarization p as

$$T_p^s(\theta_s, \phi_s, \vartheta_g, \varphi_g, t, u_{10}, \varphi_w) = e^{-\tau \sec \theta_s} \left[A_p^{(0)}(\theta_s, \phi_s, \vartheta_g, \varphi_g, t, u_{10}) + A_p^{(2)}(\theta_s, \phi_s, \vartheta_g, \varphi_g, t, u_{10}) \cos(2\varphi_w^r) + B_p^{(2)}(\theta_s, \phi_s, \vartheta_g, \varphi_g, t, u_{10}) \sin(2\varphi_w^r) \right] \quad 4.4.81$$

where

$$\begin{aligned} A_p^{(0)} &= \frac{1}{4\pi \cos \theta_s} \int_0^{\pi^2} \int_0^{2\pi} T_{sky}(\theta_o, \phi_o, \vartheta_g, \varphi_g, t) a_p^{(0)} \sin \theta_o d\phi_o d\theta_o, \\ A_p^{(2)} &= \frac{1}{4\pi \cos \theta_s} \int_0^{\pi^2} \int_0^{2\pi} T_{sky}(\theta_o, \phi_o, \vartheta_g, \varphi_g, t) a_p^{(2)} \sin \theta_o d\phi_o d\theta_o, \\ B_p^{(2)} &= \frac{1}{4\pi \cos \theta_s} \int_0^{\pi^2} \int_0^{2\pi} T_{sky}(\theta_o, \phi_o, \vartheta_g, \varphi_g, t) b_p^{(2)} \sin \theta_o d\phi_o d\theta_o. \end{aligned} \quad 4.4.82$$

As noted previously, the above representation of the scattered signal harmonics is still not sufficiently convenient for fast implementation, since much of the variation in scattered signal is expected to be related to changes in the specular location in the celestial sphere, and this specular location can change dramatically with changing radiometer incidence and azimuth angles. However, we can use the previously developed transformation involving the angle ψ_{uh} and express the harmonic coefficients in terms of the specular location in the celestial sphere along with the orientation angle ψ_{uh} , so that we obtain the representation

$$\begin{aligned} T_p^s(\alpha_{spec}, \delta_{spec}, \theta_{spec}, \psi_{uh}, u_{10}, \varphi_w) &= e^{-\tau \sec \theta_{spec}} \left[A_p^{(0)}(\alpha_{spec}, \delta_{spec}, \theta_{spec}, \psi_{uh}, u_{10}) \right. \\ &+ A_p^{(2)}(\alpha_{spec}, \delta_{spec}, \theta_{spec}, \psi_{uh}, u_{10}) \cos(2\varphi_w^r) \\ &+ B_p^{(2)}(\alpha_{spec}, \delta_{spec}, \theta_{spec}, \psi_{uh}, u_{10}) \sin(2\varphi_w^r) \left. \right] \quad 4.4.83 \end{aligned}$$

where the methodology to determine the angle ψ_{uh} is detailed in the previous section. Equation 4.4.83 provides a very useful representation of the sky noise scattered signals at surface level to allow fast operational processing making use of pre-computed Look up tables for the coefficients $A_p^{(0)}$, $A_p^{(2)}$ and $B_p^{(2)}$. Readers may wonder why it is needed here to consider second wind direction harmonics of the sky scattered signals when it is already known that the second wind direction harmonics of the rough sea surface emissivity alone is relatively small at L-band. In fact, as demonstrated in IFREMER technical note, it turns out that depending on the specular location in the celestial sphere, the amplitude of $A_p^{(2)}$ and $B_p^{(2)}$ can be as large as the surface emissivity second harmonics amplitude but with a phase that can be very different due to the existence of the $B_p^{(2)}$ term in (4.4.83), that is always zero for surface emissivity while it can be significant for the sky glitter signals. Although it needs

further investigation, that term might be a plausible physical cause for wiggles observed during the airborne campaign LOSAC.

Making use of LUTS for the coefficients $A_p^{(0)}$, $A_p^{(2)}$ and $B_p^{(2)}$, the processor will only have to perform the following processing to evaluate surface scattered signals:

- 1) determine the following parameters for a given L1C data:

Parameter	Description
α_{spec}	Right ascension of the specular direction with respect to the radiometer look direction [deg]
δ_{spec}	Declination of the specular direction with respect to the radiometer look direction [deg]
θ_{spec}	Specular Incidence angle at target, which is directly the radiometer incidence angle at target
ψ_{uh}	Upper Hemisphere orientation angle
u_{10}	10-meter height wind speed at target
ϕ_w^r	Relative angle between the direction towards which the 10-meter wind is blowing and the scattering direction towards the radiometer.
τ	Atmospheric attenuation coefficient evaluated at target

- 2) Interpolate the coefficients $A_p^{(0)}$, $A_p^{(2)}$ and $B_p^{(2)}$ from the LUTs using a dedicated Hermite interpolation method described in detail in appendix D.
- 3) Evaluate the sum in equation (4.4.83)

The methodology we used to pre-compute the LUTS for the Sky glitter Harmonics coefficients, namely, $A_p^{(0)}$, $A_p^{(2)}$ and $B_p^{(2)}$ is described in detailed in the companion galactic noise TGRD note.

To construct these lookup tables, we discretized all five dimensions ($\alpha_{spec}, \delta_{spec}, \theta_{spec}, \psi_{uh}, u_{10}$) of the coefficients. By analysing the dependence on each dimension, and weighing the accuracy constraint with constraints imposed by computational resources, we have determined that a reasonable discretization is the following:

$$\begin{aligned} \{u_{10}\} &= \{3,5,7,10,15,25\} \quad m/s, \\ \{\theta_{spec}\} &= \{0^\circ, 10^\circ, 20^\circ, 25^\circ, 30^\circ, 35^\circ, 40^\circ, 45^\circ, 50^\circ, 55^\circ, 60^\circ, 70^\circ, 80^\circ\}. \end{aligned}$$

The grid for ψ_{uh} is regular and defined (in degrees, mathematical convention) by the set

$$\{-\psi_{uh}\} = \{22.5n\},$$

where n is a integer ranging from 0 through 16. The grid for the specular right ascension α_{spec} is regular and defined (also in degrees) by the set

$$\{\alpha_{spec}\} = \{3.75n\},$$

where n is a integer ranging from 0 through 96. Finally, the grid for the specular declination δ_{spec} is regular and defined (in degrees) by the set

$$\{\delta_{spec}\} = \{3.75n\},$$

where n is an integer ranging from 0 through 96. It should be noted that the lookup table is defined in B1950 celestial coordinates, not the J2000 coordinate system. The lookup tables are stored in a MATLAB Version 7 file. The following table lists the correspondence between variable names and quantities described above.

Table 2: Mapping Between MATLAB Variable Names and Physical Quantities in the Lookup Tables

MATLAB Variable Name	Physical Quantity	Independent Variables
dec_b1950	B1950 declination δ_{spec} [deg]	δ_{spec}
ra_b1950	B1950 right ascension α_{spec} [deg]	α_{spec}
ws	10-m wind speed [m s ⁻¹]	u_{10}
eia	radiometer incidence angle [deg]	θ_{spec}
psi	Upper Hemisphere orientation angle - ψ_{uh} [deg]	ψ_{uh}
th_symm	$\tilde{A}_h^{(0)}$: symmetric H-pol component [K]	$(\delta_{spec}, \alpha_{spec}, u_{10}, \theta_{spec}, \psi_{uh})$
tv_symm	$\tilde{A}_v^{(0)}$: symmetric V-pol component [K]	$(\delta_{spec}, \alpha_{spec}, u_{10}, \theta_{spec}, \psi_{uh})$
th_hc	$\tilde{A}_h^{(2)}$: $\cos(2\phi_w)$ harmonic amplitude H-pol [K]	$(\delta_{spec}, \alpha_{spec}, u_{10}, \theta_{spec}, \psi_{uh})$
th_vc	$\tilde{A}_v^{(2)}$: $\cos(2\phi_w)$ harmonic amplitude V-pol [K]	$(\delta_{spec}, \alpha_{spec}, u_{10}, \theta_{spec}, \psi_{uh})$



th_hs	$\tilde{B}_h^{(2)}$: $\sin(2\phi_w)$ harmonic amplitude H-pol [K]	$(\delta_{spec}, \alpha_{spec}, u_{10}, \theta_{spec}, \psi_{uh})$
th_vs	$\tilde{B}_v^{(2)}$: $\sin(2\phi_w)$ harmonic amplitude V-pol [K]	$(\delta_{spec}, \alpha_{spec}, u_{10}, \theta_{spec}, \psi_{uh})$

The LUTs were derived for both the Kirchhoff or the SSA-1 scattering asymptotic model, since it is not known which model perform the best at the moment. However, for the first operational implementation of the algorithm, we wish to employ the Kirchhoff approach as it minimizes errors in the predicted polarization ratios.

The scattering model is not expected to work properly in the range of wind speed strictly greater than zero and less than 3 ms^{-1} . In that range of wind speed, a “drop off” transition occurs in the scattering mechanism between purely specular reflection and rough sea surface scattering. It is expected that the threshold wind speed at which this drop off occur will be highly variable, depending on the low wind speed induced roughness variability within SMOS pixel. Therefore, the processing shall be based on three wind speed conditions based on the decision tree outputs:

- 1) if $u_{10}=0 \text{ ms}^{-1}$, than purely flat reflection model shall be implemented to evaluate surface signals with associated transport at antenna level (equation (4.4.32) above).
- 2) If $0 < u_{10} < 3 \text{ ms}^{-1}$, although it is certainly not a physically based solution, we suggest at first to perform a linear interpolation between predictions of the flat reflection model at 0 m/s and the scattering model outputs at 3 ms^{-1} . Transport at antenna level shall then be performed using the rough sea case equation (equation (4.4.32) above).
- 3) If $u_{10} \geq 3 \text{ m/s}$, apply the rough sea surface processing (equations (4.4.83) plus (4.4.25)).

In addition to the proposed corrections, a flag shall then be defined based on the wind speed value conditions detailed above.

4.4.8 Error budget estimates

Main sources of errors in the estimation of the sky glitter contribution will be

- Errors on the estimation of the bistatic scattering coefficients of the sea surface at L-band, and
- Errors on the estimation of the sky brightness temperature at 1.4 GHz

An estimate of the errors on the modelling of the bistatic scattering coefficients of the sea surface at L-band can be based on the estimated errors of the asymptotic electromagnetic models, namely the SSA-1 and KA approximation. These two approaches can be considered to provide the asymptotic limits within a consistent framework of scattering slope expansions. Importantly, these two approaches lack directly considering the surface geometrical properties to predict the level of polarization. With the proposed models, this polarization level is independent of roughness states. SSA-1 is expected to exaggerate the polarization effects while KA will minimize them. SSA-1 overestimates HH and underestimates VV so that SSA-1 systematically overestimates the H/V ratio with a mean of order +20%. The errors on the sea surface roughness statistics, particularly those associated with the mean square slope and curvature levels within the spectrum are difficult to estimate but will clearly have an important impact as well.

In 90 % of the future SMOS measurements, we found that the numerical implementation method proposed here is in error with the exact asymptotic calculation with an error less than 0.1 K. Therefore, errors associated with the use of our simplified numerical approach are expected to be of this order.

A specific case of importance in the scattering model error budget is very low wind speed conditions ($0 < u_{10} < 3$ m/s), where (i) the reflected signal energy is expected to be the highest, (ii) the surface variability will be very large and (iii) the proposed linear interpolation model is not physically based.

Another source of error might be the unpolarised sky assumption. Although the polarization signatures of sky radiations at L-band are expected to be less than about 0.1 K, we neglected signal polarization basis transformation and Faraday rotation during the sky radiation downward path as well as the complete polarized scattering mechanisms at the surface.

4.4.9 Practical consideration

4.4.9.1 Calibration and validation

Dedicated CAL/VAL activities should be envisaged for the SMOS sky glitter correction model with two main components:

- an Earth-based campaign aiming at measuring precisely the sky glitter scattering features at L-band (e.g., experiment similar to CoSMOS) with high-quality attitude control measurements as well as surface roughness information to calibrate and validate the bistatic-scattering coefficient models.
- a SMOS-data based analysis given the fact that the sky glitter will exhibit a predictable seasonal and geographical contamination. Re-analysis of the correction terms and measured brightness as function of position within the FOV, time of year, ascending

ARGANS Ltd.



or descending passes and wind speed for which good quality (close in time and space) co-localized auxiliary wind and surface roughness data are available shall be performed to assess the efficiency of the model.

4.4.9.2 Exception handling

If any parameter goes out of LUT range during the retrieval, different flags

Fg_OoR_gam2_dec
Fg_OoR_gam2_ra
Fg_OoR_gam2_WSn
Fg_OoR_gam2_theta
Fg_OoR_gam2_psi

are raised. No extrapolation is done and the boundary value is taken.

References

- [1] C. T. Swift and R. E. McIntosh, "Considerations for microwave remote sensing of ocean-surface salinity," *IEEE Transactions on Geoscience and Remote Sensing*, vol. GE-21, no. 4, pp. 480–491, 1983.
- [2] S. H. Yueh, R. West, W. J. Wilson, F. K. Li, E. G. Njoku, and Y. Rahmat-Samii, "Error sources and feasibility for microwave remote sensing of ocean salinity," *IEEE Trans. Geosci. Remote Sensing*, vol. 39, no. 5, pp. 1049–1060, May 2001.
- [3] D. M. LeVine and S. Abraham, "Galactic noise and passive microwave remote sensing from space at L-band," *IEEE Trans. Geosci. Remote Sensing*, vol. 42, no. 1, pp. 119–129, Jan. 2004.
- [4] D. M. LeVine, S. Abraham, Y. Kerr, W. Wilson, N. Skou, and S. Sobjaerg, "Comparison of model prediction with measurements of galactic background noise at L-band," *IEEE Trans. Geosci. Remote Sensing*, vol. 43, no. 9, pp. 2018–2023, Sept. 2005.
- [5] W. Reich, "A radio continuum survey of the northern sky at 1420 Mhzpart I," *Astron. Astrophys. Suppl. Series*, vol. 48, pp. 219–297, July 1982.
- [6] P. Reich and W. Reich, "A radio continuum survey of the northern sky at 1420 mhz-part II," *Astron. Astrophys. Suppl. Series*, vol. 63, pp. 205–292, July 1986.
- [7] P. Reich, J. C. Testori, and W. Reich, "A radio continuum survey of the northern sky at 1420 mhz, the atlas of contour maps," *Astron. Astrophys.*, vol. 376, pp. 861–877, July 2001.



[8] E. M. Arnal, E. Bajaja, J. J. Larrarte, R. Morras, and W. G. L. Pöppel, "A high sensitivity Hi survey of the sky at $\sim -25\sigma$," *Astronom. Astrophys. Suppl. Series*, vol. 142, pp. 35–40, Feb. 2000.

[9] J. C. Testori, P. Reich, J. A. Bava, F. R. Colomb, E. E. Hurrel, J. J. Larrarte, W. Reich, and A. J. Sanz, "A radio continuum survey of the southern sky at 1420 MHz. Observations and data reduction," *Astronomy and Astrophysics*, vol. 368, pp. 1123–1132, Mar. 2001.

[10] D. Hartmann and W. B. Burton, *Atlas of Galactic Neutral Hydrogen*. Atlas of Galactic Neutral Hydrogen, by Dap Hartmann and W. Butler Burton, pp. 243. ISBN 0521471117. Cambridge, UK: Cambridge University Press, February 1997., Feb. 1997.

[11] S. Schmidl Søjbjerg, J. Rotbøll, and N. Skou, "Wind effects and angular dependence at L-band polarimetric data: first results of LOSAC," in *ESA SP-525: EuroSTARRS, WISE, LOSAC Campaigns. Proceedings of the First Results Workshop*, P. Fletcher, Ed., Mar. 2003, pp. 181–189.

[12] J. Etcheto, E. P. Dinnat, J. Boutin, A. Camps, J. Miller, S. Contardo, J. Wesson, J. Font, and D. Long, "Wind speed effect on L-band brightness temperature inferred from EuroSTARRS and WISE2001 field experiments," *IEEE Trans. Geosci. and Remote Sens.*, vol. 42, no. 10, pp. 2206–2213, 2004.

[13] A. Camps, J. Font, M. Vall-Ilossera, C. Gabarro, R. Villarino, L. Enrique, J. Miranda, I. Corbella, N. Duo, F. Torres, S. Blanch, J. Arenas, A. Julia, J. Etcheto, V. Caselles, A. Weill, J. Boutin, S. Contardo, R. Niclos, R. Rivas, S. Reising, P. Wursteisen, M. Berger, and M. Martn-Neira, "The WISE 2000 and 2001 Campaigns in support of the SMOS Mission: Sea surface L-band Brightness Temperature Observations and their application to Multi-Angular Salinity Retrieval," *IEEE Trans. Geosci. Remote Sensing*, vol. 42, no. 4, pp. 1039–1048, 2004.

[14] W. J. Wilson, S. H. Yueh, S. J. Dinardo, S. L. Chazanoff, A. Kitiyakara, F. K. Li, and Y. Rahmat-Samii, "Passive active l- and s-band (pals) microwave sensor for ocean salinity and soil moisture measurements," *IEEE Transactions on Geoscience and Remote Sensing*, vol. 39, no. 5, pp. 1039–1048, 2001.

[15] P. Waldteufel and S. Zine, "Impact of the variable angular apodization function on galactic contribution," CBSA, Tech. Rep., 2005.

[16] J. P. Hollinger, "Passive microwave measurements of sea surface roughness," *IEEE Trans. Geosci. Electron.*, vol. GE-9, no. 3, pp. 165–169, 1971.



[17] C. T. Swift, "Microwave radiometer measurements of the Cape Cod Cannal," *Radio Sci.*, vol. 9, no. 7, pp. 641–653, 1976.

[18] W. J. Webster, T. T. Wilheit, D. B. Ross, and P. Gloersen, "Spectral characteristics of the microwave emission from a wind-driven covered sea," *J. Geophys. Res.*, vol. 81, no. 18, pp. 3095–3099, 1976.

[19] R. M. Lerner and J. P. Hollinger, "Analysis of microwave radiometric measurements from skylab," NRL, Tech. Rep., Apr. 1976, 93 p.

[20] A. Camps, J. Font, J. Etcheto, V. Caselles, A. Weill, I. Corbella, M. Vall-Ilossera, N. Duffo, F. Torres, R. Villarino, L. Enrique, A. Julia, C. Gabarro, J. Boutin, E. Rubio, S. C. Reising, P. Wursteisen, M. Berger, and M. Martin-Neira, "Sea surface emissivity observations at L-band: First results of the wind and salinity experiment wise 2000," *IEEE Trans. Geosci. and Remote Sens.*, vol. 40, no. 10, pp. 2117–2129, 2002.

[21] P. M. W. Kalberla, W. B. Burton, D. Hartmann, E. M. Arnal, E. Bajaja, R. Morras, and W. G. L. Pöppel, "The Leiden/Argentine/Bonn (LAB) Survey of Galactic HI. Final data release of the combined LDS and IAR surveys with improved stray-radiation corrections," *Astronomy and Astrophysics*, vol. 440, pp. 775–782, Sept. 2005.

[22] E. Bajaja, E. M. Arnal, J. J. Larrarte, R. Morras, W. G. L. Pöppel, and P. M. W. Kalberla, "A high sensitivity HI survey of the sky at -25° . Final data release," *Astronomy and Astrophysics*, vol. 440, pp. 767–773, Sept. 2005.

[23] W. Reich, P. Reich, and E. Fuerst, "The Effelsberg 21 CM radio continuum survey of the Galactic plane between $L = 357$ deg and $L = 95.5$ deg," *Astronom. Astrophys. Suppl. Series*, vol. 83, pp. 539–568, June 1990.

[24] W. Reich, P. Reich, and E. Furst, "21cm radio continuum survey. I. (Reich+ 1990)," *VizieR Online Data Catalog*, vol. 408, pp. 30 539–+, Nov. 1997.

[25] A. Wright and R. Otrupcek, "Parkes Catalog, 1990, Australia telescope national facility." in *PKS Catalog (1990)*, 1990, pp. 0–+.

[26] D. E. Barrick and E. Bahar, "Rough surface scattering using specular point theory," *IEEE Trans. Antennas Propag.*, vol. AP-29, no. 5, pp. 798–800, Sept. 1981.

[27] D. E. Barrick, "Relationship between slope probability density function and the physical optics integral in rough surface scattering," *Proceedings of the IEEE*, vol. 56, no. 10, pp. 1728–1729, Oct. 1968.



[28] —, “Correction to: Relationship between slope probability density function and the physical optics integral in rough surface scattering,” *Proceedings of the IEEE*, vol. 57, no. 2, p. 256, Feb. 1969.

[29] R. D. Kodis, “A note on the theory of scattering from an irregular surface,” *IEEE Trans. Antennas Propag.*, vol. AP-14, no. 1, pp. 77–82, Jan. 1966.

[30] D. E. Barrick, “Rough surface scattering based on the specular point theory,” *IEEE Trans. Antennas Propag.*, vol. AP-16, no. 4, pp. 449–454, July 1981.

[31] A. Stogryn, “The apparent temperature of the sea at microwave frequencies,” *IEEE Trans. Antennas Propag.*, vol. AP-15, no. 2, pp. 278–286, Mar. 1967.

[32] A. J. Camps and S. C. Reising, “Wind direction azimuthal signature in the Stokes emission vector from the ocean surface at microwave frequencies,” *Microwave and Opt. Tech. Lett.*, vol. 29, no. 6, pp. 426–432, 2001.

[33] F. M. Breon and N. Henriot, “Spaceborne observations of ocean glint reflectance and modeling of wave slope distributions,” *J. Geophys. Res.*, vol. 111, no. C06005, 2006.

[34] C. Cox and W. Munk, “Measurements of the roughness of the sea surface from photographs of the sun’s glitter,” *J. Opt. Soc. Am.*, vol. 44, pp. 838–850, 1954.

[35] T. Meissner and F J Wentz, “[The emissivity of the ocean surface between 6 - 90 GHz over a large range of wind speeds and Earth incidence angles](#),” *IEEE Transactions on Geoscience and Remote Sensing*, 50, 3004-3026.

[36] T. T. Wilheit, Jr., “A model for the microwave emissivity of the ocean’s surface as a function of wind speed,” *IEEE Trans. Geosci. Electron.*, vol. GE-9, no. 4, pp. 244–249, 1979.

[37] D. R. Thompson, T. M. Elfouhaily, and J. Garrison, “An improved geometrical optics model for bistatic GPS scattering from the ocean surface,” *IEEE Trans. Geosci. and Remote Sens.*, vol. 43, no. 12, pp. 2810–2821, 2005.

[38] J. P. Hollinger, “Passive microwave measurements of sea surface roughness,” *IEEE Trans. Geosci. Electron.*, vol. GE-9, no. 3, pp. 165–169, 1971.



APPENDIX A *Auxiliary datasets used in the generation of the sky map*

A. The Effelsberg survey

The Effelsberg survey [23,24] was conducted over the Galactic plane between $57^{\circ} \leq l \leq 95.5^{\circ}$ and $-4^{\circ} \leq b \leq 4^{\circ}$ with the Effelsberg 100-m radio telescope. This survey covers the surroundings of the galactic plane. This survey is specifically used to complement the continuum survey around Cassiopeia A. Effelsberg survey does not include any data for Cygnus A.

Data provided in the Effelsberg survey can be converted to fit into the Reich continuum map. Indeed:

- The resolution of the 100m Effelsberg telescope (HPBW of 9.4') is higher than the one of the Stockert telescope used for the Reich continuum survey
- Data for Effelsberg survey are provided in main beam brightness temperature whereas Stockert data are provided in full beam brightness temperature.
- An associated catalog of strong sources also exist.

B. The NRAO VLA Sky Survey (NVSS).

Conducted by the National Radio Astronomy Observatory, the NRAO VLA Sky Survey (NVSS) is a 1.4 GHz continuum survey covering the entire sky north of -40° declination. A detailed description appears in [26]. In addition to the images, a source catalogue was extracted by fitting elliptical Gaussians to all significant peaks. For more information, see <http://www.cv.nrao.edu/nvss/>. The sources flux proposed in NVSS are given an accuracy of 3 % .

C. The Parkes survey

The Parkes database [25] consists of radio and optical data for 8264 radio sources. It covers essentially all the sky south of declination $+27$ degrees but largely excludes the Galactic Plane and the Magellanic Cloud regions. This survey is used for strong sources in the Southern sky.

D. Cross comparison NVSS-Effelsberg catalogues

A first check of the validity of the approach can be done by comparing integrated NVSS flux to the Effelsberg survey of sources in the galactic plane. The NVSS sources are extracted for the coordinates identified in the Effelsberg catalogue and their flux is integrated. Comparison shows a rms error of around 0.5 Jy (0.25 Jy if the strongest source is not considered). This corresponds to approximately 0.5 K rms at the scale of the Reich and Reich continuum map and to 0.005 K at the scale of SMOS main beam. Some of the observed discrepancies come from the lack of compatibility between the protocols that describe the extraction of the

ARGANS Ltd.

Commercial in Confidence

Page 121

Use, duplication, or disclosure of this document or any information contained herein is subject to the restriction on the title page of this document.



sources from the catalogues (e.g. circular or square box). Only a few sources may contribute to a noticeable error at the scale of SMOS beam. For an error threshold selected at 0.05K, sources where discrepancies are larger than 5 Jy must be carefully considered.

E. Strong sources: Cassiopeia A, Cygnus A, Taurus A, Virgo A

Some very strong sources are present in the sky, which flux was measured at a range of frequencies. Among these, Cassiopeia A is characterised by a strong variation of its flux with time. Consequently, even if an estimation of its flux can be provided, it is not advised to use it in any correction procedure. Virgo A is a small source which is surrounded by a halo which is a strong contributor in emission at low frequencies.

F. Calibration sources

Another set of sources is usually used for calibration purpose as their angular extension is very small and their flux is stable in time. The position / intensity of all these sources is found in literature and can be used to check the values of the sources extracted from the catalogue, as seen below where NVSS output is compared to what is found in literature. Discrepancies are mostly caused by the presence of a strong halo which is a strong contributor in emission; this is the case of Cassiopeia A and of Virgo A (at low frequencies).

APPENDIX B Reference frames and transformation matrices

A. Reference frames

We begin by establishing several reference frames.

Earth Fixed Reference Frame

The first is the Earth Fixed Reference Frame, or E , centered at the center of the Earth Reference Ellipsoid, with cartesian basis $(\hat{x}_e, \hat{y}_e, \hat{z}_e)$.

\hat{x}_e points outward along the equatorial plane towards the Greenwich meridian,
 \hat{y}_e points outward along the equatorial plane towards 90° E, and
 \hat{z}_e points towards the North Pole.

Altitude-Azimuth frame

The second frame is the so-called alt-azimuth frame, or A , with cartesian basis $(\hat{x}_i, \hat{y}_i, \hat{z}_i)$, with



\hat{x}_t pointing eastward,
 \hat{y}_t pointing northward, and
 \hat{z}_t pointing upward (zenith).

This frame is the same as the topocentric frame defined in the EE CFI Mission Convention Document and is the natural frame in which to express the surface scattering problem since the scattering geometry is typically defined relative to the local surface orientation. Since this coordinate frame is defined relative to the location on the Earth's surface, the projection of the cartesian basis vectors for this frame in the Earth Fixed Coordinate System depends on latitude and longitude.

True of Date (TOD) Celestial Frame

The third frame is the True of Date (TOD) Celestial Frame, or C , with cartesian basis $(\hat{x}_c, \hat{y}_c, \hat{z}_c)$, in which the galactic noise map is provided. This frame is aligned with the Earth Fixed Frame except for a time-dependent rotation of (\hat{x}_c, \hat{y}_c) relative to (\hat{x}_e, \hat{y}_e) . The centre of the frame coincides with the centre of the Earth, and the x-axis coincides with the direction of the true vernal equinox of date. This coordinate system's orientation accounts for the nutation of the Earth owing to a periodic effect of the gravitation fields of the moon and other planets acting on the Earth's equatorial bulge. Using the terminology in the EE CFI MCD, to transform a vector from the TOD Celestial Frame to the Earth Fixed Frame we apply a rotation about the \hat{z}_e -axis by the Earth rotation angle, H , which in turn is the sum of the Greenwich sidereal angle G and a nutation angle μ .

B. Frames transformation

The transformation from one frame to another can be written as a 3×3 matrix, and we denote the transform from frame I to frame J as T_{IJ} . The matrices are built with the help of EE CFI. As mentioned above, the transformation from the Earth Fixed Frame to the TOD Celestial Frame, denoted T_{ec} , is a rotation about the \hat{z}_e -axis by an angle H . Introducing the rotation matrix R_z for a counter clockwise rotation by angle ϕ of the coordinate system about the $\hat{z}_c = \hat{z}_e$ -axis

$$R_z(\phi) = \begin{pmatrix} \cos \phi & \sin \phi & 0 \\ -\sin \phi & \cos \phi & 0 \\ 0 & 0 & 1 \end{pmatrix}. \quad 4.4.84$$

we can write the E to C transformation as



$$T_{ec} = R_z(-H) = R_z(-G - \mu), \quad 4.4.85$$

Its inverse is

$$T_{ce} = T_{ec}^{-1} = R_z(H) = R_z(G + \mu). \quad 4.4.86$$

G is a third-order polynomial in time. When G is expressed in degrees and T is the so-called Universal Time (UT1) expressed in the Modified Julian Day 2000 (MJD2000) date convention, the formula for G is

$$G = 99.9677946 + 360.985647 + 3662860 T + 0.29079 \times 10^{-12} T^2. \quad 4.4.87$$

Universal Time, UT1, is very close to the common Coordinated Universal Time (UTC), but differs slightly from it in that it does not differ from actual atomic clock time (TAI) by a constant integer number of seconds, whereas UTC time does. Since both UT1 and UTC are defined to be consistent with the mean diurnal motion of the Earth relative to the stars, they must be adjusted periodically, but the adjustment is accomplished differently in the two systems. For UT1 time this is done smoothly, whereas for UTC time this is accomplished by inserting leap seconds at scheduled times into UTC when it is predicted to lag behind UT1 time by a threshold (.9 s). This introduces discontinuities in UTC. In UT1, no discontinuities exist since the adjustment is continuous.

In the Modified Julian Day 2000 (MJD2000) J_m date convention time, either in the UT1 system or in the UTC system, is expressed as the interval of time in days (including fractional days) since midnight January 1, 2000. It differs from true Julian date J_d by a constant value of 2451544.5 decimal days, so that in decimal days we have

$$J_d = J_m + 2451544.5. \quad 4.4.88$$

As previously mentioned, the transformation between the alt-azimuth frame A and another frame is complicated by the fact that the alt-azimuth frame depends on location of the origin on the surface of the Earth, so that $A = A(\mathcal{G}_s, \varphi_s)$, where \mathcal{G}_s is geodetic latitude and φ_s is the geodetic longitude. Here we take the geodetic longitude to be equal to the geocentric longitude. The geodetic latitude is the angle between the equatorial plane and the local normal to the Earth's surface at the point in question. It is related to the spherical coordinate latitude θ_s by the relation

$$\theta_s = \tan^{-1}((1-e_2)\tan\vartheta_g), \quad 4.4.89$$

where

$$e = \sqrt{\frac{A_e^2 - B_e^2}{A_e^2}}, \quad 4.4.90$$

is the eccentricity of the ellipsoidal Earth, $A_e=6378137$ m is the Earth's major axis (equatorial) radius and $B_e=6356752.3142$ m is the Earth's minor axis radius. To determine explicitly the transformation from A to E we introduce a second rotation matrix that rotates the coordinate system counter clockwise about the x -axis,

$$R_x(\varphi) = \begin{pmatrix} 1 & 0 & 0 \\ 0 & \cos \varphi & \sin \varphi \\ 0 & -\sin \varphi & \cos \varphi \end{pmatrix}; \quad 4.4.91$$

To compute the composite transformation from A to E , we rotate the local alt-azimuth frame about the \hat{x}_i -axis by the angle $\phi = \vartheta_g - \frac{\pi}{2}$ to align \hat{z}_i with \hat{z}_e , and then we rotate the resulting intermediate (primed) frame about the new \hat{z} -axis \hat{z}_i by the angle $-\varphi_g - \frac{\pi}{2}$ to align \hat{x}_i with x_e . The resulting composite transformation from A to E can be written as

$$T_{ae}(\vartheta_g, \phi_g) = R_z\left(-\phi_g - \frac{\pi}{2}\right) R_x\left(\vartheta_g - \frac{\pi}{2}\right), \quad 4.4.92$$

and its inverse, mapping vectors from E to A , is simply

$$T_{ea}(\vartheta_g, \phi_g) = R_x\left(-\vartheta_g + \frac{\pi}{2}\right) R_z\left(\phi_g + \frac{\pi}{2}\right). \quad 4.4.93$$

To organize the results of the scattering calculations and to compare results with specular reflection calculations, it is also useful to be able to compute the specular direction for a given incidence/azimuth angle. This can be accomplished by applying a transformation matrix T_{ref} which rotates a vector by 180° about the \hat{z}_i axis in the alt-azimuth coordinate system:

$$T_{ref} = R_z(\pi). \quad 4.4.94$$

The fourth frame is the Instrument Reference Frame, I . By our convention, cartesian basis vectors for this frame, denoted $(\hat{x}_i, \hat{y}_i, \hat{z}_i)$ are such that \hat{x}_i points to the right of instrument motion, normal to the orbital plane, \hat{y}_i points in the direction of spacecraft motion, and \hat{z}_i points upward normal to the instrument plane containing \hat{x}_i and \hat{y}_i . The sign convention we adopt here for \hat{x}_i and \hat{y}_i is opposite that in EE CFI, in which \hat{y}_i is directed along spacecraft velocity vector towards the rear, while \hat{x}_i is directed normal to the orbital plane to the left of the spacecraft velocity vector. This reference frame is complicated by the fact that the spacecraft position and orientation, or attitude, are functions of time in E , so the transformation matrix between I and E is a function of time. Using CFI, at a particular time t (expressed in UTC) we obtain the transformation matrix $T_{ie}(t)$ transforming a vector from the instrument frame to the Earth Fixed Frame E and the inverse transform T_{ei} .

To find the transformation from the alt-azimuth frame to the celestial frame C , we first transform from alt-azimuth to the Earth Fixed Frame and then transform the resulting vector from the Earth fixed Frame to the celestial frame. The resulting transformation matrix is thus

$$T_{ac} = T_{ec} T_{ae}, \quad 4.4.95$$

and its inverse, going from celestial coordinates to alt-azimuth coordinates, is

$$T_{ca} = T_{ac}^{-1} = T_{ea} T_{ce}. \quad 4.4.96$$

In each of the above frames we can represent vectors in a spherical coordinate system, related to the corresponding cartesian coordinate system by the relations

$$\begin{aligned} x_k &= r_k \cos \theta_k \cos \varphi_k, \\ y_k &= r_k \cos \theta_k \sin \varphi_k, \\ z_k &= r_k \sin \theta_k, \end{aligned} \quad 4.4.97$$

where k refers to the coordinate system, θ_k is the altitude (or latitude), φ_k is the azimuth, and r_k is range. In the Instrument Frame, we follow convention and introduce the additional director cosine representation of the spherical coordinates,

$$\begin{aligned} \xi &= \sin \theta_b \cos \varphi_i, \\ \eta &= \sin \theta_b \sin \varphi_i, \end{aligned} \quad 4.4.98$$

where $\theta_b = \frac{\pi}{2} - \theta$ is the angle from boresight. In considering the finite beamwidth of the synthetic antenna we will need to integrate over the solid angle

$$d\Omega = \sin \theta_b d\theta_b d\varphi = \sin \theta_b J^{-1}(\theta_b, \varphi) d\xi d\eta \quad 4.4.99$$

subtended by the beam, where J is the Jacobian of the transformation from (θ_b, φ) to (ξ, η) . The Jacobian is

$$J(\theta_b, \varphi) = (\xi, \eta)(\theta_b, \varphi) = \begin{vmatrix} \xi \theta_b & \xi \varphi \\ \eta \theta_b & \eta \varphi \end{vmatrix} = \begin{vmatrix} \cos \theta_b \cos \varphi & -\sin \theta_b \sin \varphi \\ \cos \theta_b \sin \varphi & \sin \theta_b \cos \varphi \end{vmatrix} = \cos \theta_b \sin \theta_b = \sqrt{1 - \xi^2 - \eta^2} \sin \theta_b. \quad 4.4.100$$

and so the transformed solid angle increment is

$$d\Omega = \sin \theta_b d\theta_b d\varphi = \frac{d\xi d\eta}{\cos \theta_b}, = \frac{d\xi d\eta}{\sqrt{1 - \xi^2 - \eta^2}}. \quad 4.4.101$$

It should be noted that in the above transformations we are concerned about transforming directions rather than absolute positions, since we assume that the galactic signal is at such a large distance that origin shifts by distances of the order of the Earth diameter do not alter significantly the direction of a particular galactic source.

A fifth frame is termed the geographic frame, G . This frame is related to the instrument frame by a rotation about the \hat{x}_i axis by a tilt angle t to align the instrument \hat{z}_i axis with the \hat{z}_t axis of the topocentric frame at the satellite subpoint $O = (\rho_{ps}, \rho_{sp})$, $A_o = A(\rho_{ps}, \rho_{sp}) = G$. Thus, \hat{x}_i is parallel to $\hat{x}_t(\rho_{ps}, \rho_{sp})$.

As mentioned above, the alt-azimuth frame is the natural frame in which to perform bistatic scattering calculation, since in this frame relevant incidence and azimuth angles are readily computed. Therefore, in performing scattering calculations for SMOS, we must establish a local alt-azimuth frame for every point in the FOV at which we wish to compute the scattered signal in the antenna frame. To this end, for each (ξ, η) in the director cosine coordinate system, we use CFI to determine the satellite location in E and we then determine the location on the Earth Reference Ellipsoid at which the line of sight (LOS) intersects the Earth. We let (x_t, y_t, z_t) be the unknown target location on the Earth's surface in E , (x_s, y_s, z_s) be the instrument location E , and we let (d_x, d_y, d_z) be the unit vector in the instrument look direction in E . Then if we let R be the range from instrument to the target, the target location is $(x_s + Rd_x, y_s + Rd_y, z_s + Rd_z)$, and it must satisfy the equation for an ellipsoid,

ARGANS Ltd.

$$\frac{(x_s + Rd_x)^2}{A_e^2} + \frac{(y_s + Rd_y)^2}{A_e^2} + \frac{(z_s + Rd_z)^2}{B_e^2} = 1. \quad 4.4.102$$

Expanding this equation and letting

$$\begin{aligned} A &= \frac{d_x^2}{A_e^2} + \frac{d_y^2}{A_e^2} + \frac{d_z^2}{B_e^2}, \\ B &= \frac{2x_s d_x}{A_e^2} + \frac{2y_s d_y}{A_e^2} + \frac{2z_s d_z}{B_e^2}, \\ C &= \frac{x_s^2}{A_e^2} + \frac{y_s^2}{A_e^2} + \frac{z_s^2}{B_e^2} - 1, \end{aligned} \quad 4.4.103$$

the solution for R, the distance to the target, is

$$R = \frac{-B \pm \sqrt{B^2 - 4AC}}{2A} \quad 4.4.104$$

If $B^2 - 4AC < 0$ or if $R < 0$ then the line of sight does not intersect the Earth surface, in which case the instrument receives radiation directly from space. In the case of multiple positive solutions, the smaller one corresponds to the first intersection of the line of sight with the Earth surface, and the other is on the other side of the Earth.

APPENDIX C Properties of the Angle Φ_{si}

Recalling the definition of Φ_{si} ,

$$\Phi_{si}(\theta_s, \phi_s, \theta_b, \phi_b) = \tan^{-1} \left(\frac{\sin \theta_s \sin \phi_s + \sin \theta_b \sin \phi_b}{\sin \theta_s \cos \phi_s + \sin \theta_b \cos \phi_b} \right) = \tan^{-1} \left(\frac{d_y}{d_x} \right), \quad 4.4.105$$

where

$$\begin{aligned} d_x &= \sin \theta_s \cos \phi_s + \sin \theta_b \cos \phi_b, \\ d_y &= \sin \theta_s \sin \phi_s + \sin \theta_b \sin \phi_b \end{aligned} \quad 4.4.106$$

Now consider a change in ϕ by some amount $\Delta\phi$. Now let ϕ change by some amount, $\Delta\phi$. Then the new value of Φ_{si} is

$$\begin{aligned}\Phi_{si}' &= \Phi_{si}(\theta, \phi + \Delta\phi, \phi + \Delta\phi, \theta) = \tan^{-1} \left(\frac{\sin \theta_s \sin(\phi + \Delta\phi) + \sin \theta_b \sin(\phi + \Delta\phi)}{\sin \theta_s \cos(\phi + \Delta\phi) + \sin \theta_b \cos(\phi + \Delta\phi)} \right) \\ &= \tan^{-1} \left(\frac{\sin \theta_s (\sin \phi \cos \Delta\phi + \cos \phi \sin \Delta\phi) + \sin \theta_b (\sin \phi \cos \Delta\phi + \cos \phi \sin \Delta\phi)}{\sin \theta_s (\cos \phi \cos \Delta\phi - \sin \phi \sin \Delta\phi) + \sin \theta_b (\cos \phi \cos \Delta\phi - \sin \phi \sin \Delta\phi)} \right)\end{aligned}\quad 4.4.107$$

Now if we choose $\Delta\phi = \Delta\phi$, then we obtain

$$\Phi_{si}' = \tan^{-1} \left(\frac{\sin \theta_s (\sin \phi \cos \Delta\phi + \cos \phi \sin \Delta\phi) + \sin \theta_b (\sin \phi \cos \Delta\phi + \cos \phi \sin \Delta\phi)}{\sin \theta_s (\cos \phi \cos \Delta\phi - \sin \phi \sin \Delta\phi) + \sin \theta_b (\cos \phi \cos \Delta\phi - \sin \phi \sin \Delta\phi)} \right)\quad 4.4.108$$

Collecting coefficients of $\cos \Delta\phi$ and $\sin \Delta\phi$, we have

$$\Phi_{si}' = \tan^{-1} \left(\frac{\cos \Delta\phi (\sin \theta_s \sin \phi + \sin \theta_b \sin \phi) + \sin \Delta\phi (\sin \theta_s \cos \phi + \sin \theta_b \cos \phi)}{\cos \Delta\phi (\sin \theta_s \cos \phi + \sin \theta_b \cos \phi) - \sin \Delta\phi (\sin \theta_s \sin \phi + \sin \theta_b \sin \phi)} \right)\quad 4.4.109$$

or

$$\Phi_{si}' = \tan^{-1} \left(\frac{(\cos \Delta\phi) d_y + (\sin \Delta\phi) d_x}{(\cos \Delta\phi) d_x - (\sin \Delta\phi) d_y} \right)\quad 4.4.110$$

Now defining

$$\begin{aligned}d_x &= (\cos \Delta\phi) d_x - (\sin \Delta\phi) d_y, \\ d_y &= (\sin \Delta\phi) d_x + (\cos \Delta\phi) d_y,\end{aligned}\quad 4.4.111$$

we have

$$\Phi_{si}' = \tan^{-1} \left(\frac{d_y}{d_x} \right)\quad 4.4.112$$

where

$$\begin{pmatrix} d_x \\ d_y \end{pmatrix} = \begin{pmatrix} \cos \Delta\phi & -\sin \Delta\phi \\ \sin \Delta\phi & \cos \Delta\phi \end{pmatrix} \begin{pmatrix} d_x \\ d_y \end{pmatrix}\quad 4.4.113$$

But this is just a counter clockwise rotation of $(d_x, d_y)^T$ by $\Delta\phi$, and so

$$\Phi_{si}' = \Phi_{si} + \Delta\phi, \quad 4.4.114$$

or

$$\Phi_{si}(\theta_o, \phi + \Delta\phi, \phi_s + \Delta\phi, \theta_s) = \Phi_{si}(\theta_o, \phi, \phi_s, \theta_s) + \Delta\phi, \quad 4.4.115$$

or

$$\Phi_{si}(\theta_o, \phi, \phi_s, \theta_s) = \Phi_{si}(\theta_o, \phi - \Delta\phi, \phi_s - \Delta\phi, \theta_s) + \Delta\phi. \quad 4.4.116$$

In words, this equation states that the Φ_{si} function at $(\theta_o, \phi, \phi_s, \theta_s)$ is identical to the same function Φ_{si} evaluated at $(\theta_o, \phi - \Delta\phi, \phi_s - \Delta\phi, \theta_s)$, except that it will be everywhere shifted in value by $+\Delta\phi$. If we let $\Delta\phi = \phi$, then

$$\Phi_{si}(\theta_o, \phi, \phi_s, \theta_s) = \Phi_{si}(\theta_o, \phi - \phi, 0, \theta_s) + \phi, \quad 4.4.117$$

so that $\Phi_{si}(\theta_o, \phi, \phi_s, \theta_s)$ may be obtained from Φ_{si} evaluated at zero ϕ merely by evaluating Φ_{si} at $\phi - \phi$.

Now let us define a reference Φ_{si}^0 , say

$$\Phi_{si}^0(\theta_o, \phi, \theta_s) = \Phi_{si}(\theta_o, \phi, 0, \theta_s), \quad 4.4.118$$

which is Φ_{si} evaluated at zero radiometer azimuth. Then from the ϕ translation property of Φ_{si} we have just established,

$$\Phi_{si}(\theta_o, \phi, \phi_s, \theta_s) = \Phi_{si}(\theta_o, \phi - \phi, 0, \theta_s) + \phi = \Phi_{si}^0(\theta_o, \phi - \phi, \theta_s) + \phi. \quad 4.4.119$$

Recalling that the joint dependence of the second harmonic on Φ_{si} and ϕ_w is of the form $\cos 2(\Phi_{si} - \phi_w)$, we have

$$\Phi_{si} - \varphi_w = \Phi_{si} - \phi - (\varphi_w - \phi), \quad 4.4.120$$

but since $\Phi_{si} - \phi = \Phi_{si}^0$, we have

$$\Phi_{si} - \varphi_w = \Phi_{si}^0 - (\varphi_w - \phi). \quad 4.4.121$$

APPENDIX D Multi-dimensional Hermite Interpolation

Denote four successive grid points in one dimension by (x_0, x_1, x_2, x_3) , and consider the problem of interpolating some discrete function F_i , whose values are given at these grid points by (F_0, F_1, F_2, F_3) , on the interval $[x_1, x_2]$. We wish this interpolating function to be continuous and to have continuous first derivatives on this interval. Noting that a cubic polynomial provides the freedom to enforce these constraints, we choose our interpolating function to be a cubic polynomial, and we determine coefficients for this polynomial to satisfy our constraints. Let

$$s = \frac{x - x_1}{x_2 - x_1}, \quad 4.4.122$$

and define the interpolating function on the interval $[x_1, x_2]$ by

$$p(s) = c_1 s^3 + c_2 s^2 + c_3 s + c_4. \quad 4.4.123$$

We wish this cubic interpolating polynomial $p(s)$ to pass through x_1 and x_2 , so we must have

$$\begin{aligned} p(s=0) &= c_4 = F_1, \\ p(s=1) &= c_1 + c_2 + c_3 + c_4 = F_2. \end{aligned} \quad 4.4.124$$

Additionally, we want the first derivatives of $p(s)$ to be constrained such that they are identical to the first derivatives of the corresponding $p(s)$ functions on the neighbouring intervals. One way to accomplish this is to use centered differences to define the derivatives at x_1 and x_2 noting that

$$p_s = p_{xx} s = (x_2 - x_1) p_x. \quad 4.4.125$$

we see that

$$\begin{aligned} p(s=0) &= c_3 = \alpha(F_1 - F_0), \\ p(s=1) &= 3c_1 + 2c_2 + c_3 = \beta(F_3 - F_1), \end{aligned} \quad \mathbf{4.4.126}$$

where

$$\begin{aligned} \alpha &= \frac{x_2 - x_1}{x_2 - x_0}, \\ \beta &= \frac{x_2 - x_1}{x_3 - x_1}. \end{aligned} \quad \mathbf{4.4.127}$$

Arranging the preceding four constraints into a matrix equation, we have

$$M_1 F_i = M_2 c_i, \quad \mathbf{4.4.128}$$

where $F_i = (F_0, F_1, F_2, F_3)^T$ and $c_i = (c_1, c_2, c_3, c_4)^T$, and

$$M_1 = \begin{pmatrix} 0 & 1 & 0 & 0 \\ 0 & 0 & 1 & 0 \\ -a & 0 & a & 0 \\ 0 & -b & 0 & b \end{pmatrix} \quad \mathbf{4.4.129}$$

and

$$M_2 = \begin{pmatrix} 0 & 0 & 0 & 1 \\ 1 & 1 & 1 & 1 \\ 0 & 0 & 1 & 0 \\ 3 & 2 & 1 & 0 \end{pmatrix}. \quad \mathbf{4.4.130}$$

Now we can write the interpolating polynomial as

$$p(s) = (s^3, s^2, s, 1) \begin{pmatrix} c_1 \\ c_2 \\ c_3 \\ c_4 \end{pmatrix} \quad \mathbf{4.4.131}$$

But since

$$c_i = M_2^{-1} M_1 F_i, \quad \mathbf{4.4.132}$$

we have

$$p(s) = (s^3, s^2, s, 1)M_2^{-1}M_1F_i, \quad \mathbf{4.4.133}$$

or

$$p(s) = \begin{pmatrix} -\alpha s^3 + 2\alpha s^2 - \alpha s \\ (2 - \beta)s^3 + (\beta - 3)s^2 + 1 \\ (\alpha - 2)s^3 + (3 - 2\alpha)s^2 + \alpha s \\ \beta(s^3 - s^2) \end{pmatrix}^T \begin{pmatrix} F_0 \\ F_1 \\ F_2 \\ F_3 \end{pmatrix} \quad \mathbf{4.4.134}$$

Note that the weights are independent of the data F_i and depend only on the desired interpolation location s and the location of grid points x_i on which the discrete function is defined.

To interpolate in more than one dimension we simply apply the above formula along each dimension separately and then multiply the appropriate weights along each dimension to obtain the weights for a given point at which F is defined. The number of points in the interpolation stencil is 4^n , where n is the number of dimensions of the function F .



4.5 Sun glint contamination

4.5.1 Theoretical description

4.5.1.1 Physics of the problem

Beyond geophysical sources of error, Yueh et al. [1] noticed that solar radiation poses a significant challenge for the remote sensing of ocean surface salinity. The sun is indeed an extremely strong radiation source at L-band, exhibiting a time-dependent blackbody temperature that ranges between 100000 K and 10 million K, depending on the solar activity [2], with the most recent solar maximum was in 2018.

Two distinct mechanisms may contribute to the solar radiation intercepted by a radiometer antenna: one is the reflection of solar radiation by the earth-surface (sun glitter or sun glint effects) and the other is the direct leakage into the antenna. Here, we only focus on the modelling for the reflected contamination over the ocean, direct contaminations being addressed by the Level 1 processor.

In [3a, 3b], it was shown that the centre of the sun's glitter pattern will never be in SMOS synthesized field of view. However, the expected range of surface winds speeds (zero wind is very uncommon) will cause the sun's glitter pattern to spread within the alias free field of view which might contaminate the useful measured signals. More specifically, frequent pixel contaminations are expected around winter solstices when the centre of the sun's glitter pattern will lie close to the right-hand border of the FOV.

Experimental evidences of the strong sun glitter impacts on the passive microwave sensing of the ocean using L-band radiometers was first given by Swift [4] in 1974, who analysed the forward scattering of sun microwave radiation from the Cape Code Canal in Massachusetts. Data were collected at 1.4, 4.0, and 7.5 GHz for horizontal and vertical polarisation at a fixed nadir viewing angle of 40°. As the sun passed through the main beam of the antennas, Swift found that the excess temperature due to reflected solar radiation increased dramatically with decreasing frequency and was polarization dependent. The sun was found to be such a dominating source at 1.4 GHz that the horizontally polarized component saturated the radiometer.

As shown by Wentz [5], these sun-glitter effects might be modelled using approximate scattering models to compute the forward scattering of the sun radiations from the rough water surface. Sun glitter does not occur frequently in practice. However, when it does, this phenomenon may have severe effects on the brightness temperature signals measured by spaceborne L- band radiometers.

If an incremental rough sea surface area dA located within the MIRAS antenna field of view is illuminated by the sun radiation along the direction of the unit vector \bar{n}_i , part of the intercepted energy might be scattered in the direction \bar{n}_s , i.e., toward the radiometer antenna. The solar energy scattered by dA in the direction \bar{n}_s at time t is represented by the radiometric temperatures $T_{ss}(\bar{n}_s, t)$, given for h and v-polarisation respectively by:

$$T_{ss}(\bar{n}_s, h, t) = \frac{1}{4\pi \cos \theta_s} \int_0^{2\pi \beta_{sun}/2} \int_0^{2\pi \beta_{sun}/2} [\sigma_{hh}^0(\bar{n}_s, \bar{n}_i) + \sigma_{hv}^0(\bar{n}_s, \bar{n}_i)] T_{sun}(\bar{n}_i, t) d\Omega_i$$

$$T_{ss}(\bar{n}_s, v, t) = \frac{1}{4\pi \cos \theta_s} \int_0^{2\pi \beta_{sun}/2} \int_0^{2\pi \beta_{sun}/2} [\sigma_{vv}^0(\bar{n}_s, \bar{n}_i) + \sigma_{vh}^0(\bar{n}_s, \bar{n}_i)] T_{sun}(\bar{n}_i, t) d\Omega_i$$

4.5.1

where $\sigma_{hh}^0, \sigma_{vv}^0, \sigma_{vh}^0$ and σ_{hv}^0 are the bistatic scattering coefficients of the sea surface at 1.4 GHz for HH, VV, VH and HV polarizations, respectively, at scattered direction \bar{n}_s and incident direction \bar{n}_i . The scattering elevation angle is denoted θ_s . The integration limits are over the solid angle subtended by the sun where $\beta_{sun}/2$ is the angular radius of the sun as viewed from the earth. At 1.4 GHz, $\beta/2 \approx 0.293^\circ$, which is 10% greater than the optical angular radius [6]. $T_{sun}(\bar{n}_i, t)$ is the brightness temperature of the sun at 1.4 GHz in the direction \bar{n}_i , and at time t .

Equations Erreur ! Source du renvoi introuvable. show that in order to estimate the contamination due to sun glint temperature at a given SMOS pixel with node corresponding to position T on the earth surface, determined by the latitude ϕ and longitude ψ of the observer, and at a given time t , the following parameters are needed :

- 1) \bar{n}_s : the direction (incidence and azimuth angles) of sun radiations at the considered earth surface position and time $T = (\phi, \psi, t)$,
- 2) \bar{n}_i : the direction (incidence and azimuth angles) of observation from MIRAS at target $T=(\phi, \psi, t)$
- 3) $T_{sun}(\bar{n}_i, t)$: the brightness temperature of the sun at 1.4 GHz in the direction \bar{n}_i and at time t , and,
- 4) $\sigma_{hh}^0, \sigma_{vv}^0, \sigma_{vh}^0$ and σ_{hv}^0 : the bistatic scattering coefficients of the sea surface for HH, VV, VH and HV polarizations, respectively, at scattered direction \bar{n}_s , incident direction \bar{n}_i , and corresponding to the sea state conditions at target $T = (\phi, \psi, t)$.

Parameters 1) can be obtained from accurate ephemerides and parameters 2) are easily deduced from SMOS observation geometry. The main difficulties in estimating $T_{ss}(\bar{n}_s, t)$ therefore consist in providing accurate estimates for the brightness temperature of the sun

at 1.4 GHz and for the sea surface bistatic coefficients at L-band. The brightness temperature of the sun at 1.4 GHz being considered here as an auxiliary parameter, we only focussed on the physical description of the bistatic coefficients model.

In the present algorithm, the bistatic scattering coefficients of the rough sea surface needed in Equations 3.6.1 are estimated using the Small Slope Approximation theory ([7], [8]), which is known to work well from moderate to high incidence angles ($40^\circ \leq \theta_i \leq 80^\circ$). The lower order-approximation (referred to as the SSA-1) is used here and is appropriate for both large- (the Kirchhoff regime) and small scale (the Bragg regime) roughness within a single theoretical scheme.

The calculation yields the following expression for a dimensionless scattering cross section $\sigma_{\alpha\alpha_0}$ for scattering of the wave of polarization α into the wave of polarisation α_0 :

$$\sigma_{\alpha\alpha_0}(\bar{n}_s, \bar{n}_i) = \frac{1}{\pi} \left| \frac{2q_k q_i}{q_k + q_i} B_{\alpha\alpha_0}(\bar{n}_s, \bar{n}_i) \right|^2 e^{-(q_k+q_i)^2 \rho(0)} \times \iint \{e^{(q_k+q_i)^2 \rho(\bar{r})} - 1\} e^{-i(\bar{n}_s - \bar{n}_i) \cdot \bar{r}} d\bar{r} \quad 4.5.2$$

where (q_k, q_i) represent the vertical projections of the wave vectors and the kernel functions $B_{\alpha\alpha_0}(\bar{n}_s, \bar{n}_i)$ are given in the Appendix of [9]. These kernels are geometric functions of the dielectric constant: we used the Klein and Swift's model [10] to estimate the dielectric constant of sea water at L-band.

Here, the function $\rho(\bar{r})$ is defined by the relation:

$$\langle \exp[iQ(h(\bar{r}_1) - h(\bar{r}_2))] \rangle = \exp[-Q(\rho(0) - \rho(\bar{r}_1 - \bar{r}_2))] \quad 4.5.3$$

where $\langle \dots \rangle$ means averaging over the space homogeneous statistical ensemble of sea surface roughness, described by the surface elevation signal $h(\bar{r}_1)$, and. $Q = q_k + q_i$. For Gaussian statistics ρ represents the correlation function of roughness and can be expressed strictly in terms of a roughness spectrum:

$$\rho(\bar{r}) = \int_0^{2\pi} \int_0^\infty W(\bar{k}) \exp[i\bar{k} \cdot \bar{r}] d\bar{k} \quad 4.5.4$$

where $W(\bar{k})$ is the directional wavenumber spectrum of the rough sea surface at surface wavenumber vector \bar{k} .

In the present work, sea surface statistics are assumed Gaussian and ρ is obtained from the sea surface spectrum model of Kudryavtsev al. [11]. In our approach, the calculation of $\sigma_{\alpha\alpha_0}$ is performed using an azimuthal harmonic decomposition for the autocorrelation function. Moreover, to calculate accurately the autocorrelation function, we introduced a sufficiently dense net on the surface wavenumber vector plane within the range $10^{-3} \leq k \leq 10^3 \text{ radm}^{-1}$, applying a uniform step with respect to $\log(k)$ rather than to k .

4.5.2 Mathematical description

4.5.2.1 Simplified scattered solar radiation contributions

An additional model simplification is used to estimate the amount of solar energy scattered by the sea surface and impinging the MIRAS antenna. We assumed that within the solid angle subtended by the sun as seen from any of the observed terrestrial targets, the local sun direction \bar{n}_i is almost constant, so that, at any target T , the radiometric sun glint temperatures $T_{ss}(\bar{n}_s, \alpha)$ of a sunglint Stokes vector component, can be approximated locally at polarisation α , by:

$$T_{ss}(\bar{n}_s, t, \alpha) \approx \frac{T_{Sun}(t)\Omega_{Sun}}{4\pi\cos\theta_s} [\sigma_{\alpha\alpha}^0(\bar{n}_s, \bar{n}_i) + \sigma_{\alpha\alpha_0}^0(\bar{n}_s, \bar{n}_i)] \quad 4.5.5$$

Where \bar{n}_s and \bar{n}_i are the local MIRAS observation and sun illumination directions at target T , respectively. Ω_{Sun} is the solid angle intercepting the sun as seen from the earth, and with $\frac{\beta_{Sun}}{2} \approx 0.293^\circ$ at 1.4 GHz:

$$\Omega_{Sun} = 2\pi \left[1 - \cos\left(\frac{\beta_{Sun}}{2}\right) \right] = 8.2 \times 10^{-5} \text{sr} \quad 4.5.6$$

To evaluate $T_{ss}(\bar{n}_s, \alpha)$ using equation (Erreur ! Source du renvoi introuvable.) at a given earth position and time, one needs the following parameters as inputs:

- 1) $[\theta_i, \phi_i]$ the local sun angles (incidence and azimuth angles) at the considered earth surface position and time, given by $T = (\phi, \psi, t)$.
- 2) $[\theta_s, \phi_s]$ the local observation angles (incidence and azimuth angles) from MIRAS antenna at target $T = (\phi, \psi, t)$.
- 3) $T_{Sun}(t)$: the brightness temperature of the sun at 1.4 GHz and at time t ,
- 4) The following ocean surface parameters at target $T = (\phi, \psi, t)$:

a) the prior sea surface salinity SSS [psu],

- b) the sea surface temperature SST [°C],
- c) the wind speed velocity at 10-meter height u_{10} ms^{-1} , and,
- d) the wind direction ϕ_w [in rad].

Assuming that the main factors influencing the spread and intensity of the sun glint pattern will be the sun brightness temperature, the wind velocity and direction, we assume for the processor algorithm constant values for $SSS=35$ psu and for $SST=15^\circ\text{C}$.

4.5.2.2 Efficient Implementation of Bistatic scattering coefficients at L-band

Bistatic scattering coefficients are functions of 6 variables:

- Incoming radiation incidence angle θ_i
- Incoming radiation azimuth angle ϕ_i
- Outgoing azimuth angle ϕ_s
- Outgoing incidence angle θ_s
- wind speed u_{10}
- wind direction ϕ_w (towards which the wind is blowing)

In the Level 2 processor, bistatic scattering coefficients are calculated based on Look-Up Tables (LUT). From LUT size and generation perspectives, it is impractical produce a LUT directly as a function of the six previously listed variables. Therefore, we make use of an efficient implementation of the lookup table for bistatic scattering coefficients in which we have separated the dependency on wind direction from the dependencies on other variables, without introducing further approximations. As detailed in [13], the 2-fold integration (Erreur ! Source du renvoi introuvable.) can indeed be reduced to a 1D integral using a zimuthal harmonics decomposition of the integrand in polar coordinates. Using harmonic decompositions of the bistatic scattering coefficients, we can write

$$\sigma_{\alpha\alpha_0}(\bar{n}_s, \bar{n}_i, u_{10}, \phi_w) = \sum_{m=0}^{\infty} \sigma_{\alpha\alpha_0}^m(\bar{n}_s, \bar{n}_i) \cos^2 m(\Phi_{si} - \phi_w) \quad 4.5.7$$

where we have explicitly included the dependence of the final scattering coefficients on the wind speed u_{10} and wind direction ϕ_w and where the scattering coefficient harmonics $\sigma_{\alpha\alpha_0}^m(\theta_i, \phi_s - \phi_i, \theta_s, u_{10})$ are independent of wind direction. Moreover, these harmonics only depend on the incoming and scattered radiation incidence angles, the wind speed, and difference between the incoming and scattered radiation azimuth angles. The angle Φ_{si} is the angle of the difference between the scattered and incident wavevectors, and can be written as

$$\Phi_{si}(\theta_i, \phi, \phi_s, \theta_s) = \tan^{-1} \left(\frac{q_{Hy}}{q_{Hx}} \right) = \tan^{-1} \left(\frac{\sin \theta_s \sin \phi_s + \sin \theta_i \sin \phi_i}{\sin \theta_s \cos \phi_s + \sin \theta_i \cos \phi_i} \right). \quad 4.5.8$$

Thus, switching from vector notation to angles, we can write the scattering coefficients as

$$\sigma_{\alpha\alpha_0}(\theta_i, \phi_i, \phi_s, \theta_s, u_{10}, \phi_w) = \sum_{m=0}^{\infty} \sigma_{\alpha\alpha_0}^m(\theta_i, \phi_s - \phi_i, \theta_s, u_{10}) \cos^2 m(\Phi_{si} - \phi_w) \quad 4.5.9$$

For processing issues, we provide a four dimension lookup table for the harmonic coefficients $\sigma_{\alpha\alpha_0}^m(\theta_i, \phi_s - \phi_i, \theta_s, u_{10})$ for even azimuthal wavenumbers $m = 0$ through 10 on a discrete grid.

An interpolation method is then needed to infer the bistatic scattering coefficients harmonics from the LUT. It is found that linear interpolation introduces artefacts in all dimensions, but especially in incidence angle dimensions whereas a cubic Hermite interpolation method removes these problems. The basic idea behind the method is to ensure continuity of the first derivative of the interpolating function. To accomplish this, a four point stencil along each dimension surrounding the interpolation point is required, so in four dimensions we obtain a 256 point stencil, but the nature of the method is such that one can compute the coefficients once for all harmonics and reuse the weights, saving a large amount of processing time.

To implement the method, we apply the interpolation scheme separately along each of the four LUT dimensions and then combine all of the weights into a set of 256 weights. In each dimension, we consider the four nearest points (i.e., the stencil) surrounding the point at which we desire a value, say x . We assume that these points can be written as x_{k-1}, x_k, x_{k+1} , and x_{k+2} , where x is between x_k and x_{k+1} . Next, we assume that our interpolating function is a cubic of the form,

$$p(\mu) = a + b + c\mu_2 + d\mu_3, \quad 4.5.10$$

where

$$\mu = \frac{x - x_k}{x_{k+1} - x_k} \quad 4.5.11$$

and the coefficients depend upon the discrete function values at lookup table grid points. In the actual implementation, for a given interpolation location, a weight for each the four stencil points is computed based on the value of μ , which ranges from 0 to 1. If we define

$$\begin{aligned} a_0 &= 2\mu^3 - 3\mu^2 + 1 \\ a_1 &= \mu^3 - 2\mu + \mu \\ a_2 &= \mu^3 - \mu^2 \\ a_3 &= 2\mu^3 + 3\mu^2 \end{aligned} \quad 4.5.12$$

then the weights for the four surrounding points are

$$\begin{aligned}
 w_{k-1} &= -\frac{1}{2}a_1 \\
 w_k &= a_0 - \frac{1}{2}a_2 \\
 w_{k+1} &= a_3 + \frac{1}{2}a_1 \\
 w_{k+2} &= \frac{1}{2}a_2
 \end{aligned}
 \tag{4.5.13}$$

and the final expression for the interpolated value at point x is

$$p(x) = \sum_{j=k-1}^{k+2} w_j y_j
 \tag{4.5.14}$$

where y_j are values from the lookup table along the given dimension.

Near boundaries, where the stencil exceeds the boundary of the lookup table, zero normal gradient extrapolation is applied along each of the four LUT dimensions, so that it is assumed that lookup table values extend beyond the table boundaries with the values at the boundaries.

As a final step, one need to implement the sum over the harmonics, given specific values for the incoming and scattered azimuths and wind direction. As it has been found that only the first few harmonics contribute significantly to the scattering coefficients, the sum is over only the first six even harmonics (including wavenumber 0), so that the processor computes

$$\sigma_{\alpha\alpha_0}(\theta_0, \phi_0, \phi_s, \theta_s, u_{10}, \phi_w) = \sum_{m=0}^{\infty} \sigma_{\alpha\alpha_0}^m(\theta_0, \phi_s - \phi_0, \theta_s, u_{10}) \cos^2 m(\Phi_{si} - \phi_w)
 \tag{4.5.15}$$

4.5.3 Error budget estimates

Main sources of errors in the estimation of $T_{ss}(\bar{n}_s, \alpha)$ using Erreur ! Source du renvoi introuvable. will be

- Errors on the estimation of the bistatic scattering coefficients of the sea surface at L-band, and
- Errors on the estimation of the sun brightness temperature at 1.4 GHz the SMOS time of acquisition.



An estimate of the errors on the modelling of the bistatic scattering coefficients of the sea surface at L-band can be based on the errors on the asymptotic electromagnetic, namely the SSA-1 approximation. SSA-1 gives qualitatively correct 3D bistatic scattering coefficient when compared to exact numerical simulation using the Method of Moment with a general agreement between SSA-1 and MoM within 3dB in VV and within 1.5 dB in HH polarizations [12]. In average, SSA-1 overestimates HH and underestimates VV so that SSA-1 systematically overestimates the H/V ratio with a mean of order +20%. The errors on the sea surface roughness statistics are difficult to estimate but will clearly have an important impact as well.

A complete error budget estimate cannot be provided without any estimate of the error on the auxiliary sun brightness temperature data at 1.4 GHz. If it comes out of the L1 processor, we need an error budget on the estimate of that parameter from L1.

4.5.4 Practical considerations

4.5.4.1 Calibration and validation

Dedicated CAL/VAL activities should be envisaged for the SMOS sun glint model with two main components:

- an earth-based campaign aiming at measuring precisely the sun glint scattering at L-band (e.g., experiment similar to [4]), with high-quality concomitant auxiliary solar fluxes measurements at 21 cm as well as surface roughness information to calibrate and validate the bistatic-scattering coefficient models.
- a SMOS-data based analysis. Re-analysis of all flagged pixels and brightness for which good quality (close in time and space) co-localized auxiliary wind and solar flux data at 21 cm are available shall be performed to assess the efficiency of the model.

4.5.4.2 Quality control and diagnostics

Assuming the major source of error in the model shall be the estimation of the sun brightness temperature at 1.4 GHz, quality control and diagnostics will strongly depend on the accuracy for that auxiliary data.

If it comes out of L1 processor (without a priori geophysical input), a complementary quality check shall be performed for that auxiliary data using earth-based solar flux measurements available at 1.4 GHz. These are available from sun-tracker radiometers by the US Air Force, at Sagamore Hill (Massachusetts), since 1966. They can be obtained through the National Geophysical Data Center at Boulder, Colorado. These data sets also include other solar fluxes measurements conducted at 1415 MHz since 1988 from radiometers in Palehua (Hawaii), San Vito (Italy) and Learmonth (Australia), and 1GHz data are also collected daily at Nobeyama Radio Observatory (Japan). If high temporal resolution solar fluxes can be obtained, the closest data in time from SMOS acquisitions shall be used to monitor quality controls, as sun brightness temperature values might evolve very significantly over short time scales. The so-

ARGANS Ltd.



called R-components of the sun brightness temperature indeed consist of the second and minute-duration bursts produced by the active sun components: sunspots (manifestations of magnetically disturbed conditions at the sun's visible surface), flares (huge explosions on the surface of the sun) and other transient activity. This high-temporal variability of the sun signals might strongly affect the quality of the forward model estimates.

4.5.4.3 Exception handling

If there is no estimation of the sun brightness temperature at 1.4 GHz output from L1 processor (e.g., sun eclipsed by MIRAS), there is a need for other source of that auxiliary data.

If some parameter goes out of LUT range during the retrieval, a flag

Fg_OoR_Sunlint_dim2_ThetaSun,
Fg_OoR_Sunlint_dim3_Phi,
Fg_OoR_Sunlint_dim4_Theta, Fg_OoR_Sunlint_dim52_WS)

is raised. No extrapolation is done, and the boundary value is taken.

4.5.5 Assumption and limitations

First assumption in the model is that within the solid angle subtended by the sun as seen from any of the observed terrestrial targets, the local sun direction \bar{n}_i is almost constant. This is not a strong assumption. However, it is as well assumed that the sun brightness temperature at 1.4 GHz is not polarized and homogeneous within the solar disc. This is known to be unrealistic [2] and certainly will limit somehow the applicability of the predicted sun glint pattern polarized features.

Another source of limitation is the bistatic coefficient modelling. The SSA-1 approximation is by essence a first-order small slope perturbation approach so that it is not expected to correctly estimate the roughness impact for sea surfaces exhibiting large slopes and most importantly, large curvature. Therefore, it is expected to fail in strong frontal conditions (strong wave-wave, wave-current or wind-wave interaction conditions) and does not account for breaking wave and foam impacts. Moreover, the sea surface state model (i.e. Kudryavtsev et al) is only accounting for wind seas and should be valid only for wind seas generated by winds stronger than about 2 ms^{-1} and less than 15 ms^{-1} . Out of these limits, it is not expected that the physics of air-sea interaction is correctly accounted for.

Therefore, we do not expect the model to perform well in presence of either strong swells, strong currents, very small and unsteady winds as well as stormy conditions. We expect however that accounting for the impact of waves on the drag coefficients will help better characterizing the impact of these parameters on roughness.

References

ARGANS Ltd.

Commercial in Confidence



- [1] S. H. Yueh, R. West, W. J. Wilson, F. K. Li, E. G. Njoku, and Y. Rahmat-Samii, Error sources and feasibility for microwave remote sensing of ocean surface salinity, *IEEE Trans. Geosci. and Remote Sens.*, vol. 39, no. 5, pp. 1049-1060, 2001.
- [2] G. A. Duck and D. E. Gary, The sun at 1.4 GHz, *Astron. Astrophys.*, vol. 124, pp. 103-107, 1983.
- [3a] N. Reul, WP1500: support for solar effects in "Retrieval Concept and Architecture Document for Sea Surface Salinity Retrieval for SMOS mission", ref. SMOS-TN-ACR-LOD-001, Issue 1, Revision 2, Dated 17/08/2004. Appendix A (contract CCN-2 of 16027/02/NL/GS)
- [3b] B. Picard, N. Reul, P. Waldeufel, and E. Anterrieu, "Impacts of Solar Radiations on sea surface salinity remote sensing from Synthetic Aperture Imaging Radiometers", Proceedings of IGARRS 2004.
- [4] C. T. Swift, Microwave radiometer measurements of the Cape Cod Cannal, *Radio Sci.*, vol. 9, no. 7, pp. 641-653, 1976.
- [5] F. Wentz, The forward scattering of microwave solar radiation from a water surface, *Radio Sci.*, vol. 13, no. 1, pp. 131-138, 1978.
- [6] J. Aarons, *Solar System Radio Astronomy*. Plenum, 1965.
- [7] A. G. Voronovich, Small-slope approximation in wave scattering by rough surfaces, *Sov. Phys.-JETP*, vol. 62, pp. 65-70, 1985.
- [8] A. G. Voronovich, Small-slope approximation for electromagnetic wave scattering at a rough interface of two dielectric half-spaces, *Waves in Random Media*, vol. 4, pp. 337-367, 1994.
- [9] A. G. Voronovich and V. U. Zavorotny, Theoretical model for scattering of radar signals in ku and c-bands from a rough sea surface with breaking waves, *Waves in Random Media*, vol. 11, pp. 247-269, 2001.
- [10] Klein L.A., and C.T. Swift, An improved model for the dielectric constant of seawater at microwave frequencies, *IEEE Trans. Antennas and Propag.*, AP-25, 1043-111, 1977.
- [11] Kudryavtsev V.N., Makin V.K. and Chapron B., Coupled sea surface-atmosphere model. 2. Spectrum of short wind waves, *J. Geophys. Res*, C4, 7625-7639, 1999.
- [12] N Reul, CA Guerin, G. Soriano, E. Bachelier, P. Borderies, F. Mattia, C. Ruiz and N. Floury, "On the Use of Rigorous Microwave Interaction Models to Support Remote Sensing of Natural Surfaces" , ESA contract 17335/03/NL/AG, 2005.
- [13] N. Reul, J. Tenerelli, B. Chapron and P. Waldteufel, « Modelling Sun glitter at L-band for the Sea Surface Salinity remote sensing with SMOS", submitted to IEEE TGRS, 2006.

4.6 Faraday rotation computation from geomagnetic field

4.6.1 Theoretical description

4.6.1.1 Physics of the problem

The Faraday rotation is caused by the effect of ionospheric electrons on the propagation of electromagnetic waves.

4.6.2 Mathematical description of algorithm

The Faraday angle ω for each view is provided by L1c data (field #09 or #10 in tables 26 or 27 of SO-IS-DME-L1PP-0002, depending on polarization mode), using auxiliary *TEC* (Total Electron nadir columnar Content) values. Therefore, the description below needs only to be implemented when introduced in the direct model, in the case where *TEC* is retrieved.

Making use of the magneto-ionic theory and using the quasi longitudinal approximation as well as assuming a plane parallel ionosphere result in the following expression for L-band ((Le Vine and Abraham 2002; Waldteufel, Flourey et al. 2004)):

$$\omega \approx 6950 \times TEC \times (\mathbf{B} \cdot \mathbf{U}_{LS}) / \cos \theta_g \quad 4.6.1$$

where:

- *TEC* is the total **vertical** electron content (*TEC* units; 1 *TEC* unit = 10^{16} m⁻²); it is obtained from L1c field #15 for each view. The range of *TEC* is about 5 to 50 tecu.

If the *TEC* is retrieved, then a unique value for the DGG node is defined as initial value by selecting the median of the values for every view. Otherwise, every individual *TEC* value can be selected for computing ω .

- $(\mathbf{B} \cdot \mathbf{U}_{LS})$ is the scalar product of the magnetic field vector \mathbf{B} by the unitary vector \mathbf{U}_{LS} giving the direction of the line of sight (from target to spacecraft).
- The magnitude $|\mathbf{B}|$ of \mathbf{B} (teslas) is obtained from L1c field #16 (expressed in nanotesla). The range of $|\mathbf{B}|$ is about 2 to 5 10^{-5} Tesla.

The vectors \mathbf{B} and \mathbf{U}_{LS} must be expressed in the same Euclidian reference frame.

- Concerning \mathbf{B} : The L1c provides (fields #17 and #18) the declination dec_B and inclination inc_B of \mathbf{B} in a local geographical frame O_{xyz} (O_x towards East, O_y toward North, O_z upwards)

In L1c data, dec_B is understood as the angle of **B** away from geographic North O_y , counted positive eastwards (clockwise); inc_B is understood as the angle of **B** away from the local horizontal plane Oxy , counted positive downwards.

Every individual $|B|$, dec_B and inc_B value can be selected for computing ω .

- Concerning \mathbf{U}_{LS} : let us define polar geographical coordinates θ_g (elevation away from the O_z axis) and φ_n (azimuth from origin O_x , counter clockwise).

Then :

$$\begin{aligned} \mathbf{B} &= [\cos(\text{inc_B}) \sin(\text{dec_B}), \cos(\text{inc_B}) \cos(\text{dec_B}), -\sin(\text{inc_B})] \\ \mathbf{U}_{LS} &= [\sin(\theta_g) \cos(\theta_n), \sin(\theta_g) \sin(\theta_n), \cos(\theta_g)]. \end{aligned} \quad 4.6.2$$

(Note that φ_n differs from the relative azimuth defined in a frame linked to the spacecraft and introduced in the SMOS).

It is expected that the EE CFI may provide directly φ_n and θ_g . Alternatively, θ_g could be inferred from the incidence angle (provided by the L1c) through adding the Earth centre angle; φ_n could be computed from the DGG node coordinates, assuming the coordinates of the subsatellite point are provided by the EE CFI.

The ω Faraday angle value is positive clockwise.

4.6.3 Assumptions and limitations

A single average magnetic field vector is used rather than altitude dependent values when carrying out an integration over the line of sight. The optimal value corresponds to altitudes which may vary between 350 and 400 km, depending on the ionospheric altitude profile. Considering the variation of B with altitude, resulting errors are not significant.

The TEC value is assumed constant over the area (up to about a 500 km size at ionospheric altitudes) concerned by a SMOS dwell line. This assumption may not be fully satisfactory in regions of strong ionospheric gradients.

It is useful to add an output flag (Fg_sc_TEC_gradient) in the User Data Product to warn against strong variations of the measured TEC over a dwell line. Every snapshot coming from L1 will carry its TEC value, but only a value (median from all snapshots) is used in the L2 computations at grid point level. When the difference between the maximum and minimum TEC values affecting a given DGG node is above a threshold (Tg_TEC_gradient) the flag will be raised. It is necessary to check if TEC data have the spatial resolution adequate for feeding such a flag.



References

DEIMOS Engenharia (2005) SMOS L1 Product Format Specification, SO-IS-DME-L1PP-0002
issue 1.4, 30 August 2005

4.7 Atmospheric effects

4.7.1 Theoretical description

This section of the ATBD takes advantage of the analysis reported in an ESA study [1: Peichl et al, 2004].

4.7.1.1 Physics of the problem:

4.7.1.1.1 The radiative transfer equation

This section assumes a bare surface and ignore the sky contribution as well as ionospheric effects. The geometrical rotation from the surface to the SMOS antenna is not considered either.

Several components of the atmosphere are radiatively active and generate effects which need to be accounted for in the **radiative transfer equation** (RTE).

In the absence of atmosphere, the measured brightness temperature Tb_m is simply the upwelling brightness temperature from the surface, Tb_s as follows,

$$Tb_m = Tb_s = SST \times \epsilon \quad 4.7.1$$

where SST is the sea surface temperature and ϵ is the sea surface emissivity.

Introducing the atmosphere, the RTE is written,

$$Tb_m = Tb_s e^{-\tau_{atm}} + Tb_{up} + \Gamma Tb_{down} e^{-\tau_{atm}} \quad 4.7.2$$

where Tb_{up} is the brightness temperature self-emitted by the atmosphere upwards and attenuated along upward path, Tb_{down} is the brightness temperature self-emitted by the atmosphere downwards and attenuated along the downwards path (In reality, when taking galactic noise into account, there are two terms (see sum of contribution equations)), Γ is the surface reflection coefficient, with $\Gamma = 1 - \epsilon$, where ϵ is computed for a rough surface as $\epsilon = \frac{Tb_{flat} + Tb_{rough}}{SST}$ and τ_{atm} is the equivalent optical thickness of the atmosphere.

The atmosphere will generate 3 terms, which are best seen when re-writing equation 4.7.2 as follows,

$$Tb_m = Tb_s + Tb_s(e^{-\tau_{atm}} - 1) + Tb_{up} + \Gamma Tb_{down} e^{-\tau_{atm}} \quad 4.7.3$$

The atmospheric attenuation, atmospheric emission upwards and the reflected downwards atmospheric emission all need to be accounted for.

Within the atmosphere, there are four components which affect the emission and absorption of radiation in the L-band to be considered: dry atmosphere, water vapour, clouds, and rain. Ideally, the quantities to be known in equation 4.7.3, (τ_{atm} , Tb_{up} , Tb_{down}) will be related simply to the four components considered.

In every case, the basic quantity from which atmospheric contributions can be estimated is normally the **linear absorption coefficient k**, generally expressed in dB km⁻¹.

4.7.1.1.2 Dry atmosphere

The radiatively active component in dry atmosphere is **molecular oxygen**. Oxygen molecules have a permanent magnetic moment; therefore, absorption and radiation in the microwave region occur due to magnetic interactions with the incidence field. This interaction produces a family of rotation absorption lines in the vicinity of 60 GHz (known as the oxygen complex) and an additional isolated line at 118.8 GHz [Crane, 1971]. Due to pressure characteristics of the lower part of the Earth's atmosphere, pressure broadening causes the complex of lines to blend to a continuous absorption band centred around 60 GHz.

The oxygen absorption and radiation change due to changes in the meteorological parameters and are dependent on the pressure $P(z)$ and the temperature $T(z)$ of the gas as a function of the height z .

A model for the absorption by oxygen for lower frequencies is described in [2: Ulaby, 1981]. For frequencies below 45 GHz, the contribution from the 118.75 GHz oxygen absorption line can be neglected, and thereby we only have the contribution from the 60 GHz absorption line. Then the linear absorption from oxygen at $f=1.413$ GHz can be written in dB km⁻¹ as:

$$k_{O_2} = 1.110^{-2} f^2 \left(\frac{P}{1013} \right) \left(\frac{300}{T} \right)^2 \gamma \left(\frac{1}{(f - f_0)^2 + \gamma^2} + \frac{1}{f^2 + \gamma^2} \right) \quad 4.7.4$$

where, f is the frequency (1.413 GHz) and f_0 is the absorption line frequency (60 GHz). The pressure is given by P in hectoPascal (hPa), the temperature by T in K and γ is the line width parameter written in GHz given by,

$$\gamma = \gamma_0 \left(\frac{P}{1013} \right) \left(\frac{300}{T} \right)^{0.085} \quad 4.7.5$$

where the line width γ_0 is pressure dependent [1], however more recent spectroscopic measurements [7] are better described when choosing $\gamma_0 = 0.59$ over the whole pressure range.

4.7.1.1.3 Water vapour

In the microwave region, water vapour has rotational absorption lines at 22.235 GHz and at 183.31 GHz. Furthermore, there are also some absorption lines above this region, which contribute to the microwave absorption spectrum. For calculation of the absorption at L band the contributions from the 183.31GHz and all the absorption lines above can be grouped in a residual term using low frequency approximation [2]. The resulting absorption coefficient k_{H_2O} can then be written as a sum of the contribution from the 22.235 GHz absorption line k_{22} and a residual term k_r ,

$$k_{H_2O} = k_{22} + k_r. \quad 4.7.6$$

According to [Waters, 1976] the 22.235 GHz absorption line is given by,

$$k_{22} = 2 f^2 \rho_v \left(\frac{300}{T} \right)^{\frac{5}{2}} e^{-\frac{644}{T}} \left(\frac{\gamma_1}{(494.4 - f^2)^2 + 4f^2\gamma_1^2} \right). \quad 4.7.7$$

where, ρ_v is the water vapour density (gm^{-3}) and γ_1 is the line width parameter (GHz),

$$\gamma_1 = 2.85 \left(\frac{P}{1013} \right) \left(\frac{300}{T} \right)^{0.626} \left(1 + 0.018 \frac{\rho_v T}{P} \right). \quad 4.7.8$$

The residual term, according to [Ulaby, 1981] is given as,

$$k_r = 2.410^{-6} f^2 \rho_v \left(\frac{300}{T} \right)^{\frac{3}{2}} \gamma_1. \quad 4.7.9$$

4.7.1.1.4 Clouds

When electromagnetic radiation interacts with particles such as those in snow, clouds, fog and rain the radiation is absorbed and scattered. However, if only water droplets, which have a diameter much smaller than the wavelength, are considered (which is the case for 1.4 GHz), then scattering is unimportant. The absorption coefficient can therefore be calculated from the Rayleigh approximation. The particles are also assumed to be randomly distributed within the volume, and therefore the contribution of the individual particles can be summed assuming an incoherent process. Furthermore, it is also assumed that the particles are spherical, which is a reasonable assumption for most atmospheric water and ice droplets. The

scattering and absorption characteristics of a spherical particle are governed by three factors: electromagnetic wavelength, index of refraction, and particle radius.

Clouds are complex phenomena, which consist of water either in liquid or frozen form or sometimes both. The amount of water and the phase of the water in the cloud depends on the altitude, the temperature and indirectly on the pressure. Clouds are described by cloud base, cloud top, the mass density of the liquid water in the cloud and principal composition of the cloud. The water content of a cloud according to [Ulaby, 1981] is typically less than 1 gm^{-3} .

Radiative effects of ice clouds are negligible at L Band. Concerning liquid water clouds, according to [1] and [2], empirical expressions have been developed by [5: Benoit, 1968] for the linear absorption coefficient. It appears that the only case where the overall radiative effect at L Band might not be negligible concerns that deep cumulus clouds. However, there is no reliable auxiliary data allowing select a depth for these clouds. In addition, they are mostly associated with rain events, which are dealt with separately.

4.7.1.1.5 Rain

Physically, rain occurrence is like clouds. However, the problem is complicated by several factors. Firstly, due to the size of raindrops, the Rayleigh approximation is no longer strictly valid, hence a dependence appears with the granulometry of rain, which is variable and not accurately known. Secondly, large raindrops are not spherical, unlike for the atmosphere. Thirdly, while ice particles do not contribute to atmospheric extinction, there is often a melting zone just below the 0°C isotherm which is very poorly predicted and may not be negligible in terms of radiative effects. Finally, the rain is often expressed in rainfall intensity, whereas the relevant quantities are linear densities (liquid water content) in the atmosphere.

For all these reasons, it does not seem practical to correct for rain. According to [1], rain in the atmosphere produce a non-negligible radiative contribution when the rain intensity exceeds about 10 mmhr^{-1} ; this is estimated to happen less than 0.2% of the time over all latitudes, up to less than 0.65% of the time over equatorial areas (these figures may be pessimistic for a 06h local time). A more in-depth analysis was carried out by Schultz [6].

Therefore, rain occurrences are a matter for flagging rather than correcting. As stated above, the heavy clouds should be associated with rain events.

However, there are obviously cases for which rain attenuation effects will be significant. This will deserve further studies, including an attempt to build and a forward model for the rain contribution, and special attention for calibration operations. This is all the truer since rain is a major component of the global water cycle, in which the SMOS mission is expected to bring improved insights.

4.7.2 Mathematical description of algorithm

4.7.2.1 Radiative transfer for gaseous components

From above, it is concluded that atmospheric contribution should be computed for oxygen and water vapour.

Numerical simulations show that, for L band, Tb_{up} and Tb_{down} radiative contributions are extremely close one to each other and can be assumed equal to a single value Tb_{atm} in equation 4.7.2. Therefore, what is needed is,

$$\tau_{atm} = \tau_{O_2} + \tau_{H_2O} \quad 4.7.10$$

$$Tb_{atm} = Tb_{O_2} + Tb_{H_2O} \quad 4.7.11$$

Equations 4.7.3 and 4.7.4 can now be written as,

$$Tb_m = Tb_s e^{-\tau_{atm}} + Tb_{atm} (1 + \Gamma e^{-\tau_{atm}}) \quad 4.7.12$$

$$Tb_m = Tb_s + Tb_s (e^{-\tau_{atm}} - 1) + Tb_{atm} (1 + \Gamma e^{-\tau_{atm}}) \quad 4.7.13$$

Contributions to absorption come from the whole thickness of the atmosphere. However, for oxygen it is not necessary to consider altitudes higher than a level $ZM \approx 30$ km, where absorption becomes completely negligible. For water vapour, the altitude range to be considered is limited to $ZM \approx 10$ km.

4.7.2.2 Monolayer model

For SMOS data inversion, a monolayer model is acceptable for simulating atmospheric effects at L-band. From equation 4.7.12 it is seen that the two quantities linked to atmospheric radiative contributions τ_{atm} and TB_{atm} are fixed during the retrieval. Looking at equation 4.7.13, it is seen however that the atmospheric contribution will vary with TB_s and Γ ; therefore, strictly speaking, this contribution cannot be considered as a fixed additive correction.

The **oxygen** overall contribution is by far the largest atmospheric contribution. It may reach up to 6 K and beyond, as described in [1]. Integrations along the vertical remain necessary in the equations. Three ways are identified to compute τ_{O_2} and Tb_{O_2} :

1. Carry out the **integrations** over the thickness of the atmosphere. The estimated necessary altitude range ZM are 20 km for O_2 , 10 km for H_2O ; the necessary resolution along the vertical is better than 100 m.

2. **Tabulate** the τ_{O_2} and Tb_{O_2} as functions of some parameters (e.g. surface atmospheric temperature T_0 , the surface pressure P_0 , some parameter describing the structure of the temperature profile, surface humidity etc.) and then interpolate from these tables.
3. Build **empirical laws** to compute τ_{O_2} and Tb_{O_2} .

The most efficient (and physically meaningful) way to do is option 2, with look up tables K by writing the emission of each component as the product of optical thickness by an **equivalent layer (physical) temperature**, which is conveniently defined by its difference ΔT with the surface air temperature T_0 ,

$$Tb_{O_2} = (T_0 - \Delta T_{O_2})\tau_{O_2} \quad 4.7.14$$

For dry atmosphere, a **quadratic** fit to results obtained using the whole radiative transfer computation has been found necessary,

$$\tau_{O_2} = 10^{-6} \times (K_{\tau_{O_2}}(0) + T_0 K_{\tau_{O_2}}(1) + P_0 K_{\tau_{O_2}}(2) + T_0^2 K_{\tau_{O_2}}(3) + P_0^2 K_{\tau_{O_2}}(4) + P_0 T_0 K_{\tau_{O_2}}(5)) \quad 4.7.15$$

$$\Delta T_{O_2} = K_{\Delta T_{O_2}}(0) + T_0 K_{\Delta T_{O_2}}(1) + P_0 K_{\Delta T_{O_2}}(2) + T_0^2 K_{\Delta T_{O_2}}(3) + P_0^2 K_{\Delta T_{O_2}}(4) + P_0 T_0 K_{\Delta T_{O_2}}(5) \quad 4.7.16$$

where T_0 is the near surface air temperature (K), P_0 is the surface pressure (hPa), τ_{O_2} is obtained in Np and ΔT_{O_2} is obtained in K.

For the water vapour contribution τ_{H_2O} and ΔT_{H_2O} , a **linear** fit is found adequate,

$$\tau_{H_2O} = \max(10^{-6} \times (K_{\tau_{H_2O}}(0) + P_0 K_{\tau_{H_2O}}(1) + TWVCK_{\tau_{H_2O}}(2)), 0.0) \quad 4.7.17$$

$$\Delta T_{H_2O} = K_{\Delta T_{H_2O}}(0) + P_0 K_{\Delta T_{H_2O}}(1) + TWVCK_{\Delta T_{H_2O}}(2) \quad 4.7.18$$

where, $TWVC$ is the total precipitable water vapour content (kg m^{-2}) from ECMWF data, τ_{H_2O} is obtained in Np and ΔT_{H_2O} in K.

Now using the values for the ΔT_{O_2} , ΔT_{H_2O} , τ_{O_2} and τ_{H_2O} , the T_{O_2} and T_{H_2O} quantities can be used following 4.7.14,

$$TB_{O_2} = (T_0 - \Delta T_{O_2})\tau_{O_2} \quad 4.7.19$$

$$TB_{H_2O} = (T_0 - \Delta T_{H_2O})\tau_{H_2O} \quad 4.7.20$$

Atmospheric term TB_{atm} and τ_{atm} are obtained using 4.7.10 and 4.7.11.

The numerical values for coefficients in eq. 4.7.16, 4.7.17, 4.7.18 and 4.7.19 are supplied in TGRD. These formulas were first written for land. For sea, the required accuracy is better than 0.05 K and this could be achieved using the same formulas but restricting the surface pressure range to [900 1100] hPa.

4.7.2.3 Error budget estimates (sensitivity analysis)

The method selected for computing gaseous radiative contributions has been selected in such a way that the resulting error on upwelling brightness temperatures due to approximating the effect of physical atmospheric properties (pressure, temperature, water vapour concentration) never exceeds 0.05 K for SMOS operating conditions. It is expected that this goal is compatible with computing power/time requirements.

Then, the major error source will be due to estimates of absorption cross sections, which in turn reflect the uncertainty on spectroscopic measurements. This uncertainty is estimated around 5%.

4.7.3 Practical considerations

4.7.3.1 Calibration and validation

Since the uncertainty on absorption cross sections cannot be overcome, the resulting error will have to be corrected within the overall SMOS validation process. If the absorption cross sections are determined correctly, the resulting uncertainty would be permanently eliminated.

4.7.4 Assumption and limitations

Assumptions have been made here are related to laboratory knowledge of spectral properties of atmospheric gases.

Limitations concern the presence of liquid (cloud or rain) water in the atmosphere, for which a flagging approach is suggested rather than a correction.

References

- [1] M Peichl, V. Wittmann, E Anterrieu, B Picard, N Skou and S. Sobjaerg: Final report: SCIENTIFIC INPUTS FOR THE SMOS LEVEL 1 PROCESSOR DEVELOPMENT, in response to ESA



contract No. 10508/02/NL/GS. The section referred to here was written by Skou and Sobjaerg.

- [2] Ulaby, Fawwaz T. and Richard K. More and Adrian K. Fung, (1981), "Microwave Remote Sensing – Active and Passive", Artech House Inc. , Vol. 1 & 3
- [3] Crane R.K. (1971). "Propagation Phenomena Affecting Satellite Communication Systems Operation in the Centimeter and Millimeter Wavelength Bands", Proceedings of the IEEE, 59, pp 173-188.
- [4] Waters, J. W. (1976), "Absorption and Emission of Microwave Radiation by Atmospheric Gases", in Methods of Experimental Physics, M.L. Meeks, ed. 12, Part B, Radio Astronomy, Academic Press, Section 2.
- [5] Benoit, A. (1968) "Signal attenuation Due to Neutral Oxygen and Water Vapor, Rain and Clouds", Microwave Journal, 11, pp. 73-80
- [6] J. Schulz, in WP1200: "Impact of rain on sea surface brightness temperature", Scientific requirements and impact of space observations of ocean salinity for modeling and climate studies, ESA study 14273/00/NL/DC, 2002, p51-43.
- [7] Liebe, H. J., G. A. Hufford, M. G. Cotton, Propagation modeling of moist air and suspended water/ice particles at frequencies below 1000 GHz, in AGARD 52nd Specialists' Meeting of the Electromagnetic Wave Propagation Panel, pp. 3-1 - 3-10, Palma de Mallorca, Spain, 1993.

4.8 Transport ground level Tb to antenna level

4.8.1 Theoretical description

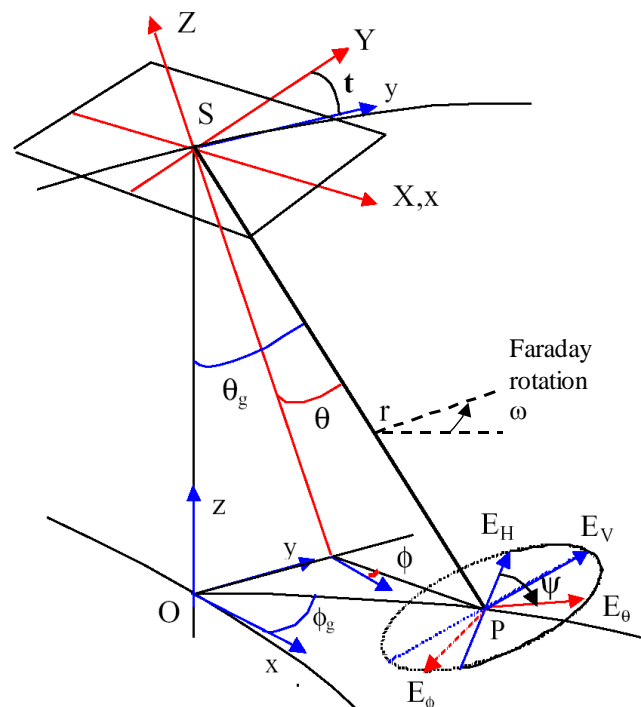
4.8.1.1 Physics of the problem

The iterative process to retrieve salinity from SMOS measurements requires comparing the measured data with Tb modelled through the algorithms described in this ATBD. All the different sub-models are describing the processes that contribute to sea surface L-band emission (flat sea, roughness, foam, ...), the effects of incoming radiation that need to be added to this emission (atmospheric, cosmic and galactic background, ...), plus the modifications to this radiation in its transit through the atmosphere. The result is the modelled value of Tb on top of the atmosphere expressed in the Earth reference frame.

The next step is to transport this Tb to the SMOS antenna reference frame, considering both the change in geometry and the ionospheric effects (Faraday rotation), to allow the comparison with the measured Tb .

4.8.2 Mathematical description of the algorithm

With the viewing geometry as defined in ACRI Reqts_L2Draft-2.doc (see figure and annex)



that follows the conventions described in Earth Explorer CFI Software Mission Convention Document (Deimos), we introduce the mathematical expressions for the angles to be used in the transport from ground to antenna reference frames.

$$\theta = \cos^{-1}[\sin t \sin \theta_g + \cos t \cos \theta_g] \quad 4.8.1$$

$$\phi = -\sin^{-1} \left[\frac{-\sin t \cos \theta_g + \cos t \sin \theta_g \sin \phi_g}{\sin \theta} \right] \quad 4.8.2$$

$$\psi = \pi - \sin^{-1} \left[\frac{\cos t \sin \theta_g + \cos t \sin \theta_g \sin \phi_g}{\sin \theta} \right] \quad 4.8.3$$

for $-\pi/2 \leq \phi_g \leq \pi/2$:

for $\pi/2 \leq \phi_g \leq 3\pi/2$: ϕ must be replaced by $\pi - \phi$ and ψ by $\pi - \psi$

We define the rotation angle $\alpha = -\phi - \psi - \omega$, being ω the Faraday rotation angle. Then, following ACRI Reqts_L2Draft-2.doc

Dual polarization mode:

Direct transformation from surface reference frame to antenna reference frame is

$$\begin{bmatrix} A1 \\ A2 \end{bmatrix} = \begin{bmatrix} \cos^2(a) & \sin^2(a) & -\cos(a)\sin(a) \\ \sin^2(a) & \cos^2(a) & \cos(a)\sin(a) \end{bmatrix} \begin{bmatrix} Tb_1 \\ Tb_2 \\ Tb_3 \end{bmatrix} = [MR2] \begin{bmatrix} Tb_1 \\ Tb_2 \\ Tb_3 \end{bmatrix} \quad 4.8.4$$

If T_3 is assumed to be zero, then the equation becomes:

$$\begin{bmatrix} A1 \\ A2 \end{bmatrix} = \begin{bmatrix} \cos^2(a) & \sin^2(a) \\ \sin^2(a) & \cos^2(a) \end{bmatrix} \begin{bmatrix} Tb_1 \\ Tb_2 \end{bmatrix} = [MR2] \begin{bmatrix} Tb_1 \\ Tb_2 \end{bmatrix} \quad 4.8.5$$

There is a singularity problem if $\cos(a) = \sin(a)$, i.e. $\alpha = \pm \pi/4$ or $\pm 3\pi/4$. In such a configuration, $A1 = A2 = (T_1 + T_2)/2$ and it is not possible to derive T_1 and T_2 from $A1$ and $A2$.

Full polarization mode:

$$\begin{bmatrix} A1 \\ A2 \\ A3 \\ A4 \end{bmatrix} = \begin{bmatrix} \cos^2(a) & \sin^2(a) & -\cos(a)\sin(a) & 0 \\ \sin^2(a) & \cos^2(a) & \cos(a)\sin(a) & 0 \\ \sin(2a) & -\sin(2a) & \cos(2a) & 0 \\ 0 & 0 & 0 & 1 \end{bmatrix} \begin{bmatrix} Tb_1 \\ Tb_2 \\ Tb_3 \\ Tb_4 \end{bmatrix} = [MR4] \begin{bmatrix} Tb_1 \\ Tb_2 \\ Tb_3 \\ Tb_4 \end{bmatrix} \quad 4.8.6$$

No singularities appear in this mode.

As it has been shown by simulation studies and experimental data that over the ocean $Tb_{hv} \approx Tb_{vh} \approx 0$, the third Stokes parameter at Earth reference frame is considered also to be 0 at first approximation. However, theoretical models provide nonzero Tb_3 and Tb_4 so we recommend keeping the possibility of considering nonzero T_3 , even in dual pol mode. Then the different sub-models provided in this SSS ATBD are valid either for dual-pol or full-pol formulation.

If the first Stokes parameter is used for the iterative retrieval $I = A1 + A2 = Tb_1 + Tb_2$ and there is no need to apply any of the above described transformations.

References

Camps, A., M. Vall-Ilossera, N. Duffo, F. Torres, and I. Corbella (2005), Performance of Sea Surface Salinity and Soil Moisture retrieval algorithms with different auxiliary datasets in 2-D L-band aperture synthesis interferometric radiometers, IEEE Trans. Geosci. Remote Sens., 43(5), May 2005

Claassen, J.P., and A.K. Fung, The Recovery of Polarized Apparent Temperature Distributions of Flat Scenes from Antenna Temperature Measurements, IEEE Transactions on Antennas and Propagation, AP-22 (3), 433-442, 1974.

Waldteufel, P. et Caudal, G. Off-axis Radiometric Measurements; Application to Interferometric Antenna Design. IEEE TGARS, 40, 6, juin 2002, 1435-1439

Waldteufel, P, Floury, N., Dinnat, E., Caudal, G., Ionospheric Effects for L-band “-D Interferometric Radiometry, IEEE TGARS, 42, 1, janvier 2004, 105-118



4.9 Sum of contributions

4.9.1 Theoretical description

4.9.1.1 Physics of the problem

This module consists in the addition of all the sub-models used to compute the brightness temperature of a specific ocean grid point at antenna level. Then it includes the forward model for L-band emissivity of a flat sea, plus correction for surface roughness, the introduction of galactic noise contamination, atmospheric effects, and finally transport from ground level to antenna level. With the present development, measurements affected by sun glint and moon contamination are flagged and discarded for retrieval. However, if in the future algorithms to adequately correct for these effects can be obtained, the measurements will be kept, and the corresponding corrections will be introduced in the sum of contributions.

4.9.1.1.1 Note on first Stokes parameter computation

As information to the rest of modules, we indicate here the detail of the first Stokes parameter ($I = Tb_h + Tb_v = A1 + A2$) computation from a complete SMOS measurement (2.4 s), in fact a pair of two consecutive measurements in orthogonal polarisations:

As $A1$ and $A2$ are measured in two consecutive (in case of dual-pol) 1.2 s snapshots, the incidence angle for a specific grid point is not exactly the same for both, but will differ (in case of dual-pol) in some 0.6° (approx. 8 km displacement at 756 km height). This will be a little bigger in case of full-pol.

It was decided (October 2006) not to perform any correction to $A1$ and $A2$ but to compute directly a 'Pseudo' First Stokes parameter:

$$I(\theta_{mean}) = A1(\theta_x) + A2(\theta_y) \quad 4.9.1$$

where

$$\theta_{mean} = (\theta_x + \theta_y)/2 \quad 4.9.2$$

We call it 'pseudo' first Stokes since both measurements have not been acquired at the same time and therefore with the same incidence angle. This parameter will be a little bit sensitive to TEC, but it does not represent a significant problem.

The way to extract proper measurements is described in the Measurements Selection section (section 4.14).

In case of full polarisation mode, the generation of the ‘pseudo’ Stokes parameter is not so straightforward, and a specific strategy must be drawn (see Technical Note by ACRI, 15/09/08). According to SMOS L1 Full Polarisation Data Processing (ref : SO-TN-DME-L1PP-0024. Issue: 1.6. Date: 16/07/07. ESA/DEIMOS) the measurement cycle consists of 26 steps spread over four 1.2 s snapshots:

Snapshot	Step	arm pol	measurements	
1	1	XXX	XX	
2	2	YYX	YY, XY, YX	} repeated 4 times
	3	XYY	YY, XY, YX	
	4	YXY	YY, XY, YX	
3	1'	YYY	YY	
4	2'	XXY	XX, XY, YX	} repeated 4 times
	3'	YXX	XX, XY, YX	
	4'	XYX	XX, XY, YX	

Three different strategies to compute the pseudo- I were proposed for implementation in the processor to be further tested during commissioning phase to decide on the optimal one:

- 1) To use the closest A1 (XX) and A2 (YY) pairs, as in dual pol case, even they have different integration times (1.2 s in snapshots 1 and 3, 0.4 s in 2 and 4) and consequently very different radiometric noises that anyway will be added in the quadratic form explained in section 4.16. If the time interval between the two members of a pair is above a specified threshold (due to missing measurements) the pseudo- I will not be computed.
- 2) To add all XX and YY measurements of a full cycle. This way both components are acquired during 4/3 of a snapshot integration time. In case of absence of one measurement, either the measurements of the whole cycle are not processed (and then discarded), or else they are processed following different procedures according to the missing measurement within the cycle (see details in the TN mentioned above).
- 3) To use only A1 and A2 acquired respectively in snapshots 1 and 3. This third strategy discards measurements made when the three arms are not in the same polarisation, to avoid problems that may arise during these complex steps of the full pol mode.

Option (2) from above was selected as final configuration for the processing.

4.9.1.1.2 Sum of modules

The iterative method for salinity retrieval requires computing T_b with expected SST, SSS and roughness descriptors values at the adequate incidence angle, add the effect of all envisaged

contaminations (galactic, sun, moon and atmospheric), and transport the resulting value to antenna level for comparison with the measured T_b (level 1c) previously corrected for bias, if necessary. This series of computations is made following the different sub-models described in sections 4.1 to 4.12 of this ATBD.

When an angular dependence is present, the computations are made for θ_{mean} .

- 1- T_{b_1} = T_{b_flat} computed with equation described in 4.1
- 2- T_{b_2} = T_{b_1} + T_{b_rough} computed with surface roughness sub-model described in 4.2. Alternative roughness models (ANNEX A and B, respectively) may be activated.
- 3- T_{b_3} = T_{b_2} with corrections for foam if applicable, following sub-model described in 4.5
- 4- T_{b_4} = T_{b_3} modified for reflected galactic noise contamination as described in 4.6 or 4.7, which is attenuated by the atmosphere, when down-welling (described in 4.9).
- 5- T_{b_5} = T_{b_4} modified by the reflected down-ward atmospheric emission as described in 4.9.
- 6- T_{b_6} = T_{b_5} attenuated by the atmosphere when travelling along the antenna-surface path (described in 4.9).
- 7- T_{b_7} = T_{b_6} modified by the atmosphere self-emission direct to antenna (described in 4.9).
- 8- T_{b_8} = T_{b_7} transported from ground to antenna level as described in 4.12 (geometry and Faraday rotation)

This T_{b_8} is the brightness temperature that must be included as “ T_b mod” in the iterative convergence module (4.14) where it is compared with the “ T_b meas” measured by SMOS

We must indicate that the choice of retrieving SSS using I or using T_h and T_v separately does not affect modules 4.1 to 4.11, that are mathematically described using T_h and T_v . It is only in step 8 above when either the T_b to be transported is T_h+T_v (then equal to A_1+A_2) or both components are transported separately and then the Faraday rotation must be considered.

4.9.2 Mathematical description of algorithm

The Sum of contributions can be expressed mathematically as follows.

Firstly, the brightness temperature of the sea at the bottom of the atmosphere is computed. Later, the atmosphere and extra-terrestrial sources are applied, and finally the transport from ground to antenna is considered.

The brightness temperature at the bottom of atmosphere (BOA) due to sea surface emission (*at BOA there is also the reflection of atm. signal + galactic signal etc*) is as follows

$$Tb_{sea} = (Tb_{flat} + Tb_{rough}) \quad 4.9.3$$

Tb_{flat} is the Tb for a flat sea, as described in section 4.1, and Tb_{rough} is the contribution of the roughness of the sea, as described in section 4.2.

Then galactic and atmospheric sources are considered (see sections 4.3, 4.4 and 4.7)

$$Tb_{BOA} = Tb_{sea} + Tb_{reflected} = Tb_{sea} + (Tb_{DN}\Gamma + (Tb_{gal_{refl}})e^{-\tau_{atm}}) \quad 4.9.4$$

where $Tb_{reflected}$ is the radiometric temperature from the sky and atmosphere scattered by the surface, which is the addition of two terms; the downward emitted atmospheric radiation (Tb_{DN}) and the brightness due to extra-terrestrial sources. The extra-terrestrial sources considered here ($Tb_{gal_{refl}}$) are the hydrogen line, the cosmic and galactic contribution already reflected on the sea surface, as explained in sections 4.3 and 4.4 of this document. $Tb_{gal_{refl}}$ is multiplied by an attenuation factor due to the atmosphere since its formulation is at top of the atmosphere. A switch is available to choose between galactic noise contamination 1 (section 4.3) or 2 (section 4.4) to compute the reflected noise (at the moment, the semi-empirical model will only use the galactic noise contamination 1 module). The atmospheric contribution term (Tb_{DN}) is multiplied by Γ , that is the reflection coefficient

To compute Tb at top of the atmosphere (without considering Faraday rotation, for practical reasons) in the Earth reference frame (sections 4.7 and 4.8):

$$Tb_{TOA}^{EARTH} = Tb_{BOA} e^{-\tau_{atm}} + Tb_{UP} \quad 4.9.5$$

where Tb_{UP} is the atmospheric self emission direct to the antenna (but computed at TOA and with Earth reference frame) and $e^{-\tau_{atm}}$ is the attenuation produced by the atmosphere. Section 4.7 specifies that Tb_{UP} and Tb_{DN} are very close, and considered equal to Tb_{atm} , which is defined in that section.

Finally, to compute this temperature at the antenna reference frame, the geometrical transformation and the ionospheric effect should be considered, following section 4.8, as

$$Tb^{ANTENNA} = [MR4] \cdot Tb_{TOA}^{EARTH} \quad 4.9.6$$

where MR4 is the matrix that describes the geometrical transformation plus the Faraday rotation.



4.9.3 Error budget estimates (sensitivity analysis)

The addition of the different modules implies an analysis of the impact of the individual errors on the overall error budget. This was planned in the ESL proposal as WP2600 and expected to be finished by the end of the study.

4.9.4 Practical considerations

4.9.4.1 Calibration and validation

The validation of this module can be done by running some tests cases with exactly the same configuration (in terms of sub-models switched on and use of auxiliary data) with the summation module used in the SRS study and the equivalent used by UPC from SEPS, to check that the result is the same.

4.9.4.2 Quality control and diagnostics

The range of validity of this module comes from the intersection of the corresponding ranges for all sub-models.

4.9.5 Assumption and limitations

The module must be applied to all grid points selected as good for salinity retrieval at the Measurement discrimination.

Dependencies table

The following table (next page) describes the dependencies between modules. What modules should be applied or not to the different roughness models. In some cases, a switch will be required to allow using or not the module, and therefore to test if using the module is beneficial or not.



	Roughness model 1 -2-Scales	Roughness model 2 -SSA	Roughness model 3 - empirical
Flat sea	Y	Y	Y
Rough mod 1	Y	N	N
Rough mod 2	N	Y	N
Rough mod 3	N	N	Y
Foam contrib.	S	S	N
Galactic noise 1	S (by default)	S (by default)	Y (by default)
Galactic noise 2	S	S	N
Galactic noise 0	S	S	S
Atmos. Effects	Y	Y	Y
Bias corr	S	S	S
Transport ground to antenna	Y	Y	Y
Sum of contributions	Y	Y	Y
Iterative scheme	Y	Y	Y

Y = Yes, apply S = Behind a switch N = Not apply

4.10 Iterative Scheme

4.10.1 Theoretical description

4.10.1.1 Physics of the problem

The iterative Levenberg and Marquard method is used in the inversion algorithm. This method was already implemented in the simulator for soil moisture study and gives very similar results to the [Jackson, 1972] method used in SR1600. The mathematical problem is described below in detail as well as in Zine et al, 2008.

The iterative scheme is applied to full polarized measurements. The iterative scheme can also be applied to measurements made in dual polarization mode, as was the case during the first six months of the SMOS mission. In the iterative scheme, both Tb theoretical error (σ_{Tb_meas}) and model error (σ_{Tb_mod}) are considered. However, it is described below the case when the model error is supposed equal to zero (case 1) and after, the general case currently used in L2OS processor for SSS retrieval (case 2).

4.10.1.1.1 Case 1 – Model error neglected

In this case the model error is considered negligible and not considered.

The set of measurements are brightness temperatures Tb_i^{meas} observed for a single grid point at different incidence angles, θ_i . These data need to be fitted into a direct model to find the solution of the parameters.

$$T_b^{mod} = f(\theta, SSS, SST, P_{rough}) \quad 4.10.1$$

where P_{rough} is a vector that includes the parameters used in the forward model to describe the sea roughness.

This implies minimization of the following constrained cost function:

$$\chi^2 = \sum_{i=0}^{Nm-1} \frac{[Tb_i^{meas} - Tb_i^{mod}(\theta, P)]^2}{\sigma_{Tb_i}^2} + \sum_{j=0}^{Np-1} \frac{[P_j - P_j^{prior}]^2}{\sigma_{P_j}^2} \quad 4.10.2$$

being P_j , the j parameters that influence the Tb : SSS , SST , WS (or other wind descriptors), and depending on the cases, also significant wave height H_s , wind direction ϕ , inverse wave-age Ω , and TEC parameter in case of not using first Stokes, etc. θ is the incidence angle of measurements from nadir. In case of cardioid retrieval, the P_j parameters are Acard and the surface temperature.

$P_{j_{prior}}$ is a value of parameter P_j known a priori to the measurements with an uncertainty σ_{P_j} (Waldteufel, 2003, Gabarró, 2004). The uncertainty of each parameter, σ_{P_j} , could change depending on the area of observation.

σ_{Tb}^2 is the uncertainty of the measurement used for each incidence angle:

$$\sigma_{Tb_i}^2 = \sigma_{Tb_{meas_i}}^2 \quad 4.10.3$$

where the value of $\sigma_{Tb_{meas_i}}^2$ is given in the L1 output product.

In this case, a global figure will be given as a linear function of auxiliary parameters (SST, SSS, wind speed – room must be kept for other parameters that might be needed) and of polarization.

Some experiments (Sabia et al., 2005) advise not using SSS as one of the constrained parameters P_j , as the retrieved value tends to the a priori value. This possibility is avoided in the L2OS processor by settling the term σ_{P_j} to a high value (e.g. 100 psu) so as to remove its impact on equation 4.10.2 (see Yin et al. 2010, Fig. 10.)

4.10.1.1.2 Case 2 Model error taken into account

For a single measurement, the variance-covariance matrix for Tb_{mod} (C_{Earth}^{mod}) is diagonal in the Earth reference frame:

$$C_{Earth}^{mod} = \begin{pmatrix} \sigma_{Tb_{hh_{model}}}^2 & 0 & 0 & 0 \\ 0 & \sigma_{Tb_{vv_{model}}}^2 & 0 & 0 \\ 0 & 0 & \sigma_{Tb_{3_{model}}}^2 & 0 \\ 0 & 0 & 0 & \sigma_{Tb_{4_{model}}}^2 \end{pmatrix} \quad 4.10.4$$

where

$$\sigma_{Tb_{hh_{model}}}^2, \sigma_{Tb_{vv_{model}}}^2, \sigma_{Tb_{3_{model}}}^2 \text{ and } \sigma_{Tb_{4_{model}}}^2$$

are the variances of the Tb_{mod} components ($Tb_{hh_{mod}}, Tb_{vv_{mod}}, Tb_{3_{mod}}, Tb_{4_{mod}}$) in the Earth reference frame. The correlation of the model error between different measurements are neglected here.

The value of the model uncertainty is given by a global figure that considers the assumptions and limitations specified in each module of each model. In this version of ATBD, it is assumed to be constant and independent of polarization. Its value is given in the TGRD in the Earth reference frame.

In the future, $\sigma_{Tb_{model}}$ could be given as an analytical function of auxiliary parameters (SST, wind speed – with room kept for others parameters that might be needed), incidence angle and polarization.

The method of transport of the error variances to the antenna reference frame is detailed below.

The variance/covariance matrix in the antenna reference frame (C_{Ant}^{mod}) for Tb_{mod} is given in the antenna reference frame by:

$$C_{Ant}^{mod} = [MR4]C_{Earth}^{mod}[MR4]^T \quad 4.10.5$$

where MR4 is the rotation matrix described in section 4.8 and T represents the transposition operation.

C_{Ant}^{mod} is then given by:

$$C_{Ant}^{mod} = \begin{pmatrix} \sigma_{A1_{model}}^2 & c_{12} & c_{13} & c_{14} \\ c_{21} & \sigma_{A2_{model}}^2 & c_{23} & c_{24} \\ c_{31} & c_{32} & \sigma_{A3_{model}}^2 & c_{34} \\ c_{41} & c_{42} & c_{43} & \sigma_{A4_{model}}^2 \end{pmatrix} \quad 4.10.6$$

with the variances:

$$\begin{aligned} \sigma_{A1_{model}}^2 &= \sigma_{Tb_{hh_{model}}}^2 \cos^4(a) + \sigma_{Tb_{vv_{model}}}^2 \sin^4(a) + \sigma_{Tb_{3_{model}}}^2 \cos^2(a) \sin^2(a) \\ \sigma_{A2_{model}}^2 &= \sigma_{Tb_{hh_{model}}}^2 \sin^4(a) + \sigma_{Tb_{vv_{model}}}^2 \cos^4(a) + \sigma_{Tb_{3_{model}}}^2 \cos^2(a) \sin^2(a) \\ \sigma_{A3_{model}}^2 &= \left(\sigma_{Tb_{hh_{model}}}^2 + \sigma_{Tb_{vv_{model}}}^2 \right) \sin^2(2a) + \sigma_{Tb_{3_{model}}}^2 \cos^2(2a) \\ \sigma_{A4_{model}}^2 &= \sigma_{Tb_{4_{model}}}^2 \end{aligned} \quad 4.10.7$$

and the covariances:

$$\begin{aligned}
 c_{21} &= (\sigma^2 Tb_{hh_{model}} + \sigma^2 Tb_{vv_{model}} - \sigma^2 Tb_{3_{model}}) \cos^2(a) \sin^2(a) \\
 c_{31} &= \sigma^2 Tb_{hh_{model}} \cos^2(a) \sin(2a) - \\
 &\quad \sigma^2 Tb_{vv_{model}} \sin^2(a) \sin(2a) - \sigma^2 Tb_{3_{model}} \cos(a) \sin(a) \cos(2a) \\
 c_{41} &= 0 \\
 c_{12} &= c_{21} \\
 c_{32} &= \sigma^2 Tb_{hh_{model}} \sin^2(a) \sin(2a) - \sigma^2 Tb_{vv_{model}} \cos^2(a) \sin(2a) \\
 &\quad + \sigma^2 Tb_{3_{model}} \cos(a) \sin(a) \cos(2a) \\
 c_{42} &= 0 \\
 c_{13} &= c_{31} \\
 c_{23} &= c_{32} \\
 c_{43} &= 0 \\
 c_{14} &= 0 \\
 c_{24} &= 0 \\
 c_{34} &= 0
 \end{aligned}$$

4.10.8

Note that this matrix is not diagonal, leading to correlated model errors in the antenna reference frame.

As the measurement error is assumed to be uncorrelated in the antenna reference frame, the variance-covariance matrix for Tb_{meas} (C^{meas}) is diagonal in the antenna reference frame:

$$C^{meas} = \begin{pmatrix} \sigma_{A1_{meas}}^2 & 0 & 0 & 0 \\ 0 & \sigma_{A2_{meas}}^2 & 0 & 0 \\ 0 & 0 & \sigma_{A3_{meas}}^2 & 0 \\ 0 & 0 & 0 & \sigma_{A4_{meas}}^2 \end{pmatrix}$$

4.10.9

where

$$\sigma_{A1_{meas}}^2, \sigma_{A2_{meas}}^2, \sigma_{A3_{meas}}^2, \sigma_{A4_{meas}}^2$$

are the variances of the Tb_{meas} components ($A1_{meas}, A2_{meas}, A3_{meas}, A4_{meas}$) in the antenna reference frame. The value of the measurement uncertainty is given in the L1 output product.

Finally, since errors are assumed to be Gaussian, the variance covariance matrix of Tb (C_{Tb}) in the antenna reference frame is given by:

$$C_{Tb} = C^{meas} + C_{Ant}^{mod}$$

4.10.10

In a first approach, the correlations are neglected and the C_{Tb} matrix is assumed to be diagonal:

$$C_{Tb} = \begin{pmatrix} \sigma_{A1meas}^2 + \sigma_{A1model}^2 & 0 & 0 & 0 \\ 0 & \sigma_{A2meas}^2 + \sigma_{A2model}^2 & 0 & 0 \\ 0 & 0 & \sigma_{A3meas}^2 + \sigma_{A3model}^2 & 0 \\ 0 & 0 & 0 & \sigma_{A4meas}^2 + \sigma_{A4model}^2 \end{pmatrix} \quad 4.10.11$$

We have above described the full polarization case, which is the more complex case. In the case of dual polarization mode, only the first sub matrix 2x2 has to be considered, so the final C_{Tb} matrix is:

$$C_{Tb} = \begin{pmatrix} \sigma_{A1meas}^2 + \sigma_{A1model}^2 & 0 \\ 0 & \sigma_{A2meas}^2 + \sigma_{A2model}^2 \end{pmatrix} \quad 4.10.12$$

The cost function to be minimized is then the same than in eq. 4.10.2, with

$$\sigma_{Tb}^2 = \sigma_{Ameas}^2 + \sigma_{Amodel}^2 \quad 4.10.13$$

The theoretical error σ_{P_i} on the geophysical parameter P_i is computed by the Levenberg and Marquardt algorithm as follows:

$$\begin{bmatrix} \sigma_{P1} \\ \dots \\ \sigma_{PM} \end{bmatrix} = \sqrt{\text{diag}(M^{-1})} \quad 4.10.14$$

M is the pseudo-Hessian, with:

$$M = F^T C_0^{-1} F \quad 4.10.15$$

where C_0 is the covariance matrix,

$$\text{diag}(C_0) = \begin{bmatrix} \sigma_{A1}^2 \\ \dots \\ \sigma_{AN}^2 \\ \sigma_{P10}^2 \\ \dots \\ \sigma_{PM0}^2 \end{bmatrix} \quad 4.10.16$$

F is the Jacobian,

$$F = \left(\frac{\partial A_n^{\text{mod}}}{\partial P_i} \right)_{\substack{n=1, \dots, N \\ i=1, \dots, M}} \quad \mathbf{4.10.17}$$

and the superscript \top is the transpose operator.

4.10.1.1.3 Parameters to be retrieved:

Different parameters P_j can be adjusted/retrieved (SSS + up to 5) in the iterative convergence. We list here those that for each case are (or can be) adjusted during the iteration process, with a different impact on the SSS retrieval that depends on the weight (associated error) introduced in the cost function.

<i>Roughness model</i>	<i>Dual pol</i>	<i>Full pol</i>
1. Two-scale	SSS SST TEC WSx WSy	SSS SST TEC WSx WSy

The exact definition of these parameters, in terms of what auxiliary data (see ECMWF SMOS DPGS Interface, XSMS-GSEG-EOPG-ID-06-0002) will be used in the retrieval process, is indicated in the variables list (section 1.2 of this ATBD).

The User Data Product (UDP, see section 6) contains, for each grid point, two salinity values (SSS_corr with an applied land sea correction and SSS_uncorr without any land sea correction) retrieved through iterative convergence using the first (Two-scale) roughness model, as well as one SST and one WS value obtained from the ECMWF auxiliary data files. The User Data Product also contains an anomaly value of SSS computed from the SSS_corr and World Ocean Atlas 2009 climatology, SSS_{WOA} as a reference.

In the Data Analysis Product (DAP, see section 6) two additional SSS values are provided: SSS2 computed from the SSA model and SSS3 computed from the empirical roughness model.

4.10.1.2 Mathematical description of algorithm

Mathematically equation 4.10.2 (including model error) can be written as follows:

$$\chi^2 = (T_b^{\text{meas}} - T_b^{\text{mod}}(\theta, \vec{P}_j))^T C_{T_b}^{-1} (T_b^{\text{meas}} - T_b^{\text{mod}}(\theta, \vec{P}_j)) + (P_j^{\text{prior}} - P_j)^T C_{P_j}^{-1} (P_j^{\text{prior}} - P_j) \quad \mathbf{4.10.18}$$

Where the Tb_{meas} are the N_m observations performed at different incidence angles, T represents the transposition operation, and C_{Tb} is the variance/covariance matrix for Tb . The diagonals of this matrix are the quadratic sum of the radiometric sensitivity of Tb measurements and of the model error. In this first approach, off diagonal elements are neglected in the antenna frame.

P_j are different parameters that should be retrieved, P_j^{prior} are the a priori knowledge of the parameters (obtained from models or satellites, the auxiliary information), and C_{Pj} is the variance/covariance matrix of these parameters. The diagonal of the matrix are the uncertainties on the a priori parameters.

Finally, the above equation can be expressed as follows:

$$\chi^2 = (X - X_{mod})^T C_z^{-1} (X - X_{mod}) \quad 4.10.19$$

Where the matrix C_z is built by aligning along the main diagonal the matrixes C_{Tb} and C_{Pj} ; the vector X has a $N_m + N_p$ length and consists of:

$$X = \begin{pmatrix} Tb(1) \\ Tb(2) \\ \dots \\ Tb(Nm) \\ P_{prior}(1) \\ P_{prior}(2) \\ \dots \\ P_{prior}(Np) \end{pmatrix} \quad 4.10.20$$

where P_{prior} is the a priori information of the parameter; X_{mod} has the same length as X and is defined as:

$$X_{\text{mod}} = \begin{pmatrix} T_b^{\text{mod}}(1, p) \\ T_b^{\text{mod}}(2, p) \\ \dots \\ T_b^{\text{mod}}(Nm, p) \\ p(1) \\ p(2) \\ \dots \\ p(Np) \end{pmatrix} \quad 4.10.21$$

Where P is the array of parameters to be retrieved that will change at each iteration. For the first iteration P is set to the first guess.

Let's call a the vector of Np parameters to be retrieved (for example $a = [SSS, SST, WS, Hs, \Omega]$).

Sufficiently close to the minimum the cost function is approximated by a quadratic form:

$$\chi^2(a) = \gamma - d \cdot a + \frac{1}{2} \cdot a \cdot D \cdot a \quad 4.10.22$$

Then jumping from current trial parameters a_{cur} (equal to a first guess value for step 0) to a minimizing one a_{min} is done by the inverse Hessian method:

$$a_{\text{min}} = a_{\text{cur}} + D^{-1} \cdot [-\nabla \chi^2(a_{\text{cur}})] \quad 4.10.23$$

But if the minimum functions could not be approximated by a quadratic form, a *steepest decent method* has to be used:

$$a_{\text{next}} = a_{\text{cur}} + \text{constant} \nabla \chi^2(a_{\text{cur}}) \quad 4.10.24$$

The gradient (d) and the Hessian (D) of χ^2 needs to be calculated:

$$d = \frac{\partial \chi^2}{\partial a_k} \quad D = \frac{\partial^2 \chi^2}{\partial a_k \partial a_l} \quad 4.10.25$$

Let,

$$\alpha_{kl} = \frac{1}{2} D \quad \beta_k = -\frac{1}{2} d \quad 4.10.26$$

The *inverse Hessian method* can then be written as:

ARGANS Ltd.

$$\sum_{i=0}^{Nm-1} \alpha_{kl} \delta a_l = \beta_K \quad 4.10.27$$

and the *steepest decent method* can be rewritten as:

$$\delta a_k = \text{constant} \times \beta_k \quad 4.10.28$$

With $\delta a = a_{\min} - a_{\text{cur}}$ or $\delta a = a_{\text{next}} - a_{\text{cur}}$ and $k \in [0: Np-1]$

The Levenberg & Marquardt method put forth a method for varying smoothly between the extremes of the *Inverse-Hessian method* and the *steepest descent method* using a factor λ . This factor will replace the constant term in the *steepest descent method*:

$$\delta a_k = \frac{1}{\lambda \alpha_{kk}} \beta_k \quad \text{with } k \in [0: Np-1] \quad 4.10.29$$

and then if we define a new matrix α' , by the following prescription:

$$\begin{cases} \alpha'_{jj} = \alpha_{jj}(1 + \lambda) \\ \alpha'_{jk} = \alpha_{jk} \quad (j \neq k) \end{cases} \quad 4.10.30$$

the two methods can be expressed as:

$$\sum_{i=0}^{Nm-1} \alpha'_{kl} \delta a_l = \beta_K \quad 4.10.31$$

When λ is very large, the matrix α' is forced into being diagonally dominant, so method is like *steepest descent method* and as λ approaches 0 method is like *Hessian gradient method*.

Given an initial guess for the set of fitted parameters a , the iterative method consists of:

- 1) Compute $\chi^2(a)$.
- 2) Select an initial modest value for λ_{ini} , say $\lambda_{ini} = 0.001$.
- 3) Solve the linear equations for δa and evaluate $\chi^2(a + \delta a)$.
- 4) If $\chi^2(a + \delta a) \geq \chi^2(a)$, increase λ by a factor Kd and go back to 3.
- 5) If λ becomes greater than a threshold Tg_lambda_diaMax the iteration should be stopped and a flag Fg_ctrl_marq raised.

- 6) If $\chi^2(a + \delta a) < \chi^2(a)$, decrease λ by a factor K_d update the trial solution $a = a + \delta a$ and go back to 3.

(Press, 1986; Marquardt 1963). (See also 'Retrieval Concept and Architecture for Sea Surface Salinity Retrieval for SMOS Mission' document from the CCN2 of contract 16027/02/NL/GS):

This iteration loop should be stopped when both convergence tests are accomplished, logical 'AND':

- Convergence test 1: If χ^2 is decreased with respect the previous iteration by less than a threshold δ_χ as an absolute value:

$$\text{abs}(\chi_{i+1}^2 - \chi_i^2) / \chi_i^2 < \delta_\chi \quad 4.10.32$$

where i is the iteration.

- Convergence test 2: If the relative parameter variation from one iteration to another is lower than the threshold δ_{sig} (i is the iteration):

$$\max\left(\frac{|p_{i+1} - p_i|}{\sigma_{prior}}\right) < \delta_{sig} \quad 4.10.33$$

where i is the iteration.

These thresholds and λ_{ini} are configurable.

If the number of iterations $Dg_num_iter_X$ reaches Tg_it_max then the flag $Fg_ctrl_reach_maxiter_X$ ($X = 1, 2, 3$ Acard as it can be different for the three forward models plus cardioid) are set to true and the output value of the process, are set to the value obtained in the last iteration.

No boundaries will be applied in the inversion process, therefore the retrieved parameters should be considered as effective values, since they could result in physically impossible values (i.e. negative wind speeds).

A test of retrieval quality will be performed, by comparing the value of the normalised cost function at the last iteration χ^2 with a threshold Tg_chi2 . If $Dg_chi2 = \chi^2 / NFD < Tg_Q\chi$ then the flag Fg_ctrl_chi2 should be set to 0 (good quality). Elsewhere it should be set to 1 remarking the low quality of the retrieval. NFD is the number of degrees of freedom (NFD = number of measurements).



Another test to be performed is: **Chi2_P**, main goodness of fit indicator; is the χ^2 high end acceptability probability. This is the probability that no anomaly occurred about the fit.

This figure is given by:

$$Dg_chi2_P = P(NFD/2, Dg_chi2*NFD/2) \quad \mathbf{4.10.34}$$

where P is the regularised gamma function.

With NFD in the range of several tens, Dg_chi2_P should go up to a high percentage when Dg_chi2 exceeds a value around 1.3 to 1.4. Note that very low values of Dg_chi2_P (when Dg_chi2_X is "too small") are suspicious also, as they raise the possibility of correlated noise which would be unduly fitted by the direct model.

The table below illustrates the values of 1 - Dg_chi2_P (= 1- P = Q the regularised upper incomplete gamma function) against χ^2/NFD (cost function normalized by the number of degrees of freedom) values.

χ^2/NFD	0.50	0.55	0.60	0.65	0.70	0.75	0.80	0.85	0.90	0.95	1.00	1.05	1.10	1.15	1.20	1.25	1.30	1.35	1.40	1.45	1.50	
NFD																						
8	.857	.819	.779	.736	.692	.647	.603	.558	.515	.473	.433	.395	.359	.326	.294	.265	.238	.213	.191	.170	.151	
10	.891	.855	.815	.772	.725	.678	.629	.580	.532	.485	.440	.398	.358	.320	.285	.253	.224	.197	.173	.151	.132	
12	.916	.883	.844	.801	.753	.703	.651	.598	.546	.495	.446	.399	.355	.314	.276	.241	.210	.182	.157	.135	.116	
15	.942	.913	.878	.835	.787	.735	.679	.622	.564	.507	.451	.399	.350	.304	.263	.225	.192	.163	.137	.115	.095	
20	.968	.946	.916	.877	.830	.776	.717	.653	.587	.522	.458	.397	.341	.289	.242	.201	.166	.135	.109	.088	.070	
25	.982	.966	.941	.907	.863	.809	.747	.679	.607	.534	.462	.394	.331	.275	.224	.181	.144	.113	.088	.068	.052	
30	.990	.978	.959	.929	.888	.835	.772	.700	.623	.544	.466	.391	.323	.261	.208	.163	.126	.096	.072	.053	.039	
35	.994	.986	.970	.945	.908	.857	.794	.719	.638	.553	.468	.388	.314	.249	.193	.147	.110	.081	.058	.041	.029	
40	.997	.991	.979	.957	.923	.875	.812	.736	.651	.561	.470	.384	.306	.238	.180	.134	.097	.069	.048	.033	.022	
45	.998	.994	.985	.967	.936	.891	.829	.752	.663	.568	.472	.381	.298	.227	.168	.121	.085	.059	.039	.026	.017	
50	.999	.996	.989	.974	.947	.904	.843	.765	.674	.574	.473	.377	.291	.217	.157	.110	.075	.050	.032	.020	.013	
60	1.00	.998	.994	.984	.963	.925	.868	.790	.693	.586	.476	.371	.277	.199	.138	.092	.059	.037	.022	.013	.007	
70	1.00	.999	.997	.990	.973	.941	.888	.810	.711	.596	.478	.364	.265	.183	.121	.077	.047	.027	.015	.008	.004	
80	1.00	1.00	.998	.994	.981	.954	.904	.828	.726	.606	.479	.358	.253	.169	.107	.065	.037	.020	.011	.005	.003	
90	1.00	1.00	.999	.996	.986	.963	.918	.844	.740	.615	.480	.352	.242	.156	.095	.054	.029	.015	.007	.003	.002	



100	1.00	1.00	.999	.997	.990	.971	.930	.858	.753	.623	.481	.346	.232	.145	.084	.046	.024	.011	.005	.002	.001
110	1.00	1.00	1.00	.998	.993	.977	.939	.870	.765	.630	.482	.341	.223	.134	.075	.039	.019	.009	.004	.001	.001
120	1.00	1.00	1.00	.999	.995	.981	.948	.881	.776	.637	.483	.336	.214	.125	.067	.033	.015	.006	.003	.001	.000

For example, for NFD=120 and $\chi^2/NFD=1.25$, the probability of a correct fit (with a Gaussian noise on the sample) amounts to 0.033. There are 96.7% of chances that a problem happened during the retrieval.

Then the following test will be done to control the quality of the retrieval: If $Tg_chi2_P_min < Dg_chi2_P_X < Tg_chi2_P_max$ then the flag $Fg_ctrl_chi2_P_X$ should be set to 0 (good quality). Elsewhere it should be set to 1 remarking the low quality of the retrieval.

4.10.1.3 Error budget estimates (sensitivity analysis)

The algorithm will iterate until χ^2 decreases less than a threshold between two consecutive iterations and the change in the parameter between successive iterations is lower than a threshold. Another reason to stop the iterative process is if the number of iterations is higher than a previously defined Tg_it_max .

Therefore, it is impossible to obtain better results if any of the two conditions described above have been accomplished.

4.10.2 Practical considerations

An external file will provide what first guesses we want to use (maybe prior values + something else specified in this external file)

If the two polarizations are used in the retrieval, the vector Tb_i^{meas} should contain first the measured Tb_{hh} at different incidence angles and secondly the Tb_{vv} for the different Tb_i . The same for Tb_i^{model} .

In the case of performing the retrieval with the 1st Stokes, then Tb_i^{meas} is a vector that contains the 1st Stokes (Tb_h+Tb_v) for the different incidence angles. The same for Tb_i^{model} . The model uncertainty is then given by:

$$\sigma^2_{ST1_model} = \sigma^2_{Th_model} + \sigma^2_{Tv_model} \tag{4.10.35}$$

The uncertainty is assumed to be the same in the Earth reference frame and in the antenna reference frame.

In ATBD issue 2.0 a new module has been introduced to retrieve a pseudo-dielectric constant using the cardioid model (see section 4.12). All the procedures described here for the SSS retrieval will be also applied to this new variable.

4.10.2.1 Quality control and diagnostics

If convergence is not achieved after Tg_it_max iterations, that is, if once Tg_it_max iterations are performed the condition $(\chi_{i+1}^2 - \chi_i^2) / \chi_i^2 < \delta_\chi$ is not true, then the flag Fg_ctrl_reach_maxiter_X should be raised, and the parameters given by the algorithms should be the value obtained in the last iteration.

For each of the different runs of the iterative scheme in parallel the following test should be done and raise the appropriate flags, which will be reported in the User Data Product:

- 1) Check if SSS retrieved is in the expected range (Tg_SSS_max, Tg_SSS_min). If the retrieved salinity value is outside the range then raise the flag Fg_ctrl_range_X (where X is 1, 2 or 3, for each roughness model).
- 2) Compute σ_{SSRet} of the retrieved SSS. Compare this σ_{SSRet} with a threshold, Tg_sigma_max. If σ_{SSRet} is higher than the threshold then the flag Fg_ctrl_sigma_X should be raised.
- 3) Compare the value of χ^2 at the last iteration, Dg_chi2_X, with the threshold Tg_Q χ . If Dg_chi2_X > Tg_Q χ (bad quality retrieval) then the flag Fg_ctrl_chi2_X should be raised.
- 4) Compare the value Dg_chi2_P_X, with the threshold Tg_chi2_P_max and Tg_chi2_P_min. If Dg_chi2_P_X < Tg_chi2_P_min or Dg_chi2_P_X > Tg_chi2_P_max (bad quality retrieval) then the flag Fg_ctrl_chi2_P_X should be raised.
- 5) Check if the overall retrieval should be considered as successful. If retrieval failed due to a processing error (Fg_ctrl_retriev_fail_X set), or the convergence algorithm failed (Fg_ctrl_reach_maxiter_X or Fg_ctrl_marq_X set), or any of the above flags (ie Fg_ctrl_range_X, Fg_ctrl_sigma_X, Fg_ctrl_chi2_X, or Fg_ctrl_chi2_P_X set), then raise the flag Fg_ctrl_poor_retrieval_X (nominal behaviour specified by "Poor_quality" & "Poor_quality_Acard" filters). This flag is also raised if Fg_ctrl_valid_X is not raised, so users can select successfully retrieved data by filtering retrievals where Fg_ctrl_poor_retrieval_X is not raised (ie = 0).
- 6) Check if there are specific geophysical conditions that may contribute to poor quality salinity retrieval. If there are many outliers (Fg_ctrl_many_outliers_X set), sun or moon glint suspected (Fg_ctrl_sunlint_X or Fg_ctrl_moonglint_X set), galactic noise/glint detected (Fg_ctrl_gal_noise_X set), a low number of measurements (Fg_ctrl_num_meas_low_X set), high TEC gradient (Fg_sc_TEC_gradient_X set), ice or rain suspected (Fg_sc_suspect_ice or Fg_sc_rain set), or any Fg_OoR_RoughX_Y flags set, then raise the flag Fg_ctrl_poor_geophysical_X. (nominal behaviour specified by "Poor_geophysical")

ARGANS Ltd.

Commercial in Confidence

Page 176

Use, duplication, or disclosure of this document or any information contained herein is subject to the restriction on the title page of this document.



& “Poor_geophysical_Acard” filters). This flag is also raised if Fg_ctrl_valid_X is not raised, so users can select retrieved data where no geophysical problems have been detected by filtering retrievals where Fg_ctrl_poor_geophysical_X is not raised (ie = 0).

- 7) The obsolete flag (Fg_ctrl_quality_SSSX) is retained for backward compatibility and is raised if either Fg_ctrl_poor_retrieval_X or Fg_ctrl_poor_geophysical_X are raised.

Users may select data from the UDP successfully retrieved data where no geophysical problems have been detected by filtering for all retrievals where Fg_ctrl_poor_retrieval_X and Fg_ctrl_poor_geophysical_X are not raised (i.e. both flags = 0).

An overall quality assessment for the two different salinities retrieved for each grid point (SSS_corr and SSS_uncorr) is needed to decide which of them is the best. General quality descriptors (Dg_quality_SSS_corr, Dg_quality_SSS_uncorr), incorporated into the User Data Product, are defined for all those grid points with Fg_ctrl_poor_retrieval_X not raised (i.e. only for successful retrievals – all others contain an out-of-range value = 999) as follows:

We consider the following error categories:

- Effect of radiometric noise and *a priori* uncertainties
- Instrument, calibration, reconstruction
- External sources (galactic noise, sun, RFI, ...)
- Forward models.

A quality index Dg_quality_SSSX is built by combining error contributions C_i , using scaling coefficients SC_i . Errors in terms of T_b are accounted for using the sensitivity function $dSSS/dT_b$, noted dS_dT , estimated from nadir simulations with Klein and Swift model (**Figure 12**). Only the SST dependence is considered. We use a linear fit for $dT_b/dSSS$, which results in:

$$dS_dT = 1/(dT_b/dSSS) = 1/(dT_dS_0 + dT_dS_1 * SST), \text{ with } dT_dS_0 = -0.224, \text{ and } dT_dS_1 = -0.0157$$

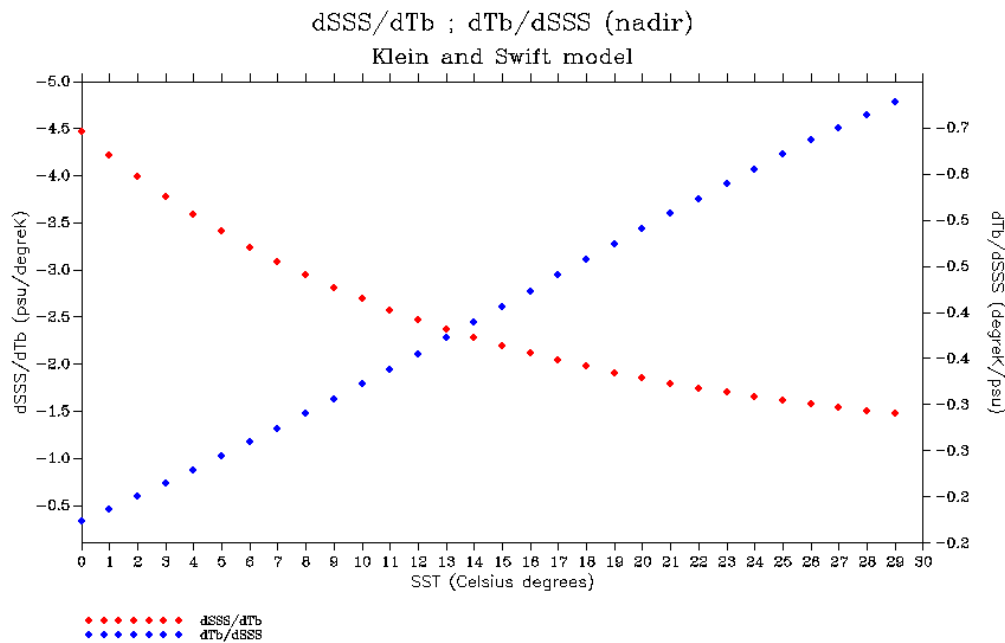


Figure 12 - Sensitivity functions dSSS/dTb and dTb/dSSS vs. SST at nadir from Klein and Swift model

Uncertainty origin	Driver D	Contribution to Dg_quality_SSS	Init Sci value	Sci unit	Comments
Instrument	$D = \text{abs}(Dg_X_swath)$	$SC11 * D * dS_dT$	0.2	K km ⁻¹	
Instrument	$D = \text{mean}(L1c \text{ Pixel_Radiometric_Accuracy}) / Dg_num_meas_l1c$	$SC21 * D * dS_dT$	10	K	
Goodness of fit	$D = Dg_chi2_X$	$SC22 * D * dS_dT$	10	K	
Calibration	Unknown for now	$SC23 * dS_dT$	0	K	
Position in FOV	If $((Dg_border_fov / Dg_num_meas_l1c) > SC24)$ then $D = 1$	$SC26 * D * dS_dT$	0.30', 100	dl, K	



Uncertainty origin	Driver D	Contribution Ci to Dg_quality_SSS	Init Sci value	Sci unit	Comments
Position in FOV	If $((Dg_af_fov / Dg_num_meas_l1c) < SC25)$ then $D=1$	$SC27 * D * dS_dT$	0.30 , 100	dl, K	
Outliers	$D = Dg_num_outliers / Dg_num_meas_l1c$	$SC32 * D * dS_dT$	40	K	1 K for 10%
L1 sun glint	$D = Dg_sunglint_L1 / Dg_num_meas_l1c$	$SC33 * D * dS_dT$	100	K	1 K for 10%
L2 sun glint	$D = Dg_sunglint_L2 / Dg_num_meas_l1c$	$SC34 * D * dS_dT$	100	K	1 K for 10%
Moon glint	$D = Dg_moonglint / Dg_num_meas_l1c$	$SC35 * D * dS_dT$	40	K	1 K for 10%
Sky	$D = Dg_sky / Dg_num_meas_l1c$	$SC36 * D * dS_dT$	40	K	0.5 K for 10%
Coast	$D=1$ if $Fg_sc_land_sea_coast1=T$ and $Fg_sc_land_sea_coast2=T$, $D=0$ otherwise	$SC41 * D * dS_dT$	40	K	
Rain	$D=0/1$ if $Fg_sc_rain = F/T$	$SC42 * D * dS_dT$	40	K	
Ice	$D = Dg_suspect_ice / Dg_num_meas_l1c$	$SC43 * D * dS_dT$	40	K	1 K for 10%
High wind	$D=1$ if $Fg_sc_low_wind = F$ and $Fg_sc_high_wind = T$, 0 otherwise	$SC44 * D * dS_dT$	24	K	
Low wind	$D=1$ if $Fg_sc_low_wind = F$ and $Fg_sc_high_wind = F$, 0 otherwise	$SC45 * D * dS_dT$	24	K	
High SST	$D=1$ if $Fg_sc_low_SST = F$ and $Fg_sc_high_SST = T$, 0 otherwise	$SC46 * D * dS_dT$	24	K	
Low SST	$D=1$ if $Fg_sc_low_SST = F$ and $Fg_sc_high_SST = F$, 0 otherwise	$SC47 * D * dS_dT$	24	K	
High SSS	$D=1$ if $Fg_sc_low_SSS = F$ and $Fg_sc_high_SSS = T$, 0 otherwise	$SC48 * D * dS_dT$	0	K	
Low SSS	$D=1$ if $Fg_sc_low_SSS = F$ and $Fg_sc_high_SSS = F$, 0 otherwise	$SC49 * D * dS_dT$	0	K	
Sea state 1	$D=1$ if $Fg_sc_sea_state_1 = T$, 0 otherwise	$SC50 * D * dS_dT$	0	K	
Sea state 2	$D=1$ if $Fg_sc_sea_state_2 = T$, 0 otherwise	$SC51 * D * dS_dT$	0	K	
Sea state 3	$D=1$ if $Fg_sc_sea_state_3 = T$, 0 otherwise	$SC52 * D * dS_dT$	0	K	

ARGANS Ltd.

Commercial in Confidence

Uncertainty origin	Driver D	Contribution Ci to Dg_quality_SSS	Init SCi value	SCi unit	Comments
Sea state 4	D=1 if Fg_sc_sea_state_4=T, 0 otherwise	SC53*D*dS_dT	0	K	
Sea state 5	D=1 if Fg_sc_sea_state_5=T, 0 otherwise	SC54*D*dS_dT	0	K	
Sea state 6	D=1 if Fg_sc_sea_state_6=T, 0 otherwise	SC55*D*dS_dT	0	K	
SST front	D=0/1 if Fg_sc_SST_front=F/T	SC56*D*dS_dT	0	K	
SSS front	D=0/1 if Fg_sc_SSS_front=F/T	SC57*D*dS_dT	0	K	

Table 3 – Contributions to the global salinity quality index Dg_quality_SSS

The global salinity quality index Dg_quality_SSSX is given by the quadratic sum of all contributions listed in **Table 3**.

$$Dg_{quality_{SSX}} = \sqrt{\sum_i C_i^2} \quad 4.10.36$$

SCi coefficients values are given in the TGRD and will be updated during the mission. The SSSX with lowest value for this index will be considered the best one.

A similar global quality index must be built for the cardioid model case. Until this is not defined, the descriptor Dg_quality_Acard will be set to 0.

5.9.2.2 Parameters update

In the iterative convergence process several parameters are retrieved depending on the roughness model used (see section 4.10.1.1). In general, we will assume that retrieved parameters are not correlated; thence guessed values at step n can be updated with parameters retrieved at step n-1.

In case of roughness model 1, retrieved wind components WSx (positive eastward) and WSy (positive northward) will be used to update wind speed and direction to estimate Tb^{mod}, as:

$$WS_n = \sqrt{WS_x^2 + WS_y^2} \quad 4.10.37$$

with $\phi_w = \arctan(WS_y/WS_x)$.

ARGANS Ltd.

Commercial in Confidence

Page 180

Use, duplication, or disclosure of this document or any information contained herein is subject to the restriction on the title page of this document.

4.10.3 Assumption and limitations

We are assuming that all the measurement errors are Gaussian and that all the parameters follow a Gaussian distribution. Filtering with different algorithms without any assumption about the error and/or considering the consistency between measurements within a SMOS sub-cycle are currently under study (Olmedo et al. 2017, Kolodziejczyk et al., 2016).

If the number of measurements **Dg_num_meas_valid** of a grid point (observed with different incidence angles) is less than **Tg_num_meas_min**, then the inversion process cannot be performed (see section 3, Measurement discrimination). This is because with not enough measures, the inversion process could lead to retrieved values with an unacceptable precision.

References

Gabarró, C., Vall-llossera, M., Font, J., and Camps, A. (2004b). Determination of Sea Surface Salinity and Wind Speed by L-band Microwave Radiometry from a fixed Platform. *International Journal of Remote Sensing*, 25(1):111–128.

Kolodziejczyk, N., J. Boutin, J.-L. Vergely, S. Marchand, N. Martin, and G. Reverdin (2016), Mitigation of systematic errors in SMOS sea surface salinity, *Remote Sensing of Environment*, doi:http://dx.doi.org/10.1016/j.rse.2016.02.061.

Marquardt, D. (1963). An algorithm for least-squares estimation of non-linear parameters. *Journal on Applied Mathematics*, 11(2):431–441.

Press, W., Teukolsky, S., Vetterling, W., Fannery, B. (1986) *Numerical Recipes*. Cambridge University Press.

Olmedo, E., Martínez, J., Turiel, A., Ballabrera-Poy, J. Portabella, M., (2017) *Debiased non-Bayesian retrieval: A novel approach to SMOS Sea Surface Salinity*, *Remote Sensing of Environment*, Vol. 193, 103-126.

Sabia, R., Camps, A., Vall-llossera, M., Reul, N. (2006) Impact on sea surface salinity retrieval of different auxiliary data within the SMOS mission. *IEEE Transactions on Geoscience and Remote Sensing*, 44(10): 2769 - 2778.

Waldteufel, P., Boutin, J., Kerr, Y. (2003) Selecting an optimal configuration for the Soil Moisture and Ocean Salinity mission. *Radio Science*, Vol. 38, No. 3, 8051, doi:10.1029/2002RS002744.

Yin X., Boutin J., Spurgeon P. (2012), First Assessment of SMOS Data Over



Open Ocean: Part I—Pacific Ocean, IEEE TRANSACTIONS ON GEOSCIENCE AND REMOTE SENSING.

Zine, S., J. Boutin, J. Font, N. Reul, P. Waldteufel, C. Gabarró, J. Tenerelli, F. Petitcolin, J. L. Vergely, M. Talone, and S. Delwart (2008), Overview of the SMOS sea surface salinity prototype processor, IEEE T. Geosci. Remote Sensing, 46, 621-645.



4.11 Post-processing

Besides the nominal retrieval algorithm for SMOS L2 SSS retrieval, several operations have been identified to be introduced as improvements for the User Data Products. Those are described in the following sections.

4.11.1 SSS Anomaly computation

4.11.1.1 Introduction

The Soil Moisture and Ocean Salinity (SMOS) of the European Space Agency (ESA) (Kerr et al., 2010 and Font et al., 2010) and the Aquarius (Lagerloef et al., 2008) satellite missions, have demonstrated the capability of L-band radiometry for monitoring Sea Surface Salinity (SSS) over the global ocean from space (e.g. Reul et al., 2014 and Lagerloef, 2012). SMOS carries an L-band Microwave Interferometric Radiometer with Aperture Synthesis (MIRAS). It is the first time that such an instrument has been used to observe the earth environment from space. With respect to a classical radiometer, it provides, for a given antenna size, a much improved spatial resolution on the ground (of 43 km on average over the SMOS field of view (FOV)) and a wide field of view (Mecklenburg et al., 2012). However the radiometric accuracy of reconstructed brightness temperatures is much larger, typically 2 K, than the one achievable with a classical radiometer and systematic errors depending on the location in the field of view are expected (Font et al., 2010 and references herein). Hence calibration of such measurements remains very challenging. The analysis of SMOS data obtained with the SMOS/ESA version 5 and 6 processors have shown temporal evolution of the systematic errors in the SMOS FOV with a marked influence of the sun but also of other instrumental factors (Gourrion et al., 2011, Yin et al., 2013, Banks et al., 2016, Khazaal et al., 2016, Kolodziejczyk et al., 2016). The Ocean Target Transformation (OTT) computed in the south-east Pacific Ocean and applied in ESA version 5/6 processing allows for correction of part of these systematic errors. Nevertheless, it cannot yet fully correct for latitudinal & seasonal variations of systematic errors, likely due to flaws of the thermal antenna model (Kainulainen et al., 2012), so that seasonal biases in SMOS SSS remain in the northern latitudes (Hernandez et al., 2014) but also in the southern hemisphere where data can be affected by solar radiations. In a first attempt to correct for these large-scale biases, Reul et al. 2011 applied a large-scale correction based on regional differences between monthly SMOS SSS and the monthly World Ocean Atlas SSS climatology derived based on historical in situ observations. Hernandez et al. (2014) later applied a large-scale correction based on regional differences between monthly SMOS SSS and Argo interpolated fields (ISAS products, Gaillard, 2012). They found that the bias-corrected fields agree within 0.15 with ship SSS in the subtropical Atlantic Ocean. These very encouraging results, the current 7-year long record of SMOS measurements, and the apparent similarity of systematic errors in different years, seasons, orbit pass-type (ascending; descending) motivated the idea of producing an SSS “anomaly” field in the level 2 OS data to better reveal the un-biased SSS signal content in SMOS data.

In what follows, we first review the traditional definition of ‘anomalies’ in the context of ocean and climate sciences. In a second section, we will review the specificities of SMOS SSS and the several approaches that have been proposed by scientists in ESL and/or SMOS Level 3/4 SSS data centres to derive SSS anomalies from SMOS. In a third section, we will define the possible way forwards to evaluate an anomaly from the data in the operational ESA Level 2 processor.

4.11.1.2 Classical definition of SSS anomaly

Let us consider the time series of a sea surface salinity (SSS) signal, $S(t,r)$, at a fixed geographical point r in the ocean. Suppose that the climate mean, or norm, of $S(t,r)$ is:

$$\overline{S(t,r)} = \frac{1}{N} \sum_{n=1}^N S(t + (n-1)t_o, r) \quad 4.11.1$$

where N is several observational years and t_o is the annual time period. Notice that the averaging (1) gives us a quasi-periodic function with period t_o .

In the following, we define the SSS anomaly as the departure of the SSS from the norm:

$$\Delta S(t,r) = S(t,r) - \overline{S(t,r)} \quad 4.11.2$$

The definitions (1) and (2) can be subject to objections. For example, in some calendar year, the annual cycle of SSS variability may not have a 1-year period but instead it can be modified by delay or early onset of any season (Lappo and Gulev, 1984). Here following tradition in oceanography, we stick to the conventional average (1) and the simple removal of the annual cycle (2). It is hard to provide another formalism that would be satisfactory in different situations. However, in certain cases, it might be useful to define the annual cycle as a superposition of the annual, semi-annual, 4-month, 3-months, and so on harmonics. Another point is that the number of observational years N_o , beyond which the SSS statistics do not vary, may not be inferred from relatively short time series of ocean measurements.

4.11.1.3 The special Case of SMOS SSS data

To estimate SSS anomalies from SMOS data we face two major issues :

1) First the number of observational years $N_o \sim 7$ is rather small to reach a stable statistic for some contributions to the mean SMOS signal. The period 2009-now does include short-term (1-2 years) climatically significant SSS anomalies induced by large-scale processes such as El-Niño/La Niña impacts (2010, 2014-2016), the signatures of the Indian Ocean Dipole inversion of 2010/2011 (Durand et al., 2012) or the long-duration *saltening* observed north of the Gulf Stream (Grotsky et al., 2017). All these short-term climatic factors might affect the mean

annual cycle statistics evaluated from the relatively short in time, SMOS data time series themselves.

2) Sea Surface Salinity (SSS) acquired by the SMOS satellite mission are subject to systematic errors originating from various signal contaminations such as land contamination or solar/galactic radiation and thermal signals impact on the antenna brightness temperature. These contaminations are tentatively corrected at Level 1 and 2 but generate residual systematic errors that can reach more than 2 pss in some regions, orbital characteristic and observational conditions (e.g., close to the land with very strong spatial gradients according to the coast orientation and the across-track position within the satellite swath. Some of these contributions such as the solar/galactic radiations induce latitudinal biases (due to the orbital relative geometry of the sensor, the sun, and the galactic equator) that varies as function of the passes and the seasons.

The mean annual cycle from SMOS data is therefore containing both the 'actual' mean SSS variation $\overline{S_{SSS}(t, \mathbf{r})}$ of the ocean but also an instrument/algorithm-related annual cycle $\overline{S_{smos}(t, \mathbf{r})}$:

$$\overline{S(t, \mathbf{r})} = \overline{S_{SSS}(t, \mathbf{r})} + \overline{S_{smos}(t, \mathbf{r})} \quad 4.11.3$$

Then SSS anomalies would be expressed as

$$\Delta S(t, \mathbf{r}) = S(t, \mathbf{r}) - \overline{S(t, \mathbf{r})} = S(t, \mathbf{r}) - \overline{S_{SSS}(t, \mathbf{r})} - \overline{S_{smos}(t, \mathbf{r})} \quad 4.11.4$$

So that

$$\Delta S(t, \mathbf{r}) = \Delta S_{SSS}(t, \mathbf{r}) - \overline{S_{smos}(t, \mathbf{r})} \quad 4.11.5$$

Ideally, we would like to generate a product free of any instrumental biases in the annual cycle:

$$\Delta S_{SSS}(t, \mathbf{r}) = \Delta S(t, \mathbf{r}) + \overline{S_{smos}(t, \mathbf{r})} \quad 4.11.6$$

The solution therefore requires evaluating the instrument-related annual cycle bias: $\overline{S_{smos}(t, \mathbf{r})}$.

Several approaches have been discussed in the ESLs to evaluate $\Delta S_{SSS}(t, \mathbf{r})$ and the instrumental biases $\overline{S_{smos}(t, \mathbf{r})}$. Of those, the following method has been selected after testing.

4.11.1.4 SMOS-based climatology production

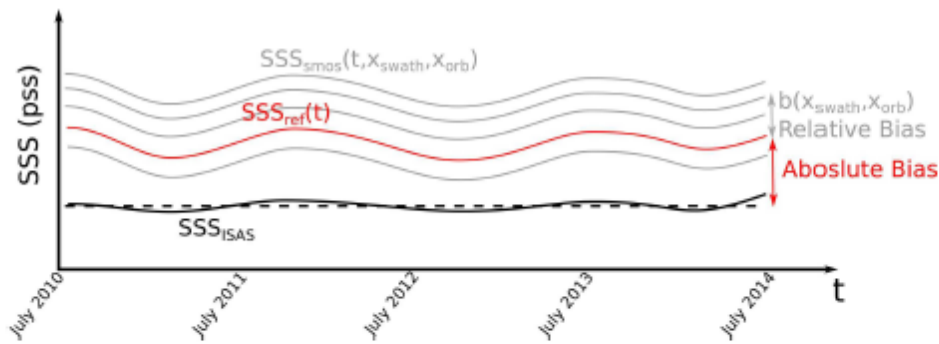
This method, referred to O1 (Kolodziejczyk et al., 2016), was thought to remove systematic biases, by considering as parameter SSS behaviour as function of the distance from the centre of the swath and by evaluating the anomaly in 2 steps:

Step 1: a relative correction is evaluated per dwell lines

Step 2: an absolute correction is evaluated with respect the ISAS 4 years mean

Step 1:

In that method, the 3-years mean bias is estimated between the dwell lines signal at a fixed across swath location X_{swath} and a reference salinity S_{ref} :



$$S_{smos}(t, r(X_{swath}), X_{orb}) = S_{ref}(t) - \overline{b(X_{swath}, X_{orb})}. \quad 4.11.7$$

S_{smos} is the instantaneous (daily) salinity at each time, t , at each across-track distance to the satellite track, X_{swath} , and for each orbit, X_{orb} . S_{ref} is the temporal variation (in relative value) of SSS, and b the relative bias estimated for each distance to the satellite track and each orbit orientation (independent on time).

This equation is solved using a Bayesian least square minimization with an a priori value computed from the median value of SMOS SSS of the central dwell computed at each grid point over the entire period. SSS in this central dwell is chosen as prior because this dwell-line contains the largest number of TB pertaining to the alias free field of view and because the spatial extension of the coast bias is reduced in this FOV region (Vergely et al., 2013).

The method does not only correct biases but also looked at the dwell line closer to ISAS, as a metric. Results showed that the so-obtained anomalies are substantially better than without performing any debiasing. However, biases are not stable, so outside the period used to generate the climatology, the correction loses performance. All the study was done

ARGANS Ltd.



considering a range between 45°N and 45°S in latitude and adding together ascending and descending. The anomalies showed better standard deviation of differences than when comparing directly SMOS with ISAS.

Step 2:

The estimated Sref is a relative estimate of the SSS temporal variability at each grid point, filtered out from outliers and corrected from a relative systematic inter-dwell and inter-orbit biases, b . The final step consists in the adjustment of the 4-year mean SSS ref on a 4 year mean SSS climatology. The climatology is taken from four years (July 2010 to June 2014) median average of ISAS SSS fields interpolated at each SMOS L3 grid point. For each grid point, the correction b_{abs} is applied on each individual SSS from SSS time series:

$$b_{abs} = \langle \text{ISAS} \rangle - \langle \text{SREF} \rangle$$

where $\langle . \rangle$ is the median operator over 4 years of SMOS observations. This approach preserves all the temporal dynamics of SMOS SSS.

This method has a variance which is the one implemented for the generation of SSS anomalies at L2 OS and known as method 02.

In method 02, 01 is applied but one take as a reference the SMOS dwell closest to ISAS. There is no final adjustment to the ISAS 3/4-years mean: this minimize the importance of ISAS information used in producing the anomaly. The seasonal bias is estimated as a function of latitude in the Pacific Ocean.

BEC (Olmedo et al., 2016) did something like this method but they considered only a year map for the reference field to avoid removing natural seasonality in the data. BEC showed how the method, based in a smart filtering of the outliers, can remove large part of the biases.

We briefly review the K2016 methodology. The K2016 correction aims at mitigating systematic errors constant with time and was shown to efficiently correct land-sea contamination in many regions. Given the 18-day sub-cycle of SMOS, a given location over the ocean is observed with the same SMOS measurement geometry every ~ 18 days; within 18 days, it is sampled by several SMOS SSS measurements which are located at various locations across the swath, X_{swath} . The K2016 methodology considers that the long term (2013-2016) SSS variability observed by SMOS must be rather similar whatever X_{swath} and the orbit orientation X_{orb} . Relative biases, b_{rel} , with respect to a reference SSS, SSS_{ref} , are derived from SMOS SSS through a least square minimization approach, and through a series of iterations that will be described below. A consistent set of SMOS SSS, $SSSK_{2016}$, is obtained as:



$$\text{SSSK2016}(t, \phi, \lambda, X_{\text{swath}}, X_{\text{orb}}) = \text{SSSref}(t, \phi, \lambda) - \text{bland}(\phi, \lambda, X_{\text{swath}}, X_{\text{orb}}) \quad 4.11.8$$

where t is the time of the measurement, ϕ , and λ , are respectively the latitude and the longitude of the considered location over the ocean. X_{swath} is sampled within 25 km wide bins.

bland and SSSref are derived as follows.

Defining $p = (\text{SSSref}, \text{bland})^T$, p_0 the a priori values of p , y_0 the SMOS SSS, the estimated values of p , p_{est} , are derived as:

$$p_{\text{est}} = p_0 + C_p \cdot G^T \cdot (G \cdot C_p \cdot G^T + R)^{-1} \cdot [y_0 - f(p_0)] \quad 4.11.9$$

where G is the matrix of derivatives of observations with respect to the parameters (also called observational operator), R is the covariance matrix for the observation error, C_p is the covariance matrix for the a priori error on the parameters p . C_p is parametrized as a function of an acceptable standard deviation of SSS, σ_{SSSref} , over a correlation timescale τ .

The minimization is repeated four times, twice with $\tau=16$ days (corresponding to an 18-day Gaussian smoothing window), then twice with $\tau=8$ days (corresponding to a 9-day Gaussian smoothing window). At each iteration, a new set of a priori values for p and for σ_{SSSref} are computed.

During the first iteration, the a priori values of SSSref , SSSref_0 , are taken as the median of SMOS SSS at the centre of its swath over the 2013-2016 period, the a priori value of bland is equal to 0, σ_{SSSref} is taken equal to 0.3 pss, and the observation errors are taken equal to the theoretical error associated with the L2 SMOS SSS retrieval, ESSS_L2 . SSSref_1 and bland_1 are computed from the p and σ_{SSSref} solutions of the first iteration.

During the second iteration, SSS outliers, linked primarily to RFI contamination, are detected using a 3-sigma outlier detection: if the difference between the L2 SMOS SSS and $(\text{SSSref}_1 - \text{bland}_1)$ is larger than 3 times ESSS_L2 , the error on the measurement indicated in the matrix R is artificially increased. SSSref_2 and bland_2 , estimated at the end of step 2, are used to produce the 18-day SSSK2016 fields. The third and fourth iterations aims at optimizing SSSref and bland at 9-day resolution. During the third iteration, SSSref_2 and bland_2 are taken as a priori parameters, τ is reduced to 8 days and σ_{SSSref} is increased to 0.5 pss resulting in SSSref_3 and bland_3 . The fourth step leading to SSSref_4 and bland_4 is like the second one using the same a priori values as in step 3. At the end, an additional term is added to the estimated bias, to ensure that the 4-year (2013-2016) median average of SSSK2016 equals the 4-year median average of ISAS SSS for each latitude and longitude:



$$b_{land}(\phi, \lambda, X_{swath}, X_{orb}) = b_{landx}(\phi, \lambda, X_{swath}, X_{orb}) - (\text{med}(\text{SSS}_{ref}(t, \phi, \lambda)) - \text{med}(\text{SSS}_{ISAS}(t, \phi, \lambda))) \quad \mathbf{4.11.10}$$

with b_{landx} equals to b_{land2} in the case of 18-day corrected field estimates, or to b_{land4} in the case of 9-day corrected fields. Note that the last term of Equation (3) is the only external information used in the entire correction process and does not modify the temporal variability of the observed fields.

This method is applied to correct SSS before L3 averaging at CATDS (CEC LOCEAN and C-PDC processing). The correction is purely static (no time dependency). Contrary to the CATDS, no latitudinal correction is applied.

The data used for this experimentation are :

- Reference SSS : ISAS.
- L2OS products : v662 DPGS products (with Joe Tenerelli TB filtering).
- 4 years of data: 2013, 2014, 2015, 2016.

Geophysical filters

- No filtering is used at this level. We consider potentially that the biases coming from RFI or other sources can be totally or partially corrected. The idea is that, in some cases, even if the biases are important, the expected signal could be meaningful (for instance, if we expect a SSS anomaly of 10 psu, a 1 or 2 psu bias could be acceptable).
- No average is done with closest neighbours. Retrieval is applied strictly at each ISEA grid point.

Retrieval filters

- The filtering is done dynamically in 2 steps. A first SSS and inter-dwell bias retrieval is done over a 18 days slipping windows (applied in a least square context). A 3-sigma detection is applied allowing to remove the influence of the L2 SSS which are too far from the expected SSS (SSS are not completely removed but associated errors are increased). A second SSS and inter-dwell bias estimation is performed.

Geometrical filter

- Selection of data close to the track with $\text{abs}(X_{swath}) < 400\text{km}$
- The X_{swath} sampling is 25 km.

LUTs for SSS anomaly computation (NetCDF format) :

ARGANS Ltd.

Commercial in Confidence

Page 189

Use, duplication, or disclosure of this document or any information contained herein is subject to the restriction on the title page of this document.



- SMOSmean_corrTB_A : correction for L2OS SMOS SSS from corrected TB, ascending orbit.
- SMOSmean_corrTB_D : correction for L2OS SMOS SSS from corrected TB, descending orbit.
- SMOSmean_nocorrTB_A: correction for L2OS SMOS SSS from uncorrected TB, ascending orbit.
- SMOSmean_nocorrTB_D: correction for L2OS SMOS SSS from uncorrected TB, descending orbit.

LUT content:

- NetCDF fields:
- GPID, lat, lon
- Xswath
- chi2_tot -> not to use
- chi2
- SSSoutlier_dwell
- SSSmean

Using the LUT:

The way to use LUTs is as follows (for a given grid point GP) :

1/ select the LUT corresponding to the orbit direction (A or D) and to the L2OS SSS (with or without TB correction).

2/ extract SSSmean and GPID_list from the LUT

3/ extract the corresponding Xswath position (km) from UDP L2OS product.

4/ compute the dwell number using the formula:

$$IDdwell = \text{floor}((Xswath + Xswathmax) / pasXswath) - 9; \quad 4.11.11$$

where Xswathmax=662.5 and pasXswath=25;

if IDdwell belongs to the interval [1 34], you can keep the GP. If not, remove the GP.

5/ compute the corresponding GPindex

$$GPindex = \text{find}(GP == GPID_list)$$

6/ the corrected SSS anomaly is computed as follows:

$$SSSanomaly = L2OS_SSS - SSSmean(GPindex, IDdwell) \quad 4.11.12$$

ARGANS Ltd.

Commercial in Confidence

Page 190

Use, duplication, or disclosure of this document or any information contained herein is subject to the restriction on the title page of this document.

4.11.1.5 Parametric dependencies of the reference SMOS fields

Based on the different previous approaches, the parametrization that would be better suited for the SMOS-based climatology, to generate SSS anomalies has been discussed among the ESL.

Best option would be to keep seasonal effects in the anomalies, if possible but this highlights the problem of the SMOS climatology used, depending on the time considered for its generation. Further investigation is required, as it is likely that it would be better if the SMOS climatology is computed by the L2OS processor, to consider, the time-varying biases.

The team agrees that subtracting a SMOS-based reference field to the swath L2 SSS retrievals that would dependent upon:

- the across (X)-swath position at pixel,
- the latitude & longitude at pixel
- the month in the year,
- separately for ascending and descending semi orbits,

would be necessary to subtracts at least the systematic time-varying biases from SMOS and obtain meaningful SSS anomalies

$$\Delta S_{asc}(t, r(\mathbf{Xswath})) = S_{asc}(t, r(\mathbf{Xswath})) - \overline{S_{asc}(t, r(\mathbf{Xswath}))}$$

$$\Delta S_{desc}(t, r(\mathbf{Xswath})) = S_{desc}(t, r(\mathbf{Xswath})) - \overline{S_{desc}(t, r(\mathbf{Xswath}))}$$

4.11.13

From an algorithm development standpoint, the L2 team will have to generate the averaged 'seasonal' reference fields from SMOS data themselves, namely:

$$\overline{S_{asc}(t, r(\mathbf{Xswath}))}$$

$$\overline{S_{desc}(t, r(\mathbf{Xswath}))}.$$

4.11.14

This can be evaluated in the frame of the Level 2 SSS reprocessed datasets.

4.11.1.6 Review of SSS Data Filtering criteria to build up the SMOS climatology

In order to build up the LUT for the reference fields, Level 2 SSS data shall be filtered according to the validation protocol, i.e.:

- Dg_af_fov > 130
- control_flag_set**
- CTRL_ECMWF

ARGANS Ltd.



control_flag_clear

- CTRL_NUM_MEAS_MIN
- CTRL_NUM_MEAS_LOW
- CTRL_MANY_OUTLIERS
- CTRL_SUNGLINT
- CTRL_MOONGLINT
- CTRL_REACH_MAXITER
- CTRL_MARQ
- CTRL_CHI2_P
- CTRL_SUSPECT_RFI

control_flag_set

- CTRL_ECMWF

control_flag_clear

- CTRL_NUM_MEAS_MIN
- CTRL_NUM_MEAS_LOW
- CTRL_MANY_OUTLIERS
- CTRL_SUNGLINT
- CTRL_MOONGLINT
- CTRL_REACH_MAXITER
- CTRL_MARQ
- CTRL_CHI2_P
- CTRL_SUSPECT_RFI

As with respect to filtering the data depending on the pixel Distance to coast, the reference fields shall be evaluated at all pixels on the ISEA grid where a valid SSS has been, at sometimes, retrieved during the mission period (e.g. last reprocessing data) so that anomalies can be evaluated on the processing flow at all pixels where an SSS will be potentially retrieved in the future.

RFI filtering in building up the reference is a trickier question in particular with respect the duration life of these spurious events for a particular instrument observation geometry. Ideally, we would like permanent RFI to be included into the reference so that their 'mean' impact could be reduced in the anomalies. However permanent RFI over the full mission period are probably rare for a given observation geometry & location. We already faced the same issue in building up the empirical LSC correction. In building up the reference fields, RFI contamination probability tables shall be derived for the same conditions scanned in the LUT for the averaged 'seasonal' reference fields: $\overline{S}_{asc}(t, \mathbf{r}(Xswath))$ & $\overline{S}_{desc}(t, \mathbf{r}(Xswath))$. i.e:

- the across (X)-swath position at pixel,
- the latitude & longitude at pixel
- the month in the year,
- separately for ascending and descending semi orbits.

The RFI probability LUTs : $\overline{P(RFI)_{asc}(t, r(X_{swath}))}$ & $\overline{P(RFI)_{desc}(t, r(X_{swath}))}$ and their variance over the mission period shall be used to establish an RFI-related QC metrics: this will help characterizing the uncertainties on the reference fields and therefore on the anomalies to be included in the product.

4.11.1.7 SMOS period of reference for SSS anomaly computation

Ideally, the period used to derive the reference fields shall be the longest as possible to improve the statistics reliability for the norms to best describe the repeated seasonal cycle bias in SMOS data. However, for the SMOS case, there are some limitations:

- (i) the commissioning phase data shall be avoided due to reduce quality,
- (ii) it is well known that the Northern Hemisphere data particularly in ascending passes, North Atlantic & North Pacific regions, were heavily contaminated by the strong and permanent radar due-line RFI signals. Canada started to refurbish their equipment in late 2011, while Greenland switched off their transmitters in March 2011. We propose to avoid that period, i.e., launch to end 2011 in deriving the reference fields for ascending passes. Taking this period into account for deriving the references would otherwise bias the SSS anomaly retrievals during the significantly less active RFI period and therefore less polluted SSS data over the period 2012-now.
- (iii) large-scale/long term climatic signals contained in the data from end 2011 to now, related to e.g. El-Nino/Indian Ocean Dipole signals will also bias the reference fields toward the extreme reached during these events (e.g., x3 extension of the fresh pool area in 2014-2016 in the East Pacific (Guimbard et al., 2017), warm/fresh pool contractions/extensions at the equator during El Niño, La-Nina events (Hasson et al., 2014) the Indian Ocean Dipole large-scale SSS anomaly in the central Indian Ocean (Durand et al., 2013). Ideally, we would like to remove only the instrument/algorithm-related biases to keep those signals in the anomaly. In practice, removing data for long period of time to remove these signals (El-Nino event last from mid-2014 to mid-2016 in the Pacific) would significantly decrease the statistical relevance of the SMOS climatic norm evaluated. So, there is a trade-off between removing large scale climatic signals from the reference and keeping enough data to build up a stable reference field.

An evaluation of the confidence intervals and variability of the reference fields depending on which years are included or not into their evaluation would be interesting to determine their impact.

A first approach can consist in keeping these signals inside the dataset used to evaluate the SMOS seasonal climatic norms and to clearly specify to the users that the anomaly proposed in the product are given with respect the SMOS period (2011-2016) seasonal averaged mean.

ARGANS Ltd.

4.11.1.8 SSS Anomaly final adjustment

A final adjustment can be done by comparing the SMOS-derived climate-norms $S_{asc}(t, r(\mathbf{Xswath}))$ & $S_{desc}(t, r(\mathbf{Xswath}))$ to the mean in situ Objectively analysed field ISAS estimated over the same period than the one used to derived the SMOS climatology, following:

$$\Delta S_{asc}(t, r(\mathbf{Xswath})) = S_{asc}(t, r(\mathbf{Xswath})) - [\overline{S_{asc}(t, r(\mathbf{Xswath}))} - S_{isas}(t, r(\mathbf{Xswath}))]$$

$$\Delta S_{desc}(t, r(\mathbf{Xswath})) = S_{desc}(t, r(\mathbf{Xswath})) - [\overline{S_{desc}(t, r(\mathbf{Xswath}))} - S_{isas}(t, r(\mathbf{Xswath}))]$$

4.11.15

4.11.1.9 SSS anomaly computation at L2 OS

The process described above shall be followed to produce an SMOS-based SSS climatology able to debias the SSS retrievals and obtain SSS anomalies of value for the community.

Such climatology values will be stored in a LUT created for that purpose and that composes one auxiliary file for data processor.

The processor shall read that LUT and find, for each grid point retrieved, the corresponding grid point associated to the coordinates in which the LUT is based: grid point ID, and position in the swath. A linear interpolation shall be carried out to find the correct value.

After retrieval of SSS is complete for a given grid point, SSS anomaly is simply computed as follows:

$$SSSanom(gp) = SSS1_{uncorr}(gp) - SSSclim(gp, Xswath)$$

4.11.16

Being $SSS1_{uncorr}$ the retrieved SMOS L2 SSS without applying land/sea contamination correction.

The resulting value is provided within the UDP.

References

Jacqueline Boutin, Nicolas Martin, Nicolas Kolodziejczyk, Gilles Reverdin. Interannual anomalies of SMOS sea surface salinity. Remote Sensing of Environment, Elsevier, 2016, 180, pp.128 - 136. <10.1016/j.rse.2016.02.053>. <hal-01414604>



Durand F, Alory Gael, Dussin Raphael, Reul Nicolas (2013). SMOS reveals the signature of Indian Ocean Dipole events . *Ocean Dynamics* , 63(11-12), 1203-1212 .

<http://doi.org/10.1007/s10236-013-0660-y>

Gaillard, F., Reynaud, T., Thierry, V., Kolodziejczyk, N., & van Schuckmann, K. (2016). In situ-based reanalysis of the Global Ocean temperature and salinity with ISAS: Variability of the heat content and steric height. *Journal of Climate*, 29, 1305–1323.

Gourrion, J., Guimbard, S., Sabia, R., Gabarro, C., Gonzalez, V., Montero, S., ... Martinez, J.(2011). Reducing systematic errors on SMOS retrieved salinity: Calibration of brightness temperature and forward model improvement. *Geoscience and Remote Sensing Symposium (IGARSS)*, 2011 IEEE International (pp. 2397–2400).

<http://dx.doi.org/10.1109/IGARSS.2011.6049693>.

Hernandez, O., Boutin, J., Kolodziejczyk, N., Reverdin, G., Martin, N., Gaillard, F., ... Vergely, J. L. (2014). SMOS salinity in the subtropical north Atlantic salinity maximum: Part I: Comparison with Aquarius and in situ salinity. *Journal of Geophysical Research*. <http://dx.doi.org/10.1002/2013JC009610>.

Hasson A., Delcroix Thierry, Boutin J., Dussin R., Ballabrera-Poy J. (2014). Analyzing the 2010-2011 La Nina signature in the tropical Pacific sea surface salinity using in situ data, SMOS observations, and a numerical simulation. *Journal of Geophysical Research.Oceans*, 119 (6), 3855-3867. ISSN 2169-9275

Khazâal A., J. Tenerelli, François Cabot, Impact of Sun glint on the SMOS Retrieved Brightness Temperature Maps for Almost Four Years of Data, *Remote Sensing of Environment*, Volume 180, July 2016, Pages 234-245, ISSN 0034-4257, <http://dx.doi.org/10.1016/j.rse.2016.02.003>.

Nicolas Kolodziejczyk, Jacqueline Boutin, Jean-Luc Vergely, Nicolas Martin, Gilles Reverdin, et al. Mitigation of systematic errors in SMOS sea surface salinity. *Remote Sensing of Environment*, Elsevier, 2016, 180, pp.164-177. <10.1016/j.rse.2016.02.061>. <hal-01331805>

G.Lagerloef, (2012), Satellite mission monitors ocean surface salinity, *Eos Trans. AGU*, 93(25), 233.

Lappo, S.S., S.K. Gulev, A.P. Metalnikov et al., 1984: Energy active areas of the World Ocean. *Doklady Earth Sciences*, v.275, n.4, 1018-1021.

Lappo, S.S. and S.K. Gulev, 1984: North Atlantic energy active areas analysis. In: *OceanAtmosphere Interaction*. Moscow, Hydrometeoizdat, 3-37.

ARGANS Ltd.

Commercial in Confidence

Page 195

Use, duplication, or disclosure of this document or any information contained herein is subject to the restriction on the title page of this document.

Guimbard Sebastien, Reul Nicolas, Chapron Bertrand, Umberto M., Maes C. Seasonal and interannual variability of the eastern tropical Pacific fresh pool . Journal of Geophysical Research: Oceans IN PRESS . <http://doi.org/10.1002/2016JC012130>

Olmedo, E., Martínez, J., Umberto, M., Hoareau, N., Portabella, M., Ballabrera, J., Turiel, A. (2016). Improving time and space resolution of SMOS salinity maps using multifractal fusion. Remote Sensing of Environment 180, 246-263. DOI: 10.1016/j.rse.2016.02.038

Oliva R., Daganzo E., Richaume P., Kerr Y., Cabot F., Soldo Y., Anterrieu E., Reul Nicolas, Gutierrez A., Barbosa J., Lopes G. (2016). Status of Radio Frequency Interference (RFI) in the 1400–1427MHz passive band based on six years of SMOS mission. Remote Sensing Of Environment, 180, 64-75. <http://doi.org/10.1016/j.rse.2016.01.013>

Reul N. and J. Tenerelli., CATDS-CECOS-SMOS Level 3 SSS products 2010-Algorithm Theoretical Breadboard Document, Ifremer-cnes technical document, 2011.

Rousseeuw, P. J. and Hubert M., Robust statistics for outlier detection, 2011, Wiley Interdisciplinary Reviews: Data Mining and Knowledge Discovery, John Wiley & Sons, Inc. p73-79, DOI: 10.1002/widm.2

Vergely, J. L., Rouffi, F., Waldteufel, P., Anterrieu, E., & Corbella, I. (2013). SMOS + Polarimetry: Product validation report., 0970-0079-PVR-ACR. available on <http://smosp.acri.fr/docs/vr.pdf>

4.11.2 Post-retrieval theoretical error adjustment

4.11.2.1 Introduction

Recently, it has been estimated that a better estimation of the random uncertainties that affect SSS estimator from TB uncertainty characterization may be done.

The characterization of the TB random uncertainties is given by the residues at level 2. The indicator which contains the L1c TB residue information is the chi2 indicator computed at the end of the L2OS retrieval. It gives the normalized residues and should follow a specific law (chi2 law) with an expected value close to 1. The probability that the chi (sqrt(normalized chi2)) is larger than 1 is even weaker than the chi is strong.

This means statistically that the TB errors have been underestimated. This occurs if part of the signal is not modeled (for instance, RFI contamination). In this condition, the SSS theoretical error (sigSSS) is likely underestimated. In this technical note, we show that by replacing sigSSS by chi.sigSSS it allows to better propagate L1c uncertainties and to reach a more reliable error estimation. This has an impact on L3 products when weighting estimated SSS with sigSSS during the averaging.

ARGANS Ltd.

Commercial in Confidence

Page 196

Use, duplication, or disclosure of this document or any information contained herein is subject to the restriction on the title page of this document.



A maximum-likelihood Bayesian approach is used in the L2 inversion algorithm, taking advantage of the a priori information available about geophysical parameters (SSS, SST, wind speed, TEC, etc.). With this formalism, errors on TB and on the retrieved geophysical parameters are assumed to be Gaussian. The SSS theoretical error σ_{SSS} is obtained by propagating a priori errors, model errors and radiometric errors to the SSS, using classical least square formulation.

Providing the L2OS users with an improved uncertainty σ_{SSS} is key for a number of application, such as proper L2 SSS merging at Level3 and 4 (σ_{SSS} can be used to properly weight multiple L2 SSS observations in a specific space-time window), or for assimilation into Ocean General Circulation models, etc. An effort is needed to improve the characterization of σ_{SSS} .

Concerning the model error, a default value is used in the current processor : 0.5K for H and V polarizations. This error is propagated to X and Y polarization by using the ground to antenna transformation matrix.

The a priori errors are taken as follows : 100 psu for SSS, 1.5 m/s for WS, 1K for SST and 10 tecu for the TEC. This means that almost no a priori information is taken for SSS. On the other side, the other parameters shall be relatively well known.

Typically, TB radiometric noise ranges from 1.5 to 3.5 K depending on the across-track distance. Radiometric accuracy is computed based in two main parameters: integration time of the snapshot and footprint size, or the equivalent area introduced into the computation of the measurement in the Fourier space. This means that it depends on incident angle and, therefore, there is a cross-track dependency/variation, but also there is dwell line dependency.

The theoretical error can be better estimated by improving the characterization of all three components of the uncertainty budget. We will successively propose improvements to describe these error sources in three subtasks:

- L1C TBs instrument noise error
- Radiative transfer forward model errors
- Our knowledge of the a priori variance of the retrieved geophysical parameters

4.11.2.2 Input L1C TB uncertainty characterization

One can estimate the TB errors indirectly by looking at the TB residuals. These residuals, associated to the estimation of one SSS at a given grid point, are obtained from the chi2. It corresponds to the likelihood part of the cost function after convergence.

A significantly large value of the chi2 after inversion indicates that there is likely a problem: e.g., spurious TBs, forward model issue, solar contamination, RFI, etc. An easy manner to account for that is to artificially increase the theoretical SSS error by a certain factor which we try to estimate hereafter. Another way is to consider the TBs with high residuals as outliers and to remove them before retrieval (the increase of the TB error is equivalent to a removal above a certain threshold).

Note that the chi2 value is used to flag SSS estimator. For a given grid point, historical behaviour of chi2 could be used to flag SSS even if the peculiar chi2 value (at a given time) is acceptable.

So, we know that, if the chi2 is too large, the SSS theoretical error is probably underestimated. Basically, the SSS and the TBs are related by the following formulation:

$$SSS = SSS_0 + \frac{\partial SSS}{\partial TB} \delta TB \quad 4.11.17$$

The theoretical error on the SSS follows the following equation:

$$\sigma_{SSS} = \frac{\partial SSS}{\partial TB} \sigma_{TB} \quad 4.11.18$$

σ_{TB} is related to the radiometric noise σ_{Rad} . A way to estimate empirically σ_{TB} is to use the TB residues after inversion. The square root of the quadratic mean of the residues gives an empirical estimation of the TB true errors.

In the retrieval scheme, we use the radiometric noise as σ_{TB} : the a posteriori error on the SSS estimator is the expected theoretical error. If the TB radiometric error is underestimated, then the SSS theoretical error is also underestimated.

A possible way to check that the error budget gives realistic results is to consider the SSS dispersion. For a given GP, if the SSS time fluctuations are neglectable, we can consider the following reduced and centered variable:

$$SSSc = (SSS - \text{mean}(SSS)) / \sigma_{SSS} \quad 4.11.19$$

If the a posteriori error SSS is Gaussian, then SSSc follows a Gaussian law with a 0 mean and a standard deviation = 1. We consider the SSSc variable independently for each grid point. The statistic on this variable is done by considering all the observation during 40 days on a given grid point. We assume that for 40 days, the SSS does not vary significantly. This means that $\text{mean}(SSS)$ is an estimator of the SSS by merging 40 days of acquisition.

If the standard deviation is larger than 1, this means that the model used for the retrieval is not adapted or that the TB noise is underestimated. If the radiometric error σ_{rad} is underestimated, it is then possible to re-estimate the error of σ_{TB} :

$$\sigma_{TB}^2 \sim \sigma_{rad}^2 + \varepsilon^2 \quad 4.11.20$$

then reduced $\text{chi} \sim \frac{\sigma_{TB}}{\sigma_{rad}}$. This means that the σ_{TB} error is simply:

$$\sigma_{TB} = \text{chi} \cdot \sigma_{rad} \quad 4.11.21$$

The distribution of SSSc is a good indicator of the TB error, if we assume that the forward model is good enough.

The same point of view can be addressed for TB. The following reduced and centred variable should follow a Gaussian law with 0 mean and a standard deviation = 1:

$$\text{TBC} = (\text{TB} - \text{TBmodel}) / \sigma_{\text{Rad}} \quad 4.11.22$$

The Xi of adjustment is given by:

$$\text{chi} = \sqrt{\langle \text{TBC}^2 \rangle} \quad 4.11.23$$

Because σ_{SSS} and σ_{TB} are linked (see Eqn. 1),

$$\begin{aligned} \widetilde{\sigma}_{SSS} &\sim \frac{\partial SSS}{\partial TB} \sigma_{TB} = \frac{\partial SSS}{\partial TB} \cdot \text{chi} \cdot \sigma_{rad} \\ &= \sigma_{SSS} \cdot \text{chi} \end{aligned} \quad 4.11.24$$

This equation shows that, if chi is significantly larger from 1, it is possible to re-estimate the TB error and propagate this new error to the SSS. This propagation does not require performing again the retrieval scheme. The new SSS error is given directly by multiplying the SSS theoretical error by the chi.

The results are presented for two sets of data:

- the SSS data resulting from TBs corrected by OTTs (SSS or SSSnocorr).
- the SSS data resulting from TBs corrected by OTTs and the LSC (SSScorr).

The notations used are those of the previous section:

- σ_{SSS} : SSS L2OS theoretical error (obtained by statistical propagation of the radiometric noise to the SSS).
- $\widetilde{\sigma}_{SSS} = \sigma_{SSS} \cdot \chi$: SSS L2OS theoretical error weighted by the normalized chi.

As a reminder, we mainly use the random variable $SSSc$, defined as follows: $SSSc = (SSS - \text{mean}(SSS)) / \widetilde{\sigma}_{SSS}$ whose std is close to 1 and the average close to 0 in the case where $\widetilde{\sigma}_{SSS}$ is realistic. Also, we will use $SSSc0 = (SSS - \text{mean}(SSS)) / \sigma_{SSS}$ which will show the quality of the theoretical error before updating with the chi. $SSSc$ and $SSSc0$ are calculated from the SMOS data. The SSS averages and standard deviations std ($SSSc$) and std ($SSSc0$) are obtained grid node per grid node on a 40-day basis. It is assumed that on this time basis, the true SSS does not vary (or little compared to the error on the mean).

Figure 13 shows the std of $SSSc0$ which, if the error is well estimated, should have a value close to 1. We find that near coasts and in some specific areas, the values obtained are much larger than 1, which shows that, for these regions, the error on SSS is underestimated. Note that regions with very high temporal variability also generate strong std. In this latter case, this obviously does not mean that the errors have been underestimated.

If we take the corrected SSS ($SSScorr$), then the std begins to tend towards 1 close to some coasts. On the other hand, in the European and Asian coastal regions (Figure 2), the std remains very significantly greater than 1. The difference in std between uncorrected SSS and corrected SSS (LSC correction for TB) is shown in Figure 15. Coastal regions show a clear decrease in the difference, which is explained by the fact that coastal bias is responsible for the strong std uncorrected SSS. Once this bias is corrected, the std decreases. In some cases, this is not the case (for example on the Asian coast) which means that the bias is not stable, ie the bias is probably due to intermittent RFI. These cannot be corrected by the LSC correction.

Regarding the distribution of χ^2 (Figure 17), it does not follow the expected distribution: too many large values are present. This means that the noise on TB is not well-estimated or that there are outliers.

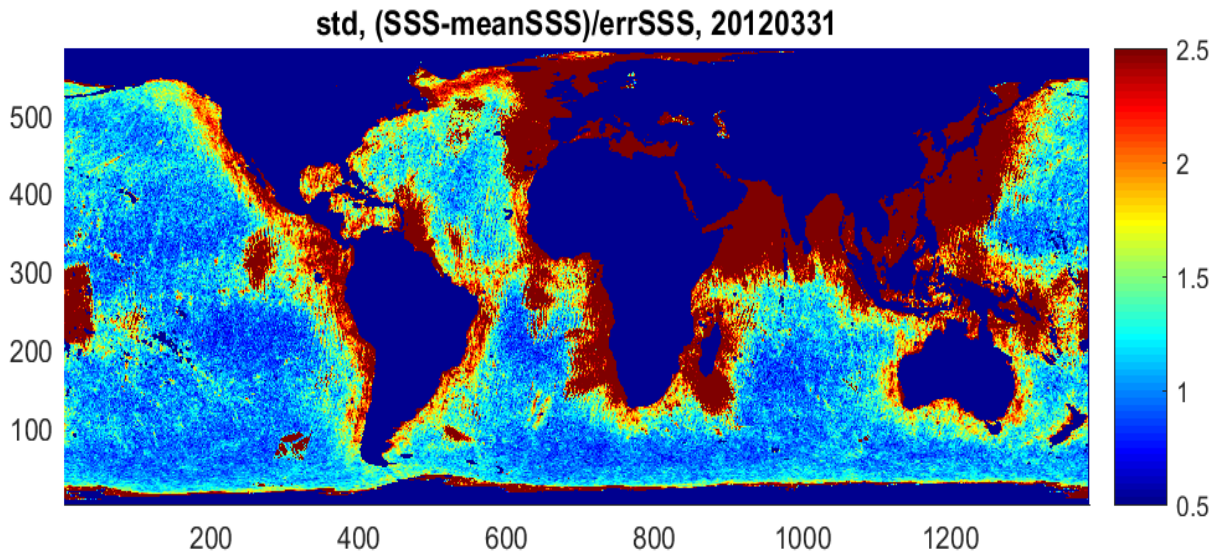


Figure 13: $\text{std}\left(\frac{\text{SSS}_{\text{nocorr}} - \text{mean}(\text{SSS})}{\sigma_{\text{SSS}}}\right)$. Values larger than 1 show underestimated SSS theoretical error.

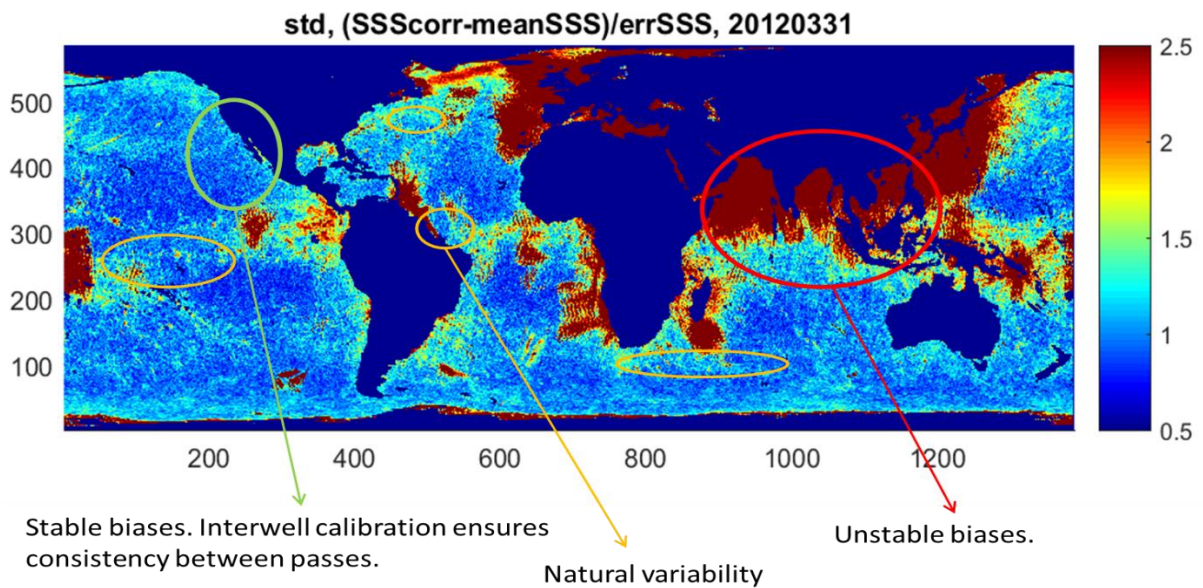


Figure 14: same than previous figure but with SSS corr (SSS obtained from LSC TBs).

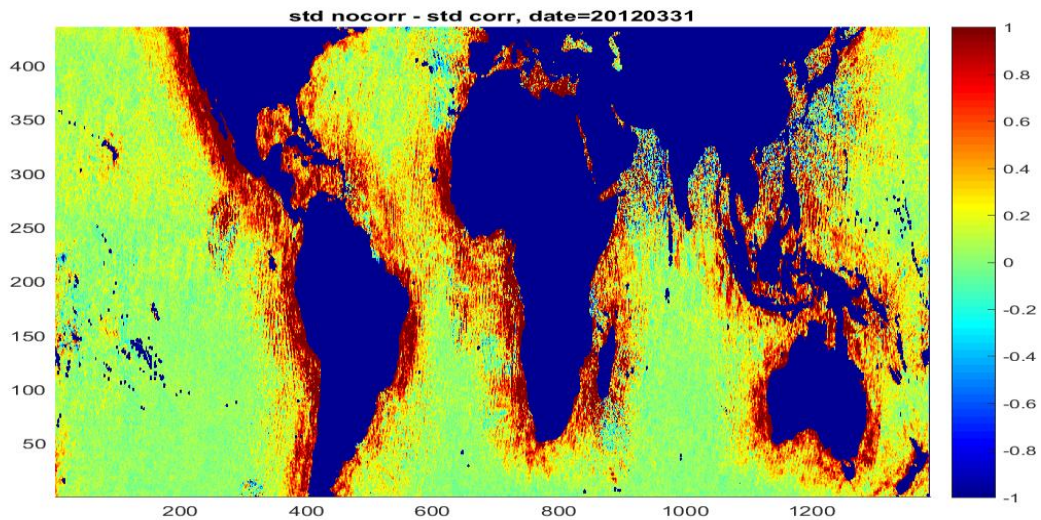


Figure 15: $\text{std}\left(\frac{SSS_{nocorr} - \langle SSS_{nocorr} \rangle}{\sigma_{SSS_{nocorr}}}\right) - \text{std}\left(\frac{SSS_{corr} - \langle SSS_{corr} \rangle}{\sigma_{SSS_{corr}}}\right)$. Some regions are not improved from LSC correction. Identification of regions with unstable LSC.

The random variables SSSc and SSSc0 must follow Gaussian distributions of zero mean and standard deviation 1 if the noise is correctly modeled. Figure 16 shows the distributions of SSSc0 for coastal pixels and full ocean pixels. In both cases, the standard deviations are far from 1 (5.4 and 2.3 for coastal and full ocean pixels respectively). If we multiply the theoretical error by the chi, we obtain the distributions presented in Figure 7 for the random variable SSSc. Standard deviations are much closer to what is expected (1.8 and 1.2 for coastal pixels and full ocean respectively). An example at the SSS level for a grid node is given in Figure 18. Overall, a map of the std (SSSc) and a map of the std (SSSc0) are given as an example in Figure 20. In some cases of contamination, the multiplication of the error by the Chi is insufficient (Figure 21, Figure 22 and Figure 23).

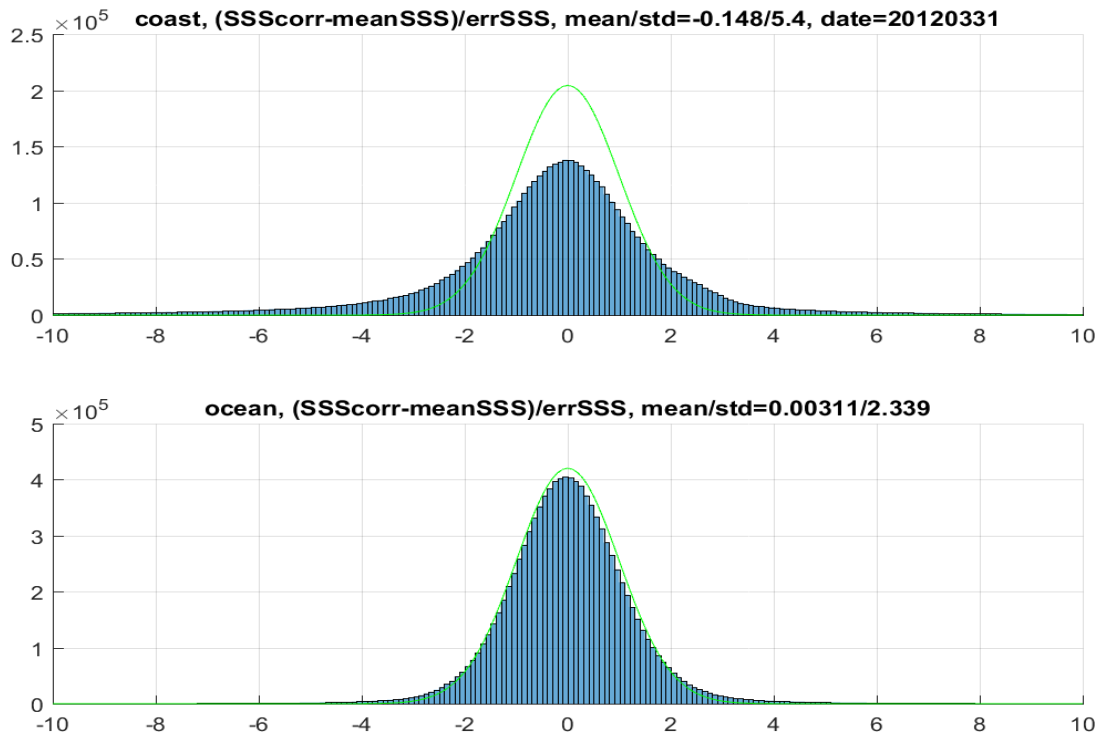


Figure 16: SSSc0 random variable distribution. Top : coast pixels (dcoast<800 km); bottom : ocean pixels (dcoast>800km). SSS corrected from LSC.

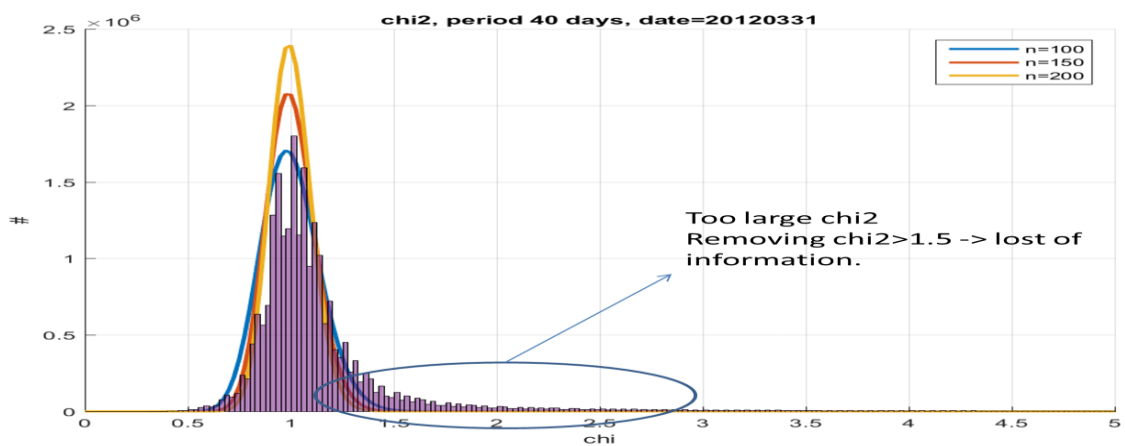


Figure 17: chi2 histogram. The tail corresponding to larger values than 1.5 is not statistically expected in comparison with the theoretical curves given for different degrees of freedom (100, 150 and 200).

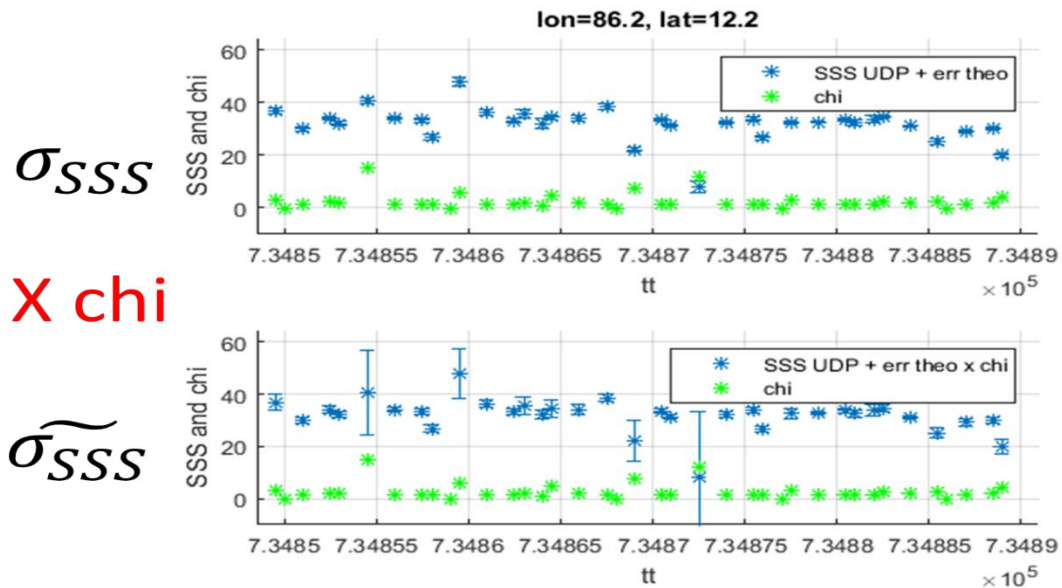


Figure 18: SSS time series for a grid point at lon=86.2°, lat=12.2°. Top: in blue, the SSS with its error bar; in green the chi value. Bottom: in blue, the SSS with its error bar weighted by the chi.

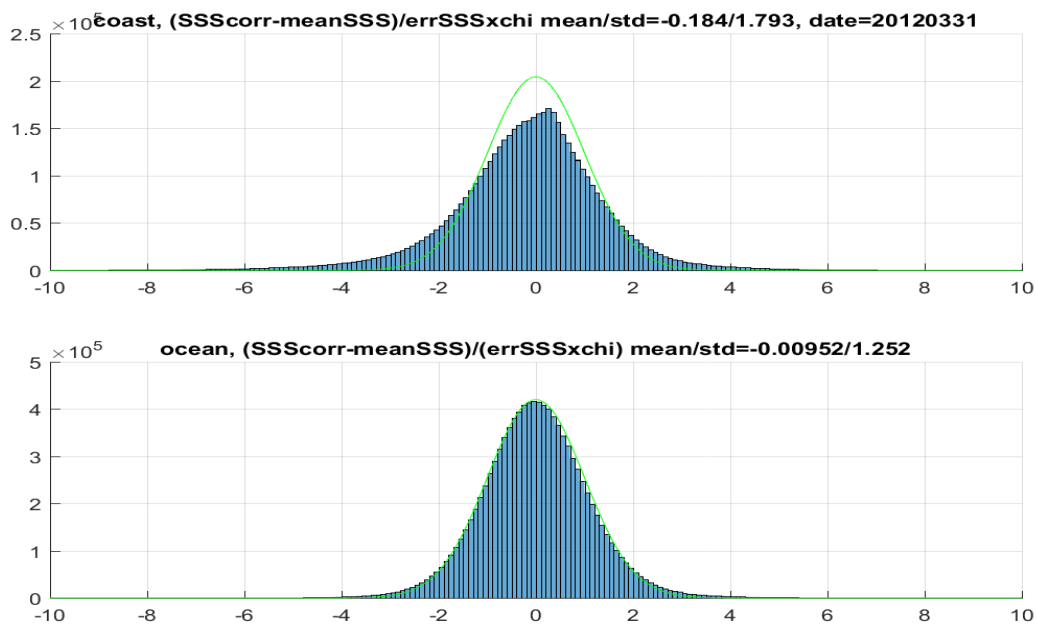
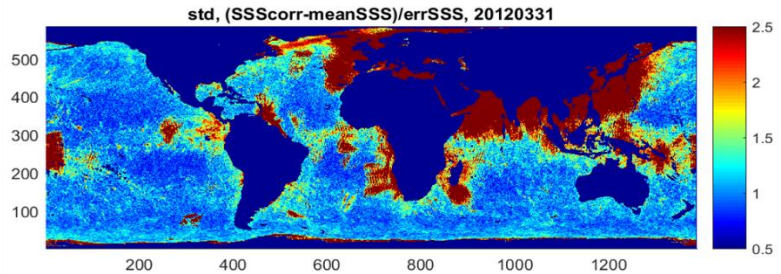


Figure 19: SMOS theoretical error more realistic after chi normalization. Coast (<400km) and ocean pixels, SSS corr.

$$(SSS - \langle SSS \rangle) / \sigma_{SSS}$$



$$(SSS - \langle SSS \rangle) / \widetilde{\sigma}_{SSS}$$

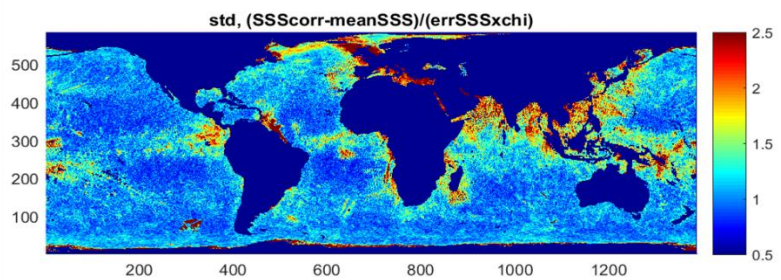
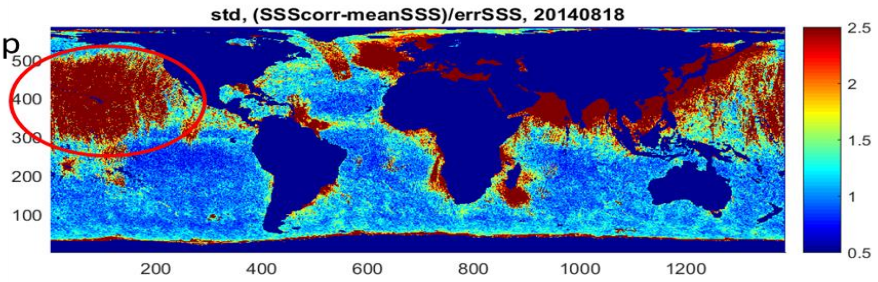


Figure 20: example of the weighting effect. Top, without weighting SSS theoretical error with the chi; bottom, with weighting.

American war ship maneuvers ?



Not perfect...

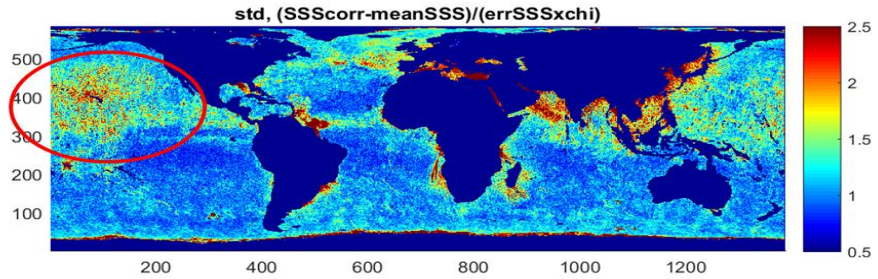
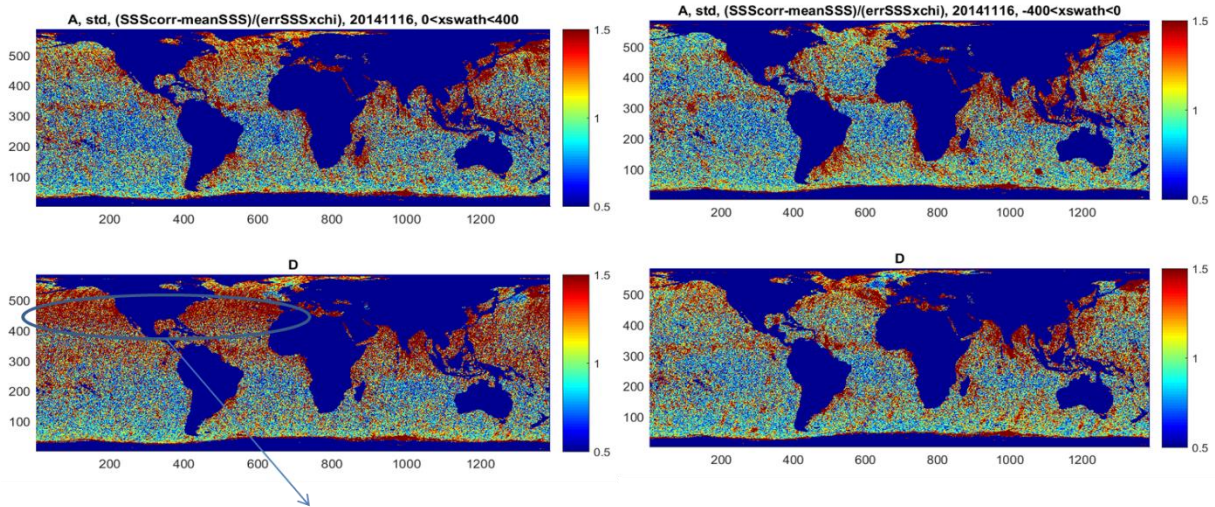


Figure 21: August 2014 : specific contamination in the North Pacific.



Chi multiplication : not enough for Desc, right part of the FOV

Figure 22: eclipse period. Top : ascending orbits (left: left part of the swath, right : right part of the swath.). Bottom : descending orbits.

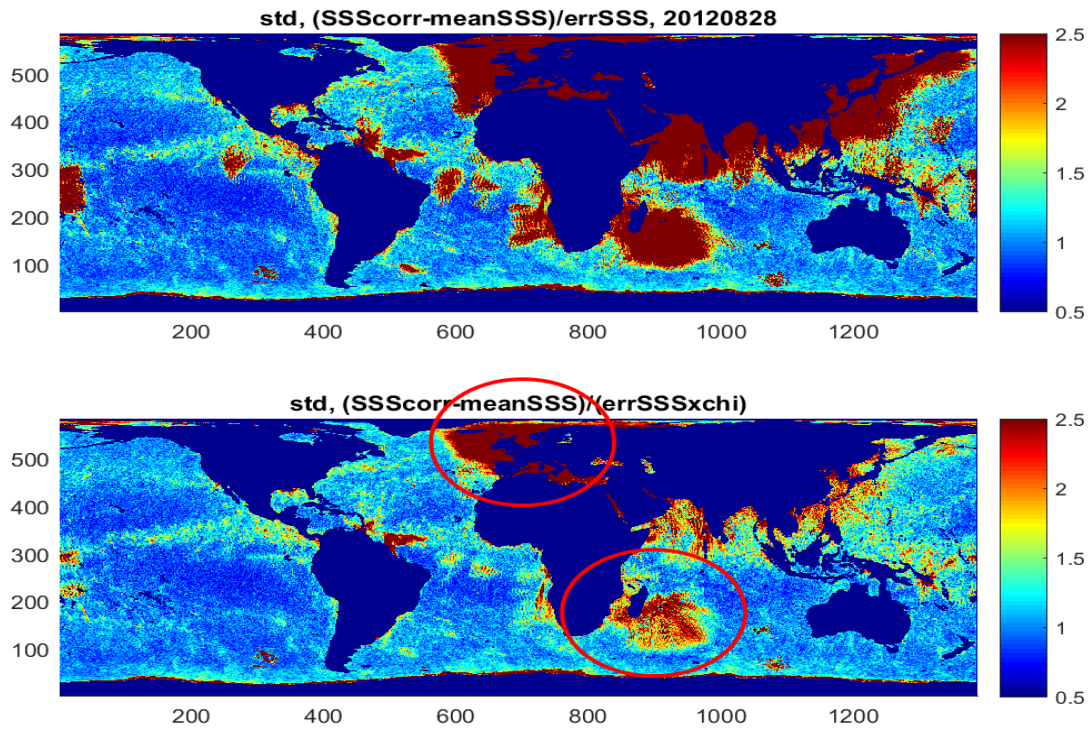


Figure 23: August 2012. Large RFI contamination in Europe and around Madagascar.

Previous maps and indicators are calculated at specific time periods. Figure 24 shows the evolution of the std (SSSc) over the period 2012-2015.

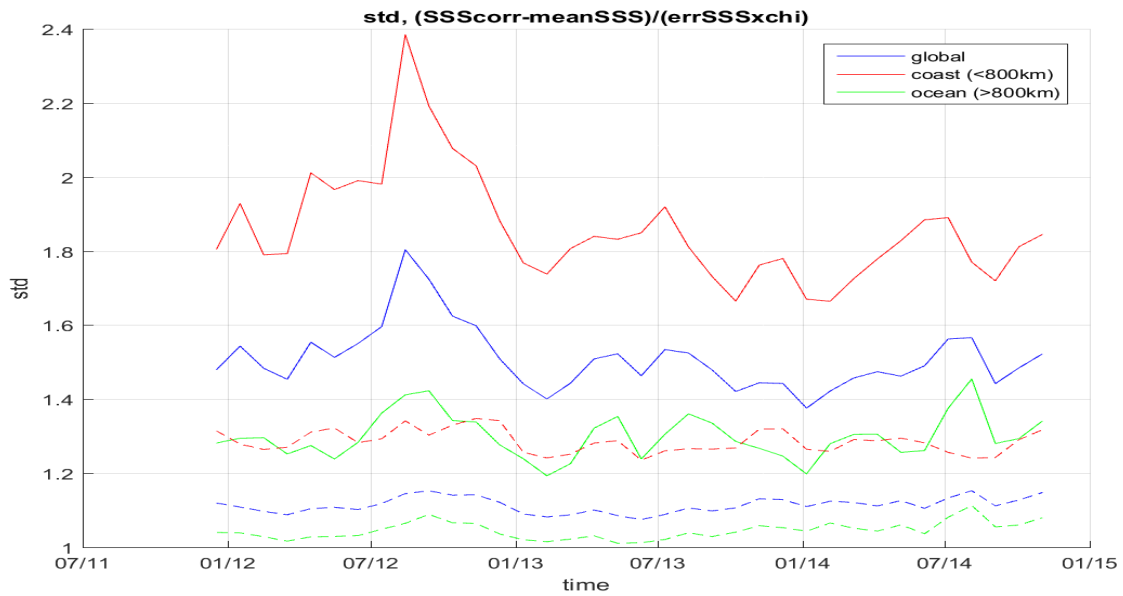


Figure 24: std(SSSc) over 2012-2015, month by month. Full curves for std, dashed curves for robust std (computed from median).

The proposed new L2 error ($\widetilde{\sigma}_{SSS}$) has an impact on the quality of the L3 products when the averages on the SSS are weighted by the error. An example of L3 product is shown in Figure 25. We see that the aberrant ascending orbit in the Pacific disappears if we use the new error. There are improvements in the RFI zones (around Madagascar, in the Gulf of Arabia, south of the Gulf of Guinea, etc ...). Overall comparisons were made month by month over a period of 4 years. The standard deviation of the SMOS-ISAS difference is given for the full ocean (Figure 26) and for near-side pixels (Figure 27). In both cases, SMOS approaches significantly more ISAS if one considers an additional weighting by the chi.

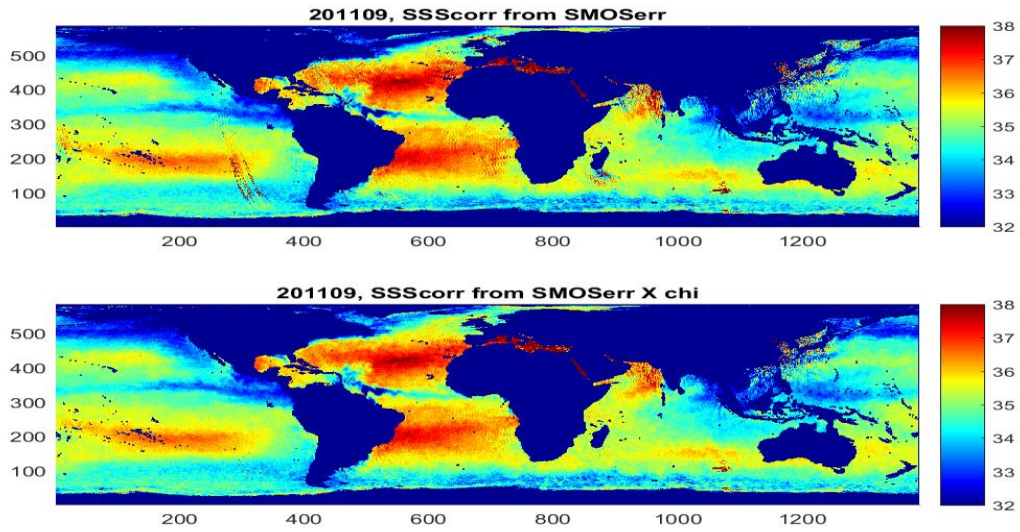


Figure 25: L3 product from L2OS SSS error (top) and from L2OS SSS error multiplied by the ch (bottom).

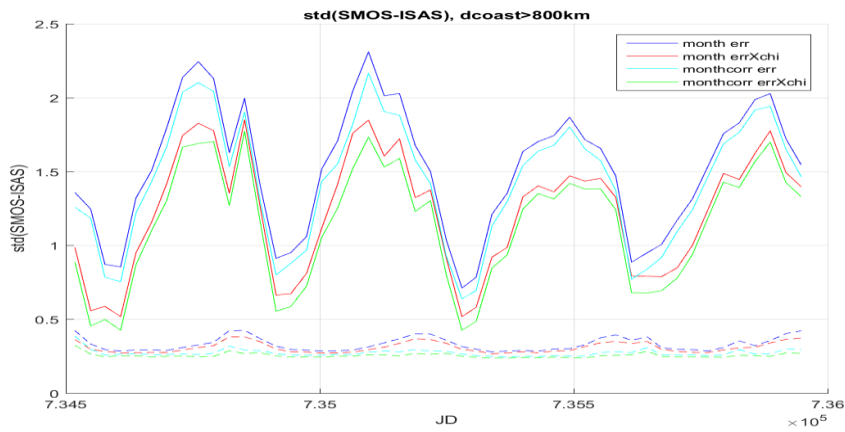


Figure 26: L3 SSS – ISAS SSS. Ocean pixels.

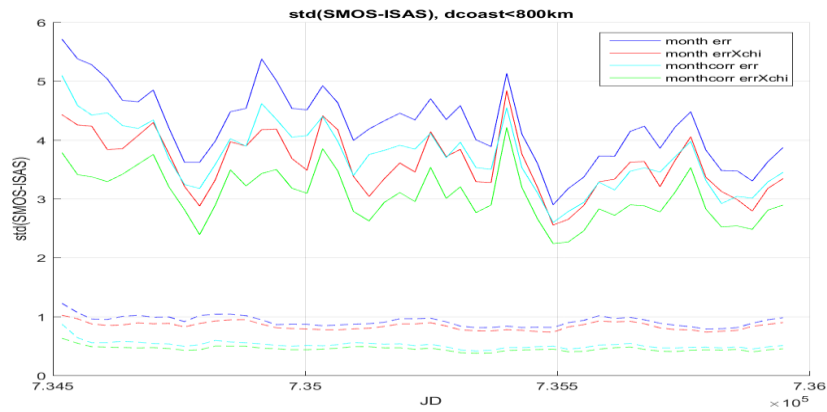


Figure 27: L3 SSS – ISAS SSS. Pixel with distance from coast < 800 km

4.11.2.3 Implementation in the algorithm

The proposed modifications to be performed are straightforward: if chi (square root of normalised chi²) is larger than 1, multiply the theoretical error by chi.

4.12 Cardioid model

As shown by Waldteufel et al. (2004), simultaneous retrieval of the real, ε' , and imaginary part, ε'' , of the dielectric constant from SMOS brightness temperatures (Tb) is an ill posed problem. The cost function (see section 4.10) , rather than a single minimum, exhibits a minimum valley that can be represented analytically using a modified cardioid model. After carrying out the following change of variable:

$$\begin{aligned}\varepsilon' &= A_{card}(1 + \cos(U_{card})) \cos(U_{card}) + B_{card} \\ \varepsilon'' &= A_{card}(1 + \cos(U_{card})) \sin(U_{card})\end{aligned}\quad 4.12.1$$

which is equivalent to:

$$\begin{aligned}A_{card} &= \frac{m_{card}^2}{(m_{card} + \varepsilon' - B_{card})} \\ U_{card} &= \tan^{-1}\left(\frac{\varepsilon''}{(\varepsilon' - B_{card})}\right) \\ \text{With } m_{card} &= ((\varepsilon' - B_{card})^2 + \varepsilon''^2)^{\frac{1}{2}}\end{aligned}\quad 4.12.2$$

with $B_{card} = 0.8$, it is possible to retrieve the parameter A_{card} with good accuracy: a minimum of χ^2 is seen as a vertical line corresponding to a constant value of A_{card} and various values of U_{card} (Figure 28) Local minima of χ^2 are also observed for unrealistic negative values of A_{card} ; as it will be described in the following, retrieval of such negative values are avoided by taking an error on prior A_{card} ; over the ocean of 20 units or by initiating the retrieval with low A_{card} value as low A_{card} are much better constrained.

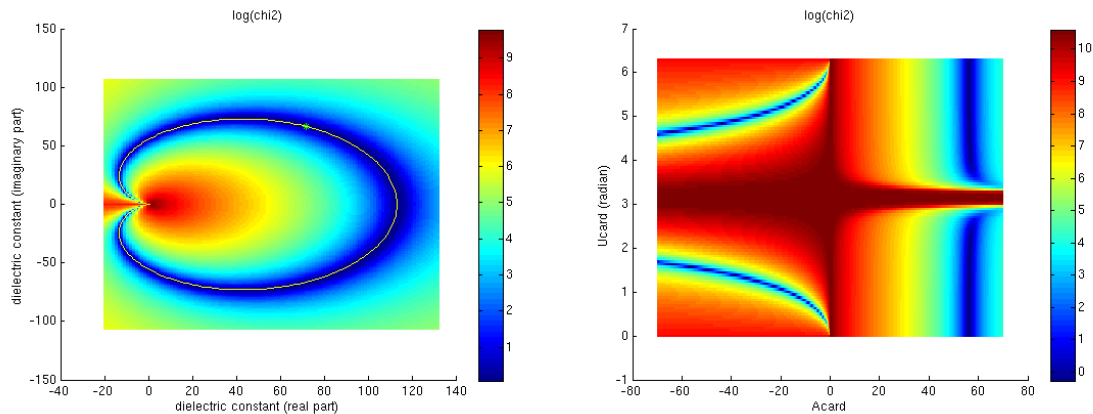


Figure 28: χ^2 (log value) in case of retrieval of (ε' , ε'') over sea water (left) plotted as function of (ε' , ε''); the green cross indicates the true value of the dielectric constant. The yellow curve corresponds to a constant A_{card} with U_{card} varying between 0 and 360 °; (right) plotted as a function of (A_{card} , U_{card}).



With these definitions and considering direct emissivity models described above: for sea ice, $A_{card}=1.2 (U_{card}=0)$; over a flat sea, A_{card} ranges between 48 and 67 depending on SSS and SST values and U_{card} between -0.9 and -0.5 radians.

It is clear that the minimization of χ^2 parameter does not allow us to retrieve a single pair of (ϵ', ϵ'') while it allows us to retrieve a single value of A_{card}, U_{card} remaining undetermined. We found that initiating the retrieval with low A_{card} , prior value ($A_{card}^{prior}=1$) and large error on A_{card} , ($\sigma(A_{card})=50$) allows to avoid retrieval of negative A_{card} values while avoiding biases on low A_{card} , values and gives the same result over ocean pixels as taking A_{card}^{prior} deduced from mean SSS and SST .

We suggest by default to use a complete model that includes the flat sea model, the roughness model plus atmospheric and constant galactic noise correction 2 in order to minimize bias between effective A_{card} and A_{card} computed from retrieved SSS and SST . This allows A_{card} to be directly linked with the dielectric constant without any other contribution.

Retrievals using the cardioid model use all the measurements except outliers and those brightness temperatures with the following flags: Fm_outlier, Fm_resol, Fm_border, Fm_L1c_instrument error, Fm_L1c_calibration_error. The brightness temperatures have the land-sea contamination correction applied before A_{card} retrieval.

In cold water, the use of the cardioid model should efficiently allow the detection of sea-ice: a flag (Fg_ice_Acard) is raised if the effective temperature $T_{eff} < Tg_SST_ice_Acard$ and $Acard < Tg_Acard_ice$ and $abs(latitude) > Tg_lat_ice_Acard$.

P. Waldteufel, J. L. Vergely, and C. Cot, "A modified cardioid model for processing multiangular radiometric observations," *IEEE Transactions on Geoscience and Remote Sensing*, vol. 42, pp. 1059-1063, 2004.

D. W. Marquardt, "An algorithm for least-squares estimation of non-linear parameters," *J. Soc. Ind. Appl. Math*, vol. 11, pp. 431-441, 1963.

4.13 Brightness temperature at surface level

One of the outputs of the SMOS SSS L2 processor can be to provide, for each grid point, the set of brightness temperatures measured by MIRAS that have been used to compute salinity. But, unlike in L1c product, these must be values at surface level (not antenna level) that can be used for example for assimilation in general circulation models, in validation exercises or in cross-calibration with Aquarius. Due to the singularity points and cross-correlated errors we do not transform measured Tb from antenna level to surface, but compute, with the forward models that correspond to the selected option, the different components of the Tb at surface level with the SSS and final auxiliary parameters as obtained during the retrieval.

Then the values will be those contributing to Tb_{BOA} , as explained in section 4.9.1.1.2

$$Tb_{BOA} = Tb_{flat} + Tb_{rough} + (Tb_{DN} \Gamma + (Tb_{gal_{ref}}) e^{-\tau_{atm}}) \quad 4.13.1$$

Due to operational constraints (size of the SMOS L2 output files), only one value ($Tb_{42.5H}$ and $Tb_{42.5V}$, with their associated uncertainties) corresponding to a fixed incidence angle ($L2a_angle$, 42.5°) will be regularly provided to users and using the default roughness model. The uncertainties will be computed using the theoretical uncertainties associated to the default forward model.

For a comparison between modelled and measured values, these $Tb_{42.5H}$ and $Tb_{42.5V}$ will be transported to antenna level with the same procedure used during the SSS retrieval, and the resulting $Tb_{42.5X}$ and $Tb_{42.5Y}$ values will be put in the UDP.

If the 42.5° angle is not included in the dwell line for the given point and given satellite pass, it will not be possible, due to model constraints, to compute these $Tb_{42.5H}$ and $Tb_{42.5V}$. Then a flag will be raised ($Fg_ctrl_no_surface.true$) and a warning value (999) will be put instead in the UDP.

The full set of modelled surface Tb values, and for the different modelling options, can be recovered by using processing tools based on the L2 SSS Prototype Processor made available by the SMOS Project.

Note: The need for a complete set of measured (not modelled) Tb at surface is considered a key point for calibration/validation activities, as stressed by several participants to the First SMOS Cal/Val Experimenters Meeting (Avila, November 2005). This issue requires further attention and a satisfactory solution should be provided. An ESA funded study has been carried out by CLS, and results reported to L2 Mid Term Review on 19 Sept 2007. The decision at MTR was to keep the possible implementation of this Tb_{BOA} computation for a further stage, and do not introduce it in the processor before launch.

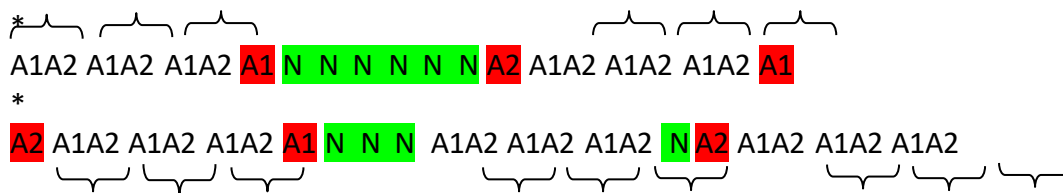
4.14 Measurements selection (polarisation)

This section describes how to select the successive MIRAS measurements for the computation of SSS, according to the polarisation mode chosen.

To perform the iterative convergence, brightness temperature must be taken in couples of H and V polarisations if the 1st Stokes parameter is used, otherwise the two polarisations are included independently in the computations. The way to extract proper measurements is as follows:

- In case of Dual Polarisation: In a specific grid point all the snapshots that include it should be used, and this will include consecutively perpendicular polarisations. However, some of them can be invalid for SSS retrieval (either classified as bad by L1 or discarded in the L2 measurement discrimination) and as a consequence some pairs of horizontal (A1) and vertical (A2) measurements will not be formed.
- In case of using the 1st Stokes parameter, and if the Scene Bias Correction (SBC, see module 4.11) is applied, the H+V pairs have always to be organised by taking first an H measurement and its immediately consecutive V. Then if the first snapshot that includes a grid point provides a V measurement, this will not be processed. In case of lack of one or more measurements in the sequence, the order should not be changed and continue by coupling first A1 and then A2. With this selection method it might happen that some measurements are not used, despite providing good data.

The following figure represents a couple of examples (grid points with very small number of measurements, for simplicity) from the first to the last view in a satellite overpass:



The brackets show the formed pairs of perpendicular polarisations in the most restrictive case (SBC with 1st Stokes), while **N** means invalid measurements and **red** marks measurements that will be lost due to the measurement selection (lack of companion polarisation). If SBC is not applied, only measurements marked with * in the examples above are lost with 1st Stokes option (end of a string with odd number of good data), as the order of complementary polarisations in a pair is not relevant. When the two polarisations are used separately, no good data must be discarded, as pairs formation is not needed.



When a correct measurement is not used in the retrieval due to this selection method, a flag on the measurement should be raised (Fm_lost_data).

In case of Full Polarisation mode: do the same as dual polarisation, but taking into consideration only HH and VV measurements, not the mixed ones.

The first Stokes value (I) is computed as described in 4.9.1.1.1 and $\sigma^2 I = \sigma^2 A1 + \sigma^2 A2$



4.15 Auxiliary geophysical parameters bias correction

Replaced and transferred to ANNEX F.

4.16 TEC estimation from Stokes 3 (A3TEC)

4.16.1 Introduction

The SMOS+ polarimetry study shows that it is possible to estimate TEC from A3 assuming St3 at ground level = 0. TEC is available in L1c product. This TEC estimation and the magnetic field (amplitude + direction) are given at the nadir for each snapshot at 450 km of altitude. Because TEC can show strong latitudinal gradient, L1c TEC can be biased at strong incidence angles when the lines of sight are far from the nadir. Moreover, SMOS allows obtaining full pol brightness temperatures. A3 contains Faraday rotation information for each observation direction: it is possible to use this information to improve TEC estimation.

4.16.2 Algorithm

4.16.2.1 Assumptions about TEC

The main assumptions about TEC are:

1. the TEC does not vary significantly across the swath. The TEC variations we are looking for are along the track. This means that TEC will be provided according to the latitude.
2. the TEC we obtained is a pseudo TEC at altitude of 450 km. The integration along the line of sight of the TEC and the magnetic field is reduced to a scalar product between the line of sight direction and the magnetic field at altitude of 450 km, weighted by the pseudo TEC.
3. the magnetic field does not vary strongly at a snapshot scale.
4. we consider that the TEC variations present latitudinal correlation. This means that it is possible to apply a correlation length to smooth the TEC variations. This smoothing step allows to remove outliers and to strongly decrease the TEC estimation.

4.16.2.2 Global processing

TEC estimator should come from SMOS measurements which are not outliers. So, the processing must be done after a first outlier detection using valid measurement.

The following steps have been identified:

step 1 : Outlier detection. This step still exists in the L2OS processor. Only TB with fm_valid flag = 1 must be used.

step 2 : Select A3 measurements with high incidence angles close to the centre of the swath. This selection must be done in the antenna frame, on an interval of ξ/η . For instance, we can have $-0.025 < \xi < 0.025$ and $0.15 < \eta < 0.2$. The ξ/η interval should be configurable.

step 3 : Compute the positions in latitude where the lines of sight cross the altitude of 450 km.

step 4 : Estimation of TEC from A3 and forward model. For one A3 value, we expect one TEC estimation. This estimation should consider the L1c TEC given as prior. In the part of the orbit where A3 is not sensitive to TEC, the retrieved value should be closest as possible of the prior value. A3 shall be corrected from OTT before TEC estimation.

step 5 : Estimation of the TEC error and outlier detection. A latitudinal slippery window is used to detect outlier and to estimate the TEC mean and TEC error according to the latitude

step 6 : Global quality of the TEC estimation. If the quality is not good enough, the L1c TEC shall be used for SSS estimation.

step 7 : Use of the TEC estimator in the SSS retrieval : compute for each line of sight the latitudinal position where the line of sight crosses the altitude of 450 km. Extract the L1c magnetic field and compute Faraday rotation (one value for each TB).

step 8 : retrieve SSS using Faraday computed in step 7. Only TX and TY should be used (A3 is still used for TEC estimation). TEC should not be retrieved at this step.

These steps make sense only if the retrieval mode is not Stokes 1.

The main steps are described in details hereafter.

4.16.2.3 Latitude position (step 3)

Each line of sight crosses the 450 km altitude at a given (lat, lon) position. The following figure shows the principle of the computation.

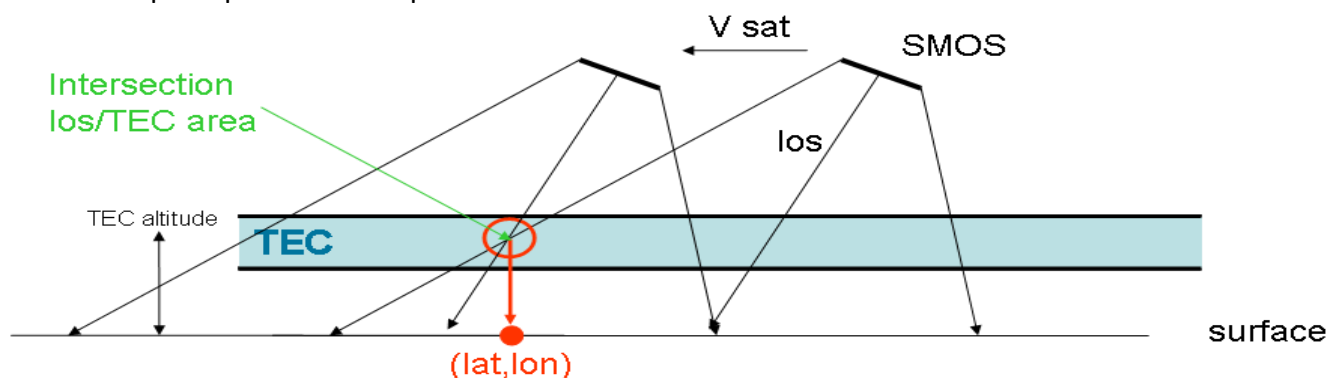


Figure 29: TEC(lat,lon) definition

We propose here an easy way to estimate the (lat,lon) position with respect to the geometrical information available in the L1c product and the knowledge of the subsatellite point position (latSat, lonSat). The TEC is at the altitude Htec (~450 km).

The use of EO CFI functions would allow obtaining more accurate results (and maybe more straightforward implementation).

We know, for each measurement, the grid point position (latGP,lonGP). In a geocentric reference frame, the coordinates of the grid point (xGP,yGP,zGP) and the satellite (xSat,ySat,zSat) are:

$$\begin{cases} x_{GP} = R_{earth} \cdot \cos(lat_{GP}) \cdot \cos(lon_{GP}) \\ y_{GP} = R_{earth} \cdot \cos(lat_{GP}) \cdot \sin(lon_{GP}) \\ z_{GP} = R_{earth} \cdot \sin(lat_{GP}) \end{cases} \quad 4.16.1$$

$$\begin{cases} x_{Sat} = (R_{earth} + H_{sat}) \cdot \cos(lat_{Sat}) \cdot \cos(lon_{Sat}) \\ y_{Sat} = (R_{earth} + H_{sat}) \cdot \cos(lat_{Sat}) \cdot \sin(lon_{Sat}) \\ z_{Sat} = (R_{earth} + H_{sat}) \cdot \sin(lat_{Sat}) \end{cases} \quad 4.16.2$$

where Rearth is the Earth radius in km and Hsat, the altitude of the satellite in km.

The line (Satellite -> Grid Point) crosses the sphere at Htec altitude. This sphere is described by the following equations:

$$\begin{cases} x = (R_{earth} + H_{tec}) \cdot \cos(lat_{TEC}) \cdot \cos(lon_{TEC}) \\ y = (R_{earth} + H_{tec}) \cdot \cos(lat_{TEC}) \cdot \sin(lon_{TEC}) \\ z = (R_{earth} + H_{tec}) \cdot \sin(lat_{TEC}) \end{cases} \quad 4.16.3$$

The intersection between the sphere and the line of sight is given by:

$$\begin{cases} (R_{earth} + H_{tec}) \cdot \cos(lat_{TEC}) \cdot \cos(lon_{TEC}) = x_{Sat} + \alpha(x_{GP} - x_{Sat}) \\ (R_{earth} + H_{tec}) \cdot \cos(lat_{TEC}) \cdot \sin(lon_{TEC}) = y_{Sat} + \alpha(y_{GP} - y_{Sat}) \\ (R_{earth} + H_{tec}) \cdot \sin(lat_{TEC}) = z_{Sat} + \alpha(z_{GP} - z_{Sat}) \end{cases} \quad 4.16.4$$

which is a system at three equations and three unknowns : latTEC, lonTEC and α .

The way to solve this system is to begin with α . The quadratic sum of the three equations allows eliminating latTEC and lonTEC.

A second order equation shall be solved for the determination of α .

$$(\text{Rearth} + \text{Htec})^2 = (\text{xSat} + \alpha(\text{xGP} - \text{xSat}))^2 + (\text{ySat} + \alpha(\text{yGP} - \text{ySat}))^2 + (\text{zSat} + \alpha(\text{zGP} - \text{zSat}))^2 \quad 4.16.5$$

After extracting α , the computation of latTEC and lonTEC is obtained using 4.16.4.

More precisely, it is possible to write 4.16.5:

$$a.\alpha^2 + 2.b.\alpha + c = 0 \quad 4.16.6$$

with :

$$\begin{aligned} a &= (\text{xGP} - \text{xSat})^2 + (\text{yGP} - \text{ySat})^2 + (\text{zGP} - \text{zSat})^2 \\ b &= \text{xSat}(\text{xGP} - \text{xSat}) + \text{ySat}(\text{yGP} - \text{ySat}) + \text{zSat}(\text{zGP} - \text{zSat}) \\ c &= \text{xSat}^2 + \text{ySat}^2 + \text{zSat}^2 - (\text{Rearth} + \text{Htec})^2 \end{aligned} \quad 4.16.7$$

Equation 4.16.6 has two roots.

The following one must be used:

$$\alpha = \frac{-b - \sqrt{b^2 - a.c}}{a} \quad 4.16.8$$

and then:

$$\text{latTEC} = \arctan 2 \left(\text{zSat} + \alpha(\text{zGP} - \text{zSat}), \sqrt{(\text{xSat} + \alpha(\text{xGP} - \text{xSat}))^2 + (\text{ySat} + \alpha(\text{yGP} - \text{ySat}))^2} \right) \quad 4.16.9$$

using the value of α found below.

Easy validation :

if Htec = 0 , latTEC = latGP

if Htec = Hsat, latTEC = latSat

4.16.2.4 TEC from Stokes 3 (step 4 and step 5)

The TEC is proportional to the Faraday rotation (ω_F) divided by a factor which depends on the geometry of observation and the magnetic field.



The level 2 forward model gives us TH and TV using ECMWF surface parameters. The L1c products give us A3 and ϕ_{psi} . Theoretically, it is possible to compute ω_F at each point of the FOV from the ratio A3/(TH-TV). However, on a large part of the FOV, TH is close to TV (for incidences $< 20^\circ$) and thus the ratio A3/(TH-TV) is difficult to manage under these conditions. Moreover, A3 is affected by an error equal to about 2 K and of a bias given by the OTT. That involves, in most of the cases, an important error on the ω_F estimation. In fact, this error depends on the sensitivity of the brightness temperatures to Faraday rotation.

To escape these problems, it is proposed to select the areas of the FOV which are the most sensitive to the TEC.

For that, the derivative of the brightness temperatures according to the TEC are built in different (ξ, η) positions. This derivative is not only computed for A3 but also for TX and TY. Figure 31 shows the value of the derivative obtained for various positions in the FOV according to the latitude.

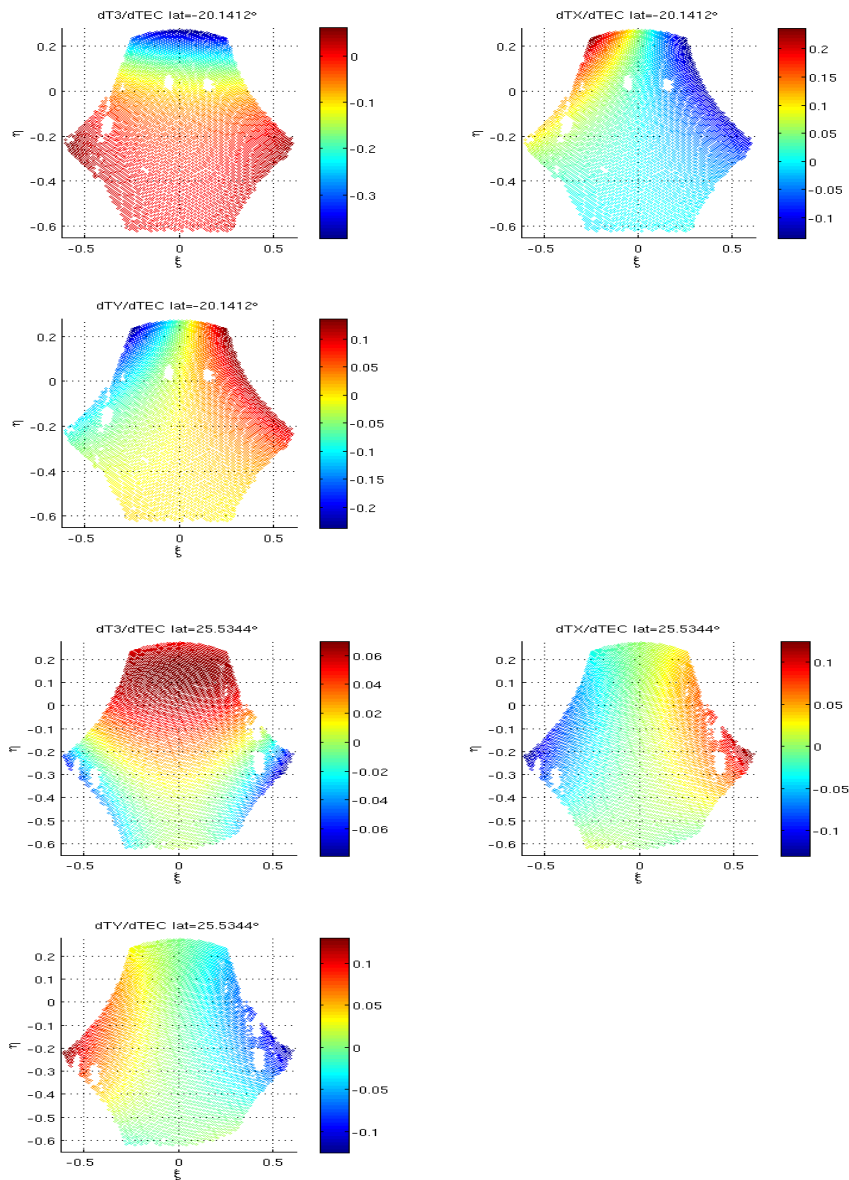


Figure 30: Estimate of forward model TB sensitivity to TEC for A3, TX and TY polarisations (descending orbits). Three upper figures: computed at 20° latitude south; three bottom figures: computed at 25° latitude north.

A3 is particularly sensitive to the TEC at large incidence angle (in front of the FOV). So, if we want to estimate the TEC from A3 polarisation, it is better to use the area in front of the FOV. The variations of $dA3/dTEC$ according to the latitude show that there exists an area where the temperatures are not very sensitive to the TEC (Figure 32).

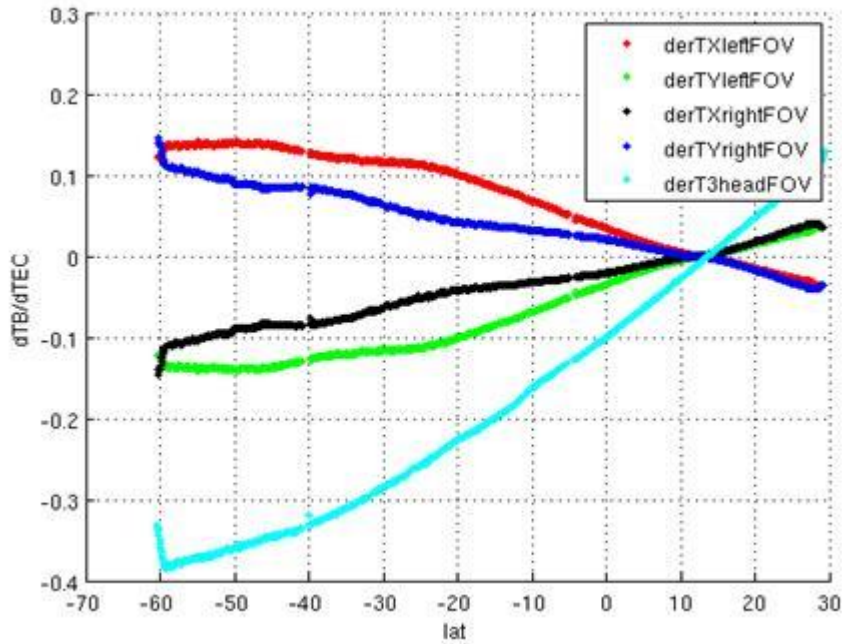


Figure 31: Estimate of forward model TB sensitivity to TEC according to the polarization, the latitude and the position on the FOV. derTXleftFOV means that the derivative of TX is computed on the left part of the FOV. Note that derTX+derTY is equal to 0 and correspond to the fact that the Stokes 1 is insensitive to TEC. The Stokes parameter the most sensitive to TEC is A3 (derT3headFOV) taken in the front of the FOV (cyan curve). The red arrows show the latitude where the derivative is computed (Figure 29).

Let us note that to estimate the TEC, the following operation can be applied:

$$TEC = TEC_0 + \frac{dTb}{dA3} \cdot (A3 - A3_{mod}(TEC_0) - OTT) \quad 4.16.10$$

where TEC_0 is the a priori TEC value (given by AUX_VTEC for example), A3 is the SMOS measurement, $A3_{mod}(TEC_0)$ is the forward model computed from ECMWF auxiliary data and OTT is the scene bias as described in section 5. Considering the low values of Faraday rotation, the linearization of the direct model is justified.

To simplify the following mathematical expression, we take $A3_{corr} = A3 - OTT$:

$$TEC = TEC_0 + \frac{dTb}{dA3} \cdot (A3_{corr} - A3_{mod}(TEC_0)) \quad 4.16.11$$

In the areas where $dA3/dTEC$ vanishes, then the estimate of the TEC could tend towards the infinite due to a small measurement error. Therefore, in these areas, it is not possible to

estimate the TEC. Moreover, a small bias due to a bad OTT correction is amplified in these areas. That undoubtedly explains why the first estimates of the TEC during the commissioning did not lead to a satisfactory result.

Since TEC varies slowly with the latitude, it is possible to retrieve the TEC by adding a space correlation on relatively large scales (500 km). That makes it possible to stabilize the result of inversion in the vicinity of the latitudes where $dA3/TEC$ vanishes.

In practice, the forward model equation is written as follows:

$$A3 = A3_{\text{mod}}(TEC_0) + \frac{dA3}{dTEC} \cdot (TEC - TEC_0) + OTT \quad 4.16.12$$

The unknown parameters are the TEC according to the latitude. The OTT which depends on the position in the (ξ, η) plan is considered as unknown and is simultaneously estimated at $(-0.025 < \xi < 0.025, 0.15 < \eta < 0.2)$. To estimate TEC, a least squares method is performed with minimization of the following cost function:

$$\chi^2 = \text{vecRes}^T C_d^{-1} \text{vecRes} + (TEC - TEC_0)^T C_m^{-1} (TEC - TEC_0) \quad 4.16.13$$

with:

$$\text{vecRes}(TEC, OTT) = \left(A3 - A3_{\text{mod}}(TEC_0) - \frac{dA3}{dTEC} \cdot (TEC - TEC_0) - OTT \right) \quad 4.16.14$$

^T meaning that the vector is transposed, C_d is the covariance of the data, C_m is the a priori covariance of the TEC and C_{OTT} the a priori covariance of the OTT.

The a priori covariance C_m is constituted by the a priori variance of the L1c TEC. This value shall be configurable and could be taken equal to 100 for first tests.

The estimated TEC is expressed as follow if we consider no latitudinal correlation:

$$TEC = TEC_0 + \left(\frac{(A3 - A3_{\text{mod}}(TEC_0) - OTT_0) \cdot \frac{dA3(TEC_0)}{dTEC}}{\left(\frac{dA3}{dTEC} \right)^2 + \frac{\sigma_{A3}^2}{\sigma_{TEC}^2} + \frac{\sigma_{OTT}^2}{\sigma_{TEC}^2}} \right) \quad 4.16.15$$

σ_{A3}^2 represents the radiometric noise of the A3 measurement and σ_{TEC}^2 the a priori covariance of the TEC (in this expression Cm is considered as a diagonal matrix with 0 off-diagonal elements).

The OTT estimator is written as follows:

$$OTT = OTT_0 + \sum \left(\frac{(A3 - A3_{mod}(TEC_0) - OTT_0)}{\left(\left(\frac{dA3}{dTEC} \right)^2 \frac{\sigma_{TEC}^2}{\sigma_{OTT}^2} + \frac{\sigma_{A3}^2}{\sigma_{OTT}^2} + 1 \right)} \right) \quad 4.16.16$$

Where σ_{OTT}^2 is the a priori covariance of the OTT and the sum is done over all SMOS measurements (along the considered half orbit).

This last expression shows that if A3 is not sensitive to TEC, $\frac{dA3}{dTEC} = 0$ and $TEC = TEC_0$.

If σ_{A3}^2 tends to infinity, we have the same effect.

If we include latitudinal correlations for TEC, Cm has off diagonal element. Considering two latitude lat_i and lat_j, the TEC covariance is written:

$$Cm(TEC(lat_i), TEC(lat_j)) = \sigma_{TEC}^2 \exp\left(- (lat_i - lat_j)^2 / \xi^2\right) \quad 4.16.17$$

ξ , the latitude smoothing length could be taken equal to 3° or 5° latitude (configurable). In this condition, the solution is written:

$$\begin{pmatrix} TEC \\ OTT \end{pmatrix} = \begin{pmatrix} TEC_0 \\ OTT_0 \end{pmatrix} + Cp.G^T (G.Cp.G^T + Cd)^{-1} (\text{vecRes}(TEC_0, OTT_0)) \quad 4.16.18$$

with

$$Cp = \begin{pmatrix} Cm & 0 \\ 0 & Cott \end{pmatrix} \quad 4.16.19$$

and G the matrix of partial derivative:

$$G = \begin{pmatrix} \frac{dA3}{dT_{EC}}(lat1) & 0 & \dots & \frac{dA3}{dOTT} \\ 0 & \frac{dA3}{dT_{EC}}(lat2) & 0 & \frac{dA3}{dOTT} \\ \vdots & \vdots & \frac{dA3}{dT_{EC}}(lat3) & \frac{dA3}{dOTT} \\ 0 & 0 & & \frac{dA3}{dOTT} \end{pmatrix} \quad 4.16.20$$

and

$$\frac{dA3}{dOTT} = 1$$

If we consider that OTT estimator has a neglectable error, the theoretical TEC error is given by:

$$\sigma_{TEC} = \sqrt{\left(\frac{\sigma_{A3}^2}{\left(\frac{dA3}{dT_{EC}}\right)^2 + \frac{\sigma_{A3}^2}{\sigma_{TEC}^2}} \right)} \quad 4.16.21$$

This expression is used in step 6.

A systematic error on the a priori knowledge of TH and TV has only little impact on A3mod. Indeed, a simple calculation shows that if, for example, the ECMWF surface temperature is biased this is equivalent, at the first order, to add a constant bias DT on TH and TV. Considering the fact that A3mod depends on (TH-TV), this bias disappears from itself. This makes the method of extraction of the TEC from A3 polarization particularly robust and not very dependent on the underlying forward model.

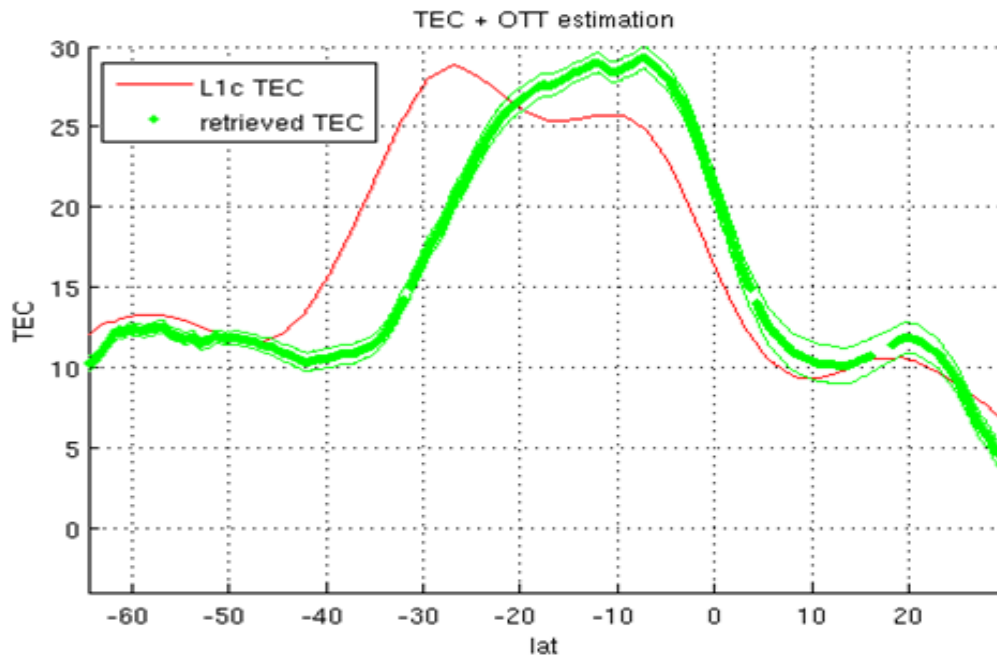


Figure 33: Example of TEC estimation using A3 (green) to be compared with L1c TEC (in red). The shift in latitude is due to the fact that retrieved TEC is obtained at large incidence angles, far from the nadir.

At this end of this step, a smoothed TEC estimation is given according to the latitude.

4.16.2.5 Quality of the TEC estimation (step 6)

In the previous section, two indicators are computed: the TEC theoretical error and the TEC standard deviation obtained from the sliding window.

These two indicators are not given in the same support.

To compare them, the mean TEC theoretical error shall be computed by using the same sliding window that the one used in the previous section.

The ratio between the standard deviation and the mean theoretical error shall be close to one. If the standard deviation is significantly larger than the theoretical error, this means that there are outliers.

An indicator giving the percentage of latitudinal cells with a ratio (TEC standard deviation / TEC error) larger than a threshold (for instance equal to 2) could be computed. This ratio shall be computed only if there are sufficient observations in the window.

If this ratio is too large, we propose to use L1c TEC value instead of estimated TEC.



4.16.2.6 Estimation of TEC for each SMOS measurement (step 7)

First, for each measurement, the position (lat,lon) of the intersection of the line of sight and the TEC layer (see section 4) is computed.

Secondly, the TEC is interpolated at the given (lat,lon) position by using the TEC estimation. This value shall be used to compute the Faraday rotation.

4.16.2.7 Link with the OTT computation

TEC algorithm allows estimating TEC latitudinal profile and OTT at FOV position ($-0.025 < \xi < 0.025, 0.15 < \eta < 0.2$) simultaneously. TEC algorithm is run without TB correction from OTT and without LSC correction.

5 Ocean Target Transformation (OTT)

5.1 Introduction

Analysis of the measured L1c (Tb_{L1c}) and modelled L2OS brightness temperature (Tb_{model}) values during commissioning phase showed that the L2OS forward model brightness temperature values do not match those from the L1c input. The differences appeared to be systematic in the (ξ, η) antenna frame in areas far from land. A correction for this systematic error was needed, so the SMOS L1c Tb can be used to retrieve salinity.

The correction consists of the reconstruction of the systematic ξ - η bias pattern by using differences in Tb values far from land, and then using that to correct the measured Tb values globally. This is called the Ocean Target Transformation (OTT).

The differences in Tb values, denoted ΔTb are obtained by,

$$\Delta Tb = Tb_{L1c} - Tb_{model}. \quad 5.1.1$$

The way in which these ΔTb are computed for each (ξ, η) point involves the empirical comparison of SMOS measurements with respect to the forward model in an area not affected by other potential sources of noise (e.g. land/sea contamination, high winds, high natural variability, high RFI). Hence, an OTT region was defined in the Pacific Ocean for both ascending and descending orbits, as is shown in Figure 32.

Snapshots acquired over the OTT region are used to compute the OTT, with a running average of 10 semi-orbits' worth of valid data in each OTT file. The single semi-orbit contribution to OTT is obtained by selecting the median ΔTb value for the specific ξ, η coordinate over the antenna reference frame. The OTT offset is then applied to each ξ, η cell simply as,

$$Tb(\xi, \eta) = Tb_{L1c}(\xi, \eta) - OTT(\xi, \eta). \quad 5.1.2$$

The ξ, η coordinate system is the antenna coordinate system, It consists of a 129 by 129 grid, where $-0.7 < \xi < 0.7$ and $-0.7 < \eta < 0.4$. To convert to ξ, η from x, y the following formulae are used:

$$\xi = \left(\frac{1.4}{128} x \right) - 0.7 \quad 5.1.3$$

$$\eta = \left(\frac{1.1}{128} y \right) - 0.7. \quad 5.1.4$$

Three auxiliary data files (ADFs) are specified for the OTT, one for each roughness model. Different OTT files are required for dual pol and full pol retrieval modes. For dual pol the OTT



only needs to correct Tb in XX and YY, while for full pol short XX, short YY and the real and imaginary components of YYX and XXY also need to be corrected. Ascending and descending orbits have different OTTs in the OTT file. The OTTxD/F file format is specified in the IODD. AUX_DTBXY files are nominally generated for each semi-orbit. These AUX_DTBXY are the seed for the OTT computation and collect the individual differences between Tb_{model} and Tb_{L1c} . Each of these files contains the pre-computed data required for its use in the OTT computation, including identifying the list of snapshots from the L1c product meeting the requirements, with special emphasis to the geographical matching between the snapshot coordinates and the defined OTT regions. A further ADF, the DTBCUR file, has the ΔTb values which are used in the current OTT generation. The AUX_DTBCUR file acts as a database of the list of semi-orbits valid for the OTT computation. The AUX_DTBCUR is updated whenever a new valid semi-orbit for OTT computation is found. At the end of the day, the post-processor (see below) uses the information of the last updated DTBCUR file to generate the OTT. The field specification of the DTBXY and DTBCUR files can be found in the IODD.

OTTs are automatically generated each day within DPGS using an OTT post-processor OSCOTT (see OTTPSUM for more information on OSCOTT). The information given here describes parts of the L2OS processor and OSCOTT which are relevant to the creation and application of the OTT.

5.2 OTT region

There are two OTT regions used in nominal processing, one for ascending (denoted using 9001) and one for descending (9002). They both fall in the Pacific Ocean, between 5°S and 45°S and are 42° wide. Region 9001 is centred at 116°E at the top and 126°E at the bottom, while region 9002 is centred at 128°E and 117°E at the top and bottom, respectively. The regions are specified in the CNFOSF/D file and can be customised. The choice of the region is based on a strict criterion of low natural SSS variability, spatial homogeneity, low RFI concurrence, and far enough from the coast to minimise land-sea contamination. The reasoning of it is trying to minimize the non-systematic contribution to the ΔTb , so the antenna patterns can be isolated within the OTT.

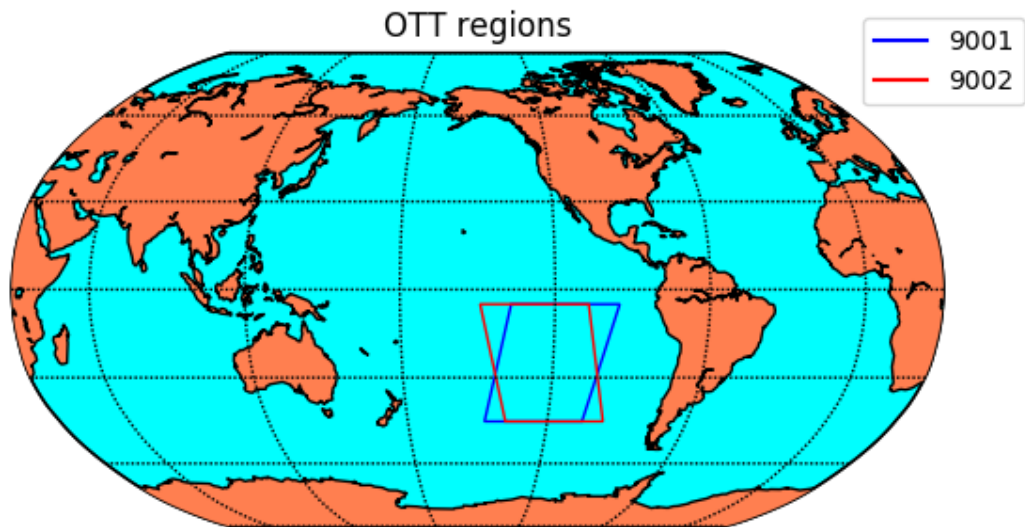
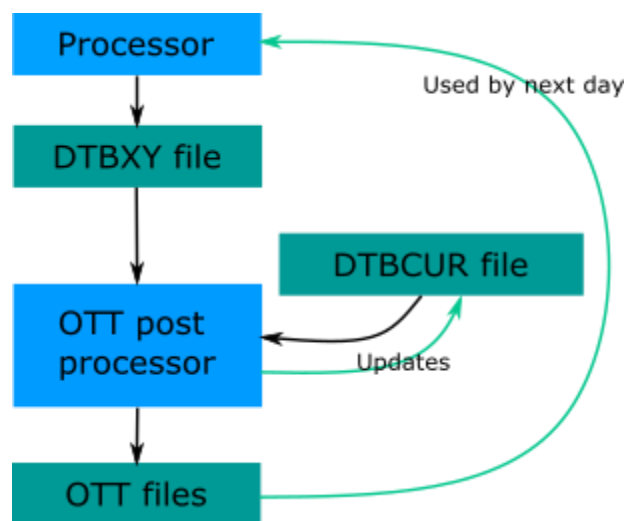


Figure 32: The OTT regions for ascending (9001) and descending (9002) orbits

A snapshot is only classed as being in the OTT region if all its measurements are in the region and proves to be valid according to a set of strict filtering criteria, as explained below. Snapshots with too many measurements damaged by sun point, tails, RFI or any of the filtering criteria are discarded entirely from the OTT computation.

5.3 OTT process

The OTT process can be simplified into five steps, as described in the schematic below. In the processor a DTBXY file is generated. If an orbit has snapshots which fall within the OTT region, then the DTBXY file has the $\Delta T b$ values for both the global (9999, i.e. all orbit latitudes) and OTT (9001/9002) regions stored.





Once a day, after processing is complete, the OTT post processor takes the existing DTBCUR file, which contains details of the current $\Delta T b$ values and DTBXY files in use for the OTT computation, along with any new DTBXY file with an OTT region. OSCOTT uses the information in these files to generate the three OTT files and update the DTBCUR with the new valid DTBXY data. The updated OTT files are then used the next day for correcting $T b$ values before salinity retrievals.

5.4 Data selection and OTT computation

Before beginning the process of data selection for the OTT, the measurements have been filtered earlier in processing. Only measurements which have been selected as valid when computing the geometry of the change of reference system (translation of modelled measurements to antenna frame) will be valid at the start of OTT selection, so any measurement which is flagged as having problems in the ancillary data (land, ice, close to coast etc.) will not be valid for the OTT.

The measurements which are output into the OTT are filtered on several scales within the process of making the DTBXY and OTT files. Various thresholds and filters are used, and these are set in the CNFOSF/D file of the L2 OS processor. Details can be found in the IODD.

On the region scale, the OTT region is only processed if there are more than Min_Snapshots (=200) valid snapshots, and more than Min_Grid_Points (=2500) valid grid cells and also more than Min_Percent_Valid_Grid_Points (=25%) and more than Min_percent_Valid_Snapshots (=25%).

A snapshot is valid if all of the measurements in the snapshot are within the OTT region, the snapshot has more than Min_Percent_Snapshot_Measurements (=50%) and they pass the OTT_snapshot_filter:

- Fm_L2_RFI_snapshot_out_of_range
- Fm_L2_RFI_high_snapshot_std
- Fm_L2_RFI_high_snapshot_std_Stokes3
- Fm_L2_RFI_high_snapshot_std_Stokes4
- Fm_L1c_software_error
- Fm_L1c_instrument_error
- Fm_L1c_calibration_error

A grid cell is rejected if there are fewer than two measurements per grid cell or the grid cell is not in the region. It is also rejected if $SSS_{ref} == 1$ and $fg_ctrl_poor_retrieval == true$.

Counters are incremented for number of grid cells based on flags as shown in Table 4.

ARGANS Ltd.

Commercial in Confidence

Page 232

Use, duplication, or disclosure of this document or any information contained herein is subject to the restriction on the title page of this document.

Table 4: OTT grid cell counters and the flags which are used to set them

Counter	Flags
nOcean	fg_sc_land_sea_coast1 == True AND fg_sc_land_sea_coast2 == True.
nIce	fg_sc_in_clim_ice == True
nMissingEcmwf	fg_ctrl_ecmwf == False
nLowWS	fg_sc_high_wind == False AND fg_sc_low_wind == False
nHighWS	fg_sc_high_wind == True AND fg_sc_low_wind == False

Finally, a grid cell must pass the OTT_Region_Filter:

```

Fg_ctrl_ignore
Fg_sc_land
Fg_sc_coast
Fg_sc_near_land
Fg_sc_suspect_ice
Fg_ctrl_missing_ECMWF
Fg_sc_rain
Fg_sc_low_wind
Fg_sc_high_wind
Fm_sun_point
Fm_L1c_RFI

```

If after all the filtering and measurement selection there are enough valid snapshots and measurements to process the OTT region, the identified semi-orbit will be used for the OTT computation, by including all the relevant valid data from the corresponding DTBXY file in the DTBCUR.

To compute the OTT three steps are applied. Firstly, the valid measurements are found and counted in ξ, η grid cells. The number of measurements in each grid cell is counted, and then measurement counters are incremented according to flags as shown in Table 5. The OTT region filter is applied again.

Table 5: Measurement counters incremented according to flags.

Counter	Flags
nSunpointL1	fml1c_sun_point == True
nSunGlint	fml1c_sun_glint_area == True OR (fm_low_sun_glint == True AND fm_low_sun_glint == False)
nMoonGlint	fml1c_moon_point == True AND fm_moon_specDir == True
nGalNoise	fm_gal_noise_error == True AND fm_high_gal_noise == True

ARGANS Ltd.

Commercial in Confidence

Page 233

Use, duplication, or disclosure of this document or any information contained herein is subject to the restriction on the title page of this document.

nSunTailsL1	Fml1c_sun_tails == True
nRFIL1	fm11c_rfi_tails == True OR fml1c_rfi_strong == True OR fml1c_rfi_mitigation == True OR fml1c_rfi_point == True
nRFIL2	fm_l2_rfi == True

In the second step the ΔTb values and statistics are put into ξ, η grid cells. The procedure in which the positions within the defined grid are identified is derived from Eq. 5.1.3 and 5.1.4. By inverting the equations (x,y) coordinates are found, using an interpolation method based on closest neighbor. For each grid cell which is valid, for all the measurements in the grid cell, the OTT flags are set according to the flags in Table 6. The Tb_{model} is calculated and then the ΔTb is calculated using 5.1.1. All the ΔTb values generated for each valid measurement, from all the valid snapshots and orbits under consideration, are accumulated at each grid cell position.

Table 6: OTT flags and the measurement flags which are used to set them

OTT flag	Measurement flag
fm_ott_sun_glint	fm_high_sun_glint == True and fm_low_sun_glint == False
fm_ott_gal_noise	fm_gal_noise_error == True OR fm_high_gal_noise == True
fm_ott_moon_glint	fm_moon_specDir == True
fm_ott_l2_rfi	fm_l2_rfi == True

The third step concerns the calculation of the median ΔTb and standard deviations for each (ξ, η) cell for metrics. Finally, the DTBXY file is then written out. The median is selected because it is significantly less sensitive to outliers and because of the low number of total points found generally into each (ξ, η) cell.

Up to this point, the required data processing happens in the pre-processor, by direct comparisons between the forward model and the actual measurement. This is intentional as the convergence algorithm – based on a Levenberg-Marquardt minimization- would lead to a mitigation of the systematic errors by adjusting the other parameters used in the retrieval. To avoid this, the OTT must be computed making use of the first guess from the model, or a prior Tb model. However, the OTT cannot be computed until all the semi-orbits of a given day are processed, so that the list of valid semi-orbits has been accordingly updated in the AUX_DTBCUR (10 valid AUX_DTBCUR files are taken into account to generate a new AUX_DTBCUR file). When this occurs, the OTT is computed and the daily OTT file generated, by the OTT post processor OSCOTT.

In OSCOTT the counters output in the DTBXY file are used for filtering on grid cells or measurements, before writing the ΔTb values to the DTBCUR files. The thresholds for each counter are found in the CNFOSF/D, details are found in the IODD., and the list of filters is shown below:

ARGANS Ltd.



L1_software_errors
L1_Instrument_Errors_Max_Percent
L1_ADF_Errors_Max_Percent
L1_Calibration_Errors_Max_Percent
TBs_Out_Of_Range_Max_Percent
High_Std_Max_Percent
High_Std_Stokes3_Max_Percent
High_Std_Stokes4_Max_Percent
Min_Measurements
L1_Sun_Tails_Max_Percent
Sun_Glint_Max_Percent
Moon_Glint_Max_Percent
L2_Gal_Noise_Max_Percent
L1_RFI_Max_Percent
L2_RFI_Max_Percent
for each model:
Max_XX_AFFOV_StdRa
Max_XX_EAFFOV_StdRa
Max_YY_AFFOV_StdRa
Max_YY_EAFFOV_StdRa
For HHV and VVH real
Max_Stokes3_AFFOV_StdRa
Max_Stokes3_EAFFOV_StdRa
For HHV and VVH imag:
Max_Stokes4_AFFOV_StdRa
Max_Stokes4_EAFFOV_StdRa

Due to the application of many filters it is possible to have missing grid cells in the OTT region, where the sun point appears, for example. If grid cells are removed due to failing the tests given, a 0 correction is applied in that grid cell. When the 10 valid semi-orbits are averaged, these 0 corrections can be preserved, for example in the case of a sun point which appears in all the DTBXY files. The OTT which is then applied has a 0 correction in that area. Figure 33 shows an OTT with a circle of zero correction.

5.5 OTT calculation

In OSCOTT the $\Delta T b$ values for the short XX/YY can be merged with the long XX/YY (where short and long refer to the integration time), and the cross-pol Stokes 3 and Stokes 4 can be merged according to the OTT strategy given in the CNFOSF. Strategy 1 is a mean of the 10 different contributions per each ξ, η cell, while 2 is a Gaussian mean, with strategy 1 being nominal.



For a full-polarization configuration, OTT_Merge_FP can be set to merge the long and short XX/YY OTTs (=1), merge the cross-pol S3 and S4 orbits (=2) or both (=3). A merge weight for short terms can be specified. This weight is computed by considering the expected variations of the theoretical radiometric noise happening at each type of snapshot (long or short integration time).

For example, the equation for merging the short and long XX pol ΔTb values in each (ξ, η) grid cell is,

$$\Delta Tb_{merged,XX} = \frac{\Delta Tb_{long,XX} * n_{long,XX} * w_{long,XX} + \Delta Tb_{short,XX} * n_{short,XX} * w_{short,XX}}{n_{long,XX} + n_{short,XX}} \quad 5.5.1$$

where n_{long} is the count of XX long measurements in that grid cell, n_{short} of YY short and w is the merge weight (nominally: $w_{short} = 0.625$ and $w_{long} = 1$). The OTT is then the mean in each (ξ, η) cell of the ΔTb values in that (ξ, η) cell.

The strategy for the start validity of the OTT (for the filename etc) is set by OTT_Validity_Start can be derived either from the first snapshot (=1), middle time between first and last snapshot (=2), the last snapshot (=3) or the validity start of the first snapshot orbit (=4).

It is worth mention that additional data filtering shall be applied, as described in the following subsection 5.8.

5.6 Applying the OTT correction

The OTT is applied in processing before the iterative scheme begins. The offset is polarisation dependent. The offset value is taken from the lookup table using either bilinear or nearest neighbour interpolation to find the closest (ξ, η) cell, as done when allocating valid measurements into the OTT grid. The choice of interpolation method is set using OTT_interpolation (0 = nearest neighbour, 1 = bilinear) in the CNFOSF. In nominal processing the bilinear interpolation is used.

The OTT value is then simply subtracted from that L1c measurement in the grid cell using 5.1.2,

$$Tb(\xi, \eta) = Tb_{L1c}(\xi, \eta) - OTT(\xi, \eta). \quad 5.6.1$$

As discussed above, as the (ξ, η) grid is initially zero, any areas without valid data result in a zero correction. These zero corrections is then applied to the TB values in that ξ, η position over the whole globe for the validity period of the OTT.

20140426T023222/OTT1

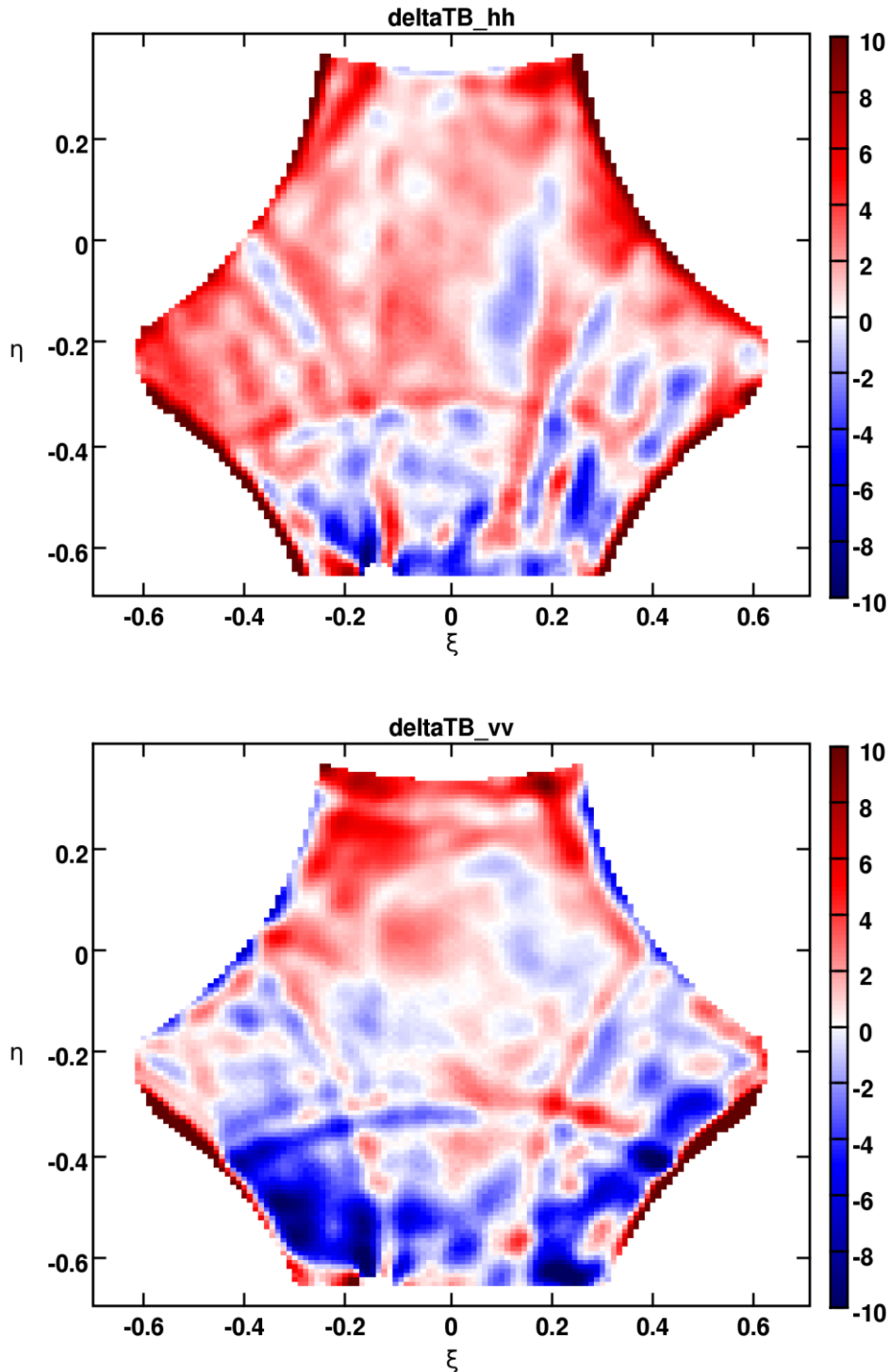


Figure 33: The region 9001 OTT valid from 26/04/2014. Note the area of zero correction at the bottom of the hexagon.

20140720T084552/OTT1

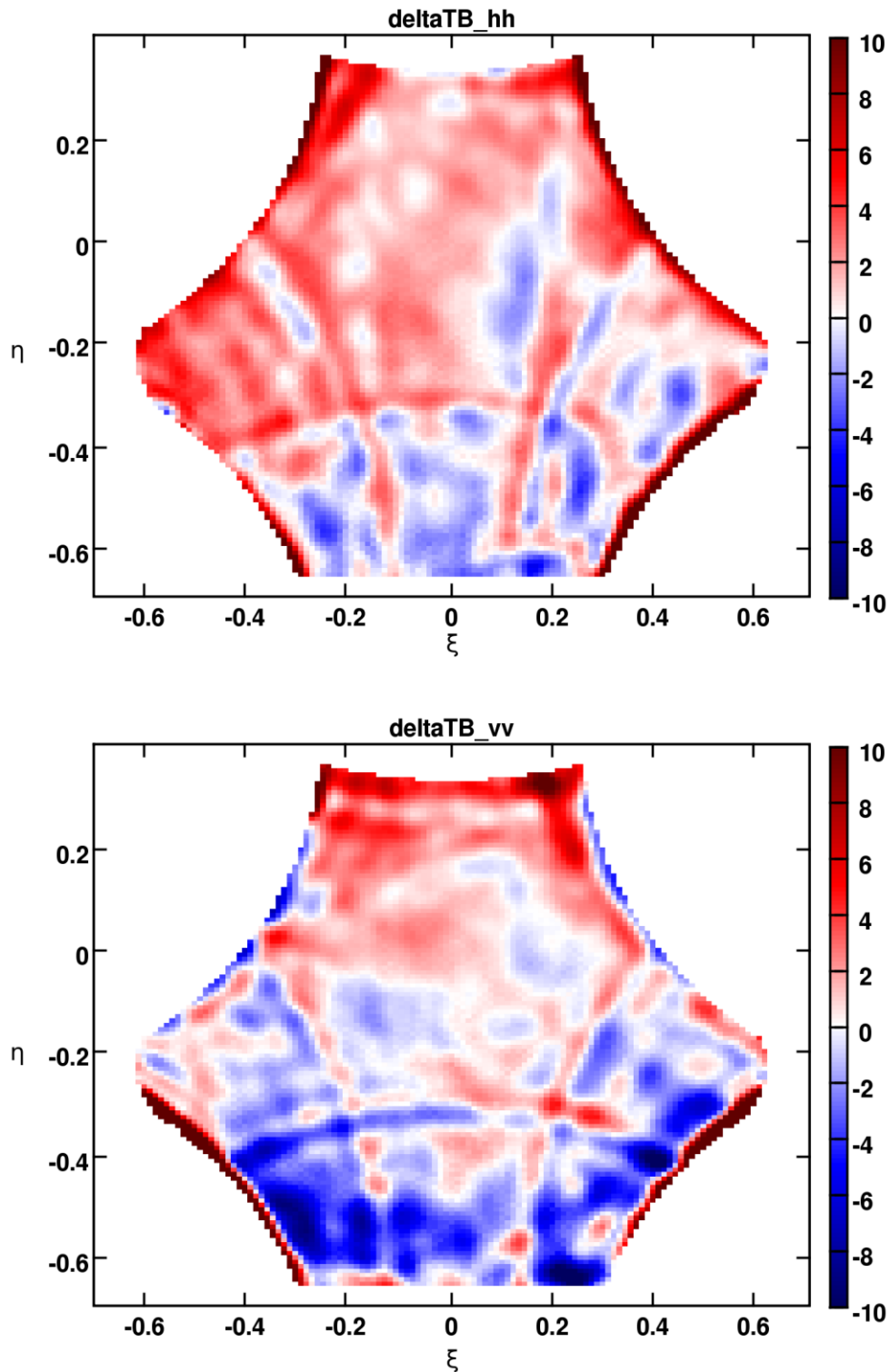


Figure 34: The region 9002 OTT valid from 20/07/2014

ARGANS Ltd.

Commercial in Confidence



5.7 Validity period of the OTT

As discussed above, the OTT is updated daily by employing the list of 10 valid semi-orbits (10 for ascending and 10 for descending) contained in the DTBCUR file. While this means that a new OTT file appears every day, it does not imply that 10 days' worth of data are used in its computation.

For instance, the defined OTT regions for ascending and descending semi-orbits allow, occasionally, for more than one semi-orbit per day complying with the criteria. If this is the case, two semi-orbits of that type are used into the OTT computation. As new semi-orbits are introduced into the DTBCUR, the oldest orbits are displaced out of it. Which means that, under normal circumstances, when this event happens OTT is computed using less than 10 days of data (but still using only 10 semi-orbits).

On the other hand, some events can yield no valid semi-orbits in each day. For instance, a particularly intense RFI event during the crossing semi-orbit in the OTT region could mean that not enough valid data is found; therefore, the semi-orbit is discarded to prevent contamination of the resulting OTT. This means that DTBCUR file could not be updated in each day, and therefore, its validity time is extended to the next day. As a consequence, the OTT of the current day is identical to that from the previous day, so its validity time is also increased. The impact of this strategy is that the data processing ensures the existence of an OTT every day, but when events prevent its update the OTT becomes "older" and less representative of the systematic errors associated to the semi-orbits to which is being applied.

While this is understood as not optimal, the impact into the retrieved SSS is far less than by allowing corrupted data entering in the computation of the OTT.

5.8 Additional considerations

5.8.1 OTT and A3TEC

With the introduction of the land/sea contamination correction and the A3TEC retrieval for Faraday rotation computation, OTT processing had to be also adjusted accordingly.

In this sense, the mixed scene contamination or land/sea contamination correction was not considered in the computation of the OTT. The rationale behind this exclusion lies in the fact that the LSC correction works in a similar way as the OTT does, by accumulating systematic errors at the antenna frame level between forward model and the observations. In this case, consideration of the geographical position is also considered, but there is no time coordinate as the correction for land/sea effect is computed using the entire mission. However, because the antenna patterns are also systematic, the LSC correction would include those too, so applying LSC correction and OTT could result into an over-correction of the systematic errors.

ARGANS Ltd.

Commercial in Confidence

Page 239

Use, duplication, or disclosure of this document or any information contained herein is subject to the restriction on the title page of this document.

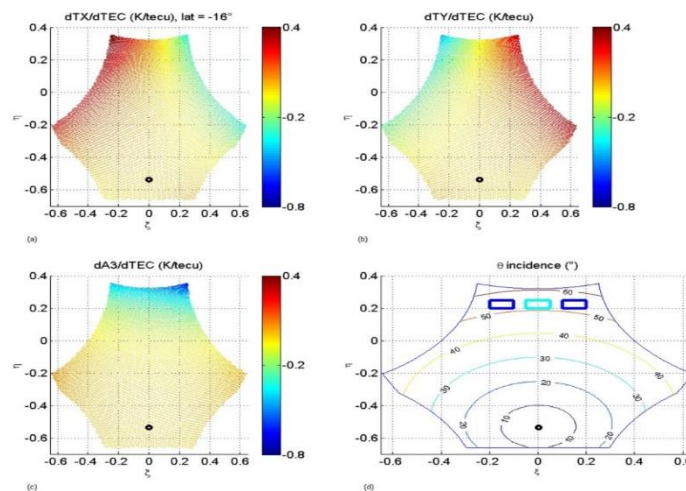
In order to prevent this, LSC correction does not apply to OTT computation, and correspondingly, OTT data is used to correct the baseline of the LSC correction, so to isolate the component only due to land/sea contamination.

For A3TEC, however, the positive effect of applying the method into the computation of the DTBXY files was considered significant. Meaning that the Faraday rotation applied to the modelled TBs is based in the estimation of TEC done by using the Stokes-3 information provided by SMOS. The choice was made to make the data processing consistent within the OTT computation and the SSS retrieval algorithm.

Nevertheless, both LSC correction and A3TEC strategy are fully configurable within the AUX_CNFOSD/F files, with the current nominal behaviour being the one indicated here.

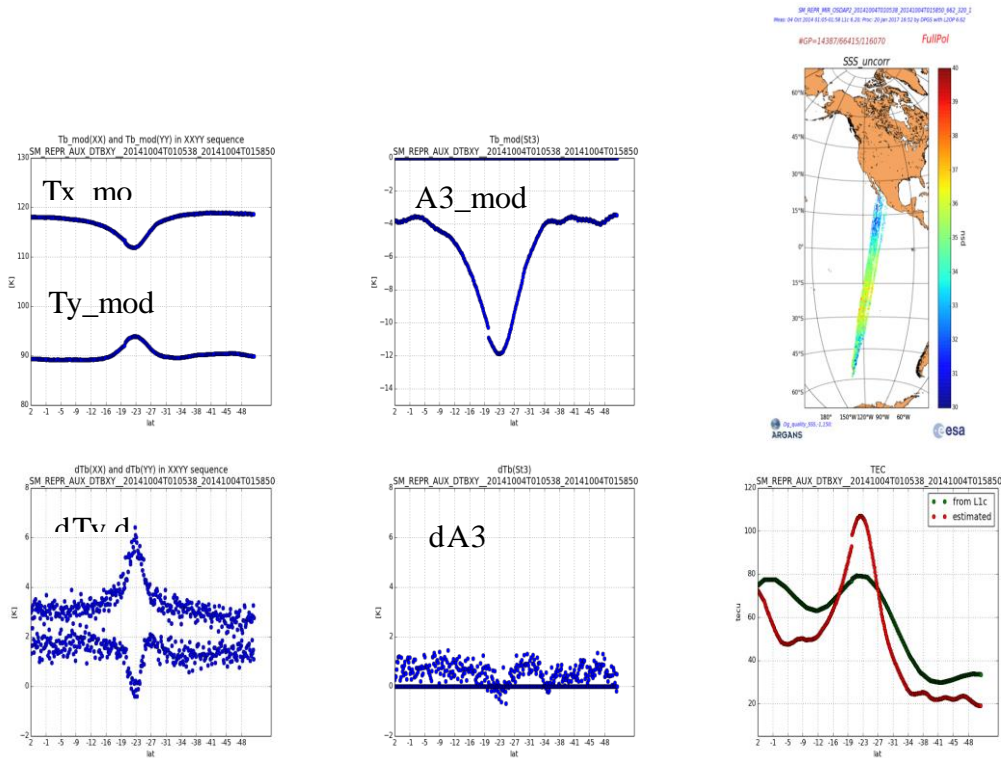
5.8.2 OTT model-related flaws

In addition to L1 calibration and image reconstruction issues, imperfections in the Tb simulated with the forward model may contribute to errors introduced in Tb recalibration generating artificial OTT variations. This may be the case of a not correct Faraday rotation angle determination, due to a not perfect Total Electron Content (TEC) information (Figure 1.2 shows the variation of brightness temperatures with TEC).



It was demonstrated that TEC estimation from the third Stokes parameter on the antenna plane reduces the standard deviation of the OTT (particularly in the front of the FOV) and a better agreement is found when comparing ground truth to retrieved SMOS salinities (Vergely, 2014). However, for some orbits, an error in the A3 OTT pre-estimation (which is computed at 15 degrees North, for a small region of the FOV around the values of $\xi = 0$, $\eta = 0.2$) or a residual error in the modelled A3 parameter (which may depend on the azimuthal wind direction, which remain to be studied systematically) may introduce a bias in Tb which

varies with latitudes and shows a maximum peak over the latitudes of maximum total electron content, see Figure 1.3.



Whenever this type of error appears, it is found that the standard deviation of the difference $T_b^{meas} - T_b^{mod}$ normalized by the radiometric accuracy degrades for X and Y polarizations on the front of MIRAS FOV, resulting in values higher than 1.1, see Figure 1.4.

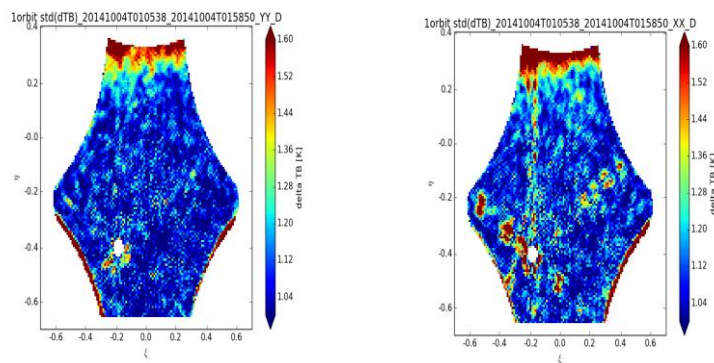


Figure 5-1. Standard deviation of $(T_b^{meas} - T_b^{mod})/Rad.Acc.$ of all snapshots falling in the OTT region, one orbit, 2014-10-04, Y (left) and X (right) polarization. Colorscale ranges from 1 to 1.6.

5.8.3 Additional steps for the OTT generation scheme

To tackle *dtb* bias appearing in some corrupted OTT orbits, a new scheme for generating the final OTT is here proposed. The filtering procedure may be explained following a block diagram as shown in Figure 5-4. The 10 AUX_DTBXY files ingested by OSCOTT post-processor for the nominal (as for L2OS v622 and v662) OTT computation are taken into account and in the first block the region of the FOV for which $\eta > 0.2$ is selected and tested: if, for both X and Y polarizations, the average of the normalized standard deviation exceeds 1.15, then the entire SMOS orbit is rejected (in other words, the AUX_DTBXY is discarded). In the second block a further filtering may be applied on the pixels of the FOV having a normalized standard deviation greater than 1.2. In a third block, the selected and filtered AUX_DTBXY files are selected, a median is done over them, and the final OTT is generated.

The analysis of the standard deviation on the front of MIRAS FOV reveals that the typical periods in which OTT orbits are rejected are around the months of February to April, and October to November, for the case of descending orbits, see Figure 5-36. The ascending orbits are obviously less sensible to TEC estimates considering the Total Electron Content value during the morning hours of the day is lower than the evening when SMOS crosses the equatorial line at 6 .p.m.

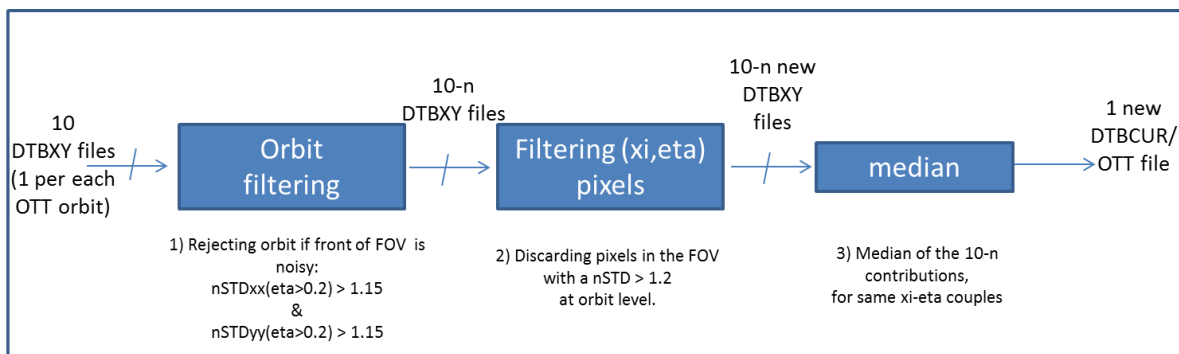


Figure 5-4. New OTT generation block diagram.

Figure 5-37 shows the evolution of the standard deviation of the OTT in the front of MIRAS FOV. Being TEC correlated to the sun activity, year 2014 is supposed to be a worst-case scenario, considering the evolution of the sun cycle.

To be noted that the selected AUX_DTBXY files will continue respecting the nominal quality filtering applied at both grid point level and measurement level, as well as the minimum number of measurements per single (ξ, η) pixel.

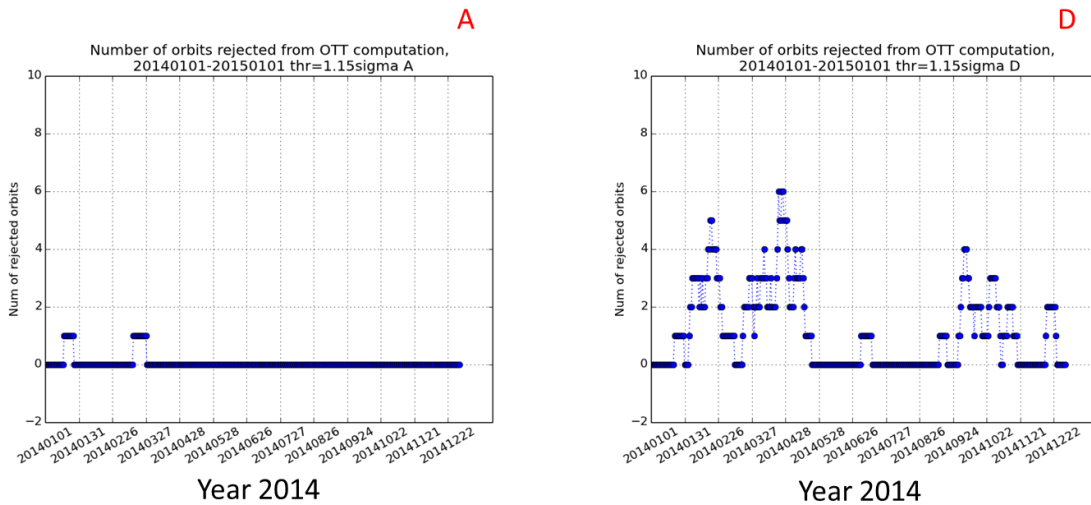


Figure 5-36. Number of orbits rejected from OTT computation for year 2014, ascending passes (left) and descending passes (right).

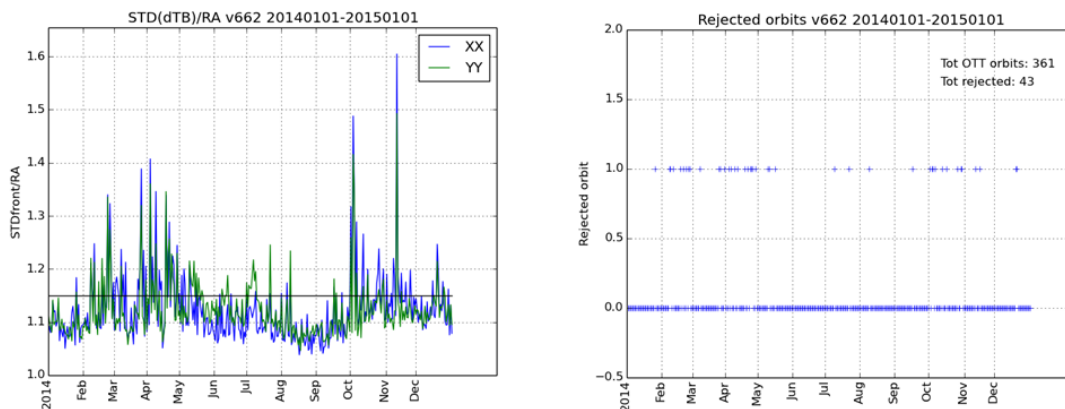


Figure 5-37. Left : average of normalized standard deviation of pixels in the FOV, $\eta > 0.2$, for all year 2014 (in black the threshold, in green Y polarization, in blue X polarization). Right : Rejected orbits during 2014 (0: orbit not rejected; 1: orbit rejected).

5.8.4 Assessment of new OTT

The assessment of the new OTT refinement strategy was done for the month of April, for both ascending and descending orbits, using version v622 of the L2OS processor and making use of v620 L1c input data. After the generation of the reviewed (*rev*) AUX_OTT and AUX_DTBCUR files, the output Level 2 User Data Product (UDP) was compared to the nominal v622 UDP product and the quality of salinity was validated with respect to ISAS ground truth, see Figure 5-38 , applying for both datasets the same usual L2OS validation protocol (LOCEAN-IPSL, 2017). The same orbits were considered for the generation of the Level 3 (L3) product.

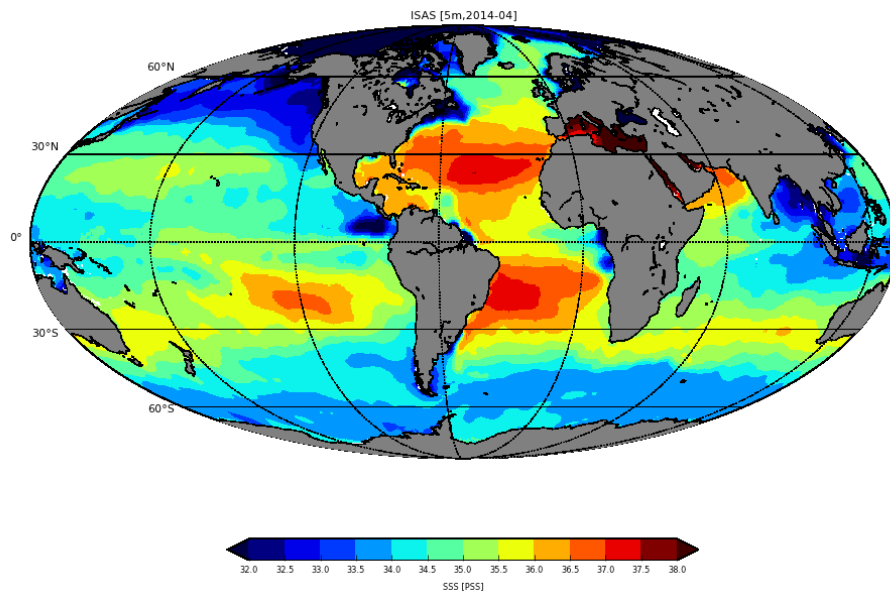


Figure 5-38. ISAS salinity for the month of April 2014 (color scale from 32 to 38 pss).

5.8.4.1 Descending orbits

The SMOS Level 3 monthly salinity maps were computed using both v622 UDP files and v622 OTT-revisited UDP files (v622rev). Below it is shown the differences between the two SMOS salinities (Figure 5-41), and their difference with respect to ISAS, see Figure 5-8 and Figure 5-9.

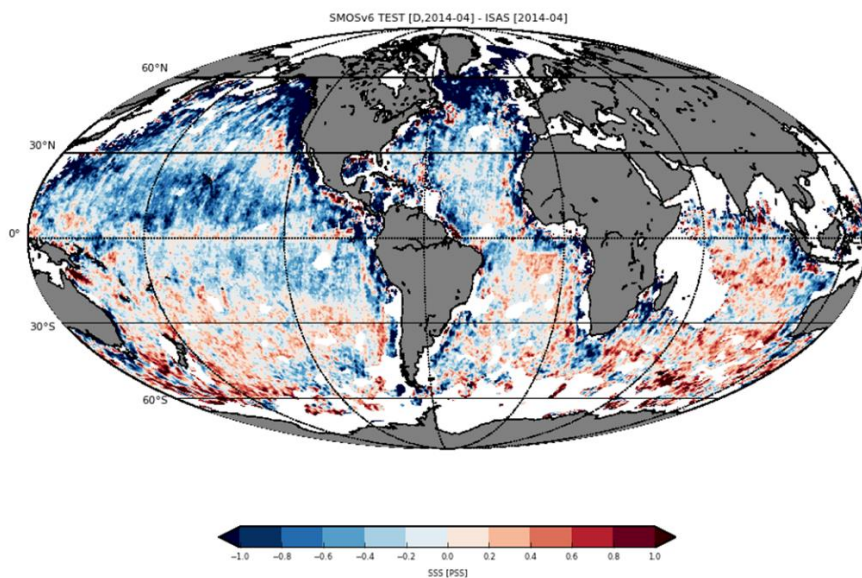


Figure 5-8. SMOS Level3 SSS – ISAS SSS, April 2014, descending passes (colorscal from -1 to 1 pss).

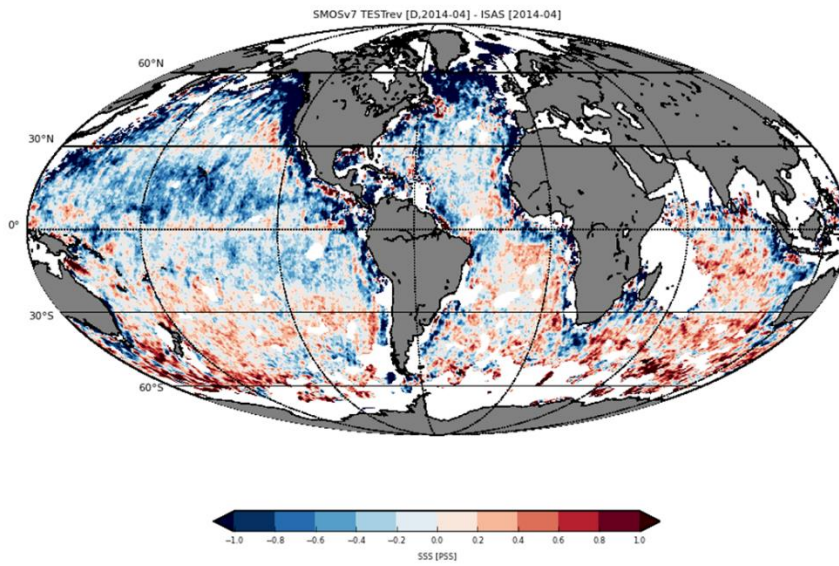


Figure 5-9. SMOS Level3 SSSrev – ISAS SSS, April 2014, descending passes (colorscal from -1 to 1 pss).

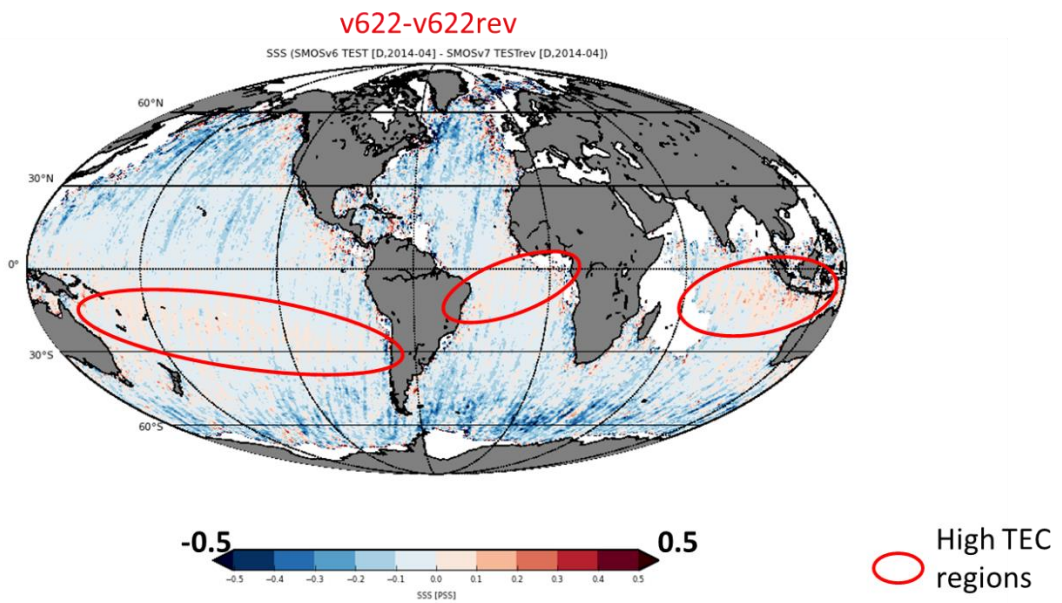


Figure 5-41. SMOS Level3 SSS – SMOS Level3 SSSrev, April 2014, descending passes (colorscal from -0.5 to 0.5 pss).



The map of the differences between the two SMOS SSS, shows that in the Northern Hemisphere, where v622 SSS is fresher with respect to ISAS, v622 SSS rev is slightly saltier, and, in high TEC regions, where v622 SSS is saltier with respect to ISAS, v622 SSSrev is slightly fresher. In both cases the SMOS bias with respect to the ground truth is slightly reduced but the large bias spatial pattern persists. See Table 5-4 and Table 5-5 for the first order statistics of SMOS SSS – ISAS SSS.

L3 pixel stats, 45S-45N, Dcoast>800km, Desc			
	N	Mean	std
V622(reviewed)-ISAS	238907	-0.107	0.377
V622-ISAS	238795	-0.154	0.390

Table 5-4. Level 3 pixel statistics for both SMOS SSS and reviewed SSS, for a coast distance greater than 800 km, in between -45 and +45 degrees of latitude.

L3 pixel stats, OTT_ZONE, Dcoast>800km, Desc			
	N	Mean	std
V622(reviewed)-ISAS	27483	-0.068	0.253
V622-ISAS	27483	-0.101	0.261

Table 5-5. Level 3 pixel statistics for both SMOS SSS and reviewed SSS, for a coast distance greater than 800 km, in the OTT region.

5.8.4.2 Ascending orbits

Below it is shown the differences between the two SMOS salinities (Figure 5-13) and their respective difference with respect to ISAS, see Figure 5-11 and Figure 5-12.

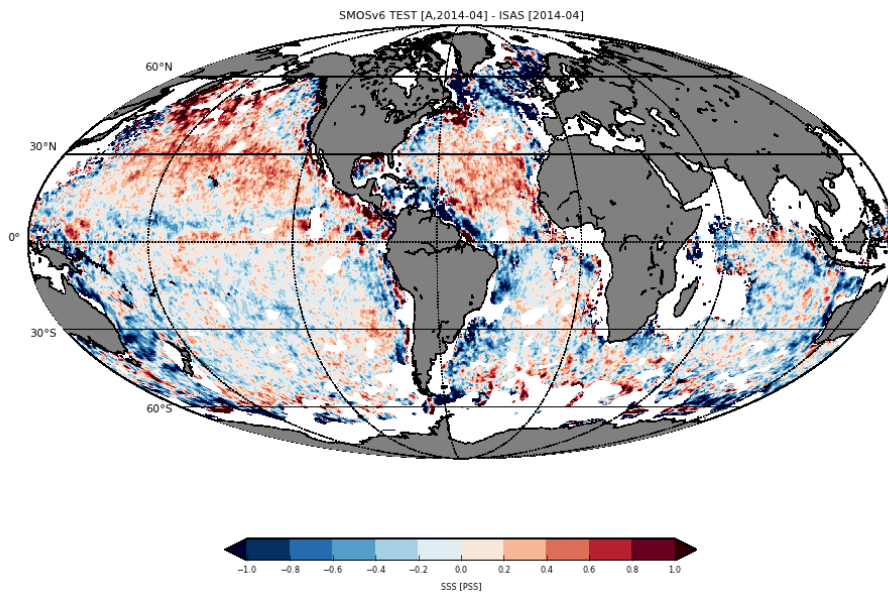


Figure 5-11. SMOS Level3 SSS – ISAS SSS, April 2014, ascending passes (colorscale from -1 to 1 pss).

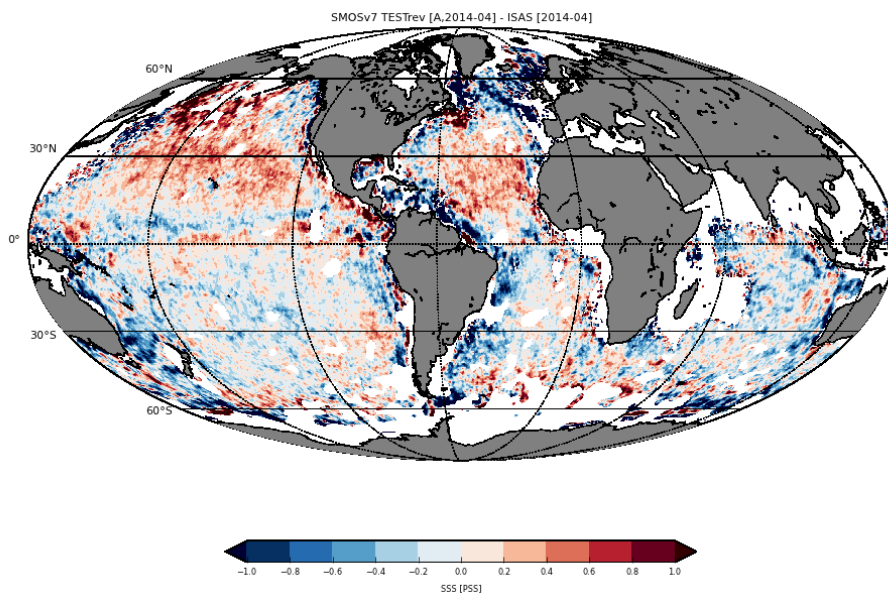


Figure 5-12. SMOS Level3 SSSrev – ISAS SSS, April 2014, ascending passes (colorscale from -1 to 1 pss).

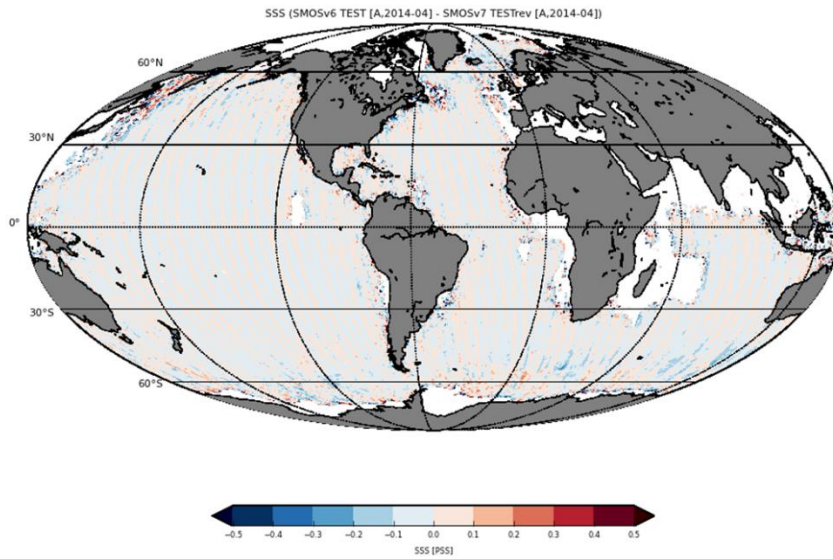


Figure 5-13. SMOS Level3 SSS – SMOS Level3 SSSrev, April 2014, ascending passes (colorscale from -0.5 to 0.5 pss).

As expected, for ascending orbits, the changes in terms of salinity quality are much smaller and statistics between one version and the other look in line (the reviewed-OTT salinity is slightly less biased than the nominal one, and the standard deviation of the difference between satellite salinity and ground truth almost match each other).

L3 pixel stats, 45S-45N, Dcoast>800km, Asc			
	N	Mean	std
V622(reviewed)-ISAS	237352	0,002	0,328
V622-ISAS	237264	-0,008	0,330

Figure 5-14. Level 3 pixel statistics for both SMOS SSS and reviewed SSS, for a coast distance greater than 800 km, in between -45 and +45 degrees of latitude.

L3 pixel stats, OTT ZONE, Dcoast>800km, Asc			
	N	Mean	std
V622(reviewed)-ISAS	27483	-0,046	0,179
V622-ISAS	27483	-0,056	0,181

Figure 5-15. Level 3 pixel statistics for both SMOS SSS and reviewed SSS, for a coast distance greater than 800 km, OTT region.



5.8.5 Conclusions and recommendations

The new SMOS OTT computation scheme was developed to guaranty high-quality AUX_DTBXY files (in terms of dTb bias and standard deviation) to be ingested by the OSCOTT processor. The filtering strategy aims to tackle OTT artificial variation due to corrupted TEC and Faraday rotation estimation.

The assessment of the salinities retrieved with v622 L2OS processor using the reviewed OTT shows a salinity quality improvement, especially for descending orbits which are considered the ones to be more affected by the presence of higher Total Electron Content in the atmosphere: for the month of April 2014, the mean SMOS salinity bias with respect to ISAS is reduced by 0.05 pss and the standard deviation of the difference between satellite and in situ salinities is reduced by 0.01 pss, in between 45 degrees South and 45 degrees North, for Level 3 pixels more than 800 km far from coast . For ascending passes the statistics for the SMOS v622 SSS and SMOS v622 reviewed SSS are much in line, and no degradation of the data quality is observed (the bias and the standard deviation of the difference with respect to ISAS are slightly smaller with the reviewed version).

It is recommended to implement the new OTT generation scheme in the release of version 700 of the L2OS processor, foreseen for the next SMOS L2OS fourth mission reprocessing.

References

- [1] R. C. P. A. Gutierrez, SMOS L1 Processor L1c Data Processing Model, 2014.
- [2] SMOS L2OS team, SMOS L2 OS Algorithm Theoretical Baseline Document, Chapter 4, 2016.
- [3] S. L. team, SMOS L2 OS Algorithm Theoretical Baseline Document, Annex 4, 2016.
- [4] J.-L. Vergely, «New total electron content retrieval improves SMOS sea surface salinity,» *Journal of Geophysical Research*, vol. 119, 2014.
- [5] LOCEAN-IPSL, «SMOS L2OS Validation Protocol, Technical Note,» 2017.

6 Land (Mixed Scene) Contamination Correction (MSOTT)

6.1 Introduction

In spaceborne radiometry, land contamination of ocean brightness temperatures refers to a bias in the brightness temperatures that occurs when land is present in the field of view of the instrument. In a real aperture radiometer, the origin land contamination is the contribution of land in the FoV to the antenna temperature, which, if not removed, will lead to a bias in the brightness temperatures obtained by either deconvolution or application of the antenna pattern correction (APC). In an interferometric radiometer such as MIRAS, land contamination may have several origins, including reconstruction bias (to be discussed below) [1,2] and inconsistencies in the cross-correlation denormalization coefficients between the zero and nonzero baselines [3].

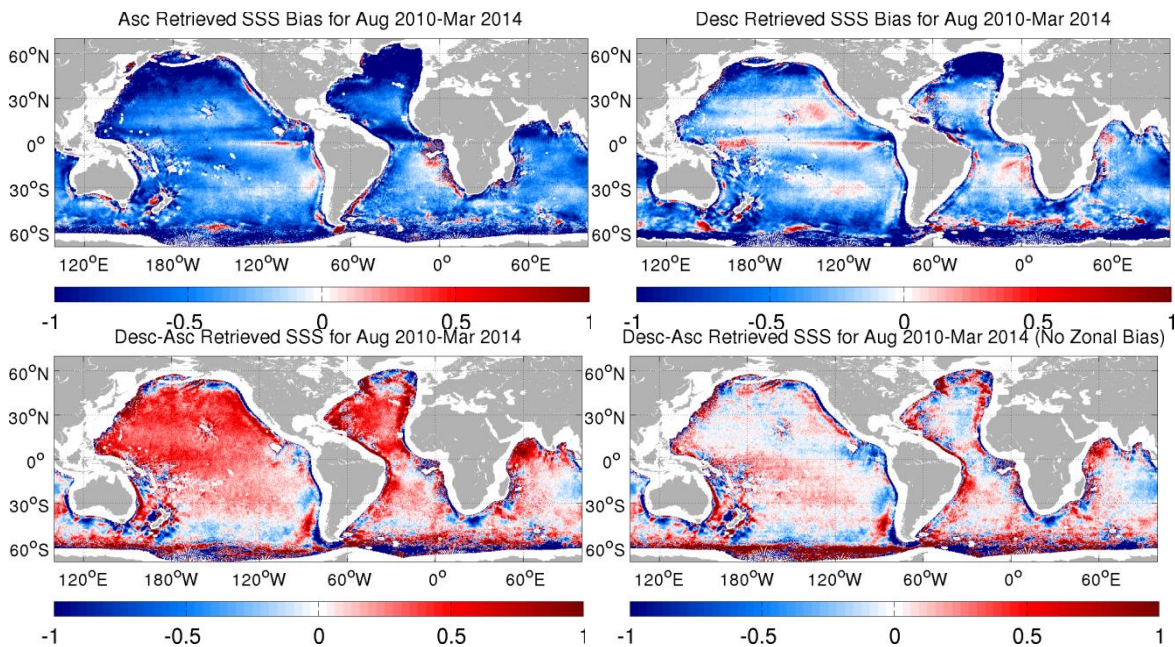


Figure 1: SMOS retrieved salinity bias from August 2010 through March 2014 after applying the hexagon RFI filter approach and a single OTT for the entire period and for both pass directions. Upper left: ascending passes; upper right: descending passes; lower left: descending minus ascending; lower right: Same as lower left but with zonally averaged bias removed at each latitude. SMOS brightness temperatures based upon 2011 ESA reprocessing campaign.

With several years of data, it is now possible to illustrate the impact of land contamination on the retrieved salinity. As an example (based upon the level 1B brightness temperature Fourier components from the 2011 ESA reprocessing), the upper panels of the figure show the retrieved salinity biases for ascending and descending passes separately as averaged from August 2010 through March 2014. For these maps we have not shown salinity where the distance to coast is less than 80 km or the fraction of earth points in the FOV that are either

land or ice exceeds 0.8. Yet despite the application of these filters, biases around the continents remain evident and exceed 1 (on the Practical Salinity Scale) in some areas.

These bias maps were created using WOA 2009 climatological SSS as a reference, so part of the bias may correspond to actual deviation of SSS from climatology. However, the lower panels of the figure show that, around the continents, the differences between ascending and descending pass biases in retrieved SSS can exceed 0.5 and vary in sign. These differences should not be sensitive to the reference SSS used in the forward model. The differences are clearer when the zonally averaged bias difference is removed.

Comparison of SMOS-derived salinities to those obtained from ARGO floats (**Figure 2**) shows the same pattern, with large negative biases in SMOS salinities, exceeding 2 psu up to 1000 km from the coastline.

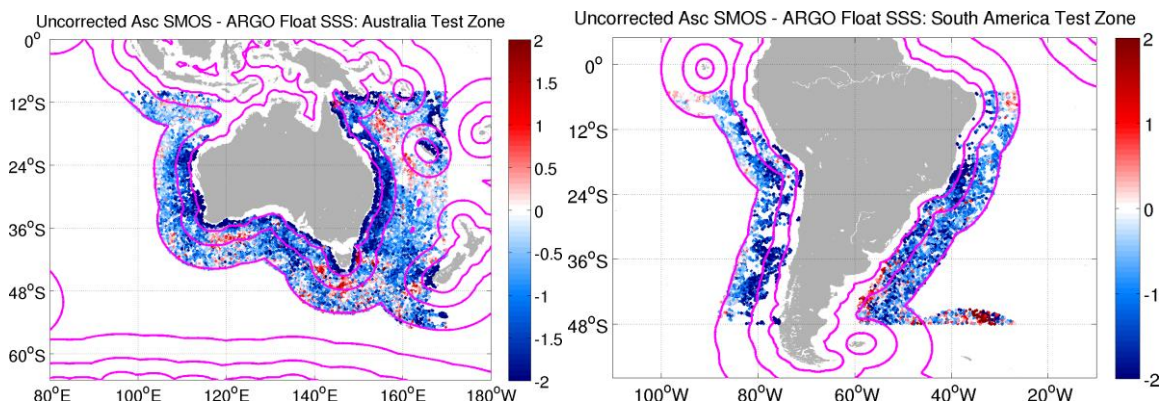


Figure 2 : Difference between surface salinity as measured by ARGO floats and those obtained from collocated SMOS brightness temperatures (as obtained from the 2011 reprocessing). Magenta curves are isolines of distance to the coast (200, 500, and 1000 km).

The problem of land contamination was anticipated long before launch in 2009 (see Anterrieu 2007 for example). Indeed, our own simulations, conducted in the months prior to launch, revealed the potential for brightness outside the fundamental hexagon to induce biases on the order of several kelvin in the first Stokes parameter inside the fundamental hexagon, and inside the alias-free field of view. An example of this contamination is shown in **Figure 3**. For this example, the scene brightness is partitioned into the portions inside and outside the fundamental hexagon. Then the instrument modelling operator (the G matrix) is applied separately to each partition and then the images are reconstructed from the partitioned visibilities. The resulting partitioned reconstruction images are then compared to the original partitioned images, and the differences are shown in the bottom panels. Most notable is the fact that the image reconstructed from the visibilities corresponding to the brightness outside the hexagon exhibits nonzero brightness inside the alias-free field of view. Indeed, the vertically polarized brightness temperature reaches nearly 5 K in the AF-FOV, yet in the idealized situation in which the instrument operator is simply a discrete Fourier transform

this reconstructed image is zero everywhere inside the alias-free field of view. Moreover, the pattern of nonzero brightness inside the AF-FOV changes in a complicated way as the brightness outside the fundamental hexagon changes.

This type of bias was analysed in Anterrieu 2007, and the solution proposed in that paper involves the introduction of a model for the scene brightness over the entire front half-space that depends on a small number of parameters (much smaller than the number of spatial frequencies in general) and is as close to reality as possible. The model is typically linear these parameters which are then determined so that the visibilities computed from this model (using the G matrix) best fits the measured visibilities. The model visibilities are then subtracted from the measured ones and the image reconstruction is applied to the perturbation visibilities, which yields a perturbation image that is then added to the model image to produce the total image.

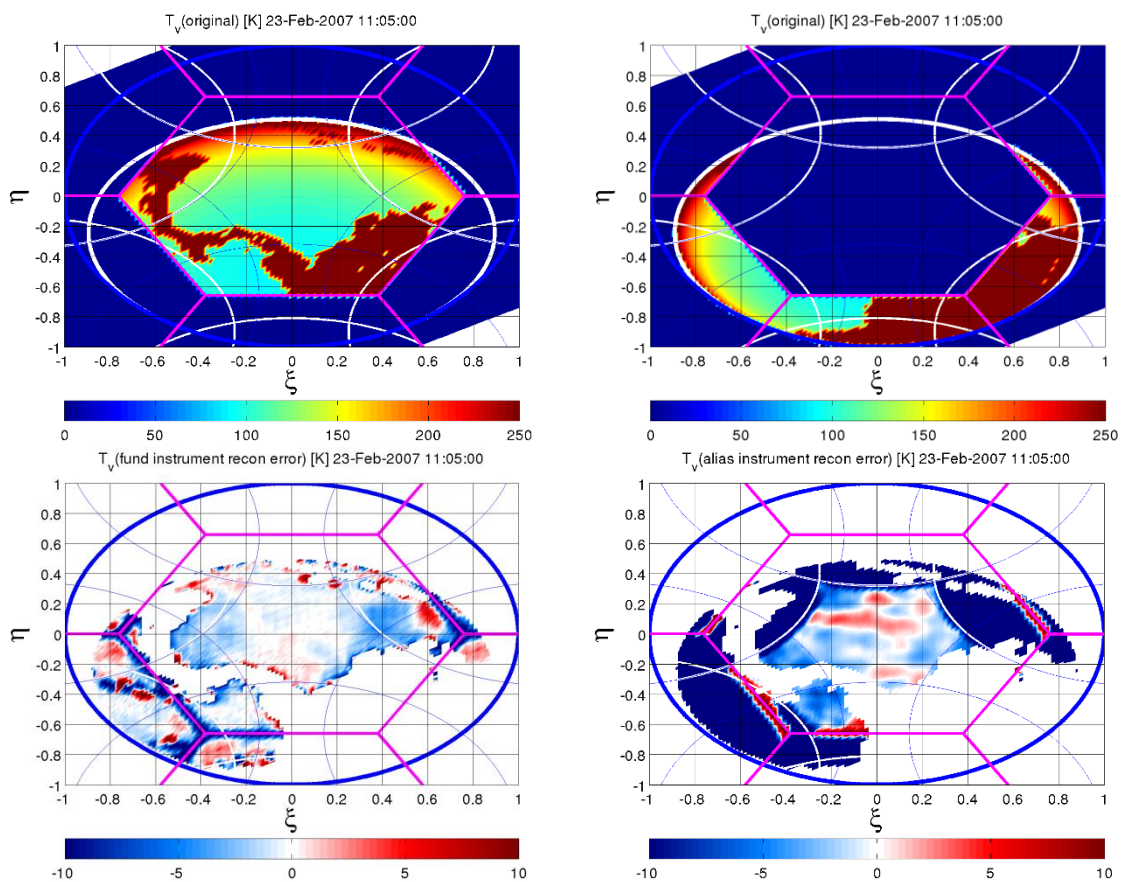


Figure 3: Comparison of reconstructed and original images (vertical polarization in the surface basis) for a scene in the Caribbean Sea. The original scene is partitioned into the portion inside the fundamental hexagon (upper left) and the portion outside this hexagon (upper right). Lower panels show the corresponding differences between the reconstructed and original scene brightness temperature for each partition.

If the G matrix is free from errors and the model is close to the actual scene, this approach should work. Yet many tests performed by the Level 1 team have shown that the method does not consistently reduce the land contamination. Therefore, at least for now, some form of practical solution must be developed.

To facilitate development of a practical solution, the land contamination must be characterized in more detail. Most generally, the land contamination may be a function of position in the field of view and the distribution of land outside the fundamental hexagon. Thus, as a first step in characterizing the problem, bias was analysed as a function of dwell line position in the FOV and as a function of land fraction outside the hexagon. **Figure 4** shows examples of the decomposition of the domains for bias calculation (green boxes) and for the land and ice fraction calculations.

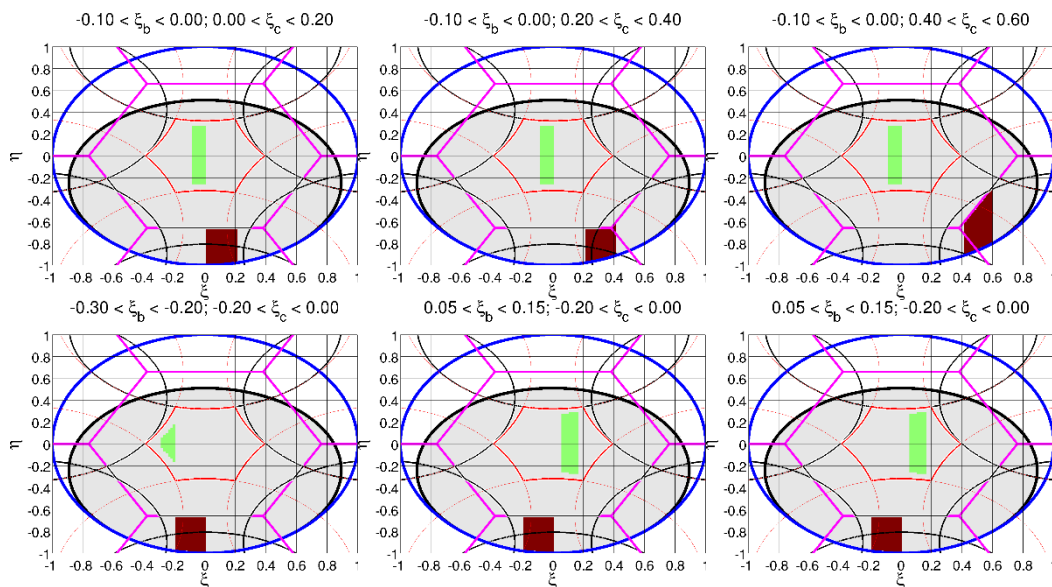


Figure 4: Examples of vertical strips for the bias calculation (green) and for the land and ice fraction calculations. The red domains lie entirely inside the region between the fundamental hexagon and the unit circle in director cosine coordinates.

One result of the calculations is a set of global maps of the fraction of earth consisting of land or ice outside the fundamental hexagon, examples of which are shown in **Figure 5** and **Figure 6**. These figures illustrate the asymmetrical nature of the land plus ice fraction and the dependence upon pass direction. Given the previously noted dependence of land contamination upon pass direction, it is of interest to examine the relationship between the land fraction patterns of the bias patterns.

Figure 5 shows the land plus ice coverage for dwell lines lying in the green rectangle shown in the left panel. The middle and right panels show the fraction of earth area in the FOV

outside the hexagon occupied by ice or land for ascending and descending passes, respectively. This domain is shown in red in the left panel.

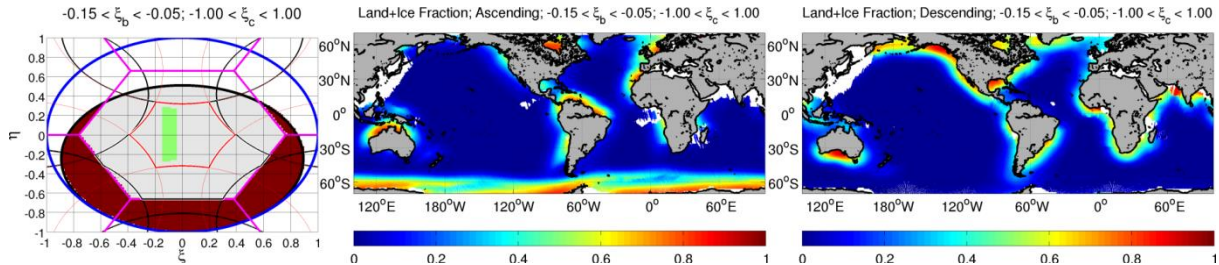


Figure 5: Example of ascending and descending pass land plus ice fraction. These maps were computed over the period Jan 2010 through Mar 2014 for all dwell lines in the green rectangle and for the land/ice fraction domain in red left panel).

Figure 6 is analogous to **Figure 5** except that all dwell lines within the green area inside the AF FOV are included, but the domain over which the land plus ice fraction is computed is reduced to the small red area outside the hexagon shown in the left panel. The corresponding land plus ice fraction maps are noticeably different that those shown in **Figure 5** and these differences serve to illustrate the potential dependence of land contamination upon both dwell line position in the FOV and the position of land outside the hexagon.

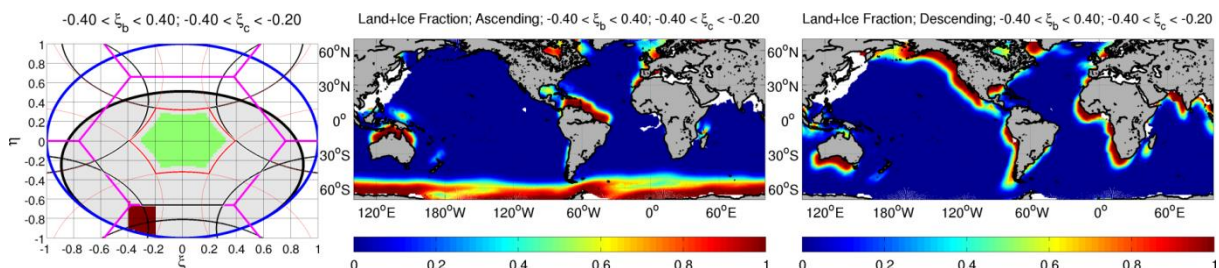


Figure 6: Same as previous figure but for averaged over all dwell lines inside the green domain in the left panel and considering the land+ice fraction inside the red domain.

Although bias maps that combine all dwell lines, like those shown above, clearly reveal the land contamination, it is impossible to determine from these maps how the land contamination manifests itself in terms of bias within the AF FOV or EAF FOV. Only further analysis of the bias as a function of both position within the FOV and the distribution of land outside the hexagon can provide further insight.

6.2 Development of the method

The approach described above has not yielded any conclusive and generally applicable relationship between the land fraction outside the fundamental hexagon and the bias pattern within the FOV. Therefore, the current approach involves expressing the land contamination

bias for polarization p as a function of position within the field of view, position on earth, and pass direction, or

$$\Delta T b_p = \Delta T b_p(D, \phi_g, \psi_g, \xi, \eta) \quad 6.2.1$$

where D is the pass direction, (ϕ_g, ψ_g) are the geographic longitude and latitude and (ξ, η) are the usual director cosine coordinates.

This is the most general form that does not include any time dependence in the bias. But note that although there is no explicit time dependence, the bias at any point on earth may vary with time as the position of that point within the satellite swath varies. This function is derived from the nearly complete set of orbits from January 2010 through June 2014. As the repeat cycle for the SMOS satellite of 149 days, it is necessary to use the largest possible set of data since a particular point on earth is viewed with the same geometry only once every 149 days.

The choice of discretization involves a trade-off between spatial resolution and noise in the bias estimates. The lookup table grid spacing is 0.025×0.025 in the director cosine coordinates and $0.5 \times 0.5^\circ$ on earth. An example of this grid is shown in **Figure 7**. This discretization has been found to provide adequate estimates of the LSC bias.

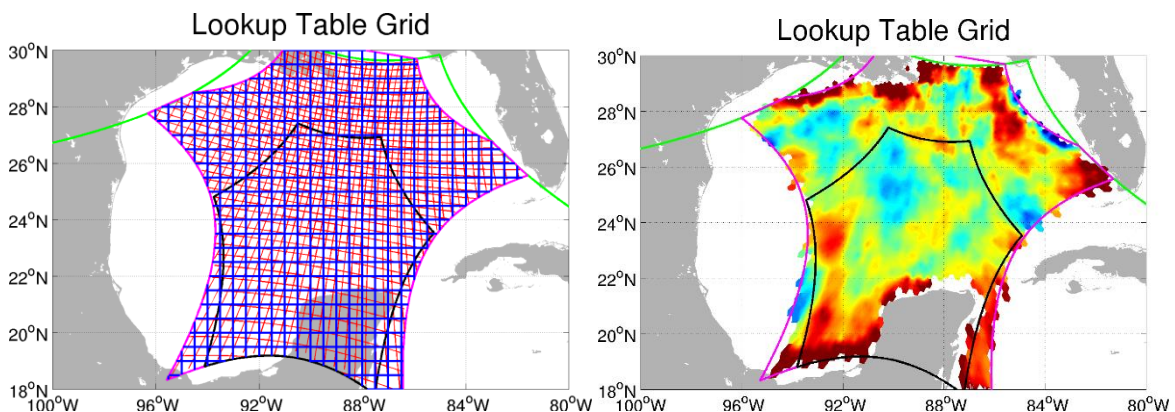


Figure 7 : Left: Example view of the grid used to compute and store the Stokes parameter biases. Blue lines show the discretization in latitude-longitude while the red lines show the discretization over the field of view (isolines in director cosine coordinates): Right: Example of the bias in the first Stokes parameter divided by two.

The LSC bias is assumed to be scene-dependent, and this has proven to be true. An example showing the scene dependence is provided in **Figure 8**, which shows the first Stokes parameter bias for two scenes at slightly different positions west of South America. Although the overall patterns of bias are similar for the two scenes, there are differences in the details and these differences grow as the separation between the scenes increases.

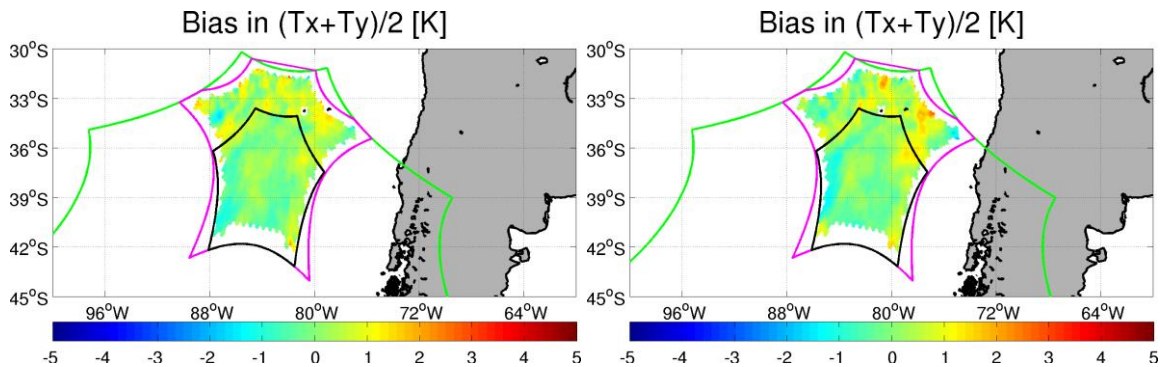


Figure 8 : The LSC bias in the first Stokes parameter divided by two over the EAF-FOV for two different snapshot positions west of South America (K).

Figure 9 shows the number of brightness temperature biases entering the average for a particular position in the FOV (left), as well as the resulting bias in the first Stokes parameter divided by two (right). The bias is zero south of 60°S owing to the presence of ice, which induces a seasonally varying bias that is not correctable using this method.

As a first step in validating the method, monthly salinity bias maps have been created using ISAS SSS maps as a reference. The left panel of **Figure 10** shows an example of the land contamination before correction for descending passes in May 2011. Only the areas around South America and Australia are shown to avoid any impact from RFI on the biases. A clear negative SSS bias is present up to about 1000 km from the coasts (indicated by the magenta curve). The right panel shows the absolute value of the SSS bias as a function of distance to coast with and without the LSC correction. The correction reduces the absolute bias by up to 1 psu about 200 km from the coast and removes the variation of the bias with distance to coast from 200 to 800 km from the coast.

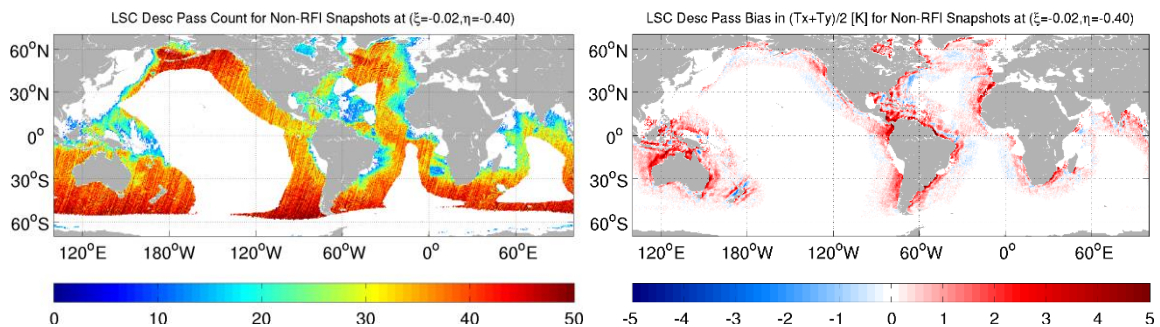


Figure 9 : Left: number of measurements used to derive the bias at a particular position in the FOV; Right: Corresponding bias in the first Stokes parameter divided by two at this position (K). Descending passes from June 2010 through June 2013.

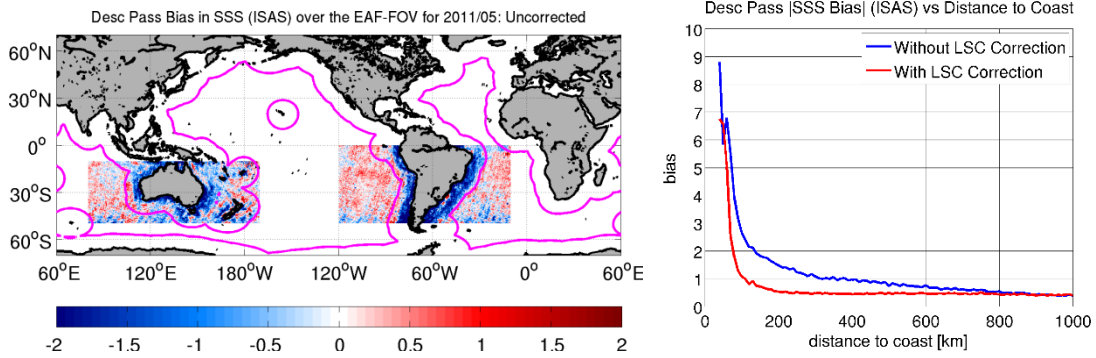


Figure 10 : Left: Bias in retrieved SSS with respect to ISAS for May 2011 plotted only within the domain used to compute the absolute bias; Right: Absolute value of the bias between retrieved and ISAS SSS with and without the LSC correction over the domain shown in the left panel, as a function of distance to the coast.

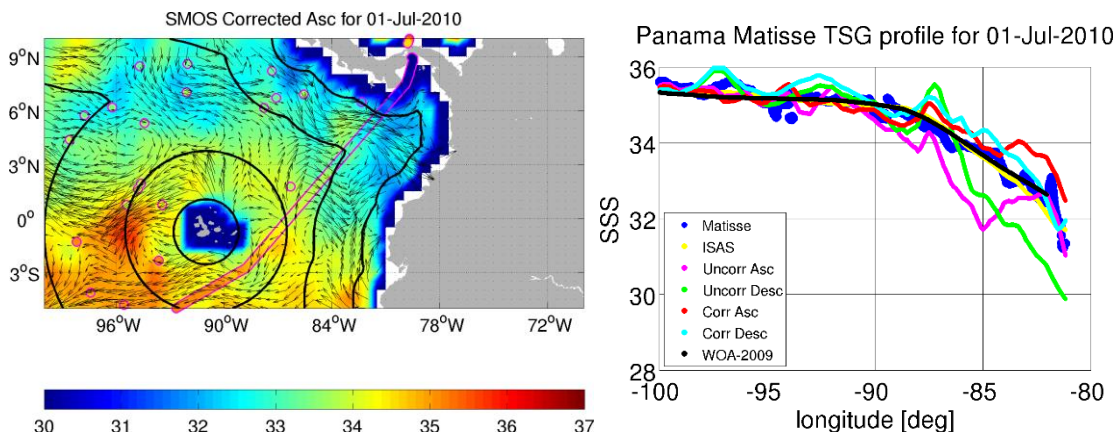


Figure 11 : Example comparison of corrected SMOS SSS with in-situ SSS as measured by a TSG on board the ship Matisse. Left: Ship SSS overlaid on temporally interpolated SSS from SMOS ascending pass 10-day maps; Right: Comparison of Matisse in-situ SSS with WOA-2009 SSS, ISAS SSS, and SMOS ascending and descending pass SSS (corrected and uncorrected).

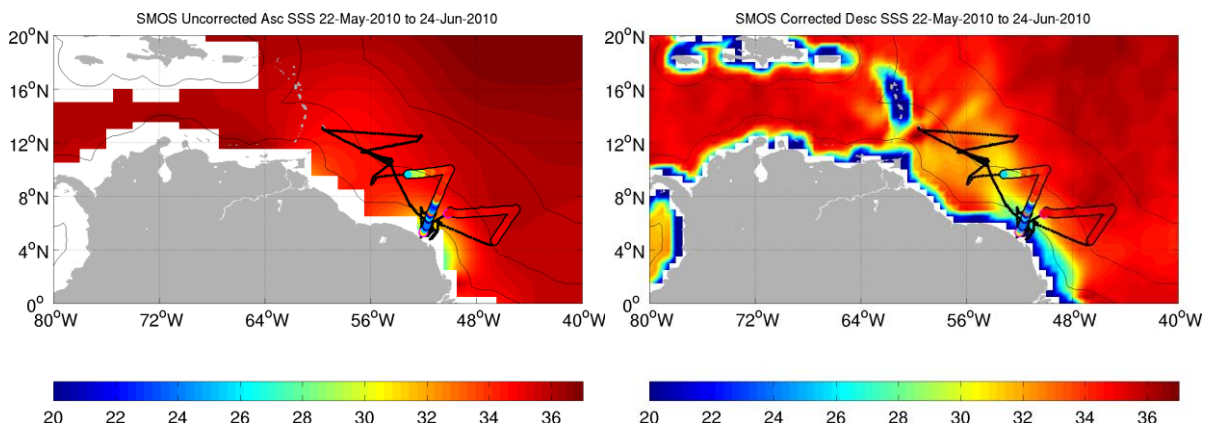


Figure 12 : Left: In-situ SSS measured by the ship Anaconda overlaid on the reference SSS used to develop the LSC correction; Right: SSS derived from LSC corrected descending pass brightness temperatures.

Comparison of the corrected salinity with in-situ data also indicated that the method is promising, even in areas where the surface salinity varies significantly. As an example, [Erreur ! Source du renvoi introuvable.](#) shows a comparison between TSG-derived salinity and SMOS salinity both before and after correction for LSC in the vicinity of Panama. Without correction for the LSC the SMOS SSS differs from the in-situ salinity by up to 2 psu. Application of the LSC correction brings the SMOS salinity in-line with the ship data.

Further evidence that the correction method can work in dynamic regions is provided in **Figure 12** and **Figure 13**, which show a comparison of SMOS and TSG-derived salinity in the vicinity of the Amazon plume. The corrected SMOS salinity (right) is closer to the ship data than the WOA-2009 SSS (left), which is used as the reference SSS to derive the LSC correction. Apparently, use of climatological salinity to derive the correction does not force SMOS salinity to climatology. Nevertheless, the correction does seem to overcorrect the salinity at two points along the ship track, and further investigation is required to find the origin of this overcorrection.

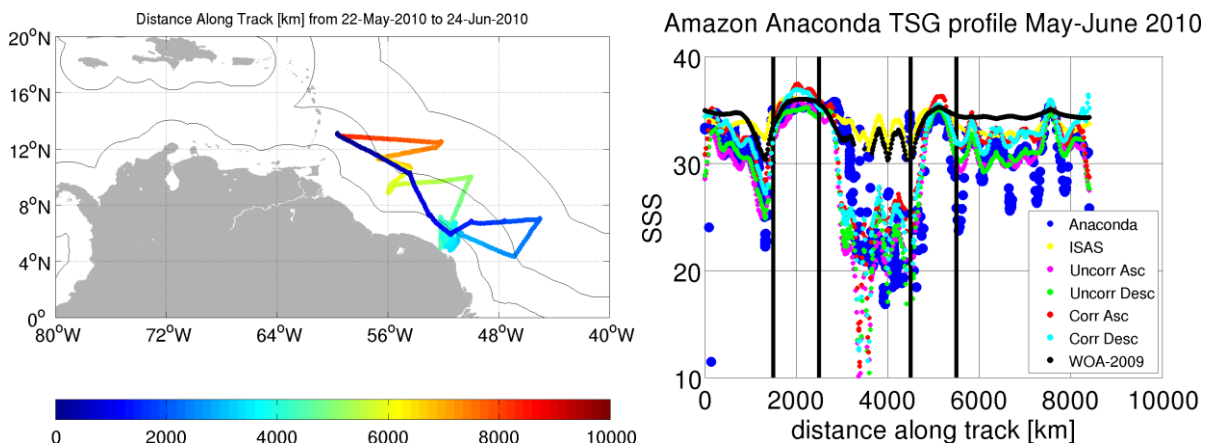


Figure 13 : Left: Anaconda ship track for May-June 2010 coloured by distance along track (km); Right: Along-track profiles of SSS from several sources including SMOS corrected and uncorrected SSS (ascending and descending passes).

6.3 Temporal stability of the correction

It turns out that one effect of the land contamination is spurious temporal variability, especially on time scales less than about 18 days. This spurious variability is mostly associated with temporal variation in the viewing geometry at any given location on earth. An example of this spurious variability is shown in **Figure 14** which shows maps of the temporal standard deviation of the 10-day mean descending pass SSS relative to the 30-day mean around South America for the period Jan 2010 through June 2014. The map obtained without correction for

LSC (left) exhibits an increase of the standard deviation by about 50% within 1000 km of the coast while the map obtained after correction for the LSC does not. **Figure 15** shows the reduction in the standard deviation (left) and the standard deviation of the LSC correction itself, which exceeds 0.5 psu out to over 500 km from the coast.

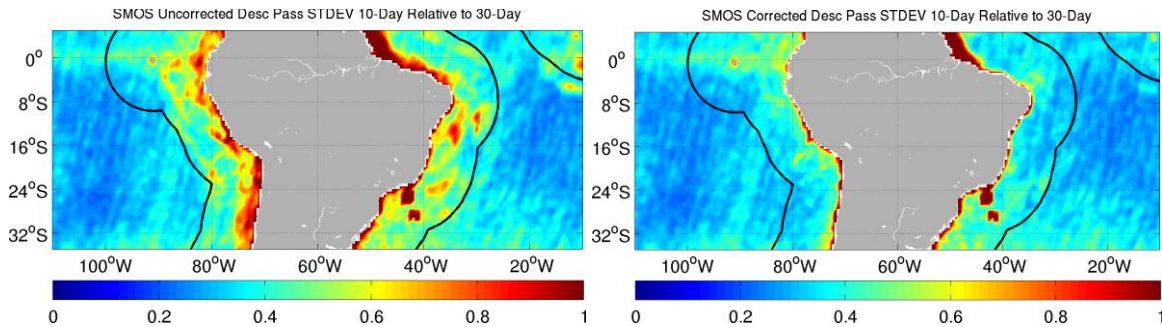


Figure 14 : Temporal standard deviation of 10-day averaged retrieved SSS relative to the corresponding 30-day running mean, computed using descending passes from January 2010 through June 2014.

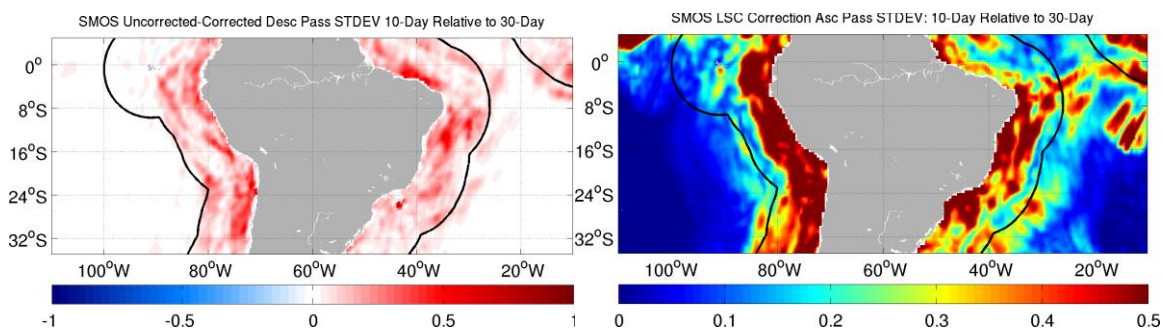


Figure 15 : Left: Reduction in the temporal standard deviation of the 10-day averaged SSS relative to the 30-day averaged SSS from January 2010-June 2014; Right: Temporal standard deviation of the 10-day averaged LSC correction relative to the 30-day correction. Only descending passes are used in the computations.

6.4 Application

The procedure above is used to generate a LUT to be used by the L2 OS algorithm and apply this correction. Further details about the computation and application of the LUT appear in the TGRD document.

In a nutshell, the resulting LUT considers the following variables: latitude, longitude, position in the xi/eta frame, and ascending/descending semi-orbit. A land fraction factor is also included in the LUT to prevent applying the values beyond a defined threshold.

The process includes reading the LUT, and determining, for each TB and according to the associated parameters of the observation, the value of the delta TB found in the LUT and to



be subtracted from the corresponding TBs. Values of the LUT are multilinearly interpolated to the exact values when they are not found matching exactly the discrete values of the LUT.

References

- [1] Anterrieu, E: 2007, On the reduction of the reconstruction bias in synthetic aperture imaging radiometry. IEEE Trans. Geosci. and Remote Sens., 45, 1084–1093.
- [2] Khazaal, A., H. Carfantan, and E. Anterrieu: 2009, On the reduction of the systematic error in imaging radiometry by aperture synthesis: A new approach for the SMOS space mission. IEEE Geosci. and Remote Sens. Letters, 6, 47–51.
- [3] Corbella, I., I. Duran, L. Wu, F. Torres, N. Duffo, A. Khazaal, and Martin-Neira: 2015, Impact of correlator efficiency errors on SMOS landsea contamination. IEEE Geosci. and Remote Sens. Letters.

7 Output Products

Two L2 Salinity Output files will be provided for each SMOS half orbit: a User Data Product (UDP), including information to be distributed to all users, and a Data Analysis Product (DAP), with auxiliary information on data processing for specific users working on algorithms improvement and products validation to allow analysing problems in the SSS retrieval. Both files have a unique Headers section plus a series of Binary fields (one per ISEA grid point, maximum 82257).

Refer to the Input/Output Data Definition document (IODD, R.D. 14) section 3.2 (UDP) and 3.3 (DAP) for complete descriptions of both output products.

In the nominal configuration (shown in figure below), the UDP contains 3 salinity products, all based on the two-scale roughness model (model 1) SSS1 retrievals: SSS_corr is SSS1 retrieved with land-sea corrected L1c TBs; SSS_uncorr is SSS1 retrieved without land-sea corrected TBs; and SSS_anom is a salinity anomaly product computed from SSS_uncorr minus SMOS SSS climatology. The DAP contains 3 salinity products (SSS1/2/3) retrieved using each of the three roughness models with land-sea corrected L1c TBs.

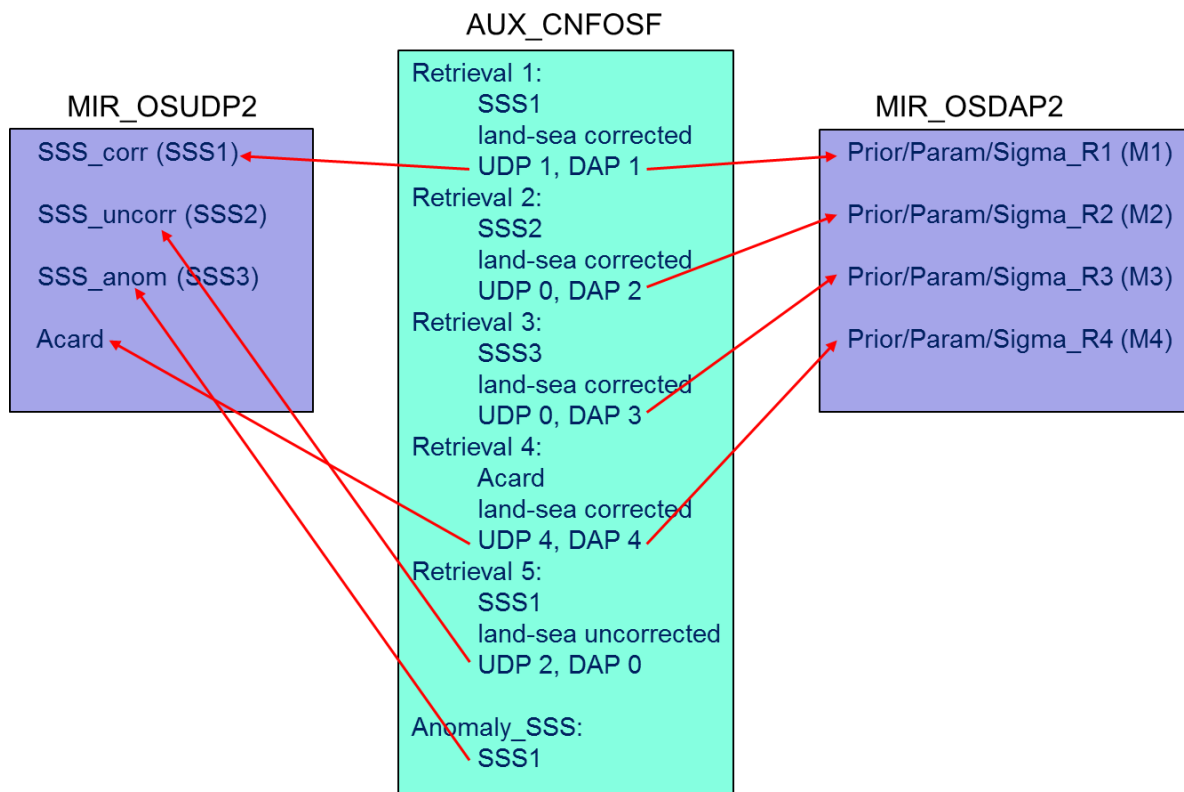


Figure 1: Nominal UDP/DAP salinity product mapping



Additionally, to this, information on intermediate processing steps, as the modelling of the different components of Tb, will be accessible through the Breakpoints Reports that will allow recomputing these intermediate values with the prototype processor and complementary software tools.



ANNEX A *Surface roughness 2: Empirically modified SSA/SPM*

Variables:

<u>Surface roughness 2: Empirically modified SSA/SPM</u>				
	surface wavenumber vector	rad m ⁻¹		
W(k,φ)	sea surface directional waveheight wavenumber spectrum	m ⁴		
g _γ	electromagnetic weighting functions	m ⁻²		
φ	Azimuthal direction relative to wind direction	deg		
Δe _γ	wind-excess emissivity Stokes vector	dl		
Δe _γ ⁽ⁿ⁾	nth azimuthal harmonics of the wind-excess emissivity stokes vector	dl		
γ	represent h, v, U or V depending on the case	dl		
Δe _B	residual Stokes vector of roughness impact	dl		
ε _{sw}	relative permittivity of sea water	dl		
Tg_WS_roughness_M2	min. WS to apply roughness correction	m s ⁻¹		
Fg_ctrl_roughness_M2	roughness correction applied	Y/N		
Tg_WS_foam_M2	minimum WS to apply foam correction	m s ⁻¹		
Fg_ctrl_foam_M2	foam correction applied	Y/N		
Fg_OoR_Rough_dim1	Prior or retrieved WS went outside of LUT range	Y/N		
Fg_OoR_Rough_dim2	Prior or retrieved Omega went outside of LUT range	Y/N		
Fg_OoR_Rough_dim3	Prior or retrieved Theta went outside of LUT range	Y/N		
Fg_OoR_Rough_dim4	Prior or retrieved SSS went outside of LUT range	Y/N		
Fg_OoR_Rough_dim5	Prior or retrieved SST went outside of LUT range	Y/N		

Theoretical description

Physics of the problem

Polarimetric passive remote sensing involves measurement of all four modified Stokes parameters of the microwave thermal emission:

$$\begin{bmatrix} T_h \\ T_v \\ T_3 \\ T_4 \end{bmatrix} = T_s \begin{bmatrix} 1 - r_h \\ 1 - r_v \\ -r_3 \\ -r_4 \end{bmatrix} \quad \text{6.4.1}$$

where T_h and T_v are the brightness temperatures measured by horizontally and vertically polarized antennas respectively, and T_3 and T_4 are proportional to the real and imaginary parts of the correlation between fields in horizontal and vertical polarizations respectively [1]. The second equality follows from Kirchhoff's Law, which relates the emissivity of a medium at constant temperature to the corresponding reflectivity (r_h , r_v , r_3 and r_4) multiplied with the surface physical temperature T_s . Reflectivities are calculated as an integral of bistatic scattering coefficients over the upper hemisphere in the reciprocal active scattering problem [2].

Special interest in sea surface salinity remote sensing is given to brightness temperature variations with surface salinity and temperature when the sea surface is assumed smooth. In that case, it is straightforward to calculate reflectivities in Equation (1) at a given incidence angle using Fresnel reflection laws provided an accurate dielectric constant model is available at L-band. However, in the various discussions of the Sea Surface Salinity (SSS) retrieval schemes applied to spaceborne L-band radiometer data ([3]-[5]), it is clear that the major uncertainty in the required modelling is the effect of the wind and wave-generated roughness on the emissivity of the ocean's surface at L-band. The purpose of this section is to document one of the three forward models, namely the "SPM/small slope approximation (SPM/SSA)" that will provide roughness impact corrections in the version of the SSS retrieval algorithm used at launch of the ESA's Soil Moisture and Ocean Salinity (SMOS) satellite mission.

Analytical and numerical models for the calculation of the rough ocean surface polarimetric thermal emission have been developed [6]–[11], primarily through application of standard surface scattering approximate methods to calculate surface emissivity using Kirchhoff's law. Models based on both the small perturbation method (SPM) and the physical optics (PO) approximation have been presented. The physical optics (PO) approximation was shown to clearly underestimate the sea surface emissivity observations at L-band [12, 13], particularly in the low incidence angle range (less than about 20-30°). This is mainly because such model

ARGANS Ltd.

does not account for scattering on small roughness elements. Recent works [8-10] has further revealed that use of the SPM for emission calculations results in a small slope, rather than small height, emission approximation identical to that which would be obtained from the small slope approximation of [14], so that the SPM can provide accurate emission predictions even for surfaces with large heights in terms of the electromagnetic wavelength. Numerical tests of the SPM for a set of canonical periodic surfaces have confirmed this statement [15]. Moreover, the success of the SPM/SSA in matching measured brightness temperature [6,16-19] has shown that the technique should be applicable for rough ocean surface brightness temperature predictions. These results motivate use of the SPM/small slope approximation (SPM/SSA) for the prediction of ocean polarimetric thermal emission at L-band.

The Stokes vector of sea surface brightness temperatures observed at radiometer frequency f , incidence angle θ and azimuth angle relative to wind direction ϕ_i can be written:

$$\begin{bmatrix} T_h(f, \theta_i, \phi_i) \\ T_v(f, \theta_i, \phi_i) \\ T_3(f, \theta_i, \phi_i) \\ T_4(f, \theta_i, \phi_i) \end{bmatrix} = T_s \begin{bmatrix} 1 - |R_{hh}^{(o)}(f, \theta_i)|^2 \\ 1 - |R_{vv}^{(o)}(f, \theta_i)|^2 \\ 0 \\ 0 \end{bmatrix} - \begin{bmatrix} \Delta e_h(f, \theta_i, \phi_i) \\ \Delta e_v(f, \theta_i, \phi_i) \\ \Delta e_3(f, \theta_i, \phi_i) \\ \Delta e_4(f, \theta_i, \phi_i) \end{bmatrix} \quad 6.4.2$$

where T_s is the sea surface temperature. $R_\gamma^{(o)}(f, \theta_i)$ are the Fresnel reflection coefficients at polarization γ , and the $\Delta e_\gamma(f, \theta_i, \phi_i)$ are the first prediction of emissivity changes due to the rough sea surface. The physics of the forward problem here is to estimate accurately the wind-excess emissivity Stokes vector $\Delta e_\gamma(f, \theta_i, \phi_i)$ at $f=1.4$ GHz for the range of (θ_i, ϕ_i) values encountered in L1C SMOS data and for a range of wind and sea state conditions representative of the global ocean.

The SPM/SSA applies standard small perturbation theory to predict the bistatic scattering coefficients of a rough surface and integrates these scattering coefficients over the upper hemisphere to obtain the reflectivity and hence brightness temperatures. The resonance behaviours observed in the critical phenomena region [20] produce a significant sensitivity of emission harmonics predicted by the SSA to ocean length scales of order equal to the electromagnetic wavelength. However, these emission harmonics are also sensitive (except for the fourth Stokes parameter) to anisotropy in ocean length scale much larger than the electromagnetic wavelength. Use of the SPM/SSA up to 2nd order produces an expansion in surface slope, with zero order terms reproducing the flat surface emission results, first order terms identically zero, and second order terms providing the first prediction of changes from flat surface brightness.

The second order terms take the form of an integral of a set of weighting functions over the surface directional spectrum, so that the wind-excess emissivity Stokes vector $\Delta e_\gamma(f, \theta_i, \phi_i)$ can be expressed as follows using the second order SPM/Small Slope Approximation theory (e.g., see [19]):

$$\begin{bmatrix} \Delta e_h \\ \Delta e_v \\ \Delta e_3 \\ \Delta e_4 \end{bmatrix} = \int_0^\infty \int_0^{2\pi} k W(k, \phi) \begin{bmatrix} g_h(f, \theta_i, \phi_i; \varepsilon_{sw}; k, \phi) \\ g_v(f, \theta_i, \phi_i; \varepsilon_{sw}; k, \phi) \\ g_3(f, \theta_i, \phi_i; \varepsilon_{sw}; k, \phi) \\ g_4(f, \theta_i, \phi_i; \varepsilon_{sw}; k, \phi) \end{bmatrix} dk d\phi \quad 6.4.3$$

where $\vec{k} = (k, \varphi)$ is a surface wavenumber vector, $W(k, \varphi)$ is the sea surface directional wave height wavenumber spectrum, ε_{sw} is the sea water dielectric constant and the g_γ kernels are electromagnetic “weighting” functions given explicitly in [19].

Note, that when deriving an asymptotic solution for EM scattering on the rough ocean surface, a key issue is to determine a tractable statistical description which specifies the sea surface geometry on a very wide range of scales (0.005-200 m). In most practical and/or theoretical studies, Gaussian statistics are assumed. Under such assumptions, the solution will then only depend upon the definition and the shape of the correlation function. Under Gaussian statistics assumption, which is used as well in the present SPM/Small Slope Approximation theory, the result can be expressed strictly in terms of a roughness spectrum. In the present algorithm, we used the Kudryatsev *et al* model [21] to estimate the sea surface roughness spectrum $W(k, \phi)$ in Equation (3), which was recently developed based on available field and wave-tank measurements, along with physical arguments concerning the dynamics of short-gravity waves. These scales indeed represent particularly important surface components for emissivity at 1.4 GHz, since they belong to the so-called “critical phenomena” region [20] within which surface components are dominant scatterers at L-band. It is important to note that this spectral model was developed without any relation to remote-sensing data. Moreover, by using the Kudryatsev *et al* spectral model, we avoided some deficiencies of the Elfouhaily *et al* spectral model as found by other (problems at the low to moderate wind speed transition).

In [19], it was shown that using a Fourier expansion in Eq (3), the wind-excess emissivity components can be separated out in individual emission azimuthal terms as follows:

$$\begin{bmatrix} \Delta e_h \\ \Delta e_v \\ \Delta e_3 \\ \Delta e_4 \end{bmatrix} = \begin{bmatrix} \Delta e_h^{(0)} + \Delta e_h^{(2)} \cos(2\varphi_i) \\ \Delta e_v^{(0)} + \Delta e_v^{(2)} \cos(2\varphi_i) \\ -\Delta e_3^{(2)} \sin(2\varphi_i) \\ -\Delta e_4^{(2)} \sin(2\varphi_i) \end{bmatrix} \quad 6.4.4$$

where the $\Delta e_\gamma^{(n)}$ terms represent the n th azimuthal harmonics of the wind-excess emissivity.

Note that due to the assumption of gaussian behaviour in the sea surface statistics, the solution can be expressed strictly in terms of a roughness spectrum. Properties of a directional spectrum result in no first azimuthal harmonic variations being obtained; introduction of non-gaussian behaviour is required to obtain first azimuthal harmonics. As second azimuthal harmonics were measured to be already very small at L-band [22, 23], only the second order SSA/SPM expansion is considered here, and no first azimuthal harmonic variations are neglected.

Mathematical description of theoretical SSA/SPM algorithm

The n th azimuthal harmonics of the wind-excess emissivity $\Delta e_\gamma^{(n)}$ terms in Eq (4) can be determined numerically by calculating integrals of the products of the n th azimuthal harmonics of the surface curvature spectrum $k^4 W(k, \phi)$ by the n th azimuthal harmonics of the electromagnetic weighting function g_γ .

Typically, the Kudryavtsev curvature spectrum model $k^4 W(k, \varphi)$ is determined as function of the following geophysical parameters:

- The wind friction velocity U^* [m/s],
- The inverse wave age parameter $\Omega = \frac{WS}{C_p}$ [dimensionless] for the wind sea, where WS is the wind speed module at 10-meter height [m/s] and C_p is the phase speed at the peak of the wind-sea spectrum [m/s]. Note that $\Omega = \frac{WS}{C_p} = \frac{2\pi WS}{gT_p}$ where g is the acceleration of gravity [m/s²], and T_p is the peak period of wind-sea [s].

The electromagnetic weighting functions g_γ can be determined as function of

- the incidence angle θ at SMOS pixel, and,
- ϵ_{sw} , the complex sea water dielectric constant, which is itself function of Sea Surface Temperature T_s and Sea Surface Salinity SSS .

Therefore, the mathematical description of the SSA roughness brightness temperature corrections includes 4 major parts:

ARGANS Ltd.

(1) A five-dimension Look-Up Table (LUT) of the $\Delta e_{\gamma}^{(n)}$ coefficients.

Two options for the look-up table are possible as follows:

Option 1: LUT1 as function of

- the neutral equivalent wind speed WS_n [m/s],
- the inverse wave age parameter Ω
- the incidence angle θ at SMOS pixel,
- the real part of ϵ_{sw} , and,
- the imaginary part of ϵ_{sw} .

Here the neutral equivalent wind speed is related to the friction velocity U^* by

$$WS_n = \frac{U^*}{\kappa} \left[\ln \left(\frac{10}{z_0} \right) \right],$$

6.4.5

where κ is the von Karman constant and z_0 is the roughness length.

Option 2: LUT2 as function of

- the neutral equivalent wind speed WS_n [m/s],
- the inverse wave age parameter Ω
- the incidence angle θ at SMOS pixel,
- the sea surface temperature T_s [K] and,
- the prior sea surface salinity SSS [psu].

Since ϵ_{sw} will be already calculated by the flat-sea surface module of the processor, it may seem advantageous to use the LUT dimensioned by the dielectric constant. However, the relationship of the dielectric constant to SSS and SST is such that for typical distributions of SSS and SST a large portion of the LUT will be unused and therefore it is not practical to use this approach. Therefore, for the processor we choose option 2 and discretize by SSS and SST, and use the same dielectric constant model as is used in the processor.

Parameter or variable ranges

- For the neutral equivalent wind speed WS_n : $0 \rightarrow 40$ [m/s],
- For the inverse wave age parameter for wind sea Ω : $0.5 \rightarrow 2.5$,
- For the incidence angle θ at SMOS pixel [degrees]: $0 \rightarrow 75^\circ$
- For the sea surface temperature T_s : $269.15 \rightarrow 309.15$ K
- For the prior sea surface salinity SSS: $0 \rightarrow 40$ psu
- For the azimuth angle relative to wind direction φ_i [in rad]: $0 \rightarrow 2\pi$
- For the real part of the dielectric constant ϵ'_{sw} [no unit]: $65 \rightarrow 90$
- For the imaginary part of the dielectric constant ϵ''_{sw} [no unit] $0 \rightarrow 100$

(2) A multi-dimensional interpolation step.

Given the four values of the "geophysical" auxiliary parameters estimated at a given SMOS pixel, namely WS_{ni} , Ω_i , $\text{Real}(\varepsilon_{sw})$, $\text{Imag}(\varepsilon_{sw})$ where Real and Imag denote real and imaginary parts (respectively, u^*_{i} , Ω_i , T_{si} and SSS_i), plus the series of incidence angles ($\theta_{i=1,\dots,N}$) associated to the L1C product considered, a linear interpolation is performed from LUT2 to evaluate the values of $\Delta e_{\gamma, i=1,\dots,N}^{(n)}$, the underlying multidimensional functions $\Delta e_{\gamma}^{(n)}$ at the pixel considered.

(3) Total roughness-induced emissivity correction.

From the value of azimuth angle relative to wind direction φ_i estimated at the pixel [in rad], the total wind-excess emissivity Stokes vector is calculated using Equation (4).

(4) Total roughness-induced brightness temperature correction.

From the estimated values of the total wind-excess emissivity Stokes vectors for each L1C incidence angle, the corresponding brightness temperature changes are derived by multiplying the results by the sea surface temperature at the pixel T_{si} [K].

Error budget estimates

In Figure 1, we show the comparison between currently available experimental data collected at L-band over water surfaces [4; 13; 22; 25-29] and the SSA/SPM model predictions of the wind speed sensitivity of surface emissivity at H and V polarization. The figures reveal that the model emissivity dependencies with wind speed agree with the data to roughly about $\pm 5 \times 10^{-4}$, in both vertical and horizontal polarizations. This translates into an error in brightness temperature of about 1 K at SST=15°C and WS=7 m/s. Note that this is a very maximized error estimate. In general, the model is found to correctly reproduce the averaged trends observed at both polarizations also it often slightly underestimates the data, particularly in V-polarization and around nadir. Discrepancies might be due to either foam, currents, slicks, and swell impacts not accounted for in the model or to radiometric uncertainties in the experimental data (see error bars given for some of the data). It is however expected that using auxiliary wind friction velocity data, a measure of wind stress that implicitly carries a response to near-surface phenomena, instead of wind speed at 10-meter height, shall improve the error budget estimate.

There is no evidence of clear azimuthal/wind direction related signatures in the few available measured brightness temperature signals at L-band [22, 23] so that it is now very difficult to estimate errors due to the wind stress directionality.

Therefore, we estimate an overall error budget on the roughness correction factor $\Delta e(\theta_i)$, as predicted by the SSA/SPM model (without accounting for wind direction impacts), of about:

ARGANS Ltd.

Commercial in Confidence

Page 269

Use, duplication, or disclosure of this document or any information contained herein is subject to the restriction on the title page of this document.

$$\begin{pmatrix} \Delta e_h(\theta_i) \\ \Delta e_v(\theta_i) \end{pmatrix} = \pm 5 \times 10^{-4} \cdot U_{10}$$

6.4.6

An additional error will be introduced by the multi-dimensional interpolation scheme from the LUT table. The error is not provided yet in the draft ATBD but will be given later.

Note that no error budget can be estimated for the third and fourth Stokes parameters as no data as function of wind speed are currently available for validation.

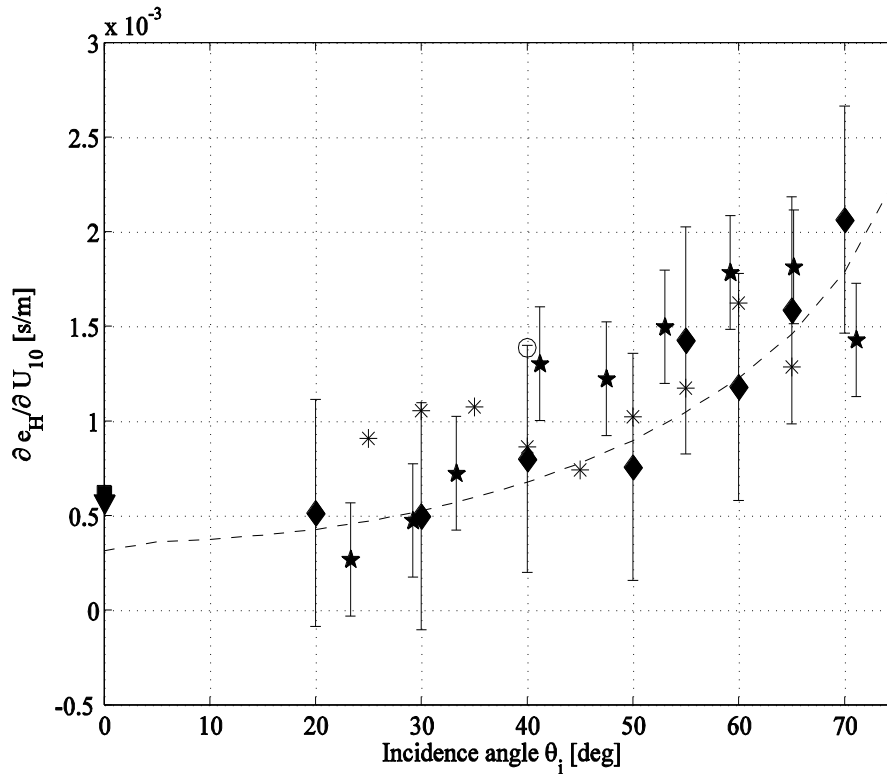


Figure 1a: for legend see next figure.

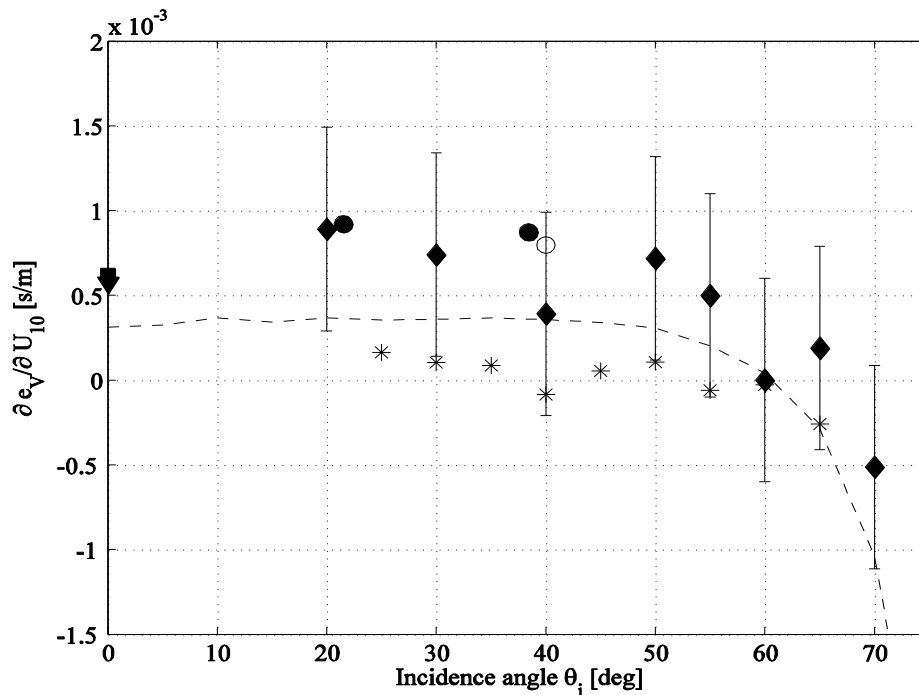


Figure 1b: Comparison between measured and calculated sensitivities of the sea surface emissivity at L-band to wind speed at 10-meter height as function of incidence angle. Figure 1a: horizontal polarisation; Figure 1b: vertical polarisation. (★): Cape Code Canal data [13]; (■): Data from Skylab S-194 [25]; (*): WISE 2000-2001 [22], [26]; (◆) : Argus Island Tower data [27]; (▼): Bering Sea Experiment [28]; (○): JPL experiment [4]; (●)EuroSTARRS [29]; (--) : predictions from the SSA/SPM model at SST=15°C and SSS=35 psu. Error bars show uncertainties in the data of [13] and [27].

Practical considerations and introduction of empirical method

Calibration and validation

Calibration and validation of the forward SSA/SPM emissivity model for roughness correction will be done during the commissioning phase and later-on by performing residual analysis of the future SMOS measurements and using a formalism proposed for and applied to NASA scatterometer (NSCAT), Special Sensor Microwave Imager (SSM/I) and ESA/ERS scatterometer measurements [see 30].

Using in situ SSS, SST and wind (TAO, Argo drifters, satellite SST and winds and ECMWF model winds) and SMOS co-localized data, the first step will be to remove the flat sea surface contribution from the SMOS surface brightness temperature data (i.e., corrected for atmospheric, ionospheric, galactic and sun glint contribution) in order to estimate the residual Stokes vector of roughness impact $\Delta e_B(\theta_i)$. The in situ and satellite SSS, SST and wind data will be the chosen reference. In addition, ECMWF analysis winds will be used as a third data source to completely determine the errors via a multiple collocation analysis. The main

ARGANS Ltd.

Commercial in Confidence

Page 271

Use, duplication, or disclosure of this document or any information contained herein is subject to the restriction on the title page of this document.



objective will be to present observed correlations between regional and seasonal model roughness correction factors $\Delta e_B(\theta_i)$ errors and nonwind oceanic and atmospheric factors such as the surface current and sea state. Following the methodology applied in [30], we shall explicitly consider the errors in the reference datasets as well as in the roughness correction factors retrieved estimates. The gain shall come in more accurate assessment of bias and variance and less possible systematic contamination that can obscure geophysical driven impacts not accounted for by the SSA/SPM model.

Empirical adjustments of the algorithm

On the basis of SMOS brightness temperatures obtained from March-October 2010, we have undertaken an initial evaluation of the SSA/SPM model described above, and on the basis of this evaluation we have introduced a new version of the roughness emission lookup table. In doing so we have maintained the same lookup table structure except for replacing the friction velocity with the neutral equivalent wind speed at 10 m above the surface.

To perform the evaluation of the theoretical model, we collected a set of several hundred Pacific Ocean passes from March through October 2010, and we identified all snapshots for which boresight latitude lies between 55 degS and 30 degN. We then extracted all SMOS brightness temperatures within the extended alias-free field of view for which the x-component of the director cosine coordinates is smaller than 0.1 in magnitude and for which the y-component is equal to or larger than the value at nadir. This provides a manageable subset of data for which the polarization basis rotation required to transport the instrument basis brightness temperatures into surface basis components is generally small. More importantly, this subset of data can be transported to the surface basis in dual-pol mode away from nadir.

We used GPS-derived total electron content to compute the Faraday rotation and transported all brightness temperatures into the surface polarization basis. As the period considered included dual-pol and full-pol mode data, we chose to perform the rotation on (Tx,Ty) only, assuming that the third Stokes parameter in the surface basis is identically zero.

Before performing the rotation to the surface basis, we subtracted from the full brightness temperatures (Tx,Ty) our best estimate of all contributions to brightness except for surface roughness emission. These contributions included rough surface scattered celestial sky noise evaluated using the model described in this document and evaluated at a wind speed of 3 m/s.

Assuming that the residual brightness temperatures are associated with surface roughness emission, we then binned the data by incidence angle and by surface wind speed. We used bin sizes of 5 deg for incidence angle and 1 m/s for wind speed. For neutral equivalent wind

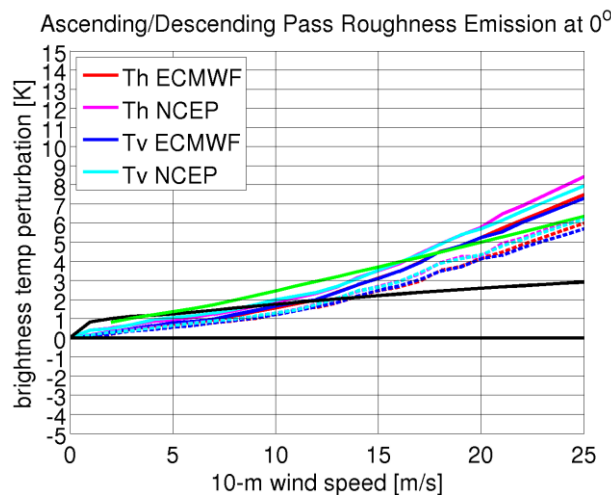
ARGANS Ltd.

speed we used both ECMWF and NCEP winds in order to obtain a measure of possible uncertainty in the results. One might suppose that using buoy winds would yield better results, however in this case the aim is to obtain a roughness correction for SMOS as a function of the surface winds used in the processor.

The following figure shows the median residual brightness temperatures as a function of ECMWF and NCEP 10-m neutral equivalent wind speed for the smallest incidence angle bin. The solid curves show results for ascending passes while the dash curves show results for descending passes.

For comparison we have also plotted the isotropic components of the 2-scale model (green curves; Th=solid, Tv=dashed) and of the SSA/SPM model described here (black curves; Th=solid, Tv=dashed). The median residual curves are slightly concave up with an overall impact of about 8 K at 25 m/s, so the overall sensitivity to wind speed of Th and Tv, based on the Pacific SMOS data, is about 0.3 K/(m/s) near nadir.

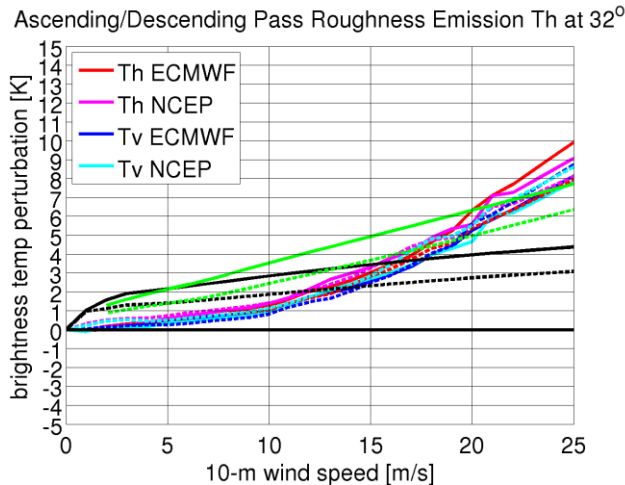
There is a slight difference between the NCEP and ECMWF results that amount to about 1 K at 25 m/s. Note that we have adjusted all curves to zero roughness emission at zero wind speed. More important differences exist between ascending and descending passes, with differences reaching 2 K at 25 m/s. This cannot be related to Faraday rotation because at this incidence angle Th and Tv are nearly equal for both ascending and descending passes (and they are exactly equal in the isotropic components of the theoretical model results).



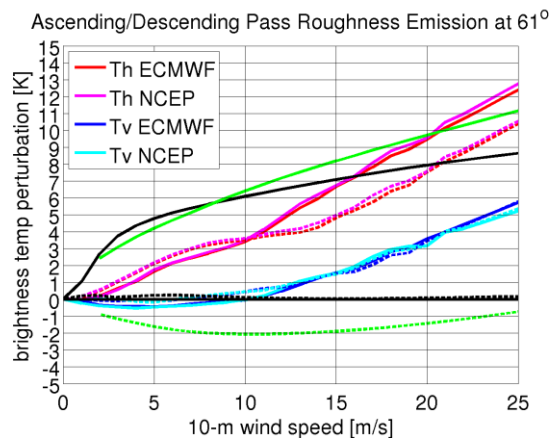
The results at 32 deg incidence angles, shown below, exhibit stronger sensitivity to wind speed (up to 10 K for Th at 25 m/s) than at nadir for Th and unchanged sensitivity for Tv. The increased sensitivity to wind speed for Th with increasing incidence angle and the unchanged sensitivity in Tv is expected based upon the theoretical results shown earlier. However, we

still see strong differences between ascending and descending passes (up to 2 K in Th at 25 m/s wind speed).

Both theoretical models clearly overestimate the roughness emission for Th and Tv below 10 m/s and underestimate roughness emission beyond 20 m/s.



At a higher incidence angle, 61 deg, SMOS residuals show weak sensitivity of Tv to wind speed up to about 10 m/s followed by a linear increase from 0 to 6 K from 10 to 25 m/s. By contrast, Th increases nearly linearly from 0 to 13 K from 0 to 25 m/s, so the sensitivity of Th to wind speed reaches 0.5 K / (m/s). Both theoretical models greatly overestimate roughness emission in Th below 15 m/s and the 2-scale model underestimates roughness impact in Tv at all wind speeds.

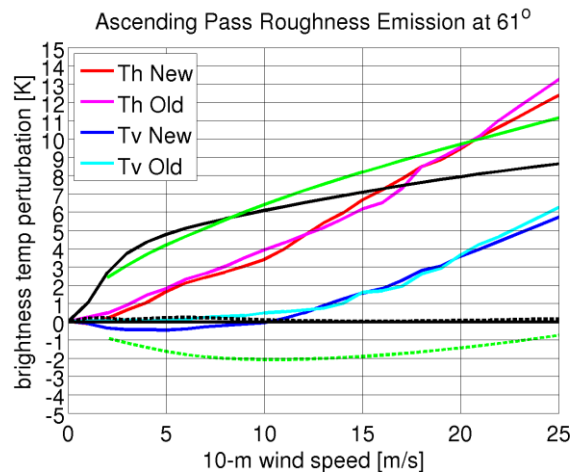


In order to examine the stability of the roughness residuals over time we have evaluated the residuals on two independence set of SMOS data: 'old' passes from March through May 2010 and 'new' passes from August through October 2010. The residuals at 61 deg incidence angles

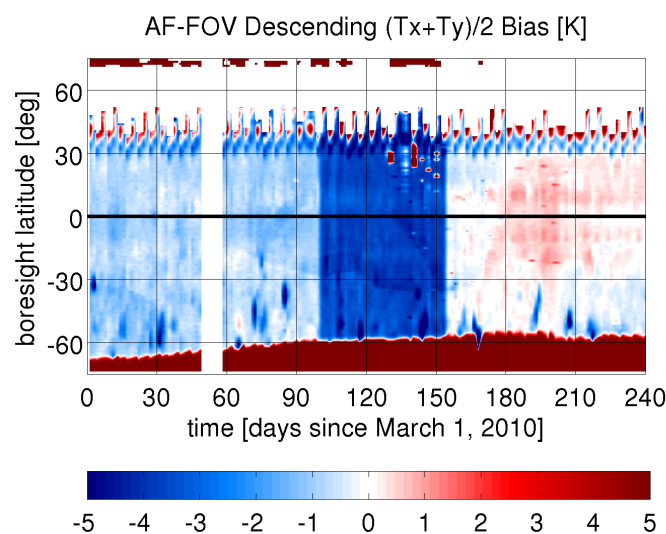
ARGANS Ltd.

Commercial in Confidence

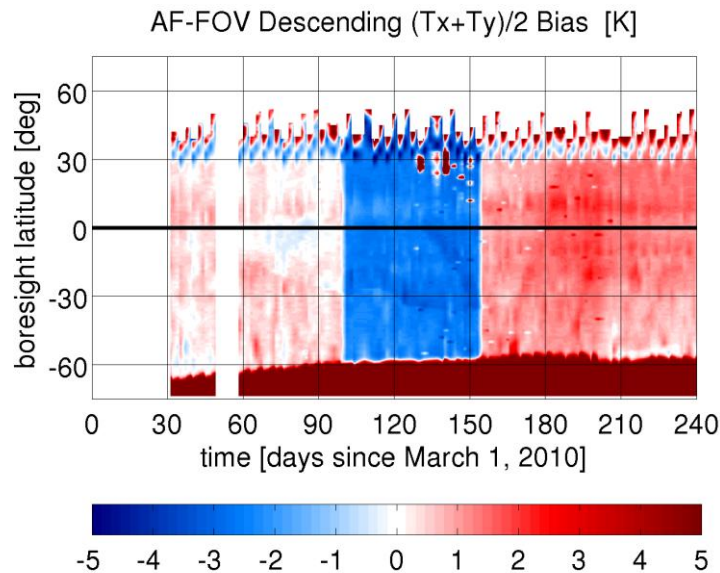
are shown below and reveal less than 1 K difference between the two sets of data at 25 m/s wind speed. This, along with the comparison between NCEP and ECMWF winds, provides an indication of the uncertainty of the roughness residuals.



To assess the impact of using the empirically determined roughness residuals instead of the theoretical residuals, we collected a set of several hundred Pacific Ocean passes and evaluated the bias between the SMOS brightness temperatures and the complete theoretical and empirical models averaged over the alias-free field of view. We collected these biases in terms of $(T_x + T_y)/2$ and plotted them as a function of time and boresight latitude, and the results for descending passes from March 1 to November 1 2010 are shown below for the theoretical SSA/SPM model. Aside from the large negative bias in June and July, we can see areas of large negative biases associated with storms in the southern hemisphere. These biases correspond to roughness emission overestimation by the sum of the SSA/SPM and foam models.



When we replace the SSA/SPM+foam model solutions with the empirical model described above, we obtain the following plot of bias in $(T_x+T_y)/2$ as a function of time and latitude. Aside from an overall change in the bias level, the large biases associated with the high-latitude storms are less evident, which reflects a more accurate modelling of high wind rough surface excess emission.



Although the empirical model does generally produce more accurate estimates of rough surface emission, the effectiveness of this approach is limited in situations in which the link between the sea surface roughness and model wind speed is affected by the strong temporal and spatial variations of wind speed, such as in the vicinity of midlatitude cyclones and hurricanes. In these situations, two problems arise. First of all, in these situations the surface wind fields produced by the numerical weather prediction models such as ECMWF can suffer from significant errors in both the positions of the storm centres (and associated fronts) as well as the distribution of winds around the storms. Secondly, sea state can vary strongly for any given surface wind speed where the wind changes strongly in space and time, so that the emission prediction can be incorrect even if there is no error in the wind speed.

Finally, it should be noted, as discussed in the section describing the theoretical model, that there may be a dependence of the roughness emission on relative angle between emission direction and wind direction, but we have not been able to see a consistent azimuthal signal in the SMOS data as of this writing, and so we current set all azimuthal harmonic coefficients to zero identically.

Quality control and diagnostics

As explained in section 4.3.3 below, the SSA/SPM model is not expected to provide correct results for wind seas generated by winds less than about 2 m/s and larger than 15 m/s. This corresponds roughly to wind friction velocity u^* less than 0.6 cm/s and larger than 0.5 m/s. The model can be applied as it is at launch for conditions out of this range however, we expect that the CAL/VAL activities will provide after commissioning phase a variability estimate at low winds and a residual foam impact at high winds which will be used to correctly tune the model.

Exception handling

There is no particular exception handling in the mathematical algorithm except if the following auxiliary data are not provided by the processor or exceed the ranges anticipated:

- the neutral equivalent wind speed [m/s], (which can be estimated from the wind speed magnitude at 10-meter height, the roughness length, and the auxiliary parameter “Coefficient of drag with waves C_d ” defined by:

$$u^* = \sqrt{C_d} \times |U_{10}|$$

- the inverse wave age parameter Ω for the wind sea (which can be deduced from estimates of both U_{10} and the mean period of wind waves T_p :

$$\Omega = \frac{2\pi U_{10}}{g T_p},$$

- the incidence angles θ at SMOS pixel,
- the sea surface temperature T_s ,
- the prior sea surface salinity SSS, and,
- the azimuth angle at SMOS pixel relative to wind direction ϕ_i .

If one of the prior values of the retrieved geophysical parameters is out of the LUT range, or if any retrieved geophysical parameter goes out of LUT range during the retrieval, different flags:

Fg_OoR_Rough_dim1
Fg_OoR_Rough_dim2
Fg_OoR_Rough_dim3
Fg_OoR_Rough_dim4
Fg_OoR_Rough_dim5

are raised. No extrapolation is done, and the boundary value is taken.

Assumption and limitations

As discussed above, the empirical model described above is expected to fail in strong storm and frontal conditions (strong wave-wave, wave-current or wind-wave interaction conditions). Furthermore, we do not expect the model to perform well in presence of either strong swells, strong currents, very small and unsteady winds where the link between surface roughness and wind speed is not direct. We expect however that accounting for the impact of waves on the drag coefficients will better characterize impact of these parameters on roughness.

References

- [1] S. H. Yueh, R. Kwok, F. K. Li, S. V. Nghiem, and W. J. Wilson, "Polarimetric passive remote sensing of ocean wind vectors," *Radio Sci.*, vol. 29, pp. 799–814, 1994.
- [2] L. Tsang, J. A. Kong, and R. T. Shin, *Theory of Microwave Remote Sensing*. New York: Wiley, 1985.
- [3] G. S. E. Lagerloef, C. T. Swift, and David M. Le Vine, Sea surface salinity : The next remote sensing challenge, *Oceanography*, vol. 8, no. 2, pp. 44-49, 1995.
- [4] S. H. Yueh, R. West, W. J. Wilson, Fuk K. Li, E. G. Njoku, and Y. Rahmat-Samii, Error sources and feasibility for microwave remote sensing of ocean surface salinity, *IEEE Trans. Geosci. and Remote Sens.*, vol. 39, no. 5, pp. 1049-1060, 2001.
- [5] E. P. Dinnat, J. Boutin, G. Caudal, J. Etcheto, and A. Camps, Issues concerning the sea emissivity modeling in L-band for retrieving surface salinity, *Radio Sci.*, vol. 38, no. 4, 2003.
- [6] S. H. Yueh, "Modeling of wind direction signals in polarimetric sea surface brightness temperatures," *IEEE Trans. Geosci. Remote Sensing*, vol. 35, pp. 1400–1418, 1997.
- [7] D. B. Kunkee and A. J. Gasiewski, "Simulation of passive microwave wind direction signatures over the ocean using an asymmetric-wave geometrical optics model," *Radio Sci.*, vol. 32, p. 59, 1997.
- [8] V. G. Irisov, "Small-slope expansion for thermal and reflected radiation from a rough surface," *Waves Random Media*, vol. 7, pp. 1–10, 1997.
- [9] J. T. Johnson, "A study of rough surface thermal emission and reflection using Voronovich's small slope approximation," *IEEE Trans. Geosc. Rem. Sens.*, Feb 2005.
- [10] A. B. Ivers, A. Puzenko, and I. M. Fuks, The local perturbation method for solving the problem of diffraction from a surface with small slope irregularities," *J. Electromagn. Waves Appl.*, vol. 5, no. 12, 1991.
- [11] V. G. Irisov, "Microwave radiation from a weakly nongaussian surface," in *Proc. IGARSS'98* vol. 5, pp. 2329–2332.
- [12] J. P. Hollinger, Passive microwave measurements of sea surface roughness, *IEEE Trans. Geosci. Electron.*, vol. GE-9, no. 3, pp. 165-169, 1971.
- [13] C. T. Swift, Microwave radiometer measurements of the Cape Cod Cannal, *Radio Sci.*, vol. 9, no. 7, pp. 641-653, 1976.



- [14] A. G. Voronovich, *Wave Scattering from Rough Surfaces*. Berlin, Germany: Springer-Verlag, 1994.
- [15] M. Zhang and J. T. Johnson, "Theoretical studies of ocean polarimetric brightness signatures," in *Proc. IGARSS'98*, vol. 5, pp. 2333–2335.
- [16] J. T. Johnson and Y. Cai, "A theoretical study of sea surface up/down wind brightness emperature differences," *IEEE Trans. Geosc. Remote Sens.*, 2002.
- [17] J. T. Johnson, "Comparison of the physical optics and small slope theories for polarimetric thermal emission from the sea surface," *IEEE Trans. Geosc. Remote Sens.*, 2002.
- [18] M. Zhang and J. T. Johnson, "Comparison of modeled and measured second azimuthal harmonics of ocean surface brightness temperatures," *IEEE Trans. Geosc. Remote Sens.*, 2001.
- [19] J. T. Johnson and M. Zhang, "Theoretical study of the small slope approximation for ocean polarimetric thermal emission," *IEEE Trans. Geosc. Remote Sens.*, 1999.
- [20] V. S. Etkin, N. N. Vorsin, Y. A. Kravtsov, V. G. Mirovskii, V. V. Nikitin, A. E. Popov, and I. A. Troitskii, "Critical phenomena with the thermal radio irradiation of a periodically uneven water surface," *Izvestiya: Radiophysics and Quantum Electronics*, vol. 21, pp. 316-318, 1978.
- [21] V. N. Kudryavtsev, V. K. Makin, and B. Chapron, "Coupled sea surface atmosphere model. 2. spectrum of short wind waves," *J. Geophys. Res.*, vol. 104, no. C4, pp. 7625-7639, 1999.
- [22] A. Camps, J. Font, M. Vall-Ilossera, C. Gabarro, R. Villarino, L. Enrique, J. Miranda, I. Corbella, N. Duo, F. Torres, S. Blanch, J. Arenas, A. Julia, J. Etcheto, V. Caselles, A. Weill, J. Boutin, S. Contardo, R. Niclos, R. Rivas, S. Reising, P. Wursteisen, M. Berger, and M. Martin-Neira, "The WISE 2000 and 2001 Campaigns in support of the SMOS Mission: Sea surface L-band Brightness Temperature Observations and their application to Multi-Angular Salinity Retrieval," *IEEE Trans. Geosci. Remote Sensing*, vol. 42, no. 4, pp. 1039-1048, 2004.
- [23] S. Sobjaerg and N. Skou, "An Airborne Campaign measuring wind signatures from the Sea Surface using an L-band polarimetric radiometer," in *Proceedings of the International Geoscience and Remote Sensing Symposium, IGARSS*, Toulouse, 2003.
- [24] L. A. Klein and C. T. Swift, "An Improved model of the dielectric constant of sea water at microwave frequencies," *IEEE Trans. Antennas Propag.*, vol. AP-25, pp. 104-111, 1977.
- [25] R. M. Lerner and J. P. Hollinger, "Analysis of 1.4 GHz Radiometric measurements from Skylab," *Remote Sens. Environm.*, vol. 6, pp. 251-269, 1977.
- [26] A. Camps, J. Font, J. Etcheto, V. Caselles, A. Weill, I. Corbella, M. Vall-Ilossera, N. Duffo, F. Torres, R. Villarino, L. Enrique, A. Julia, C. Gabarro, J. Boutin, E. Rubio, S. C. Reising, P. Wursteisen, M. Berger, and M. Martin-Neira, "Sea surface emissivity observations at L-band: First results of the wind and salinity experiment wise 2000," *IEEE Trans. Geosci. and Remote Sens.*, vol. 40, no. 10, pp. 2117-2129, 2002.
- [27] J. P. Hollinger, "Passive microwave measurements of sea surface roughness," *IEEE Trans. Geosci. Electron.*, vol. GE-9, no. 3, pp. 165-169, 1971.
- [28] W. J. Webster, T. T. Wilheit, D. B. Ross, and P. Gloersen, "Spectral characteristics of the microwave emission from a wind-driven covered sea," *J. Geophys. Res.*, vol. 81, no. 18, pp. 3095-3099, 1976.

ARGANS Ltd.

Commercial in Confidence

Page 279

Use, duplication, or disclosure of this document or any information contained herein is subject to the restriction on the title page of this document.



[29] J. Etcheto, E. P. Dinnat, J. Boutin, A Camps, J. Miller, S. Contardo, J. Wesson, J. Font, and D. Long, Wind speed effect on L-band brightness temperature inferred from EuroSTARRS and WISE2001 field experiments, *IEEE Trans. Geosci. and Remote Sens.*, vol. 42, no. 10, pp. 2206-2213, 2004.

[30] Y. Quilfen, B. Chapron and D. Vandemark, "The ERS Scatterometer Wind measurement accuracy: evidence of seasonal and regional biases", *Journal of Atmospheric and Oceanic Technology*, vol 18, p 1684-1697, 2001.

ANNEX B *Surface roughness 3: empirical*

Surface roughness 3: empirical				
WS	Wind speed	m/s		
ϕ	Azimuthal direction relative to wind direction	deg		
Hs	Significant wave height	m		
Ω	Inverse wave age	dl		
Cp	Phase speed	m/s		
g	Gravity of the earth	m/s ²		
T _p	Mean period of wind waves	dl		
U*	Wind friction velocity	m/s		
C _d	Coefficient of drag	dl		
MSQS	Mean square slope of waves	dl		
Tg_WS_roughness_M3	min. WS to apply roughness correction	m s ⁻¹		
Fg_ctrl_roughness_M3	Roughness correction applied	Y/N		
Fg_OoR_Rough_dim1	Prior or retrieved Theta went outside of LUT range	Y/N		
Fg_OoR_Rough_dim2	Prior or retrieved WS went outside of LUT range	Y/N		
Fg_OoR_Rough_dim3	Prior or retrieved phi_wsn went outside of LUT range	Y/N		
Fg_OoR_Rough_dim4	Prior or retrieved Hs went outside of LUT range	Y/N		

Theoretical description

Physics of the problem

The brightness temperature can be expressed as the sum of two terms: the brightness temperature in the case of completely flat sea and the brightness temperature (ΔT_b) due to the surface roughness:

$$T_{b,p}(\theta_i, SST, SSS, P_{rough}) = T_{bflat,p}(\theta_i, SST, SSS) + \Delta T_{b\ rough,p}(\theta_i, SST, SSS, \overrightarrow{P_{rough}}) \quad 6.4.7$$

where the first term is T_b due to specular reflection, which is well described by the Fresnel equations. The second term is the increment of brightness temperature due to sea roughness indicated here by a vector P_{rough} , which includes the effect of some of the parameters that



modify the surface roughness, like wind speed (WS), significant wave height (H_s), inverse wave age (Ω)... Furthermore, T_b is polarization dependent.

Several models describe this increment on T_b in a theoretical basis as in the modules 2 and 3. However, these theoretical models are not fully well validated.

This module proposes to use an empirical model describing T_b through several physically measurable parameters and coefficients which are derived from measurements.

The most important parameter that affects the roughness of the sea is the wind speed, due to the stress on its surface and then this is the main (and usually the only) parameter used in the description of the sea roughness. However, this impact is not linear with all wind speeds as shown in several works (Etcheto et al, 2004, Vall-Ilossera et al., 2003).

Miranda et al. (2003), using several wind speed sequences recorded during WISE 2000 and 2001 campaigns (Camps et al, 2004, Camps et al, 2002), found large differences between measured spectra and theoretical fully-developed spectra obtained with the measured local wind speed. This can produce errors on T_b of about a fraction of a Kelvin in both polarizations with opposite sign (therefore, these errors could be minimized by using the first Stokes parameter).

This is the case when swell is present, where some events of low local wind speed and high wave height are possible and therefore roughness cannot be properly described only by the wind speed.

In Gabarró et al, 2004a, a new empirical model is proposed to describe the increment of T_b due to the roughness of the sea as function of wind speed and significant wave height. That model is derived from WISE 2001 campaign measurements. Gabarró, 2004b compares the behaviour of this model with respect to other models which are only dependent on WS , and better performances are observed when the proposed model is used.

In Camps et al., 2004 authors have observed that azimuthal variations of the measured T_b during WISE 2000 at 25°, 35°, 45°, and 55° incidence angles, and at both polarizations, are within 0.5 K. However, they can be due to differences between calibrations, and the authors do not think there is any measurable azimuthal signature below 10 m/s. Only during very large storms (as the case of WISE2001, with a wind speed of 11m/s and very large waves ($3\text{ m} < H_s < 5\text{ m}$)), the azimuthal signature has been observed. However, in Yueh et al. 2010, authors show a dependency of T_{bH} and T_{bV} on the wind direction at relatively high wind speeds (more than 14m/s) has been observed in a field campaign in North Atlantic. They say it can represent an increment of 1K at 14m/s and 2K at 24m/s.



A LUT is proposed to describe the T_{brough} as a function of the parameters. This LUT depends on 4 parameters: θ (incidence angle), WS_n (neutral wind speed from the WS components), ϕ_{WS} (wind direction) and H_s (wave height).

The model regression analysis will be performed with auxiliary data coming from ECMWF models since such data are globally available at high temporal frequency and can therefore maximize the collocation dataset of SMOS and auxiliary information. A comprehensive analysis of the different error contributions (notably measurement and auxiliary data errors, and fitting errors) will be carried out, as well as a correlation analysis among the different parameters (notably the roughness ones), to derive the most suitable model.

The T_b information to create the LUT is obtained from SMOS L1b and transformed to sea surface brightness temperature. The vector \vec{P} can comprise any relevant geophysical parameters, for the implementations that we consider the following parameters will be used, namely incidence angle, wind speed (WS), wind direction (ϕ) and significant wave height (H_s).

To diminish the impact of yet-unsolved processing problems (correction of galactic noise, land contamination, TEC, Faraday rotation, etc) a very restrictive dataset of valid TB's will be considered; this gives more generality and stability to our results, so diminishing the expected impact on the GMF when a reprocessing is done. However, this also restricts the range of valid values for our LUT and implies the necessity of implementing an extrapolation strategy to extend it out of the sampling range.

The tabulation of the LUT will be provided by incidence angle between 0 and 75°, WS_n between 0 and 50 m/s, wind direction ϕ between 0 and 360° and H_s between 0 and 15m. The outputs of the LUT are T_{bh} , T_{bv} , third stokes vector (U) and fourth stokes vector (V).

Mathematical description of algorithm

To permit a rapid computation of the T_b due to roughness a LUT has been created to determine the T_{brough} empirically from SMOS L1b data and the geophysical parameters that describe this T_{brough} .

The parameters used as input to the LUT are:

- Incidence angle θ_i at SMOS pixel
- Neutral wind speed, WS_n , computed from its components by:
$$WS_n = \sqrt{WS_x^2 + WS_y^2}$$
- Wind direction, obtained from the neutral components by:
$$\phi = \arctan(WS_x^2 / WS_y^2)$$
- Wave Height (H_s), obtained from the ECMWF wave model.

The outputs are:

$$Tb_{rough} = \begin{pmatrix} Tb_{rough_h} \\ Tb_{rough_v} \\ U \\ V \end{pmatrix}$$

where U is the thirds Stokes parameter and V the fourth Stokes parameter.

The parameters range as follows:

Dimension	Number of Values	Units	Coordinate Values
Radiometric Incidence angle	76	Deg	[0,1,2,3,..... Δ θ =1 ...73,74,75]
Neutral Wind speed WSn	111	m/s	[0 ...ΔWS=0.25 ... 20][21 ... ΔWS=1...50]
Wind direction	36	Deg	[0...Δφ=10.....360]]
Significant Wave height - Hs	40	m	Hs (m) = [0 ...ΔHs=0.25 ... 8][9 ... ΔHs=1...15

Since the model is empirical the effect of foam is already included in the computed Tb, so the foam correction described in module 4.5 is never to be applied to roughness model 3.

Practical derivation of the empirical TB modulation

In spite of the apparent cumbersome mathematics, in practice the computation of $E[Tb_p]$ is very easy: for each fixed value of \vec{P} (vector of the geophysical parameters), all the values of Tb associated to that value of \vec{P} are averaged together. This implies that an uncertainty or quantization range on the vector \vec{P} must be given, as we cannot expect a precise value of \vec{P} to be exactly repeated ever. Hence, a suitable quantization vector $\Delta\vec{P}$ must be constructed, which is defined as the quantization range for each of the components in \vec{P} .

The discretization shown above is based on considerations about the probability distribution of the geophysical parameters as well as about the trade-off between lookup table size and resolution of nonlinear variations of emissivity corrections.

The values shown define the discretization ranges for each geophysical parameter p^a ; we consider the n -th range of values of p^a , $C_{p^a}^n$, given by:

$$C_{p^a}^n \equiv [p_n^a - \Delta p_n^a, p_n^a + \Delta p_n^a] \quad 6.4.8$$

where p_n^a is the n -th value that the parameter p^a can take, $n = 1, \dots, N^a$, and $\Delta p_n = (p_n - p_{n-1})/2$ (when sampling is not uniform this definition is modified to avoid overlaps). Given this discretization, the empirical estimate of the Tb modulation (i.e., empirical histogram) is then defined for those representative values P_n^a . We will denote the empirical Tb modulation by $\hat{T}b(\vec{p})$; it is given by:

$$\hat{T}b(\vec{p}_n) = \frac{1}{N_{\vec{n}}} \sum_{\vec{p} \in C_{\vec{p}}^{\vec{n}}} Tb \quad 6.4.9$$

where \vec{n} designates the vector of discrete indexes for all geophysical parameters, and $N_{\vec{n}}$ stands for the number of points such that $\vec{p} \in C_{\vec{p}}^{\vec{n}}$.

Uncertainty on the empirical TB modulation

The quantization on the geophysical vector \vec{p} (that allows to pass from continuous \vec{p} to a discrete collection $\vec{p}_{\vec{n}}$) will forcefully impact our estimate of Tb modulation. We can evaluate the impact of the quantization by computing the conditioned standard deviation of Tb by \vec{P} , denoted by $\sigma_{Tb}(\vec{p})$, which is theoretically given by the following formula:

$$\sigma_{Tb}^2(\vec{p}_{\vec{n}}) = \int dTb \quad Tb \quad \rho(Tb|\vec{p}) - E[Tb|\vec{p}]^2 \quad 6.4.10$$

Again, the practical computation of the conditioned standard deviation $\sigma_{Tb}(\vec{p})$ is straightforward, as it just requires to compute the standard deviation of TB on $C_{\vec{p}}^{\vec{n}}$, namely:

$$\sigma_{Tb}(\vec{p}_{\vec{n}}) = \frac{1}{N_{\vec{n}}} \sum_{\vec{p} \in C_{\vec{p}}^{\vec{n}}} Tb - \hat{T}b(\vec{p}_{\vec{n}})^2 \quad 6.4.11$$

This conditioned standard deviation provides an accurate estimate of the marginal uncertainty on the value of the Tb as retrieved using the GMF LUT. It may happen, however, that the uncertainty is larger than what we would like. This would imply the necessity of improving the uncertainties of the geophysical variables. Notice, however, that even if the uncertainty on Tb may be large, as far as the amount of averaged data is large enough and the sampling errors are unbiased and independent, the quality of the LUT may still be good. So the key point is to know the significance of the LUT.



Error budget estimates (sensitivity analysis)

In Camps et al., 2004, authors observe that the uncertainty of the brightness temperature sensitivity to wind speed is of the order of 0.1 K/(m/s) for all incidence angles, when using the model only dependent on WS. Therefore, for WS=10 m/s, the uncertainty of the brightness temperature T_b is about 1 K. Taking into account the brightness temperature sensitivity to SSS (0.35-0.8 K/psu at V-pol, and 0.20-0.6 K/psu at H-pol), it translates at 10 m/s into a Δ SSS within 1.2-5 psu.

Practical considerations

Calibration and validation

Roughness model 3 will be validated comparing SMOS SSS retrieved maps with this roughness model with SSS maps created with interpolated ARGO data.

Quality control and diagnostics

Because of its empirical derivation, the model's accuracy will be degraded for exceptional geophysical conditions, such as winds above 15m/s and wave height above 8m, for which very few SMOS observations are available.

Exception handling

There is no exception handling in the algorithm except if the following auxiliary data are not provided by the processor or exceed the ranges of the LUT:

- the wind speed, WS
- the significant wave height, H_s
- the incidence angles θ_i at SMOS pixel

If one of the prior values of the retrieved geophysical parameters is out of the LUT range, or if any retrieved geophysical parameter goes out of LUT range during the retrieval, different flags

Fg_OoR_Rough_dim1
Fg_OoR_Rough_dim2
Fg_OoR_Rough_dim3
Fg_OoR_Rough_dim4

are raised. No extrapolation is done, and the boundary value is taken.



Assumption and limitations

When a significantly heavy rain is present in the FOV, the model cannot be applied. This information will be known from the ECMWF data. Also, in the case of presence of surface slicks, from natural or not natural origin, the model will not work properly.

There is the possibility (controlled by a switch) that no roughness correction is applied in wind speeds below $Tg_WS_rougness_M3$ (due to lack of confidence in the model), and in such case a flag will be raised ($Fg_ctrl_roughness_M3$, *false*). Elsewhere, the flag is set to true ($Fg_ctrl_roughness_M3$, *true*)

New update of the empirical model: fitting T_b with neural network

The last updates of the empirical roughness model use a neural network for the fitting of the Brightness temperatures. A first update was proposed in Guimbard et al, 2012. After that, a new update has been implemented where the hidden layer of the network considers not 4 but ten neurons. In this last update, L1B v623 has been used.

References

Camps, A., Font, J., Vall-Ilossera, M., Gabarró, C., Villarino, R., Enrique, L., Miranda, J., Corbella, I., Duffo, N., Torres, F., Blanch, S., Arenas, J., Julià, A., Etcheto, J., Caselles, V., Weill, A., Boutin, J., Contardo, S., Niclòs, R., Rivas, R., Reising, S., Wursteisen, P., Berger, M., and Martín-Neira, M. (2004a). The WISE 2000 and 2001 Campaigns in Support of the SMOS Mission: Sea Surface L-band Brightness Temperature Observations and their Application to Multi-Angular Salinity Retrieval. *IEEE Transactions on Geoscience and Remote Sensing*, 42(4):804–823.

Camps, A., Font, J., Etcheto, J., Caselles, V., Weill, A., Corbella, I., Vall-Ilossera, M., Duffo, N., Torres, F., Villarino, R., Enrique, L., Julià, A., Gabarró, C., Boutin, J., Rubio, E., Reising, S., Wursteisen, P., Berger, M., and Martín-Neira, M. (2002b). Sea Surface Emissivity Observations at L-band: First Results of the Wind and Salinity Experiment WISE-2000. *IEEE Transactions on Geoscience and Remote Sensing*, 40(10):2117–2130.

Camps, A., Font, J., Gabarró, C., Miranda, J., Obligis, E., Labroue, S., Boone, C., Sabia, R., Vall-Ilossera, M., Reul, N., June 2004. WP1100, ESTEC ITT 1-4505/03/NL/Cb

Camps, A., Vall-Ilossera, M., Villarino, R., Reul, N., Chapron, B., Corbella, I., Duffo, N., Torres, F., Miranda, J.J., Sabia, R., Moneris, A., and Rodríguez, R. (2005c). The Emissivity of Foam-Covered Water Surface at L-Band: Theoretical Modeling and Experimental Results from the Frog 2003 Field Experiment. *IEEE Transactions on Geoscience and Remote Sensing*, 43(5):925-937.

ARGANS Ltd.

Commercial in Confidence

Page 287



Etcheto, J., Dinnat, E., Boutin, J., Camps, A., Miller, J., Contardo, S., Wesson, J., Font, J., and Long, D. (2004). Wind speed effect on L-band brightness temperature inferred from EuroSTARRS and WISE 2001 field experiments. *IEEE Transactions on Geoscience and Remote Sensing* (in press).

Gabarró, C., Font, J., Camps, A., Vall-Ilossera, M., and Julià, A. (2004a). A New Empirical Model of Sea Surface Microwave Emissivity for Salinity Remote Sensing. *Geophysical Research Letters*, 31(L01309):1–5.

Gabarró, C. (2004b). Study of salinity retrieval errors for the SMOS mission. PhD thesis, Universitat Politècnica de Catalunya.

Guimbar, S., J. Gourrion, M. Portabella, A. Turiel, C. Gabarró, J. Font, 2012, SMOS Semi-Empirical Ocean Forward Model Adjuntment, *Trans. Geosci. Rem. Sens.*: 50 (5), 1676-1687

Miranda, J., Vall-Ilossera, M., Camps, A., Duffo, N., Corbella, I., and Etcheto, J. (2003). Sea State on the Sea Surface Emissivity at L-Band. *IEEE Transactions of Geoscience and Remote Sensing*, 41(10):2307–2315.

Yueh, S., Dinardo, S. J., Fore, A. F., Li, F.K. (2010). Passive and Active L-Band Microwave Observations and Modeling of Ocean Surface Winds. *IEEE Transactions of Geoscience and Remote Sensing*, 48(8):3087–3100.

Vall-Ilossera, M., Miranda, J., Camps, A., and Villarino, R. (2003). Sea Surface Emissivity Modeling At L-Band: An InterComparison Study. *Proceedings of the WISE/LOSAC/EuroSTARRS campaigns Workshop*. ESA, SP-525:143–154.

ANNEX C

Foam Contribution

4.5 Foam contribution		
F	Fraction of sea surface area covered by whitecaps	dl
h	thickness of the white caps	m
δ	thickness of the typical sea foam layer	m
Ts	physical temperature of foam	K
$e^{\text{typ}}_{\text{foam}}$	emissivity of typical sea foam-layer	dl
r	radius of the coated bubbles	m
ϵ_a	permittivity of the core of the bubbles made of air	dl
ϵ_w	permittivity of the surrounded area (region 2)	dl
$\epsilon_{N\alpha}$	effective permittivity	dl
d	thickness of the layer called region 1	m
ψ	attenuation factor	dl
R_p^{01}	Fresnel reflection coefficient between region 0 and 1, for p pol	dl
R_p^{12}	Fresnel reflection coefficient between region 1 and 2, for p pol	dl
N	volumetric concentration of bubbles	dl
α	complex polarizability of a single bubble	dl
k	packing coefficient or stickiness parameter	dl
p_f	normalized probability distribution function	dl
q	distribution of the bubble's filling factor	dl
f	distribution of coating thicknesses	dl
A	parameters of the distribution	dl
B	parameters of the distribution	dl
		dl
		dl
f_a	fraction of volume occupied by air bubbles	dl
Fc	coverage of actively breaking crests or active foam	dl

ARGANS Ltd.

Commercial in Confidence

Page 289

Use, duplication, or disclosure of this document or any information contained herein is subject to the restriction on the title page of this document.

F _s	coverage of passive foam or static foam	dl
α_c	constant for 'crest-foam coverage'	dl
β_c	constant for 'crest-foam coverage'	dl
α_s	constant for 'static-foam coverage'	dl
β_s	constant for 'static-foam coverage'	dl
ΔT	air-sea temperature difference	°C
T _a	temperature of air	°C
e ^{tYP} _{Bfp}	???????????	dl
Fg_OoR_Foam_dim1_WS	WS went out of LUT range during retrieval	Y/N
Fg_OoR_Foam_dim2_TseaAir	TseaAir went out of LUT range during retrieval	Y/N
Fg_OoR_Foam_dim3_SSS	SSS went out of LUT range during retrieval	Y/N
Fg_OoR_Foam_dim4_SST	SST went out of LUT range during retrieval	Y/N
Fg_OoR_Foam_dim5_Theta	Theta went out of LUT range during retrieval	Y/N

Theoretical description

Physics of the problem

Although foam generated by breaking waves typically covers only a few percent of the sea surface, it has a profound effect on the average microwave brightness of the ocean surface [1-8]. For surface wind speeds greater than 15 m/s, foam-induced effects may provide as much as half of the total sea surface signature to an orbiting microwave radiometer [9;10].

At L-band, WISE [11] and FROG [12] experiments have provided detailed L-band emissivity measurements of the sea foam over a wide range of incidence angles and salinities at both polarizations. Although foam has a weaker impact at 1.4 GHz than at higher frequencies, it was shown that the presence of foam also increases the emitted brightness temperature at L-band, since it acts as a transition layer that adapts the wave impedance of the two media: water and air. The increase depends on the fraction of the sea surface covered by foam and its thickness, which can be parameterized in terms of the local wind strength, but it depends as well on other factors, such as the air-sea temperature difference, the sea water temperature, the fetch, etc... FROG 2003 experiments revealed that at a salinity of 37 psu, the foam-induced emissivity increase is ~0.007 per mm of foam thickness (extrapolated at nadir), increasing with increasing incidence angles at vertical polarization, and decreasing with increasing incidence angles at horizontal polarization. According to the model developed by

ARGANS Ltd.

Commercial in Confidence

Page 290

Use, duplication, or disclosure of this document or any information contained herein is subject to the restriction on the title page of this document.

[13], for a 12 m/s wind speed, one should expect in average a coverage-weighted foam thickness of about 0.5 cm: this translates to an increase in brightness temperature of about 0.2 K at an SST of about 15°C. At 20 m/s, the calculation predicts a 0.5 K increases: this might have a non-negligible impact for salinity retrieval accuracy.

In [12], it was shown that the emissivity model proposed by [14] correctly predicts the measured foam emissivity at L-band provided some auxiliary parameter describing the foam-water system are tuned. The purpose of this section is to document this forward foam emissivity model, which is used here to provide foam impact corrections in the version of the SSS retrieval algorithm used at launch of the ESA's Soil Moisture and Ocean Salinity (SMOS) satellite mission.

As proposed by [13], foam formations contribute to the total sea surface brightness temperature measured by a radiometer as function of wind speed WS following:

$$T_{b,foam}(f, p, \theta_i, WS) = T_s \cdot \int e^{typ}_{foam;p}(f, p, \theta_i, h) \cdot F(WS, h) dh \quad 6.4.12$$

where

- f, p and θ_i are the receiving electromagnetic frequency, polarization, and incidence angle of the radiometer respectively,
- $F(WS, h)$ is the fraction of sea surface area covered by whitecaps with thickness h at wind speed WS ,
- T_s is the physical temperature of foam, usually assumed the same as the bulk sea surface temperature and,
- e^{typ}_{foam} is the emissivity of typical sea foam-layer with thickness δ .

This model is used in the present algorithm to provide foam impact corrections for SMOS. It contains two sub-models: one to parametrize the emissivity of typical sea foam-layer with thickness h and the second to model the fraction of sea surface area covered by whitecaps with thickness h at wind speed WS . Both are successively detailed hereafter.

Emissivity modelling of the foam-water system

Following Guo et al. [6], it is assumed that foam on the ocean surface is composed of nearly spherical coated bubbles described by an outer radius r , made of an air core with permittivity ϵ_a , surrounded by a shell of sea water with thickness δ and permittivity ϵ_w . The foam-covered ocean is modelled by the succession of three media: the air (region 0), a foam layer defined as a region of effective permittivity $\epsilon_{N\alpha}$ with a layer thickness d (region 1), and the underlying seawater with some air bubbles (region 2) with permittivity ϵ_w . Boundaries between each region are assumed flat.

The emissivity of a typical foam-water system at incidence angle θ and polarization $p = h$ (horizontal) or v (vertical) is given by:

$$e^{\text{typ}}_{\text{foam},p} = 1 - |R_p(\theta_i)|^2 \quad 6.4.13$$

where the coefficient R_p is the spectral reflection coefficient of the foam layer medium with the effective dielectric constant $\epsilon_{N\alpha}$ and is given by

$$R_p(\theta_i) = \frac{R_p^{01}(\theta_i)e^{-j2\psi} + R_p^{12}(\theta_i)}{e^{-j2\psi} + R_p^{01}(\theta_i)R_p^{12}(\theta_i)} \quad 6.4.14$$

where ψ is an attenuation factor that depends on the foam layer thickness d , the electromagnetic wavelength λ_0 , and the effective permittivity $\epsilon_{N\alpha}$:

$$\psi = \frac{2\pi d}{\lambda_0} \sqrt{\epsilon_{N\alpha} - \sin^2 \theta_i} \quad 6.4.15$$

Note that for the foam-covered ocean, Stokes-3 and Stokes-4 = 0.

In Eq.(3), R_p^{01} are the Fresnel reflection coefficients between the air (region 0) and the foam (region 1):

$$R_h^{01}(\theta_i) = \frac{\cos(\theta_i) - \sqrt{\epsilon_{N\alpha} - \sin^2 \theta_i}}{\cos(\theta_i) + \sqrt{\epsilon_{N\alpha} - \sin^2 \theta_i}} \quad 6.4.16$$

and

$$R_v^{01}(\theta_i) = \frac{\epsilon_{N\alpha} \cos(\theta_i) - \sqrt{\epsilon_{N\alpha} - \sin^2 \theta_i}}{\epsilon_{N\alpha} \cos(\theta_i) + \sqrt{\epsilon_{N\alpha} - \sin^2 \theta_i}} \quad 6.4.17$$

and R_p^{12} are the Fresnel reflection coefficients between foam (region 1) and water (region 2):

$$R_h^{12}(\theta_i) = \frac{\sqrt{\epsilon_{N\alpha} - \sin^2(\theta_i)} - \sqrt{\epsilon_w - \sin^2 \theta_i}}{\sqrt{\epsilon_{N\alpha} - \sin^2(\theta_i)} + \sqrt{\epsilon_w - \sin^2 \theta_i}} \quad 6.4.18$$

and

$$R_h^{12}(\theta_i) = \frac{\varepsilon_w \sqrt{\varepsilon_{N\alpha} - \sin^2(\theta_i)} - \varepsilon_{N\alpha} \sqrt{\varepsilon_w - \sin^2 \theta_i}}{\varepsilon_w \sqrt{\varepsilon_{N\alpha} - \sin^2(\theta_i)} + \varepsilon_{N\alpha} \sqrt{\varepsilon_w - \sin^2 \theta_i}} \quad 6.4.19$$

Region 2 consists of air bubbles embedded in the ocean background and is assumed to be absorptive. To solve the previous equations (2-6), one needs to define an effective permittivity for region 1, namely $\varepsilon_{N\alpha}$, and for region 2, namely ε_w .

The main parameter of the previous multi-layer emissivity model for foam is the effective permittivity $\varepsilon_{N\alpha}$ of the foam-layer considered. To define this parameter, the well-known *Lorenz-Lorentz* and *Hulst* equations can be used and modified for the poly-dispersed system of bubbles. The first formula considers *dipole interaction* of bubbles in a close-packed dispersed system (the quasi static approximation). The Hulst equations describe the contribution of the *multi-pole moment* of bubbles into effective permittivity of the system. Spectral calculations by Cherny and Raizer [15] show that first resonant electromagnetic effects by Hulst's mechanism occur for bubbles radius $a \approx \lambda_0/4$. At L-band ($\lambda_0=21$ cm), this corresponds to bubble diameters on order of 10 cm. Such very large bubbles are extremely rare at the sea surface and therefore, the multi-pole mechanism may be neglected at L-band for which the dipole term might be considered only. In the present work, we use the dipole approximation model developed by Dombrovskiy and Raizer [16] to describe the effective permittivity of the system. It involves the use of a modification of the Lorenz-Lorentz equation and yields to the following simple formula for the complex effective permittivity $\varepsilon_{N\alpha}$ of a foam-layer [15, 16]:

$$\varepsilon_{N\alpha} = \frac{1 + \frac{8}{3} \overline{\pi N \alpha}}{1 - \frac{4}{3} \overline{\pi N \alpha}} \quad 6.4.20$$

where

$$\overline{N \alpha} = \frac{\kappa \int \alpha(r) p_f(r) dr}{\frac{4}{3} \int r^3 p_f(r) dr} \quad 6.4.21$$

and N is the volumetric concentration of the bubbles, $\alpha(r)$ is the complex polarizability of a single bubble with external radius r , κ is the so-called packing coefficient or *stickiness parameter*, and $p_f(r)$ is the normalized probability distribution function of the bubbles' size. In natural media such as foam, the densely packed particles can have adhesive forces that make them adhere to form aggregates. This effect is accounted for in the model by the *stickiness parameter* κ , which is inversely proportional to the strength of the attractive forces between bubbles [17].

According to Dombrovskiy and Raizer [16], the complex polarizability depends on the external radius of the bubbles r , the complex permittivity of the shell medium (salt water) ε_w , and the bubble's filling factor $q = 1 - \frac{\delta}{r}$ following

$$\alpha(r) = r^3 \frac{(\varepsilon_w - 1)(2\varepsilon_w + 1)(1 - q^3)}{(\varepsilon_w + 2)(2\varepsilon_w + 1)(1 - q^3) + 9\varepsilon_w q^3} \quad 6.4.22$$

Experimental measurements on stable foam reveal that the effective permittivity might be dependent on the vertical position within the foam layer, i.e., $\varepsilon_{N\alpha} = \varepsilon_{N\alpha}(z)$. In the simplest case, the foam-water system may be modeled as a succession of elementary foam-layers, each of them having a homogeneous effective dielectric constant. However, the exact dependence of such function with the vertical position, which depends on the vertical distribution of the bubble's size, is very poorly known. It is very likely that the vertical distribution of the bubble's size $p_f(r, z)$ is a function of the intensity and scale of the underlying breaking event. Moreover, it will certainly strongly evolve during a transient breaking event. Nevertheless, in order to keep a tractable number of parameters in the present model, we choose to consider a uniform vertical distribution of bubbles sizes $p_f(r, z) = p_f(r)$ within the foam layer.

The foam void fraction (i.e., the ratio of the volume of air to the total volume of the foam) depends on the distribution of the bubble's filling factor q . Therefore, the distribution of bubbles radii $p_f(r)$ together with the distribution of coating thicknesses $f(\delta)$ determine the foam layer void fraction. In the present simplified model, we fixed the value of the shell thickness, but the outer bubble radius r is randomly distributed. According to Dombrovskiy [18], this approximation reflects an experimentally established fact for an emulsion layer of foam (young foam), but it requires verification for a foam with honeycomb structure (aged foam). Numerous observations of oceanic bubble size distributions are reported in the literature based on acoustic, photographic, optical, and holographic methods [19]. Currently, it is not clear how to parameterize the ocean surface bubble size distribution. Following Bordonskiy et al. [18] and Dombrovskiy and Raizer [16], we used a Gamma distribution for the size distribution function of the bubbles:

$$p_f(r) = \frac{A^{B+1}}{\Gamma(B+1)} r^B e^{-Ar} \quad 6.4.23$$

where A and B are parameters of the distribution defined with $r_p = A/B$ being the most probable radius. Finally, to calculate ε_w , a simple physical model based on induced dipoles is used. Let ε_{sw} denote the permittivity of the seawater at L-band, and f_a the fractional volume occupied by the air bubbles. Then, the effective permittivity ε_w , is given by the Maxwell-Garnett mixing formula [6]:

$$\varepsilon_w = \varepsilon_{sw} \frac{1 + 2f_a y}{1 - f_a y} \quad 6.4.24$$

where

$$y = \frac{1 - \varepsilon_{sw}}{1 + 2\varepsilon_{sw}} \quad 6.4.25$$

Note that the effective permittivity ε_w here does not include scattering extinction, which is small due to the fact that the seawater is heavily absorptive.

According to our simplified model, the emissivity induced by a typical sea foam layer at L-band is a function of:

$$e^{typ}_{Bf} = function(\theta_i, p, T_s, r_p, \delta, \kappa, f_a, d, SSS, SST) \quad 6.4.26$$

where θ_i is the radiometer incidence angle, p is the polarization, T_s is the foam physical temperature, r_p is the most probable radius, δ is the bubble's water coating thickness, κ is the bubble's packing coefficient, d is the foam layer thickness, f_a is the void fraction beneath the foam layer, and finally, SSS and SST are the sea surface salinity and temperature respectively.

Foam coverage Model

In [13], it was shown that the fractional sea surface covered by foam-layers with thicknesses between h and $h+dh$ at wind speed WS , namely, the term $F(WS,h)dh$ in Equation (1), can be decomposed as follows:

$$dF(WS,h)=F(WS,h)dh= dF_c(WS,h)+ dF_s(WS,h) \quad 6.4.27$$

where $dF_c(WS,h)$ and $dF_s(WS,h)$ are the contributions to the coverage of actively breaking crests or active foam and of the passive foam, or static-foam formations (see [7] for detailed terminology), respectively.

The model which is used for these two terms is a modified form of that described in detail in [13], where the following empirical expression for $dF_c(WS,h)$ was derived:

$$dF_c(WS,h) = \left[2.9 \times 10^{-5} \cdot WS^3 \sqrt{h} \cdot e^{-4.48\sqrt{h}} dh \right] \times e^{(\alpha_c \Delta T - \beta_c)} \quad 6.4.28$$

where WS is the 10-meter height wind speed, α_c and β_c are numerical constants and ΔT is the air-sea temperature difference. Instead of using this form directly, however, we begin with empirical distribution functions for foam-generating breaker length per unit area per unit breaker speed interval as derived in [13] and then generalize these equations to accommodate improvement in the foam coverage distributions.

The breaker length distribution function is a modified form of that derived from measurements of Melville and Matusov (2002),

$$\Lambda(WS, c) = \tilde{A} \left(\frac{WS}{10} \right)^3 \times 3.3 \times 10^{-4} \cdot e^{-.64 \tilde{B} \left(\frac{c}{WS} \right)} \quad 6.4.29$$

where \tilde{A} and \tilde{B} are constants to be specified. This distribution function differs from the empirical form of Melville and Matusov (2002) in that the exponent is a function of wave age rather than breaker phase speed.

Using the preceding formulation of the crest length distribution function, we can write the crest and static foam incremental coverages in terms of wind speed and breaker phase speed as

$$dF_c(WS, c) = \left[\frac{2\pi a_1}{g} c^2 \Lambda(WS, c) dc \right] \times e^{(\alpha_s \Delta T - \beta_s)} \quad 6.4.30$$

and

$$dF_s(WS, c) = \left[\frac{2\pi a_2}{g} c^2 \Lambda(WS, c) dc \right] \times e^{(\alpha_s \Delta T - \beta_s)}, \quad 6.4.31$$

respectively. The final exponentials in the two previous equations are stability correction factors, which have a significant impact on the foam coverage. The free parameters in these correction factors are given fixed values. The constants a_1 and a_2 in the above equations are constants that reflect the persistence time of the foam layers, which is typically much larger for static than for crest foam.

In the modified formulation, we note that the incremental foam fractional coverage for both static and crest foam is a function of

- generating breaking front speed c ,
- the 10 m wind speed, and
- the air-sea temperature difference.

The parameters dF_c and dF_s of the thermal correction factors were determined in [13] for both 'crest-foam' and 'static-foam' by best fitting the model to Monahan and Woolf [1989]'s empirical laws [19]. Using a least-square method, the determined numerical values for α and β_c are: $\alpha_c = 0.198$ and $\beta_c = 0.91$ for 'crest-foam coverage', and $\alpha_s = 0.086$ and $\beta_s = 0.38$ for 'static-foam coverage'.

To compute the total contribution of foam to the measured brightness temperature, we must determine the distribution of foam as a function of characteristic foam thickness, from which time dependence has been removed by assuming that foam layers associated with fronts moving at a given speed have equal probability of being at any stage of development. Using this assumption together with a simple model for the time dependence of foam layer depth, we obtain for crest foam the depth

$$\bar{\delta}_{\tau^*}(c) = \frac{0.4c^2}{g}, \quad 6.4.32$$

and for static foam we obtain

$$\bar{\delta}_{\tau}(c) = \frac{0.4c}{2\pi a} \left[\frac{5c}{2g} + \tau' \left(1 - e^{-\frac{c}{g\tau'}(2\pi a - 5)} \right) \right]. \quad 6.4.33$$

In the above equations, g is the acceleration of gravity and c is the breaker phase speed, and τ' is the exponential decay time of the foam depth after the mean duration time of the breaking events (nominally taken to be 3.8 s for salt water). These expressions can be used to transform the differential foam coverage expressions into expressions for the incremental coverage per unit foam thickness.

Mathematical description

The total contribution of foam formations to the sea surface brightness temperature measured at L-band as given in Eq. (1) will be mathematically expressed for implementation into the processor using:

1) Three Look-Up tables (LUTs) that will provide (1) the foam-induced sea surface brightness temperature (one LUT1 for H and LUT2 for V polarization) and (2) an additional LUT (LUT3) that will also provide the total foam-coverage.

LUT1 and LUT2 will be provided as function of the following parameters (with associated ranges):

- the incidence angle θ_i at SMOS pixel [deg], ($0 \rightarrow 75^\circ$)
- the sea surface temperature T_s [K], ($269.15 \rightarrow 309.15$ K)

- the prior sea surface salinity SSS [psu] (0 → 40 psu)
- the wind speed WS at 10-meter height [m/s], (0 → 30 m/s) and,
- the temperature difference between air at 2 m height and sea surface: $\Delta T = T_s - T_a$, [°C], (-30 → 30°C*)

LUT3 will be provided as function of the following parameters (with associated ranges):

- the wind speed WS at 10-meter height [m/s], and,
- the temperature difference between air at 2 m height and sea surface: $\Delta T = T_s - T_a$, [°C], (-30 → 30°C*)

LUT1 and LUT2 will directly provide Tb_{foam} (H or V), expressed as the result of the integral in Eq. 1 times SST. The reason why we provide LUT3 as well is that in Eq 1, only incremental foam coverages dF as function of thickness are included and NOT the total foam coverage, namely $F(U)$. However, the processor will need the later to evaluate the total surface contribution including foam and no-foam surface contributions (flat+rough), as follows:

$$Tb_{\text{surface}} = (1-F)(Tb_{\text{flat}} + Tb_{\text{rough}}) + Tb_{\text{foam}} \quad 6.4.34$$

Note that in the mathematical expression for $e^{tp_{Bf}}$, the numerical values for r_p , the most probable bubble radius, for δ , the bubble's water coating thickness, for κ , the bubble's packing coefficient, and for f_a , the void fraction beneath the foam layer will be assigned constant values derived by best-tuning the model to the data observed during FROG campaign [12]. These values are not provided yet in the draft ATBD but will be given later.

2) Multi-dimensional interpolation schemes

Given the four values of the "geophysical" auxiliary parameters estimated at a given SMOS pixel, namely T_{si} , SSS_i , WS and ΔT plus the series of incidence angles ($\theta_{=1, \dots, N}$) associated to the L1C product considered, a multi-dimensional linear interpolation scheme will be applied to LUT1 and LUT2 to evaluate, the values of $T_{Bf, i=1, \dots, N}^{(n)}$, at both H and V polarization. An additional 2D cubic spline interpolation scheme will be applied to LUT3 as function of WS and ΔT , to determine the total foam coverage.

Error budget estimates

Inter-comparison between the FROG measurements [12] of the foam emissivity scaled at 100% coverage and the theoretical values computed with the model described above for $e^{tp_{Bf}}$ using as inputs the measured foam parameters have been performed in [12]. The values of the stickiness parameter κ , which were not measured during FROG, used in the model are the optimum ones found at each salinity, which in general increases with SSS as the bubbles are more densely packed.

The rms error between the measured data and the theoretical foam emissivity model was found to vary from 0.008 to 0.017 at H-polarization, and from 0.011 to 0.033 at V-polarization. In general, the agreement is much better at H-polarization than at V-polarization. At V-polarization, the measured values show a larger variation with the incidence angle than the model predictions, which requires further analysis and refinement of the model. At H-polarization the agreement is excellent, except at low salinities, where there is a bias between the measured and predicted emissivity at all incidence angles.

A much higher uncertainty source in the model is the whitecap coverage model. Indeed, the model derived by [13] to parameterize $F(U,h)$ is constructed to match the empirical laws derived by [20]. It is well known that extremely large scatter in the whitecap coverage data as reported from one author to the other, which might yield to uncertainties of 100% to 600 % on empirical fits for $F(U,h)$. However, being the only source of validation, we have, these empirical fits shall be used here as the basis for modelling.

Accounting for an error of 100% in the foam coverage and assuming a maximum coverage of 10%, we expect a maximum rms error budget on the foam emissivity contribution modelling of about:

$$\text{Max}(Rms\ error) \left(\left[\begin{array}{c} e^{typ}_{Bfh}(\theta_i) \\ e^{typ}_{Bfv}(\theta_i) \end{array} \right] \right) \leq \left[\begin{array}{c} 1.7 \times 10^{-3} \\ 3.3 \times 10^{-3} \end{array} \right] \quad 6.4.35$$

This translates into about 0.5 K and 0.9 K maximal errors at H and V polarization, respectively.

Practical consideration

The model is not expected to provide significant contribution for wind speeds less than about 10 m/s. We could practically consider performing that correction only for wind speeds more than that threshold value, using the measurement discrimination.

Note as well that when foam correction is applied to SMOS Tbs, the foam-free surface contribution (i.e. flat sea surface+ roughness correction) has to be weighted by $1-F(U)$, the free foam fractional surface so that F is an output of the present forward model.

Calibration and validation

Calibration and validation of the forward foam emissivity model for roughness correction will be done during the commissioning phase, and later-on, by performing residual analysis of the future SMOS measurements and using a formalism proposed for and applied to NASA



scatterometer (NSCAT), Special Sensor Microwave Imager (SSM/I) and ESA/ERS scatterometer measurements [see 21].

Using in situ SSS, SST and wind (TAO, Argo drifters, satellite SST and winds and ECMWF model winds) and SMOS co-localized data, the first step will be to remove the modelled flat sea surface and free-foam roughness contributions from the SMOS surface brightness temperature data (i.e., corrected for atmospheric, ionospheric, galactic and sun glint contribution) in order to estimate the residual foam impact. This shall be done in selected ocean area with strong winds (Southern Ocean and North seas). The in situ and satellite SSS, SST and wind data will be the chosen reference. In addition, ECMWF analysis winds will be used as a third data source to completely determine the errors via a multiple collocation analysis. The main objective will be to present observed correlations between regional and seasonal model predictions of the foam correction factors errors and nonwind oceanic and atmospheric factors such as the surface current and sea state. Following the methodology applied in [30], we shall explicitly consider the errors in the reference datasets as well as in the foam correction factors retrieved estimates. The gain shall come in more accurate assessment of bias and variance and less possible systematic contamination that can obscure geophysical driven impacts not accounted for by the foam model.

Quality control and diagnostics

As explained in section below, the foam correction model is based on fixed geophysical parameters (bubbles radius, stickiness factors, etc) which might generate biases on the estimated correction.

The model can be applied as it is at launch, but we expect that the CAL/VAL activities will provide after commissioning phase a possible tuning for these parameters.

Exception handling

In presence of very stormy conditions (Hurricane like situations) it is likely that high foam coverage will be associated with high rain rates. Foam correction in that case would be non-physical if no atmospheric correction to account for rain absorptivity is also provided by the processor.

If some parameter goes out of LUT range during the retrieval, a flag

Fg_OoR_Foam_dim1_WS
Fg_OoR_Foam_dim2_TseaAir
Fg_OoR_Foam_dim3_SSS
Fg_OoR_Foam_dim4_SST
Fg_OoR_Foam_dim5_Theta

ARGANS Ltd.

Commercial in Confidence

Page 300

Use, duplication, or disclosure of this document or any information contained herein is subject to the restriction on the title page of this document.

is raised. No extrapolation is done, and the boundary value is taken.

Assumption and limitations

*: Note that there is no impact of stratification when atmosphere is stable, i.e., $\Delta T < 0$ so that, the tables will be computed only for ranges where it has an impact and where the model is thought to be valid, i.e., $\Delta T: 0 \rightarrow 15^\circ\text{C}$. Out of this range, the LUTs will duplicate values at extreme borders of the validity range.

A strong limitation may come from the fact that the numerical values for r_p , the most probable bubble radius, for δ , the bubble's water coating thickness, for κ , the bubble's packing coefficient, and for f_a , the void fraction beneath the foam layer are assigned constant values derived by best-tuning the model to the data observed during FROG campaign [12]. This is a strong assumption, as these parameters clearly evolve as function of the synoptic wind and wave forcing conditions.

This foam contribution can be applied to the T_b roughness correction modelled according to modules 4.2 or 4.3 (it has no sense in the empirical option 4.4). A switch will be established for selection (based on a threshold for wind speed) and a flag raised to describe if foam contribution has been taken into account (Fg_ctrl_foam_MX, *true*, X=1,2).

References

- [1] Rosenkranz, P. W., and D. H. Staelin, Microwave emissivity of ocean foam and its effect on nadiral radiometric measurements, *J. Geophys. Res.*, 77, 6528-6537, 1972.
- [2] Stogryn, A., The emissivity of sea foam at microwave frequencies, *J. Geophys. Res.*, 77, 1658-1666, 1972.
- [3] Ross, D. B., and V. Cardone, Observations of oceanic whitecaps and their relation to remote measurements of surface wind speed, *J. Geophys. Res.*, 79, 444-452, 1974.
- [4] Smith, P. M., The emissivity of sea foam at 19 and 37 GHz, *IEEE Trans. Geosci. and Remote Sens.*, 26, 541-547, 1988.
- [5] Kunke, D. B., and A. J. Gasiewski, Simulation of passive microwave wind direction signatures over the ocean using an asymmetric-wave geometrical optics model, *Radio Sci.*, 32, 59-78, 1997.
- [6] Guo, J., L. Tsang, W. Asher, K.-H. Ding, and C.-T. Chen, Applications of dense media radiative transfer theory for passive microwave remote sensing of foam-covered ocean, *IEEE Trans. Geosci. and Remote Sens.*, 39, 1019-1027, 2001.



- [7] Monahan, E., Oceanic whitecaps: Sea surface features detectable via satellite that are indicators of the air-sea gas transfer coefficient, in Proc. Indian Acad. Sci. (Earth Planet Sci.), vol.111, pp. 315-319, 2002.
- [8] Anguelova, M., Whitecaps, sea-salt aerosols, and climate, Ph.D. thesis, Graduate College of Marine Studies, University of Delaware, Lewes, Delaware, 2002.
- [9] Droppleman, J. D., Apparent microwave emissivity of sea foam, J. Geophys. Res., 79,696-698, 1970.
- [10] Barber, R. P., and J. Wu, Sea brightness temperature effects of spray and whitecaps, J. Geophys. Res., 102, 5823-5827, 1997.
- [11] A. Camps, J. Font, M. Vall-Ilossera, C. Gabarro, R. Villarino, L. Enrique, J. Miranda, I. Corbella, N. Duo, F. Torres, S. Blanch, J. Arenas, A. Julia, J. Etcheto, V. Caselles, A. Weill, J. Boutin, S. Contardo, R. Niclos, R. Rivas, S. Reising, P. Wursteisen, M. Berger, and M. Martn-Neira, The WISE 2000 and 2001 Campaigns in support of the SMOS Mission: Sea surface L-band Brightness Temperature Observations and their application to Multi-Angular Salinity Retrieval, *IEEE Trans. Geosci. Remote Sensing*, vol. 42, no. 4, pp. 1039-1048, 2004.
- [12] A. Camps, M. Vall-Ilossera, R. Villarino, N. Reul, B. Chapron, I. Corbella, N. Duff, F. Torres, J. Miranda, R. Sabia, A. Monerris, R. Rodríguez, "The Emissivity Of Foam-Covered Water Surface at L-Band: Theoretical Modeling And Experimental Results From The Frog 2003 Field Experiment", *IEEE Transactions on Geoscience and Remote Sensing*, vol 43, No 5, pp 925-937, 2005.
- [13] N.Reul and B. Chapron, "A model of sea-foam thickness distribution for passive microwave remote sensing applications", *J. Geophys. Res.*, 108 (C10), Oct, 2003.
- [14] N.Reul and B. Chapron, "Effects of foam on the emissivity of the sea surface at L-band", WP1300 Report, ESA contract N°15165/01/NL/SF, April 2001.
- [15] V. Cherny and V. Y. Raizer, *Passive Microwave Remote Sensing of Oceans*, wiley-praxis series in remote sensing ed. Wiley, 1998.
- [16] Dombrovskiy, L. A., and V. Y. Raizer, Microwave model of a two-phase medium at the ocean surface, *Izvestiya, Atmospheric and Oceanic Physics*, 28, 650-656, 1992.
- [17] L. M. Zurk, L. Tsang, K. H. Ding, and D. P. Winebrenner, .Monte carlo simulations of the extinction rate of densely packed spheres with clustered and non-clustered geometries, *J. Opt. Soc. America*, vol. 12, pp. 1772.1781, Aug. 1995.
- [18] L. A. Dombrovskiy, .Calculation of the thermal radiation emission of foam on the sea surface, *Izvestiya, Atmospheric and Oceanic Physics*, vol. 15, no. 3, pp. 193.198, 1979.
- [19] J. Wu, .Variation of whitecap coverage with wind stress and water temperature. *J. Phys. Oceanogr.*, vol. 18, pp. 1448.1453, 1988.
- [20] Monahan, E., and D. K. Woolf, Comments on variations of white-cap coverage with wind stress and water temperature, *J. Phys. Oceanogr.*, 19, 706-709, 1989.
- [21] Y. Quilfen, B. Chapron and D. Vandemark, "The ERS Scatterometer Wind measurement accuracy: evidence of seasonal and regional biases", *Journal of Atmospheric and Oceanic Technology*, vol 18, p 1684-1697, 2001.



ANNEX D *Technical note on geometry conventions for SMOS*

This annex aims at clarifying the conventions and formulae used for angles transformation in the SMOS L2 SSS ATBD, especially relevant in cases like Faraday rotation and change of coordinate frame from Earth to antenna.

The technical note has been generated as an independent document (smos-geom-jt-20080519.pdf) that will not be integrated in the Word working versions of the ATBD, but only in the formal PDF deliverables.



ANNEX E *Technical note on the calculation of Stokes 1 parameter in full polarisation*

Introduction

The purpose of this technical note is to propose strategies which could be used for the calculation of Stokes 1 from the MIRAS full polarization measurement mode.

In next section, the sequence of available measurements in full polarization mode is described. The following section we present ways of exploiting this sequence and shows various possible strategies for computing Stokes 1. Finally, the Stokes 1 radiometric noise computation is explained.

Polarisation sequence in full polarisation mode

Recalling dual polarization mode, correlations are obtained of antenna pairs in the same polarization state. This acquisition mode only allows deriving XX and YY brightness temperature maps from correlation products.

In addition to measuring temperatures in polarization XX and YY, full polarization mode includes measuring the cross-correlation of antenna pairs in different polarization states. In the latter case, three temperature maps are obtained (for one snapshot): XX or YY, XY and YX.

A cycle in full polarization mode exists of 26 steps spread over 4 snapshots:

1. step 1: XX measurements, as in dual pol mode
2. repeat 4 times:
 - step 2: YY, XY and YX measurements
 - step 3: YY, XY and YX measurements
 - step 4: YY, XY and YX measurements
3. step 1': YY measurements, as in dual pol mode
4. repeat 4 times:
 - step 2': XX, XY and YX measurements
 - step 3': XX, XY and YX measurements
 - step 4': XX, XY and YX measurements

Snapshot	Step	arm pol	measurements	
1	1	XXX	XX	
2	2	YYX	YY, XY, YX	} repeated 4 times
	3	XYY	YY, XY, YX	
	4	YXY	YY, XY, YX	
3	1'	YYY	YY	
4	2'	XXY	XX, XY, YX	} repeated 4 times
	3'	YXX	XX, XY, YX	
	4'	XYX	XX, XY, YX	

These steps concern MIRAS acquisitions and not the TB product itself. The latter one is an aggregation of information coming from several acquisitions.

Figure 1 shows the sequence of polarization measurements and the different steps.

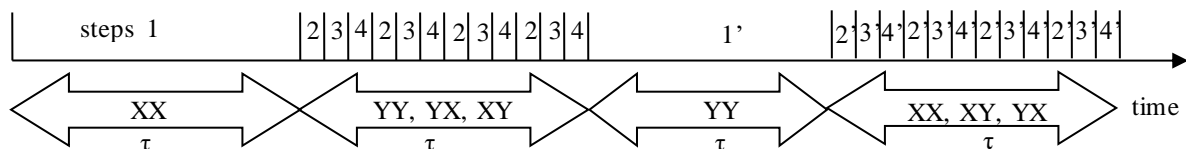


Figure 16 : Steps in one full polarization mode cycle.

In steps 2, 3 and 4, one third of the (u,v) domain is covered at each step for YY, XY and YX polarizations. At the end of the three steps (steps 2, 3 and 4), the full (u,v) domain is covered for YY, XY and YX polarizations.

Figure 2 presents, for a configuration close to that of SMOS, the first four steps.

If τ is the nominal integration time equal to 1.2 s, during one full polarization mode cycle the different steps have the following duration:

- step 1 : τ
- step 2 : $4 \times \tau/12 = \tau/3$
- step 3 : $4 \times \tau/12 = \tau/3$
- step 4 : $4 \times \tau/12 = \tau/3$
- step 1' : τ
- step 2' : $4 \times \tau/12 = \tau/3$
- step 3' : $4 \times \tau/12 = \tau/3$
- step 4' : $4 \times \tau/12 = \tau/3$

During step 1, on the full (u,v) domain, XX is observed during τ .

During the step 2, 3 and 4, on full (u,v) domain, YY is observed during $\tau/3$, XY during $\tau/3$ and YX during $\tau/3$.

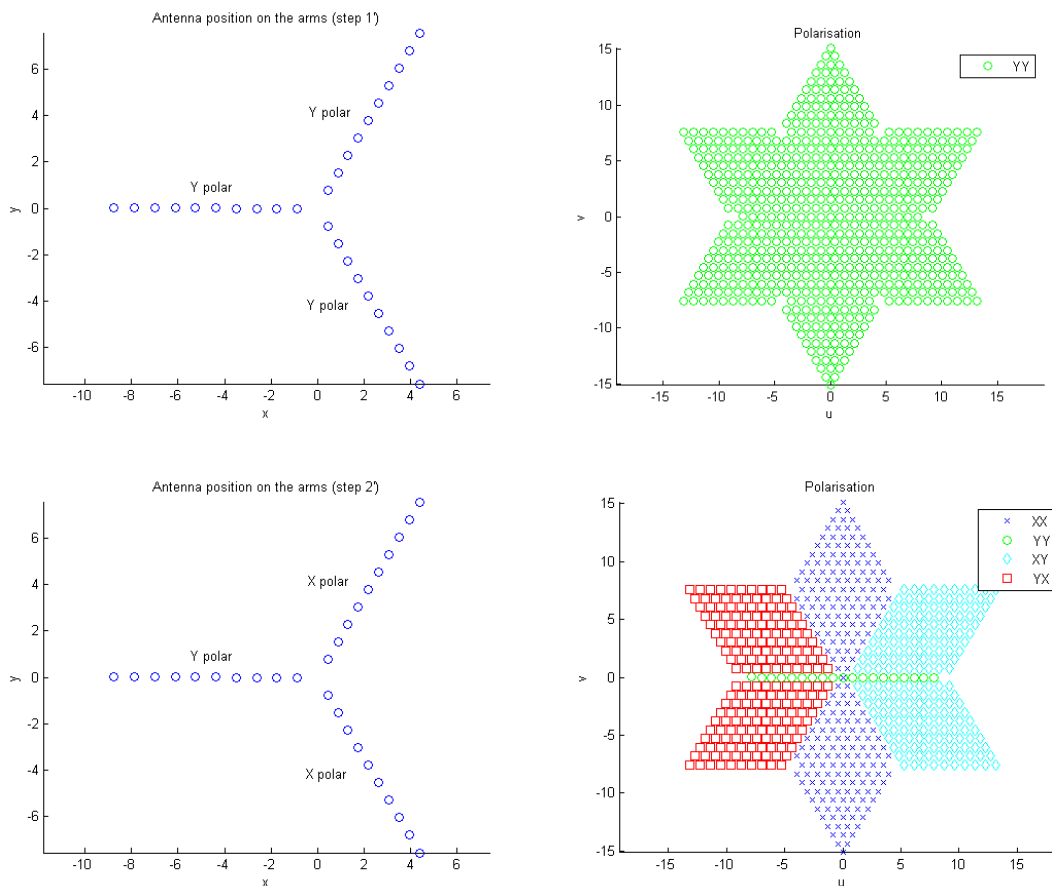
Because of the Hermitian property $XY=YX^*$, Stokes 3 and 4 are observed during $2\tau/3$ during one cycle.

Thus, during the steps 1, 2, 3, 4, 1', 2', 3', 4', on the full (u,v) domain and for the period 4τ (complete cycle), this yield:

- XX is observed during $\tau + \tau/3 = 4\tau/3$
- YY is observed during $\tau + \tau/3 = 4\tau/3$
- XY is observed during $\tau/3 + \tau/3 = 2\tau/3$
- YX is observed during $\tau/3 + \tau/3 = 2\tau/3$

Consequently, during one complete cycle, XX, YY and XY temperatures are obtained with the same integration time.

In the L1c product, after aggregation, we obtain for four consecutive snapshots representing a full cycle:



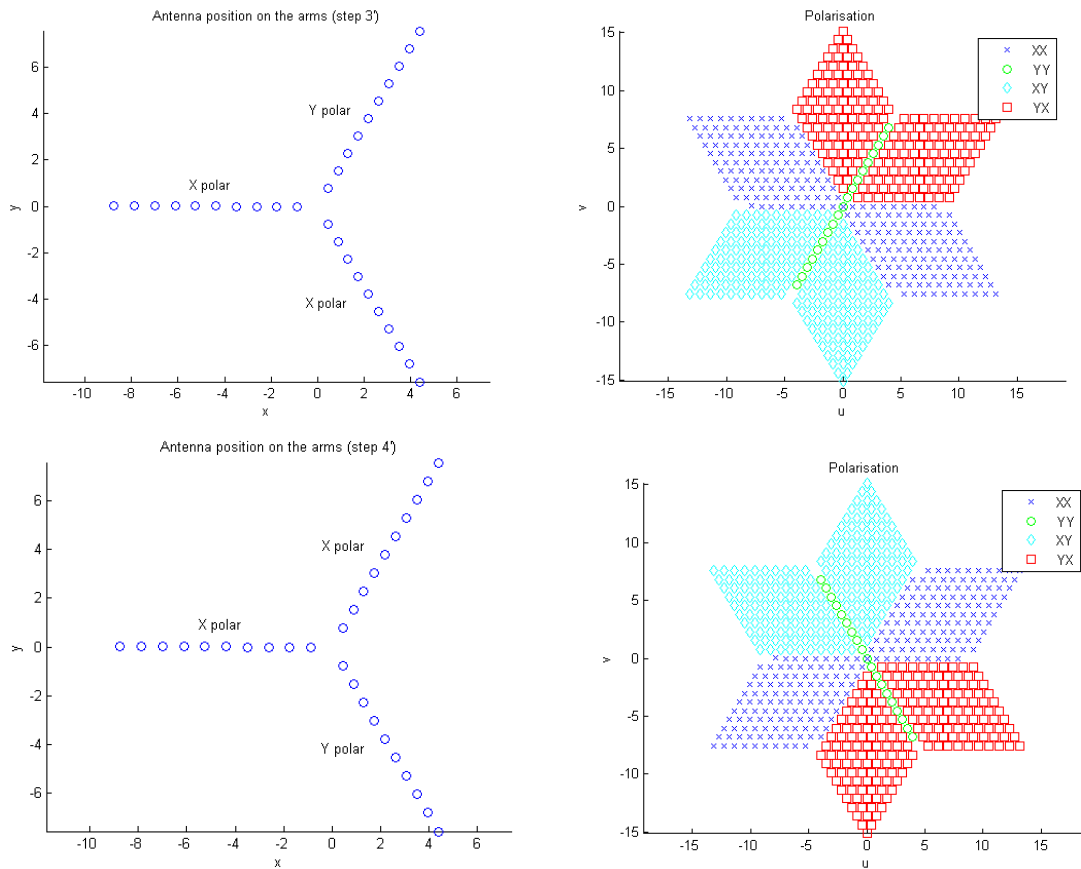


Figure 17 : Four steps (1', 2', 3' and 4') in full polarization mode. Top: the receivers of the three arms switch to Y polarisation. In the corresponding visibility domain, all baselines are YY. Middle and bottom: the receivers of two arms are in opposite polarisation as the receivers of the third arm. In such cases, baselines are XX, YY, XY or YX.

- snap1: TB_XX1 (real number) -> corresponds to step 1
- snap2: TB_YY2 (real number) -> corresponds to step 2, 3 and 4 (repeated 4 times)
- snap2: TB_XY1 (complex number) -> corresponds to step 2, 3 and 4 (repeated 4 times)
- snap3: TB_YY1 (real number) -> corresponds to step 1'
- snap4: TB_XX2 (real number) -> corresponds to step 2', 3' and 4' (repeated 4 times)
- snap4: TB_XY2 (complex number) -> corresponds to step 2', 3' and 4' (repeated 4 times).

Stokes 1 computation strategy

In section 2, we noted that:

- A full cycle is described on a 4τ integration time, contrary to dual polarization mode which is described on a cycle of 2τ .
- In contrast to dual polarization, polarizations XX and YY (integrated over a period of τ) are never adjacent but are always separated by τ .
- The radiometric noise associated to XX and YY varies according to the integration time by a factor $\sqrt{3}$.

Three different strategies are suggested to compute Stokes 1:

1. to use measurements from a full cycle (i.e. four snapshots),
2. to use measurements coming from step 1 and 1' only,
3. to use successive measurements without considering the cycle which is associated to them.

1. Use of measurements of a full cycle.

In this strategy, all the TB's in XX and YY polarizations are added during one full cycle in order to obtain a value of Stokes 1 per cycle. In the same way the Stokes 1 radiometric errors (quadratic sum) are obtained (Figure 18).

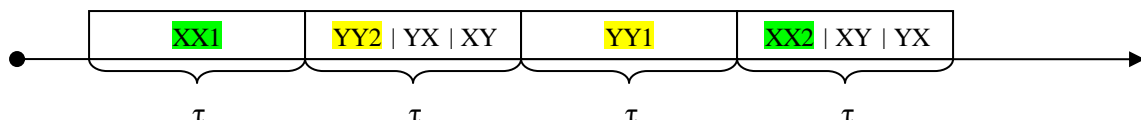


Figure 18: All measurements in XX pol (green) and all in YY pol (yellow) are summed up to yield Stokes 1.

In case of the absence of one measurement, either the measurements of the whole cycle are not processed (and then discarded), or else they are processed as follows:

- If the missing measurement is TB_XX2 or TB_YY2, only TB_XX1 and TB_YY1 are used.
- If the missing measurement is TB_XX1 or TB_YY1, only TB_XX2 and TB_YY2 are used.

In the case of the absence of two measurements, either the measurements of the whole cycle are discarded, or they are processed as follows:

ARGANS Ltd.

Commercial in Confidence

Page 308

Use, duplication, or disclosure of this document or any information contained herein is subject to the restriction on the title page of this document.

- If the two missing measurements are TB_XX2 and TB_YY2, only TB_XX1 and TB_YY1 are used.
- If the two missing measurements are TB_XX1 and TB_YY1, only TB_XX2 and TB_YY2 are used.
- If the two missing measurements are TB_XX1 and TB_YY2 or TB_XX2 and TB_YY1, measurements of the whole cycle are not processed.

In case of one or more measurements missing from one whole cycle, a test could be implemented to decide whether different measurements can be added up.

A comparison between TB_XX1 and TB_XX2, TB_YY1 and TB_YY2 or TB_XX1+TB_YY1 and TB_XX2+TB_YY2 could be done. If the comparison yields result below a certain threshold the considered cycle (or pair of measurements) is rejected.

2. Use of measurements from step 1 and 1'.

In this strategy, only step 1 and step 1' measurements (XX1 and YY1) are used in order to compute Stokes 1 without using snapshots in cross polarisation mode (Figure 19). It allows adding measurements which have the same origin than in dual polarisation mode.

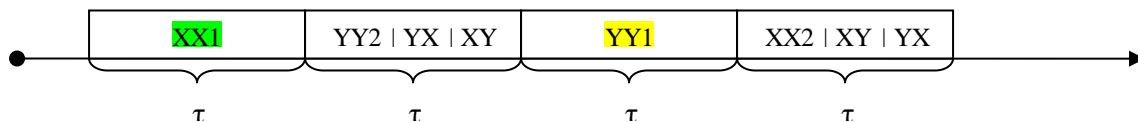


Figure 19: Only step 1 measurement (XX pol in green) and successive step 1' measurement (YY pol in yellow) are summed up to yield Stokes 1.

If one measurement is missing (step 1 or step 1'), the cycle could be shifted in order to lose the less possible of measurements.

3. Use of successive measurements

In this strategy, we do not consider a full cycle as the time basis of the measurement aggregation.

XX and YY are measurements separated by a maximal time interval between them. If the time interval between XX and YY or YY and XX is larger than some threshold, Stokes 1 is not calculated (Figure 20).

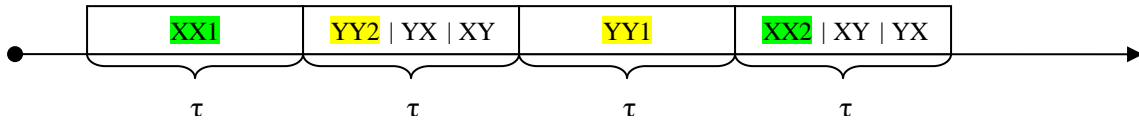


Figure 20: In this example, only successive XX and YY measurements (not necessarily from the same cycle) are selected to yield Stokes 1.

This strategy is similar to what is done in dual polarization mode, except that polarizations XX and YY can have a very different radiometric noise, depending from which step they originate (for instance, TB_XX1 could be combined with TB_YY2 and YY1 with XX2). No overlapping is considered.

Stokes 1 radiometric noise computation.

For all strategies, the Stokes 1 radiometric noise is computed using XX and YY radiometric noises added in a quadratic way:

$$\begin{aligned} \sigma_{ST1} &= \sqrt{\sigma_{XX1}^2 + \sigma_{YY2}^2 + \sigma_{XX2}^2 + \sigma_{YY1}^2}, && \text{in nominal case of strategy 1} \\ \sigma_{ST1} &= \sqrt{\sigma_{XX1}^2 + \sigma_{YY1}^2}, && \text{in nominal case of strategy 2} \\ \sigma_{ST1} &= \sqrt{\sigma_{XX1}^2 + \sigma_{YY2}^2} \text{ or } \sigma_{ST1} = \sqrt{\sigma_{XX2}^2 + \sigma_{YY1}^2}, && \text{in nominal case of strategy 3} \end{aligned}$$

where σ_{XX1} , σ_{XX2} , σ_{YY1} and σ_{YY2} are respectively the radiometric noises of XX1, XX2, YY1 and YY2 coming from L1c product.

Because no overlapping is considered, no error correlations are expected between successive Stokes 1.

References

« SMOS L1 Full Polarisation Data Processing ». ref : SO-TN-DME-L1PP-0024. Issue: 1.6. Date : 16/07/07. ESA/DEIMOS.

PhD thesis: « Calibration, Validation and Polarimetry in 2D Aperture Synthesis: Application to MIRAS », Serni Ribo Vedrilla, Univesitat Politecnica de Catalunya, 05/05

ANNEX F *Auxiliary geophysical parameters bias correction*

A separate document (SMOS ECMWF Pre-Processor, SO-TN-GMV-GS-4405) describes the geophysical auxiliary data needs of the L2 Ocean Surface Salinity Processor, and details how the data will be obtained from ECMWF and transformed into information usable by the inversion algorithm. A first version (at that moment named SMOS Level 2 Ocean Salinity Auxiliary Geophysical Data Processor Specification, hereafter AGDP) was incorporated as an annex to the OS L2 ATBD from draft 4 in October 2005, but from issue 1.1b the annex was removed and only a section dealing with bias correction is kept here.

Given the sensitivity of surface emissivity at L-band to SST and surface roughness, we must ensure, to the extent possible, that auxiliary data be free of bias. Below we outline approaches to bias correction for SST and wind speed. Figure below shows the flow of data through the bias correction module.

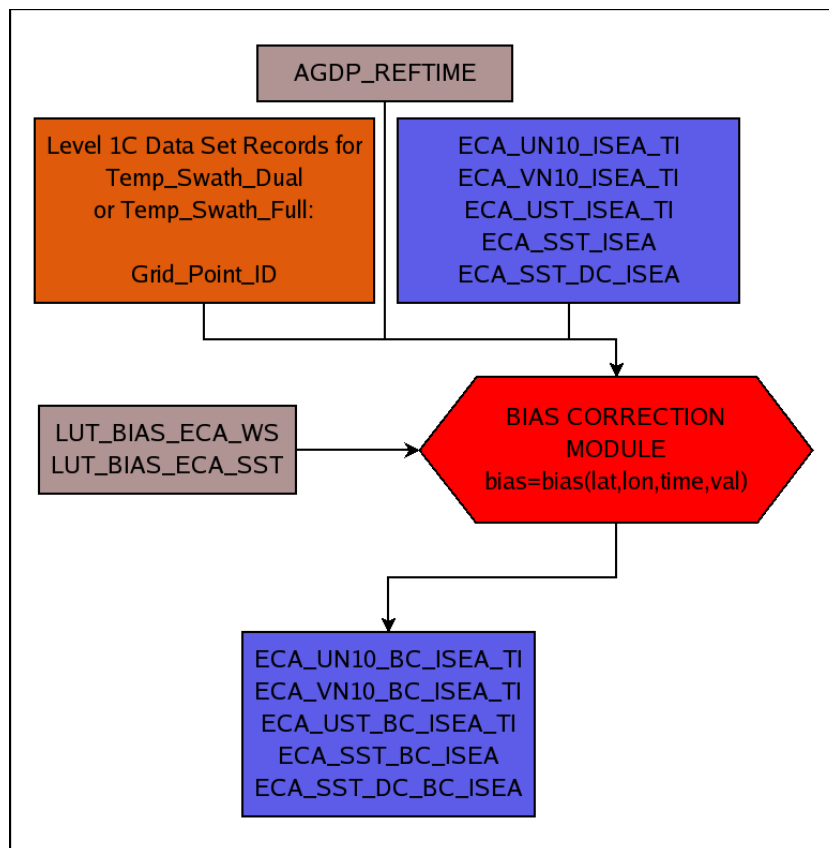


Figure 21: Schematic showing data flow through the bias correction module.

1.1 Sea Surface Temperature

Most SST analyses (including those obtained from ECMWF) are derived from much of the available in-situ and satellite observations, and many of these analyses have already been processed by bias-removal schemes. We propose including a lookup table of SST bias as a function of latitude, longitude, time of year, and SST. The lookup table will be discretized into bins of $1.0^\circ \times 1.0^\circ$ in space, monthly in time, and 2°C in SST ($0 - 30^\circ\text{C}$). The table will consume 50 Mb assuming a 4-byte representation of bias values. Multilinear interpolation from this lookup table to the location and SST for each retrieval shall be performed using all 4 coordinates.

Table 1: Lookup Table for SST Bias Removal

LUT Dimension	Starting Value	Ending Value	Interval	Number of Values
Latitude	-90°N	90°N	1°	181
Longitude	0°E	359°E	1°	360
Time of year	January	December	1 month	12
SST	0°C	30°C	2°C	16

1.2. Wind Speed

In general, it is difficult to estimate error characteristics of numerical model output. In the IFS system, error variances and covariances for assimilated quantities are required to build covariance matrices for the variation data assimilation system. How to obtain such error covariance matrices is an area of active research currently, however ECMWF routinely computes them using information from past forecasts. Bias removal in assimilated observations is also an integral part of the IFS assimilation system, but methods to obtain required bias adjustments are generally very approximate.

One approach to determining error characteristics is to compare ECMWF 10 m wind speed to that derived from other sources, such as buoys and scatterometers. Such comparisons have been performed in the past by various investigators.

One problem with such comparisons is the fact that all observation systems are potentially contaminated by random error and bias, and so simple model-buoy or model-scatterometer comparisons may not yield useful information on model bias and error variance. One of the more promising techniques that attempts to address this problem involves simultaneously comparing three noisy systems, which, with some assumptions, allows one to estimate the noise amplitude of all three and the bias in two of the systems.

$$\widehat{W}_i^2 = [(\alpha_i W_t + \beta_i) \cos(\phi) + \delta_i n_{xi}]^2 + [(\alpha_i W_t + \beta_i) \sin(\phi) + \delta_i n_{yi}]^2, \quad 6.4.36$$

One such “triple-collocation” technique is that of Freilich and Vanhoff (1999). To compare scatterometer, radiometer, and buoy derived wind speeds, they introduced the nonlinear noisy wind speed model

$$P(W_t) = CW_t^{c-1}A^{-c} \exp\left\{-\left(\frac{W_t}{A}\right)^c\right\} \quad 6.4.37$$

which maps a given true wind speed W_t and wind direction φ to an observed wind speed for observation system i . α_i is the wind speed gain, β_i is the wind speed bias, n_{xi} and n_{yi} represent normally distributed noise with zero mean and unit amplitude, and δ_i is the amplitude of the normally distributed random noise applied to each wind component. As shown by Freilich and Vanhoff, if we introduce 3 observing systems and if we assume that the true wind speed follows a two-parameter Weibull distribution of the form

$$P(W_t) = CW_t^{c-1}A^{-c} \exp\left\{-\left(\frac{W_t}{A}\right)^c\right\} \quad 6.4.38$$

where A and C are free parameters known as the scale and shape parameters, respectively, then it is possible to uniquely resolve all of the calibration parameters as well as the Weibull scale and shape parameters, so long as one of the observing systems has known bias and gain (typically assumed to be zero and 1, respectively). The above error model together with the Weibull distribution yields the expressions for the second and fourth order moments and cross moments, which can be used to extract the calibration coefficients for three systems. In our case, since we are interested in obtaining calibration coefficients for ECMWF, we use ECMWF IFS wind speed as one of the observing systems and we use buoys and QuikSCAT as the other two.

Figure 22 shows the distribution of true wind for a given small range of ECMWF wind speed. The blue curves show the true wind speed distribution without adjusting ECMWF for bias and gain, while the red curves show the true wind speed distribution after adjusting ECMWF for bias and gain. The standard deviation of these true wind speed distributions is a measure of the uncertainty in the true wind speed.

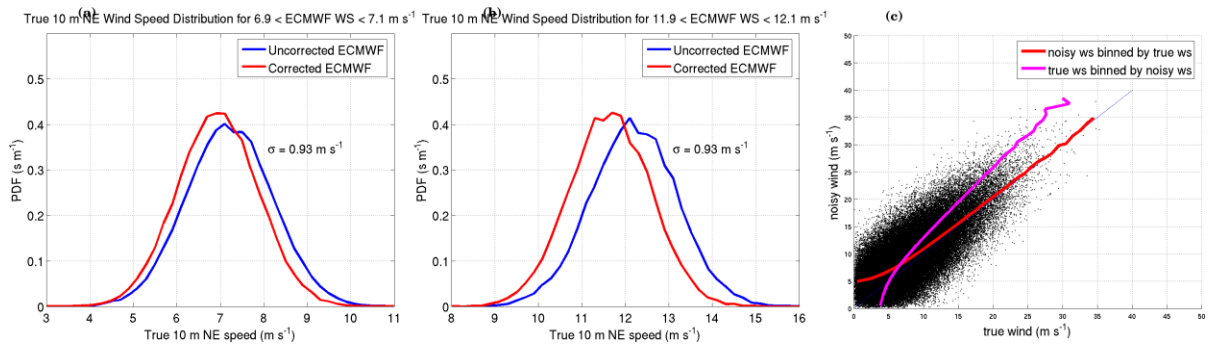


Figure 22: (a) Probability density function of the true 10 m neutral equivalent wind speed (m s^{-1}) for ECMWF ISF wind speed between 6.9 and 7.1 m s^{-1} . Blue curve shows the PDF for the uncorrected ECMWF wind speed with noise, gain, and bias derived from the triplet analysis. Red curve shows the distribution derived by retaining the noise but setting the gain to unity and bias to zero. Standard deviation of the true wind speed is shown. (b) Same as (a) except for an ECMWF wind speed range of 11.9 to 12.1 m s^{-1} . (c) Scatterplot of an idealized simulation in which a sequence of Weibull distributed true wind speed is used to generate a noisy sequence with a component noise level of 4 m s^{-1} . Red curve shows average bias of noisy wind relative to true wind averaged in true wind speed bins of 1 m s^{-1} . Magenta curve shows difference between true wind and noisy wind averaged in noisy wind speed bins of 1 m s^{-1} .

Note that there remains a residual bias associated with the noise in ECMWF wind speed, and it is anticipated that we may introduce a bias correction module to adjust for this. Figure 18c illustrates how noise in an unbiased but noisy system can lead to an apparent bias in the noisy system when the true wind data are binned by the noisy data.

We anticipate providing bias correction as a function of space, time of year, and 10 m NE wind speed. The following table summarizes the structure of the lookup table. Assuming that the values are represented as 4-byte floating point variables, the lookup table will consume approximately 50 MB. Multilinear interpolation from this lookup table to the location and wind speed for each retrieval shall be performed using all 4 coordinates.

Table 9: Lookup Table for 10 m NE Wind Speed Bias Removal

LUT Dimension	Starting Value	Ending Value	Interval	Number of Values
Latitude	-90°N	90°N	1°	181
Longitude	0°E	359°E	1°	360
Time of year	January	December	1 month	12
10 m NE wind speed	0 m/s	30 m/s	2 m/s	16

1.3. Other parameters

Besides sea surface temperature and wind speed, other auxiliary parameters (wind direction, TEC, inverse wave age, mean square slope of waves, friction velocity, significant wave height) can be also affected by bias problems.

Then the processor must be prepared to apply scale factor and offset corrections to these parameters. An approach based on Look-up Tables, like the one described for SST and wind speed, is expected to be used if necessary (see TGRD section 2.3.1.3). These additional parameters are:

LUT Dimension	Start value	End value	Interval	Number of values
Mean square slope (MSQS)	0	0.05	variable	16
Inverse wave age (omega)	0	12	variable	16
Neutral wind direction (phi_WSn)	0°	360°	5°	72
Sea surface salinity (SSS)	30 psu	40 psu	variable	10
Friction velocity from surface layer module (UST)	0 m/s	1 m/s	0.1	11
10 metre neutral equivalent wind – zonal & meridional components UN10, VN10	0 m/s	30 m/s	variable	16
Total electron count (TEC)	0 TECu	80 TECu	variable	16
Wave height (HS)	0	15m	1m	16
Cardioid model (Acard)				

1.4. Practical considerations

It might happen that during the computations some values in a grid point went out of range of the values defined in the LUTs above. In such cases warning flags will be raised: Fg_OoR_LUTAGDPT_lat (if at least one measurement went outside of the acceptable latitude limits in the auxiliary file), Fg_OoR_LUTAGDPT_lon (same for longitude), Fg_OoR_LUTAGDPT_month (if the month value went outside of acceptable limits), Fg_OoR_LUTAGDPT_param (same for value of the concerned parameter) and the parameter in the grid point will not be computed.

With the present information it is very difficult to evaluate the existence of these potential biases and their impact on the overall salinity retrieval. This will have to be analysed during the Commissioning Phase and beyond. Then, in the present configuration of the SMOS SSS L2 processor this auxiliary data bias correction will not be implemented, and it will be addressed in the reprocessing ATBD.

ARGANS Ltd.

Commercial in Confidence

Page 315

Use, duplication, or disclosure of this document or any information contained herein is subject to the restriction on the title page of this document.



End of document